



HAL
open science

Using nonlinear analysis of EEG signals in reconstructing movement trajectories

Johan Medrano

► **To cite this version:**

Johan Medrano. Using nonlinear analysis of EEG signals in reconstructing movement trajectories. Neurons and Cognition [q-bio.NC]. Université de Montpellier, 2022. English. NNT : 2022UMONS089 . tel-04122538

HAL Id: tel-04122538

<https://theses.hal.science/tel-04122538>

Submitted on 8 Jun 2023

HAL is a multi-disciplinary open access archive for the deposit and dissemination of scientific research documents, whether they are published or not. The documents may come from teaching and research institutions in France or abroad, or from public or private research centers.

L'archive ouverte pluridisciplinaire **HAL**, est destinée au dépôt et à la diffusion de documents scientifiques de niveau recherche, publiés ou non, émanant des établissements d'enseignement et de recherche français ou étrangers, des laboratoires publics ou privés.

THÈSE POUR OBTENIR LE GRADE DE DOCTEUR DE L'UNIVERSITÉ DE MONTPELLIER

En Systèmes Automatiques et Micro-Électroniques

École doctorale Information, Structures, Systèmes

Unité de recherche UMR 5506

USING NONLINEAR ANALYSIS OF EEG SIGNALS IN RECONSTRUCTING MOVEMENT TRAJECTORIES.

Présentée par Johan Medrano
le 09 Décembre 2022

Sous la direction de Sofiane Ramdani
et Abderrahmane Kheddar

Devant le jury composé de

Philippe Faure, Directeur de Recherche, CNRS
Julien Modolo, Chargé de Recherche, HdR, INSERM
Annick Lesne, Directrice de Recherche, CNRS
Viktor Jirsa, Directeur de Recherche, CNRS
Sofiane Ramdani, Maître de Conférence, Université de Montpellier
Abderrahmane Kheddar, Directeur de Recherche, CNRS

Rapporteur
Rapporteur
Examinatrice, *Présidente*
Examineur
Directeur de thèse
Directeur de thèse



UNIVERSITÉ
DE MONTPELLIER

Abstract

Electroencephalography (EEG) is a widely-used noninvasive method to record brain activity. The high time resolution of EEG signals makes it a convenient method to analyze the time course of cortical activity during a prescribed task. Here, we focus on the task of reconstructing self-paced upper-limb movements directly from EEG signals. Numerous studies reported coherence between motoneuron activity and cortical activity in motor areas during motor tasks. Motoneuron activity relates to muscle force and thus to joint torque. Therefore, it is reasonable to presume that cortical activity reflects some aspects of joint kinematics during movement. However, EEG only captures a partial and filtered version of cortical activity. Our objective is to evaluate to what extent joint trajectories can be reconstructed from EEG signals.

We address identifying features and locations of EEG signals that may reflect joint kinematics. First, we investigate measures to represent EEG signals. As EEG signals exhibit properties of nonlinear dynamical systems, we use complexity measures from chaos theory and statistical physics to complement classical spectral features in characterizing EEG signals. The quality of the complexity measures considered here depends on carefully selecting a resolution parameter. We propose a novel approach to determine this parameter that allows robust estimation of the measures. We validate our method on both simulated and real-world EEG data. Second, we evaluate the correlation of EEG complexity measures with EMG activity and joint kinematics. We recorded EEG, electromyography (EMG), and joint trajectories of 9 subjects performing self-paced cyclic elbow movements. By building statistical parametric maps of nonlinear EEG features, we identify the locations and features most correlated with movement.

We then focus on reconstructing movement trajectories from EEG signals. In particular, we observe that the performance of models reconstructing motion trajectory from EEG signals is generally evaluated with correlation coefficients. We show that the test distribution of the coefficient degenerates for strongly correlated series such as movement trajectory. In that case, the test distribution of the correlation coefficient can be approximated by correcting its number of degrees of freedom. We propose a new parametric approach to estimate the number of degrees of freedom, which gives the appropriate test statistics. In light of the corrected distribution, we show the limited performances of models decoding movement trajectories from EEG signals. Finally, we construct a biologically-plausible model of the task involving a dynamic arm, a Hill-type muscle, a model of the spinal cord, and a neural mass model. We show perspectives and limitations arising from using a complex biophysical model with a state-of-the-art Bayesian inversion scheme.

Contents

Abstract	i
Contents	iii
List of Figures	vii
List of Tables	xi
Acknowledgments	xiii
1 Introduction	1
1 Preamble	1
2 Estimating nonlinear complexity measures	1
3 Finding the appropriate application	2
4 Reconstructing movement trajectories	5
5 Another approach to the question	6
6 Overview	7
2 Selecting a threshold parameter to compute nonlinear measures	9
1 Introduction	9
2 Correlation sum and correlation dimension	11
3 Kernel density estimation	11
4 A reference rule for the optimal radius	12
4.1 Criterion to select the radius	12
4.2 Derivation of a reference rule for the optimal radius	13
4.2.a Estimation of the spread \hat{s}	13
4.2.b Derivation of the reference factor $\alpha_{p,d}$	14
4.3 Identification of a meaningful range for a variable radius	14
5 Estimation of the correlation dimension	15
5.1 The Grassberger and Proccacia algorithm	15
5.2 Procedure for generating reconstructed trajectories	15
5.3 Numerical results for the radius range	15
5.4 Influence of the time series length	16
5.5 Influence of observational white noise	19

6	Estimation of Kolmogorov-Sinai entropy using recurrence plots	20
6.1	Recurrence plots and Kolmogorov-Sinai entropy	20
6.1.a	Recurrence plots	20
6.1.b	Estimating Kolmogorov-Sinai entropy from recurrence plots	20
6.2	Numerical experiments for the Hénon map	21
6.3	Application to EEG signals in the context of epilepsy	22
7	Discussion and conclusion	23
3	Identifying statistical changes in dynamical invariants	25
1	Introduction	25
2	Recurrence Quantification Analysis and dynamical invariants	26
2.1	Recurrence plot	26
2.2	Recurrence histograms	26
2.3	Recurrence quantification analysis	27
2.4	Windowed RQA: applications, limitations, and motivations	27
3	Data collection and preprocessing	29
3.1	Experiment setup	29
3.2	Data collection and preprocessing	31
3.2.a	Streaming and synchronization	31
3.2.b	Motion capture data	31
3.2.c	Electrophysiological signals	31
3.2.d	Computation of WRQA measures	32
3.3	Statistical parametric mapping	33
4	Results and discussion	35
4.1	Preliminary analysis of movement data	35
4.2	EEG - EMG dynamical coherence in single subjects	36
4.2.a	Single subject model	36
4.2.b	Results	36
4.3	EEG - EMG dynamical coherence in multiple subjects	38
4.3.a	Multiple subject model	38
4.3.b	Results	39
4.4	Decreased EEG complexity with movement	40
4.4.a	Related work	40
4.4.b	Results	41
4.5	Analysis of EEG-EMG dynamical coherence during continuous movement	43
4.5.a	Multiple subject model	43
4.5.b	Results	44
5	Conclusion	46
4	On degrees of freedom correction for the correlation coefficient of time series	47
1	Introduction	47
2	Problem statement	48
3	Related work	50
3.1	Preamble	50
3.2	Methods for finding the number of e.d.f.	51

3.3	Link with Welch-Satterthwaite approximation	51
3.4	Problem with current approaches	52
4	A parametric approach to estimate the effective degrees of freedom for time series	53
4.1	Asymptotic effective degrees of freedoms	53
4.2	Laplace approximation of the autocorrelation function	53
4.3	An unbiased estimator of smoothness	54
4.4	Relationship with resolution elements in neuroimaging	56
5	Numerical experiments	57
5.1	False positive rate for Gaussian processes with known smoothness	57
5.2	False positive rate for Gaussian processes with unknown smoothness	58
6	Application to movement trajectories	58
6.1	Detecting synchronous movements from motion capture data	58
6.2	Accuracy of models reconstructing movement trajectories from EEG signals	60
6.2.a	Results and discussion	62
7	Conclusion	64
5	Modelling the movement and the brain: perspectives and challenges	67
1	Introduction	67
2	Bayesian inversion of nonlinear dynamical systems	68
2.1	Kalman Filtering and generalization	68
2.2	Dynamic Expectation Maximization	69
2.2.a	Hierarchical dynamic model	69
2.2.b	Condensed notation	70
2.2.c	Variational Free Energy	70
2.2.d	Mean-field approximation	71
2.2.e	Inversion scheme	71
2.2.f	Generalized coordinates	72
2.3	Implementation details	73
2.4	Comparison of the extended Kalman filter with DEM filtering	73
3	On modelling the arm	76
3.1	Dynamic model of the arm	76
3.2	Face validity: generating and inverting some movement trajectories	78
3.3	Second-order models from classical mechanics, generalized coordinates, and generalized fluctuations	78
3.3.a	Random fluctuations in rigid body systems	78
3.3.b	Problem statement	80
3.3.c	Workaround and perspectives	82
4	On modelling musculo-spinal loops	83
4.1	Modelling the muscles	83
4.2	Modelling the spinal control loops	84
4.2.a	Type Ia and Ib afferents model	84
4.2.b	A model of the spinal cord	84
4.3	Face validity	85
4.4	Closing the loop: the problem with hierarchical models	87

5	On modelling cortical columns	87
5.1	Time-resolved inversion of neural mass models	87
5.2	Neural mass model of spectral responses	88
6	Conclusion and future work	89
6	Discussion and conclusion	91
1	Towards naturalistic experiments	91
2	Modeling multiscale systems	92
3	A systematic approach to behavior modeling	93
	Appendix	97
A	Mathematical derivation of the optimal radius	97
1	Volume of generalized balls	97
2	Derivation of a reference rule for the uniform kernel	97
3	Simplification of the reference rule for common norms	99
B	Additional figures for Chapter 3	101
C	Supplementary material for Chapter 4	111
1	Derivation of Welch-Satterthwaite approximation of some stationary processes	111
2	Additional figures	112
D	Supplementary material for Chapter 5	115
1	Proof of the embedding theorem for generalized coordinates	115
2	Parameter tables	116
3	Spectral neural mass model	119
3.1	Equations	119
3.2	Transfer functions	119
	Bibliography	123
	Présentation en français	138
	Résumé	i
	Remerciements	i
	Récapitulatif	iii
1	Préambule	v
2	Estimer des mesures de complexité dynamique	v
3	Trouver l'application appropriée	vi
4	Reconstruire des trajectoires de mouvement	ix
5	Une autre approche	x
6	Synthèse	xi

List of Figures

2.1	Sample series for the Lorenz attractor, the Rössler attractor, and the Hénon map.	16
2.2	Log-log plot of correlation sums versus radius.	17
2.3	Influence of the number of points on the estimation of the correlation dimension.	18
2.4	Estimation of the correlation dimension under different levels of noise.	19
2.5	Kolmogorov-Sinai entropy for Hénon map with different lengths n .	21
2.6	Log-Mean Square Error of the Kolmogorov-Sinai entropy estimator.	22
2.7	Kolmogorov-Sinai entropy to discriminate epileptic from healthy EEG signals.	23
3.1	WRQA measures for 4 simulated signals	29
3.2	Lorenz system initialized near an unstable fixed point.	30
3.3	Description of the experiment	30
3.4	Preprocessing pipeline for EEG (a), EMG (b), and motion capture (c) signals.	31
3.5	Sensor layout of the EEG headcap.	32
3.6	Movement statistics for all subjects and group average.	35
3.7	Typical movement trajectories for three representative subjects.	36
3.8	Design matrix for the single subject regression model.	37
3.9	Normal Q-Q plot of the residuals of DET, $\langle V \rangle$, LMAX, WENTR for subject 3.	38
3.10	Topographic maps of the LMAX measure for some subjects.	39
3.11	Design matrix for the multiple subject regression model.	40
3.12	Normal Q-Q plot of the LMAX residuals for RR, DET, LAM, and ENTR for the multiple subjects model.	41
3.13	Multiple subject SPMs for several nonlinear complexity measures.	42
3.14	DET and WENTR of EEG and biceps EMG signals during arm movements.	43
3.15	Relative change from baseline for 3RB, 4Z, and 3LB during arm hand movements.	44
3.16	Design matrix for the multiple subject regression model.	45
3.17	Multiple subject SPMs for several nonlinear complexity measures.	45
3.18	Multiple subject SPMs for several nonlinear complexity measures.	46
4.1	Pearson correlation coefficient computed from stochastic processes with Gaussian autocorrelation.	49
4.2	False positive rate of the Pearson correlation test applied to stochastic processes with Gaussian autocorrelation.	50

4.3	Correction factor, defined as the number of <i>e.d.f.</i> divided by the number of points, as a function of the smoothness parameter.	55
4.4	Distinguishing features on an image.	56
4.5	False Positive Rate of the Pearson correlation test with the correction of the number of degrees of freedom.	57
4.6	False positive rate of the correlation test with the <i>e.d.f.</i> correction proposed by Bayley and Hammersley (a) and our approach (b).	59
4.7	Sample movement trajectories showing significant correlation according to the Pearson coefficient.	60
4.8	Probability-probability plots of the bootstrap versus theoretical <i>p</i> -values.	61
4.9	Per-subject reconstruction score for right- and left-arm movements.	62
4.10	Sample executed and reconstructed movement trajectories, associated with low <i>p</i> -values and high <i>p</i> value.	63
4.11	<i>p</i> -value of the decoding accuracy of the linear decoding model versus of mean and standard deviation of movement cycles.	63
4.12	Two sample trajectories with similar correlation coefficient.	64
5.1	Comparison of EKF, EKF-RTS, and DEM algorithm to invert the Lorenz system with unknown initial state.	75
5.2	Realized phase-space trajectories for the Lorenz system and reconstructions by the EKF-RTS and DEM algorithm.	77
5.3	Schematic of 2-d arm model.	78
5.4	Sample generated and inverted trajectories of the arm model in response to a cosine torque.	79
5.5	Mean squared error between the first derivative of the position in generalized coordinates and the mean velocity.	83
5.6	A model of the spinal cord. Reproduced with permission from (Li et al., 2015).	85
5.7	Sample trajectories for the spino-musculo-skeletal model. The first row represent the variables of the spinal model, where $a \equiv \alpha$ and $g \equiv \gamma$	86
5.8	Continuous changes in slow variables inducing changes in the spectral response of an neural mass model.	90
B.1	Typical independent components marked as muscular artifacts	101
B.2	Normal Q-Q plot of the LMAX residuals for the multiple subjects model.	102
B.3	Normal Q-Q plot of the LMAX residuals for the multiple subjects model.	103
B.4	Multiple subject SPMs for several nonlinear complexity measures.	104
B.4	Multiple subject SPMs for several nonlinear complexity measures.	105
B.5	RQA measures and Sampen of EEG and biceps EMG signals during arm movements.	106
B.6	Multiple subject SPMs for several nonlinear complexity measures.	108
B.6	Multiple subject SPMs for several nonlinear complexity measures.	109
B.7	Multiple subject SPMs for several nonlinear complexity measures.	110
C.1	Sample executed and reconstructed movement trajectories, associated with low <i>p</i> -values (first row) and high <i>p</i> value (second row). Trajectories are reconstructed with the Kalman filter model.	112

C.2	<i>p</i> -value of the decoding accuracy of the Kalman filter model versus of mean and standard deviation of movement cycles.	113
D.1	Change in spectral content with model parameters.	120
D.1	Change in spectral content with model parameters.	121

List of Tables

2.1	Rounded values of the coefficient $\alpha_{p,d}$ for common norms and dimensions.	14
3.1	Definition of RQA measures from functionals and structures histograms.	28
4.1	Empirical degrees of freedoms for some common autocorrelation functions	54
4.2	Related work on decoding movement trajectories from EEG signals.	66
D.1	Parameters of the skeletal model.	116
D.2	Parameters of the muscle models.	117
D.3	Parameters of the spinal cord model.	118

Acknowledgments

The completion of this manuscript would not have been possible without the huge support of my advisors, colleagues, friends, and family. I shall first express my gratitude to my advisors, Sofiane Ramdani and Abderrahmane Kheddar. Since the very first interview for the position, which ended up in an exciting whiteboard session, I have always enjoyed the long discussions with Sofiane — nearly half of which being on cinema. Sofiane has always listened to my suggestions with consideration and provided me with thoughtful feedback, and I owe him much of my scientific assurance. I also loved working with Abderrahmane, who has always encouraged me to push back my limits. My scientific methodology really benefited from Abderrahmane sharp questions and his challenge-seeking mindset largely contributed to finding the thrilling questions that we have tried to address in the research work.

In addition, I thank Philippe Faure and Julien Modolo, for reviewing this dissertation, and Viktor Jirsa and Annick Lesne for examining this thesis. I am also grateful to Peter Zeidman and to the 4th floor office at the FIL for exciting discussions which greatly contributed to the introduction and discussion, and more in general, to my understanding of the ongoing research questions. I would also like to thank Karl Friston, for kindly sharing his extensive knowledge on Bayesian methods for dynamical systems, and for his technical suggestions on applying variational filtering to classical mechanical systems. I would like to thank Annick Lesne for kindly sharing her expertise on recurrence plots, dynamical systems, and complex systems in general. Finally, I have to thank Amaury Dechaux for thrilling night-long discussions about neuroscience, brain-computer interfaces, active inference, the Copenhagen interpretation, and many other topics.

I really enjoyed the time spent at the LIRMM, especially thanks to many friends from the Interactive Digital Humans team. I am grateful to Julien Roux, Célia Saghour, Antonin Dallard, Carole Fournier, Hugo Lefèvre, Camille Mutschler, Louise Scherrer, and many others, for all the great moments we have had nearly everyday in Montpellier. In addition, I would also like to thank Mathis Girault, Romain Barrat, Cédric Jannot, Théo Lassaube, Arnaud Lapicorey, Lucas Gavotto, as well as my family, for their continuous support since so many years. I am deeply grateful to Bruno Bidaud and Jean-Cristophe Leduc for igniting my scientific curiosity and guiding me on my academic journey.

Finally, I want to express my deepest gratitude to my parents for the constant devoted support and encouragements they have given me throughout my life, and to my brothers, for all these great moments that we always share, for having kept on following their dreams, and thus for having generated such an emulating atmosphere.

I want to tell you how I got to be a statistician. I was, of course, born in England and in 1939, I was 19 years old. I had been shooting my mouth off throughout my teens about the British Government and the fact that they were doing nothing to stop Hitler. So when war broke out in September of that year, although I was close to getting a degree in Chemistry, I abandoned that and joined the Army. They put me in the Engineers (and when I see a bridge I still catch myself calculating where I would put the charges to blow it up).

Before I could actually do any of that I was moved to a highly secret experimental station in the south of England. At the time they were bombing London every night and our job was to help to find out what to do if, one night, they used poisonous gas. Some of England's best scientists were there. There were a lot of experiments with small animals, I was a lab assistant making biochemical determinations, my boss was a professor of physiology dressed up as a colonel, and I was dressed up as a staff sergeant.

The results I was getting were very variable and I told my colonel that what we really needed was a statistician. He said "we can't get one, what do you know about it?" I said "Nothing, I once tried to read a book about it by someone called R. A. Fisher but I didn't understand it". He said "You've read the book so you better do it", so I said, "Yes sir".

— George E. P. Box, *An Accidental Statistician*

"And men believed that dream for the next forty years. They believed that prediction was just a function of keeping track of things. If you knew enough, you could predict anything. That's been a cherished scientific belief since Newton."

"And?"

"Chaos theory throws it right out the window."

— Michael Crichton, *Jurassic Park*

"With so much chaos, someone will do something stupid. And when they do, things will turn nasty."

— Alan Moore, *V for Vendetta*

Chapter 1

Introduction

1 Preamble

The initial objective of our research was to contribute to EEG-based brain-computer interfaces under the idea that EEG signals are generated by chaotic dynamical systems. Indeed, EEG signals are most commonly dealt with using linear methods such as the Fourier transform (Cohen, 2014). EEG signals have dense power spectral densities and some portions of their power spectra appear to be modulated almost independently from others. Therefore, analyzing power spectra undeniably gives an insight on the cortical responses induced by particular event or condition. However, frequency-based methods inherently integrate out the time course of EEG signals, which is often aperiodic and irregular. Therefore, analyzing the evolution of EEG signals may highlight parts of the cortical responses that are missed by classical linear analyses. In particular, looking at EEG signals through the perspective of nonlinear dynamical systems is appealing because as stated in (Lehnertz, 1999): “deterministic chaos offers a striking explanation for apparently irregular behavior, a characteristic feature of brain electrical activity”. In other words, the apparent evolution of EEG signals justifies to complete frequencies analysis with methods arising from chaos theory, without particular assumptions on the chaotic nature of brain activity (which has already been largely debated, see (Korn & Faure, 2003)). The direction followed here is that nonlinear complexity measures may be suitable to complement frequency analysis. By the term nonlinear complexity measures, we denote generically various quantities that capture some important aspects of chaotic dynamical systems, for instance fractal dimensions or metric entropies. We follow the definition of chaos as “aperiodic bounded dynamics in a deterministic system with sensitive dependence on initial conditions” (Kaplan & Glass, 1997, Sec. 1.7, p.p. 27-28).

2 Estimating nonlinear complexity measures

Having in mind that we would need compute nonlinear complexity measures, the first question that we address is a general one: how to select the parameters to estimate nonlinear complexity measures? There are three parameters that appear repeatedly in different nonlinear complexity measures. The first two parameters configure the delay embedding of a time series. Delay embedding follows from Takens theorem (Takens, 1981), which states that we can use delay coordinates to reconstruct the phase space trajectory of a time series generated by a

chaotic dynamical system, up to a nonlinear change of coordinates. Delay coordinates are vectors composed of lagged observations from the time series. The *embedding dimension* defines the dimension of the vector space of the reconstructed trajectory, i.e. the number of lagged observations in each vector. There are methods to empirically select the embedding dimension, e.g. (Cao, 1997). In general, selecting the embedding dimension is not problematic because chaotic attractors have a finite dimension; hence, nonlinear complexity measures converge to a finite value when the embedding dimension becomes large. Then, the *embedding lag* parameter defines the time lag between consecutive delay coordinates. The lag is selected from critical points of the autocorrelation function and of the mutual information such that the coordinates are mostly pairwise independent (Fraser & Swinney, 1986). The third parameter to select is the radius, also called threshold or resolution, depending on the literature. This parameter defines the size of a neighborhood in phase space and is used to construct a *correlation sum* which estimates the average number of phase-space neighbors. The correlation sum is related to several complexity measures such as the correlation dimension, the Kolmogorov-Sinai entropy, or measures from the Recurrence Quantification Analysis framework. Despite of its importance in computing nonlinear complexity measures, there were only few rigorous method to select the radius parameter.

In Chapter 2, we propose a method to rigorously select the radius parameter. We notice that the relative mean integrate squared error of the correlation sum is indeed the mean integrated squared error of a kernel density estimator. In other words, we observe that the problem of selecting the radius parameter is, to some extent, the same as selecting the optimal bin width to construct an histogram of the phase-space density. This change of perspective is important because the problem of selecting an optimal bin width has been extensively studied in the statistics literature. Thus, there is a rich variety of methods to pick from. We follow a popular method proposed in (Silverman, 1986) to derive a reference rule to select the radius. We obtain a closed-form expression which scales the radius with the number of points in the series – we can use a smaller radius when the series is longer because the point density is higher – and with the “scale” of the series – we need a larger radius when a wider volume of the phase space is occupied. Crucially, under common empirical setups, our reference rule yields values that are close to values obtained with rule-of-thumbs deduced from empirical observations. Hence, our approach justifies the validity of empirical rules found in the litterature and extends them to more general empirical conditions. We confirm the adequacy of our method with both numerical experiments and an application to EEG data.

3 Finding the appropriate application

After having identified a suitable parameter selection method to obtain robust estimates of nonlinear complexity measures, we searched for an interesting application of nonlinear complexity measures. In the literature, nonlinear complexity measures have been used to identify regimes of cortical activity during certain conditions, for instance to detect epileptic seizures (Ocak, 2009) or to recognize emotion (Yang et al., 2018). In these applications, nonlinear complexity measures are used as features for classification. Indeed, complexity measures provide a representation of the EEG signals in which the different conditions can be easily distinguished. We attempt to use nonlinear complexity measures to address a more challenging problem: re-

gressing the time course of continuous variables from EEG signals. As compared to classification use-cases, regression is a more complex problem. A classification task requires to construct a map from a source domain to a *countable* set which is usually unordered (for instance, there is no natural order between the two classes “epileptic” and “healthy” used in epilepsy detection). The countable-unordered nature of the target domain implies that classification amounts to defining decision boundaries in the source domain (Bishop & Nasrabadi, 2006). In contrast, regression needs to construct a map to an *uncountable* target domain which admits a topology (for instance, an elbow angle of 90° is larger than an elbow angle of 70° , and closer to an angle of 89° than an angle of 83°). Hence, reconstructing continuous variables from EEG signals is a challenging question because the regression map needs to link the topology of the source domain to that of the target domain.

We focused on reconstructing human arm movement from EEG signals. Our choice was motivated by several reasons. First, movement is easy to measure and restricting motion to specific joints or groups of muscles is relatively straightforward. Then, successfully reconstructing movement from EEG signals would be a first step towards several biomedical applications, for instance, exoskeleton control or movement restoration for disabled people (Chapin et al., 1999) or humanoid control (Gergondet et al., 2011) and embodiment (Aymerich-Franch et al., 2016). Finally, reconstructing movement trajectories from EEG signals seems feasible from a physiological point-of-view. Indeed, the question of reconstructing movement from cortical activity is not new. Works with electrode arrays on nonhuman primates have highlighted various properties of the motor cortex during movement (Georgopoulos et al., 1986). This resulted in applications to movement decoding in rats (Chapin et al., 1999), rhesus macaques (Wessberg et al., 2000) and finally in human MEG (Georgopoulos et al., 2005) and ECoG (Schalk et al., 2007). Following works on MEG and ECoG, researchers have tried to reconstruct movement trajectories from EEG signals. Since the first efforts of (Bradberry et al., 2010), more than twenty articles have addressed movement reconstruction from EEG signals with various degrees of success. This collection of works constitutes a valuable knowledge from which we may build methods to reconstruct movement trajectories from nonlinear complexity measures of EEG signals.

To our best knowledge, no other works used nonlinear complexity measures to reconstruct movement trajectories from EEG signals. Therefore, it is legitimate to question on the motivations with respect to our aim. Our motivation comes from various works that observe the multiscale behavior of complex systems. An important theoretical work is (Haken, 1978) which considers that systems composed of a large number of individual components may exhibit quite simple behavior. Haken is interested with framing the apparent reduction of the number of degrees of freedom of complex systems. The approach of synergetics is to realize that a few collective variables, the *order parameters*, evolve slowly in time and govern the small-scale behavior of individual components. Synergetics has been admirably applied to formulate a model of phase-synchronization during finger movements (Haken et al., 1985). To summarize, synergetics defends the idea that large and complex systems such as the brain (D’Angelo & Jirsa, 2022; Haken, 2006, 2013) may be decomposed in interacting slow collective parameters and fast individual states. This idea is also found in (Lesne, 2013), where time-scale separation is considered as a temporal equivalent to classical mean-field approaches and appears in multiscale complex systems. In the specific case of the brain, (Kiebel et al., 2008) argues that the hierarchy of temporal scales between integrated levels of sensory processing is indeed a

necessary feature to adapt to an environment which evolves at different time scales.

We may still wonder whether these theories apply to EEG signals measured during movement. The methodology to find such time-scale separation would be to analyze the time-frequency representation of EEG signals, simply because changes of the power spectra over time indicate that the spectral composition of “fast” components of the signal changes over time. Indeed, modulation of the spectral composition of EEG signals during movement has been repeatedly observed ([van Wijk et al., 2012](#)). In particular, a modulation of gamma-band activity during movement was observed for MEG ([Cheyne et al., 2008](#)) and EEG signals ([Ball et al., 2008](#)). Modulation of high-frequency activity has been also observed in the case of treadmill walking, where the stepping frequency is reflected in the amplitude of the gamma-band activity ([Seeber et al., 2015](#)). Thus, empirical results in the literature suggest that a kind of slow-fast decomposition occurs during movement. We can construct an analogous of time-frequency analysis with nonlinear complexity measures using windowing ([Zbilut et al., 2002](#)). In that case, we expect windowed nonlinear complexity measures to reflect slow changes in the dynamics of fast variables.

In summary, we support the idea that movement could be a suitable application to investigate methods to regress variables from EEG signals. Under the assumption that complex systems such as the brain admit a slow-fast decomposition, we propose to track the slow changes in the fast dynamics of EEG signals using windowed nonlinear complexity measures. Our proposition is supported by observations found in the literature, which indirectly observe a slow-fast decomposition in time-frequency representation of EEG signals during movement. We shall now identify the variable to regress from EEG signals.

Considering the neuroscience literature, there are several movement variables that we may try to regress from EEG signals. In particular, we may try to reconstruct directly a position, velocity, or acceleration. Decoding position and velocity would be motivated by observations on the behavior of neural activity in the primary motor cortex during movement ([Churchland et al., 2006](#); [Kakei et al., 1999](#); [W. Wang et al., 2007](#)), and decoding acceleration might be motivated by relation of motor cortical activity with force ([Cheney & Fetz, 1980](#); [Georgopoulos et al., 1992](#)). It is important to note that one must select a reference frame to decode position, velocity, or acceleration; for instance Cartesian or joint space. Understanding in which reference frame neural signals code movement trajectories is far from being a trivial question. Globally, it is assumed that movement is decomposed from high-level, extrinsic reference frame to low-level, intrinsic reference frame ([Bear et al., 2020](#); [Kakei et al., 2001](#)). Indeed, there is no evidence supporting that movement is decomposed in a common reference frame and it is also likely that the brain does not use any of the reference frame we are familiar with ([Wu & Hatsopoulos, 2006](#)). In contrast, the coherence between muscle activity and primary motor cortex activity during movement is well documented ([Baker et al., 1997](#); [Conway et al., 1995](#); [Mima & Hallett, 1999](#)) and does not necessitate to select a particular kinematic variable nor reference frame. Therefore in a first time, we directly focus on reconstructing some aspects of muscle activity.

In Chapter 3, we introduce our experimental setup and data gathering method. We collected movement data together with EEG and EMG signals from 9 healthy participants. Participants were asked to performed continuous, self-paced, unilateral elbow flexion/extension movements during trials of about 23 to 24 seconds. The task – self-paced movements with long durations – was selected to reproduce naturalistic movement conditions. We computed Windowed Recurrence Quantification Analysis measures of both EEG and EMG signals. Im-

portantly, we high-pass filtered both EEG and EMG signals before computing the measures to remove spurious interactions with the low-frequency components of signals. We then conducted a parametric analysis to investigate the relationships between WRQA measures of EEG and EMG signals during movement. Our results indicate that there is an apparent decrease of EEG signals “complexity” at movement onset which is maintained during movement. Indeed, the result was already reported by (Pitsik et al., 2020) and our work rigorously completes these findings with scalp maps of the correlation between WRQA measures of EEG and EMG signals during movement. We observe significant negative correlations between measures from EMG signals of the moving arm and measures for the EEG signals of the contralateral side of the brain.

4 Reconstructing movement trajectories

After observing that there are significant correlation between nonlinear complexity measures of EEG and EMG signals during movement, we try to address the question of reconstructed movement trajectories from EEG signals. Before trying to reconstruct movement from nonlinear complexity measures of EEG signals, we attempted to reproduce the literature on movement “decoding” from low-frequency EEG signals, e.g. (Bradberry et al., 2010; Ofner & Müller-Putz, 2012). The objective of this intermediate step was to gain insight on movement decoding and have a baseline to compare other methods with. Surprisingly, we observed that model used in the literature performed heterogeneously on our data. In particular, model performance seem to negatively relate to movement variability and positively relate to movement speed. Our observations motivated us to analyze more thoroughly the question of evaluating the performance of the reconstruction models.

In the literature, Pearson’s correlation coefficient is the method of choice to evaluate the performance of models reconstructing movement trajectories from EEG signals. In general, related works report correlation coefficients of ~ 0.3 , which is low as compared to the standards of the statistics literature. However, we may expect a large number of outliers on a reconstruction task and thus we might accept that a low correlation coefficient is already a good result. In other words, we may accept that a good reconstruction model would perform poorly due to the low signal-to-noise ratio of EEG signals and the presence of artifacts. Here, we accept this reasonable assumption but point out that using Pearson’s correlation coefficient as a performance metrics brings another important problem.

In Chapter 4, we investigate the behavior of Pearson’s and Spearman’s correlation coefficient in the case of time series. In particular, we report that large correlations coefficients between two random, independent series are frequently observed when the series are strongly autocorrelated. In fact, it is possible to correct the test distribution of the correlation coefficient, which is derived under the assumption that samples are uncorrelated, to take in account the autocorrelation of the series (M. Bartlett, 1935). The correction simply requires to configure the test distribution with a number of effective degrees of freedoms, i.e. the size of an independent sample which would produce the same test statistics as the autocorrelated series (Afyouni et al., 2019). The number of degrees of freedoms used to configure the test distribution is important because it determines how sharp is the test distribution and thus how is the correlation coefficient between random series likely to be observed far from 0.

We propose a parametric method to compute the number of effective degrees of freedoms which is more simple than methods found in the literature and particularly suitable for our application. Our approach fits the autocorrelation of the series using the autocorrelation of a Gaussian process, which allows us to derive an expression to compute the number of effective degrees of freedoms of a series. In addition, we use Rice's formula (Rice, 1944), which gives the expected number of zero crossings of a stochastic process (Cox & Miller, 2017). This is to express the number of effective degrees of freedoms of a stochastic process as the expected number of zero crossings of the process scaled by $\sqrt{\pi}$. We first confirm the adequacy of our method with numerical experiments. Then, we reproduce two models to reconstruct movement trajectories from low-frequency EEG signals. We take a closer look at the relationship between model performance and movement parameters under the light of the expression derived from Rice's formula. We observe that movements with long or variable peak-to-peak duration are systematically associated with insignificant reconstruction performance. In other words, reconstruction models only give significant result with fast-oscillating movements, i.e. with a large number of effective degrees of freedoms, and little movement variability.

5 Another approach to the question

The results of Chapter 4 mitigate the adequacy of models found in the literature on our data. An alternative would be to construct more complex and expressive models. More complex models could theoretically represent more complex regression maps. The extreme end of this approach would be to use deep learning models to reconstruct movement data from EEG signals. Indeed, our attempts to use deep learning models did not result in groundbreaking performances. In addition, we realized that deep learning models should be used with care on EEG signals: deep learning models may learn to reconstruct the task from artifacts rather than from brain signals. This is due to the low signal-to-noise ratio of EEG signals together with the complexity of the task and the repeated presence of artifacts due to movement. For instance, contraction of neck muscles or eye movements tracking the hand could be used by the model to reconstruct movement trajectories, as already observed in linear models which for EOG contributes largely to reconstruction performance (Ofner & Müller-Putz, 2012). Therefore, even if a deep learning model could reconstruct movement trajectory from EEG signals, it would be hard to defend that the model "decodes" movement from cortical activity. Therefore, we decided to abandon deep learning models in favor of a Bayesian approach based on "biologically-plausible" models, that is, models composed of physically meaningful parameters which can be estimated to explain the data.

The structure and parameters of such models are guided by physical or physiological evidence (or intuition). Such models are especially useful in uncover processes underlying specific medical conditions, for instance epilepsy (Cooray et al., 2016; Jirsa et al., 2014; Papadopoulou et al., 2015) or Parkinson disease (Rowe et al., 2010; van Wijk et al., 2018). The distribution of model parameters can be estimated from data using Bayesian inversion schemes that allow to modulate the values of parameters that would well explain the data (i.e. the likelihood) by expert or empirical knowledge about their distribution (i.e., priors) (Penny et al., 2011). Crucially, the specific form of Bayesian models allows to easily compare models (Stephan et al., 2009) and therefore to test hypothesis about model structure, e.g. about

the connectivity between different regions (K. J. Friston, 2011).

The kind of biologically-plausible models we are considering here is neuro-musculo-skeletal (NMS) models. NMS models incorporate together models of brain activity, of muscle activity, and of the skeletal. Although considering a general case would require complicated modeling, we can construct a simplified yet realistic model of our elbow movement task. In Chapter 5, we build up a toy NMS model of elbow movements by assembling models of the arm, of triceps and biceps muscles, and of cortical columns. Our skeletal model is a simplified two-dimensional arm model with two degrees of freedom, which simply follows rigid body dynamics. We use Hill's muscle model (Hill, 1938) for both the elbow flexor, *biceps brachii*, and elbow extensor, *triceps brachii*. Hill's muscle models give a relationship between the firing rate of the muscle motor units and the linear force generated by muscle fibers. In addition, we modeled muscle "sensing" units, type Ia and Ib afferents, using a linear relationship found in the literature (Teka et al., 2017). We then use a model of the spinal cord (Li et al., 2015), which transforms motor cortical activity into muscles inputs. Spinal cord is necessary to account for the joint exhibition-inhibition of the flexor-extensor pairs (Bear et al., 2020; Li et al., 2015). Finally, we propose to model the cortical activity using neural mass models (David & Friston, 2003).

The objective of Chapter 5 is to highlight the perspectives of using such models but also to point out current limitations of existing, state-of-the-art inversion methods. In theory, we could investigate hypotheses about the particular timecourse of cortical activity during particular movements using our NMS model. However, it is highly complicated to invert such a model or to formulate hypotheses due to the particular nature of the model considered here – a hierarchical dynamical model, i.e. a cascade of input-state-output models – and to the continuous nature of our experiment. We implemented one of the state-of-the-art method for inverting dynamical systems, namely the Dynamic Expectation Maximization (DEM) algorithm (K. J. Friston et al., 2008). DEM allows to solve triple estimation problems, i.e. estimating dynamical states, model parameters, and model hyperparameters (for instance, the noise variance). Trying to invert our NMS with DEM uncovers important problems arising when estimate a complex model with multiple temporal scales during naturalistic experiments. We believe that addressing these questions is necessary to enable exploring hypotheses about brain responses during such experiments.

6 Overview

In this thesis, we aimed to challenge estimating human arm movement trajectories considering nonlinear dynamical properties of EEG signal. We addressed several facets of the problems in our quest of achieving this goal. In Chapter 2, we propose a novel approach to determine an important parameter in estimating nonlinear complexity measures, which provides robust estimates in experimental conditions. In Chapter 3, we investigate the relationships between the nonlinear complexity measures of EEG and EMG signals during movement. To that end, we collected data in a calibrated experiment that involved self-paced elbow flexion-extension. In Chapter 4, we propose a new method to correctly estimate the significance of correlation coefficient in the case of strongly autocorrelated time series. By applying our method to common models reconstructing movement trajectories from EEG signals, we highlight potential

caveats of using the correlation coefficient as a performance metrics. In Chapter 5, we consider the question of identifying a biologically-plausible model of our task to decode movement from EEG signals, and identify perspectives as well as important challenges that arise from such a complicated modeling question. Finally, lessons learned and possible extensions of this work are presented in Chapter 6.

Chapter 2

Selecting a threshold parameter to compute nonlinear measures

Published as Medrano, J., Kheddar, A., Lesne, A., & Ramdani, S. (2021). Radius selection using kernel density estimation for the computation of nonlinear measures. *Chaos: An Interdisciplinary Journal of Nonlinear Science*, 31(8), 083131. <https://doi.org/10.1063/5.0055797>.

Nonlinear measures computed from discrete time series are widely used to characterize and identify their underlying dynamics. Such measures include entropies, dimensions and indices that are derived from recurrence plots. These indices, all based on the fundamental concept of correlation sum, have been shown to be effective in distinguishing dynamical processes based on experimental data in various fields, e.g. mechanics, physiology, etc. One crucial parameter involved in their estimation is the radius used to define neighbors in the state space. Although many rule of thumbs are available, there is a need of well-grounded theoretical criteria to correctly select this radius parameter. We propose to address this issue using Kernel Density Estimation (KDE). We first demonstrate the theoretical link between the correlation sum and the KDE framework. We then derive a loss function, whose optimization is equivalent to the minimization of the mean integrated squared error of a kernel density estimator, leading to a closed-form criterion for the radius parameter selection. These findings moreover show how the estimator bias-variance trade-off determines a range for the radius values. Numerical experiments on both simulated (chaotic, corrupted by additive noise) and real-world data are presented to assess our approach.

1 Introduction

Nonlinearity and chaos govern a wide variety of systems. They are found in neurons firing patterns (Faure & Korn, 2001) and related electrophysiological signals (Freeman, 2003), and in unpredictable changes of Earth climate (Ghil et al., 2008), to cite few examples. Nonlinear measures of such systems are made more accurate thanks to an increasing interest in numerical tools suitable for nonlinear phenomena. Indeed, data generated by such systems are more suitable to nonlinear time series analysis, which provide complementary information to traditional linear methods such as power spectrum analysis (Yang et al., 2018).

Our work focuses on estimating various metrics, measures (in the sense of quantitative indices), and invariants that rely on the computation of a correlation sum. The correlation sum is the estimator of the correlation integral, which is the mean probability that two points of the phase space trajectory of a dynamical system are neighbors (Ott, 2002), i.e. the mean probability that their distance is less than a parameter called *radius*, *threshold* or *tolerance* depending on the application domain. The correlation

sum captures important aspects of the nonlinear dynamics. Therefore, it is a fundamental quantity in various nonlinear measures: correlation dimension (Grassberger & Procaccia, 1983a), Kolmogorov-Sinai entropy (Eckmann & Ruelle, 1985; Faure & Korn, 1998; Grassberger & Procaccia, 1983b), its approximate versions ApEn (Pincus, 1991) and SampEn (Richman & Moorman, 2000), Rényi's entropies (Principe, 2010; Singh & Priéncipe, 2011), recurrence plots (Eckmann et al., 1987; Marwan et al., 2007) and related metrics of recurrence quantification analysis (Grendár et al., 2013), etc.

In different nonlinear measures, the radius appears either as a variable or as a parameter. For instance, the correlation dimension is computed by estimating a scaling factor on a logarithmic plot of the correlation sum versus the radius. In contrast, a recurrence plot displays neighboring points on a black and white image and requires to fix the radius parameter beforehand. In both cases, the radius is selected as small as possible. As a correlation sum computed from a finite-length time series will likely tend to 0 together with the radius parameter, the challenge is to identify a radius range corresponding to a statistically useful distribution of neighbors. Eckmann and Ruelle (Eckmann & Ruelle, 1985) (Section V.A.1.a.) refer to it as a “meaningful range” for the radius parameter. In our approach, we first derive an expression of the optimal radius. Then, we introduce a range to select a radius parameter or to study the properties of a function of the radius.

Several empirical rules exist to select a value or a range of values for the radius; however, they generally focused on a particular nonlinear measure (Pincus, 1991; Webber & Marwan, 2015; Zbilut & Webber Jr, 1992). Here, we introduce a method which can be applied to any nonlinear measure derived from the correlation sum. Observing that log-correlation sums are particularly used in nonlinear indices and that relative error arises from logarithmic error terms, we focus on minimizing a relative error between the correlation sum and the correlation integral. We show that minimizing the relative error term is equivalent to minimizing a well-known error used in the framework of Kernel Density Estimation (KDE), widely studied in statistics (Silverman, 1986) and in signal processing (Gunduz & Principe, 2009; Singh & Priéncipe, 2011).

KDE denotes a family of non-parametric density estimation methods which generalize the well-known histogram methods (Silverman, 1986). Simple probability functions called *kernels* are placed at sample data points to approximate the underlying density function. In the KDE framework, the choice of the kernel width influences the degree of smoothing of the estimated density function. Selecting the kernel width is known as the *bandwidth selection problem*. The latter can be formulated simply as a bias-variance trade-off. Bandwidth selection is an extensively studied problem (see (Jones et al., 1996) for a brief review) with notable usages in signal processing, e.g. mutual information estimation (Moon et al., 1995). The convergence of kernel density estimators for mixing dynamical systems was recently shown in (Hang et al., 2018).

The relation between kernel density estimation and the correlation sum is noted in (Yu et al., 2000) to estimate dynamical invariants in noisy situations. More recently, Gaussian kernels estimators of the correlation integral are applied to estimate Rényi's entropies (Erdogmus & Principe, 2006; Principe, 2010; Singh & Priéncipe, 2011). Here, KDE is used not to derive new estimators of nonlinear measures but rather as a framework providing a systematic rule to select the radius in computing nonlinear measures. We show that the radius minimizing the relative error of the correlation sum estimator is equivalent to the bandwidth minimizing the Mean Integrated Squared Error (MISE) of a density estimator (Section 3.1). Therefore, we use a bandwidth selection method from KDE to derive a closed-form expression for the optimal radius (Section 3.2) and define a “meaningful range” for the radius variable relatively to our optimum (Section 3.3). We conduct numerical experiments on well-known dynamical systems. First, we study the behavior of the correlation sum estimator in the “meaningful range” for signals of different lengths and noise levels (Section 4). Then, we estimate the Kolmogorov-Sinai entropy of both simulated and real signals, using recurrence plots computed with an optimal radius (Section 5).

2 Correlation sum and correlation dimension

Let $(\mathcal{X}, \mathcal{A}, \mu, T)$ be a measure-preserving dynamical system with $\mathcal{X} \subset \mathbb{R}^d$ and μ the invariant measure (probability distribution in the phase space invariant upon the dynamics). The *correlation integral* $c(r)$ is the mean probability to find a pair of points at two different time $x, y \in \mathcal{X}$ arbitrarily close, such that the distance between x and y is less than a small radius parameter r (Ott, 2002; Singh & Priéncipe, 2011):

$$c(r) = \mathbb{P}((x, y) : \|x - y\|_p < r) = \int_{x \in \mathcal{X}} \mu(B_r(x)) d\mu(x) \quad (2.1)$$

where $B_r(x) = \{y \in \mathcal{X} : \|x - y\|_p < r\}$ is the generalized d -dimensional ball in L_p space, with radius r and center x . In practice, an estimator of the correlation integral can be computed from a sample trajectory $x_i \in \mathbb{R}^d, 1 \leq i \leq n$ (Grassberger & Procaccia, 1983a):

$$C(r, n) = \frac{1}{n^2} \sum_{i,j=1}^n \Theta(r - \|x_i - x_j\|_p) \xrightarrow{n \rightarrow \infty} c(r) \quad (2.2)$$

where Θ is Heaviside step function and $C(r, n)$ is called the *correlation sum* (Grassberger & Procaccia, 1983a; Pesin, 2008). For small values of r , the correlation integral grows as a power law:

$$c(r) \approx \text{const} \times r^{D_2} \quad (2.3)$$

The quantity D_2 is called the *correlation dimension*.

3 Kernel density estimation

A probability density function f may be estimated by placing *smoothing kernels* at each sample point. A smoothing kernel K is defined as a valid probability density function, which satisfies (Silverman, 1986):

$$\int K(u) du = 1 \quad \forall u \in \mathbb{R}, K(u) \geq 0 \quad (2.4)$$

Without loss of generality, we introduce a scaled version of the kernel with a L_p norm and a scaling factor $h > 0$, $K_h(u) = h^{-d} K(u/h)$, which is a valid kernel when K is a valid kernel. A simple kernel is the *uniform* or *boxcar* kernel, which remains constant over a domain:

$$K_h(u) = \frac{1}{\tau_{p,d} h^d} \Theta(h - \|u\|_p) \quad (2.5)$$

where Θ is Heaviside step function and $\tau_{p,d}$ is the volume of the unit ball defined by the norm p in a d -dimensional space (see Appendix 1). Given samples $x_i \in \mathbb{R}^d, 1 \leq i \leq n$, distributed according to a density f , a kernel density estimator of f is:

$$\hat{f}_h(x) = n^{-1} \sum_{i=1}^n K_h(x - x_i) \quad (2.6)$$

While kernel density estimators are consistent for i.i.d. samples, independence between consecutive samples cannot generally be assumed for dynamical systems. Hang *et al.* (Hang *et al.*, 2018) showed that kernel density estimators are also consistent for dynamical systems with mixing properties and weakly-continuous density function (more specifically \mathcal{C} -mixing systems with pointwise α -Hölder controllable density, see (Hang *et al.*, 2018) defs. 1 and 2).

The *bandwidth* parameter h determines the “width” of the kernels and consequently the degree of smoothing of the estimator. A plethora of methods exist to select the bandwidth parameter, see (Jones *et al.*, 1996). Among existing bandwidth selection methods, minimizing the Asymptotic Mean Integrated Squared Error (AMISE), a Taylor expansion of the MISE of the estimator $\mathbb{E}[\int_{\mathbb{R}^d} (f(x) - \hat{f}(x))^2 dx]$, is

appealing for practical applications as it allows to derive a closed-form expression of an approximately optimal bandwidth (Silverman, 1986):

$$h_{\text{AMISE}} = \left[\frac{W_1(K) \times d}{n \times [W_2(K)]^2 \times W_1(\nabla^2 f)} \right]^{1/(d+4)} \quad (2.7)$$

where the functionals W_i are defined as $W_1(g) = \int_{\mathbb{R}^d} g^2(x) dx$ and $W_2(g) = \int_{\mathbb{R}^d} x_1^2 g(x) dx$, where x_1 is a scalar component of x . Reference rules (Scott, 1979; Silverman, 1986) can be easily obtained by replacing the unknown quantity $W_1(\nabla^2 f)$ with the quantity computed using a reference distribution, generally a Gaussian distribution.

4 A reference rule for the optimal radius

To derive the expression of an optimal radius, we proceed as follows. First, we show that the radius minimizing the relative error of the correlation sum estimator is equivalent to the bandwidth minimizing the MISE of a particular density estimator. Second, we derive the closed-form expression of the radius minimizing the AMISE of the estimator. Finally, we identify a meaningful range to select a variable radius.

4.1 Criterion to select the radius

The correlation integral, $c(r) = \mathbb{E}_\mu [\mu(B_r(x))]$, is generally estimated by the correlation sum, $\hat{C}(r, n) = n^{-1} \sum_{i=1}^n \hat{\mu}(B_r(x_i))$ (Eq. (2.1) and Eq. (2.2)). To obtain a good estimation of the correlation sum, we shall minimize the error between an estimator of the invariant measure of a ball, $\hat{\mu}(B_r(x))$, and the true quantity $\mu(B_r(x))$. However, minimizing such error is not sufficient to provide a good estimation for small r : the scale of the error decreases with r and systematically leads to the trivial solution $r = 0$. Indeed, when r decreases, the absolute error decreases while the relative error is multiplied by a factor proportional to $1/r$ (Eq. (2.3)) and consequently blows up. Therefore, we want to find the radius minimizing a relative error criterion on $\hat{\mu}(B_r(x))$. Let λ be the Lebesgue measure, such that $\lambda(B_r)$ is the volume of a ball with radius r . We use the fact that $\mu(B_r(\cdot))$ is proportional to r (see (Eckmann & Ruelle, 1985), Section V.A.) and consequently that $\mu(B_r(\cdot)) \propto \lambda(B_r)$ to simplify the expression of the relative error and express the following local relative error:

$$L(r, x) = \mathbb{E} \left[\left(\frac{\mu(B_r(x)) - \hat{\mu}(B_r(x))}{\lambda(B_r)} \right)^2 \right] \quad (2.8)$$

where the expectation is taken over samples used to construct the estimator. Given a fixed r , $\mu(B_r(\cdot))$ is a bounded function on \mathcal{X} . We denote ρ the normalized density of $\mu(B_r(\cdot))$, such that

$$\rho(x) = \frac{\mu(B_r(x))}{\int_{\mathcal{X}} \mu(B_r(x)) dx} = \frac{\mu(B_r(x))}{\lambda(B_r)} \quad (2.9)$$

and, similarly, $\hat{\rho}_r(x) = \hat{\mu}(B_r(x)) / \lambda(B_r)$ the estimator of the normalized density ρ . After replacing in Eq. (2.8), we obtain:

$$L(r, x) = \mathbb{E} \left[(\rho(x) - \hat{\rho}_r(x))^2 \right] \quad (2.10)$$

Then, integrating Eq. (2.10) over possible values of x gives a global criterion to select the optimal radius r_{opt} :

$$r_{\text{opt}} = \arg \min_r \mathcal{L}(r) \quad (2.11)$$

where

$$\mathcal{L}(r) = \int_{\mathcal{X}} \mathbb{E} \left[(\rho(x) - \hat{\rho}_r(x))^2 \right] dx \quad (2.12)$$

With simple manipulations, we see that Eq. (2.12) is indeed the MISE between the estimator of the normalized density $\hat{\rho}_r$ and the true normalized density ρ (Silverman, 1986). Finally, $\hat{\rho}_r$ can be identified by replacing $\hat{\mu}(B_r(x))$ with $\hat{\rho}_r$ in the expression of the correlation sum estimator (Eq. (2.2)):

$$C(r, n) = \frac{\lambda(B_r)}{n} \sum_{i=1}^n \hat{\rho}_r(x_i) = \frac{1}{n^2} \sum_{i,j=1}^n \Theta(r - \|x_i - x_j\|)$$

yielding

$$\hat{\rho}_r(x) = \frac{1}{n\lambda(B_r)} \sum_{i=1}^n \Theta(r - \|x - x_i\|) \quad (2.13)$$

As $\lambda(B_r^{p,d}) = \lambda(B_1^{p,d})r^d$ (1), we observe that $\hat{\rho}_r$ is a kernel density estimator with a uniform kernel and a bandwidth parameter r (Eq. (2.5)). Hence, it follows from Eq. (2.11) that the bandwidth minimizing the MISE of the estimator $\hat{\rho}_r$ can provide a good approximation of the optimal radius r_{opt} minimizing the relative error on the correlation sum estimator. Moreover, the AMISE method (Eq. (2.7)) can be used to approximate r_{opt} with a simple, closed-form expression that resembles to the empirical rules currently used. In the next section, we use the AMISE minimization method to derive a reference rule for the optimal radius.

4.2 Derivation of a reference rule for the optimal radius

As presented in section 3, a Taylor expansion of the MISE can be used to derive a closed-form expression of the optimal bandwidth for an estimator. A particular interest for this method is motivated by the possibility of deriving a closed-form expression of the optimal bandwidth. We use a reference Gaussian distribution in Eq. (2.7) and derive the expressions for $W_1(K)$ and $W_2(K)$ for the uniform kernel (see Appendix 2). Then, substituting these expressions into Eq. (2.7) gives the main result of the paper: a *reference rule radius* r_{opt} defined as

$$r_{\text{opt}} = \alpha_{p,d} \times \hat{s} \times n^{-1/(d+4)} \quad (2.14)$$

where $\alpha_{p,d}$, depending on the norm and dimension, rescales r_{opt} ; \hat{s} is an estimate of the spread of data; and n is the length of the trajectory in phase space.

Remark 2.1. *In practice, the phase space is reconstructed using a time delay embedding procedure (according to Takens theorem (Takens, 1981)) ; hence, if N denotes the length of the univariate time series, d the embedding dimension and τ the delay, the length of the trajectory in reconstructed phase space is $n = N - (d - 1)\tau$.*

4.2.a Estimation of the spread \hat{s}

A first choice for the spread \hat{s} is the average marginal sample standard deviation, defined by $\hat{\sigma} = \sqrt{d^{-1} \sum_i S_{i,i}}$, $S \in \mathbb{R}^{d \times d}$ is the sample covariance matrix. When the d -dimensional sample is constructed from an univariate time series using delay embedding, components on the diagonal of the sample covariance matrix are equal: $\hat{\sigma}$ is then the sample standard deviation of the time series. Alternatively, as the interquartile range IQR is a good alternative to standard deviation for non-Gaussian data (see (Silverman, 1986) for discussion), a common choice for \hat{s} is:

$$\hat{s} = \min \left(\hat{\sigma}, \frac{\text{IQR}}{1.34} \right). \quad (2.15)$$

4.2.b Derivation of the reference factor $\alpha_{p,d}$

The expression for the 1-dimensional reference factor is relatively straightforward: $\alpha_{p,1} = (12\sqrt{\pi})^{1/5} \approx 1.843$. The general closed-form expression for $\alpha_{p,d}$ is more complex (see Appendix 2, Eq. (??)); however, the expression can be simplified for common norms (Appendix 3):

$$\alpha_{1,d} = \left[(d+2)! (d+1) (\sqrt{\pi})^d \right]^{1/(d+4)} \quad (2.16)$$

$$\alpha_{2,d} = 2 \times \left[\frac{\Gamma\left(\frac{d}{2} + 2\right)}{2} \right]^{1/(d+4)} \quad (2.17)$$

$$\alpha_{\infty,d} = \left[\frac{36(\sqrt{\pi})^d}{d+2} \right]^{1/(d+4)} \quad (2.18)$$

Moreover, $\alpha_{p,d}$ is to be computed only once for common dimensions and norms. Hence, we report in Table 2.1 some values of $\alpha_{p,d}$ that can be used in Eq. (2.14).

$\alpha_{p,d}$	p			
	1	2	∞	
1	1.843	1.843	1.843	
2	2.468	2.000	1.745	
d	3	3.087	2.150	1.694
	4	3.705	2.294	1.666
	5	4.325	2.432	1.649

Table 2.1: Rounded values of the coefficient $\alpha_{p,d}$ for common norms and dimensions. The values can directly be used in reference rule radius, $r_{\text{opt}} = \alpha_{p,d} \times \min(\hat{\sigma}, \text{IQR}/1.34) \times n^{-1/(d+4)}$.

4.3 Identification of a meaningful range for a variable radius

As discussed above, some nonlinear indices require selecting the range of radius values in which the quantity is estimated. For instance, this applies to nonlinear indices quantifying a scaling exponent of the form $\lim_{r \rightarrow 0} \frac{\log \nu(B_r)}{\log r}$ (with ν a (with nu a probability distribution in the phase space), as often encountered in the chaotic systems literature (see e.g. (Ott, 2002; Pesin, 2008)). In practice, the limit $r \rightarrow 0$ is generally intractable, and estimations of ν for small r are highly variable due to poor statistics (Eckmann & Ruelle, 1985). On the other hand, at a certain point, large r will not capture the desired scaling effect. Hence, there is a range of values which must be selected to support a good estimation of the nonlinear measure. Here, we introduce our arguments to guide the selection of a meaningful range for a variable radius.

The AMISE can be expanded in an integrated squared bias and integrated variance of the density estimator, giving the following expressions of bias and variance as functions of r (Silverman, 1986):

$$\text{bias}(r) \simeq \frac{r^2}{2} W_2(K) \nabla^2 \rho(x) \quad (2.19)$$

$$\text{var}(r) \simeq \frac{W_1(K)}{nr^d} \rho(x) \quad (2.20)$$

The behavior of the relative error with r can be understood from Eq. (2.19) and Eq. (2.20): the bias is proportional to r whereas the variance is inversely proportional to r . As r_{opt} minimizes the AMISE, the bias contribution increases with r while the variance decreases with r . However, the bias term only

depends on r whereas the variance term decreases when the number of points increases. This observation –considering that usually the bandwidth minimizing the AMISE is too large, suggests selecting the optimal radius r_{opt} as the upper bound for the meaningful range. We introduce a range parameter $0 < \beta < 1$ to select the lower bound as a fraction of r_{opt} , such that the radius values lie within the range:

$$\mathcal{R} = [\beta r_{\text{opt}}, r_{\text{opt}}] \quad (2.21)$$

Due to the relations Eq. (2.19) and Eq. (2.20), we argue that the value of β shall be decreased when increasing the number of points.

5 Estimation of the correlation dimension

In the following, we investigate the behavior of the Grassberger and Proccacia algorithm for the estimation of the correlation dimension. We compare the spread and bias of estimations in the full range of available scales with estimations in the meaningful range derived in subsection 4.3.

5.1 The Grassberger and Proccacia algorithm

The correlation dimension D_2 can be expressed as:

$$D_2 = \lim_{r \rightarrow 0} \frac{\log c(r)}{\log r} = \lim_{r \rightarrow 0} \lim_{n \rightarrow \infty} \frac{\log C(r, n)}{\log r} \quad (2.22)$$

The Grassberger and Proccacia algorithm (Grassberger & Procaccia, 1983a) for the empirical estimation of the correlation dimension consists in computing the correlation sum for different values of r and plotting $\log C(r, n)$ versus $\log r$. The slope of the linear region in this logarithmic plot provide the desired estimation of the correlation dimension D_2 (Ott, 2002). Similarly to the original paper (Grassberger & Procaccia, 1983a), we use linear regression to estimate the slope.

5.2 Procedure for generating reconstructed trajectories

We conducted numerical experiments on the Lorenz system (Lorenz, 1963) ($\sigma = 10$, $\beta = \frac{8}{3}$, $\rho = 28$, $dt = 0.01$), the Rössler system (Rössler, 1976) ($a = 0.1$, $b = 0.1$, $c = 14$, $dt = 0.05$) and the Hénon map (Hénon, 1976) ($a = 1.4$, $b = 0.3$). We apply the following procedure to generate random time series of different length. After drawing a random initial state, we generate time series for all systems – using a Runge-Kutta 4/5 method for Lorenz and Rössler – such that the length of the time series is N after removing transients (sample series are presented in Figure 2.1). Then, the trajectory is reconstructed using Takens delay embedding (series from the x coordinates were systematically used). The original system dimension is used as embedding dimension d . The time delay parameter τ is set to 1 for the Hénon map and selected as the first minimum of the time-delayed mutual information function (Fraser & Swinney, 1986) for the Lorenz and Rössler systems. Please note that the length of the reconstructed trajectories, $n = N - (d - 1)\tau$, is used to compute the optimal radius using Eq. (2.14) (see Remark 2.1).

Remark 2.2. Here, we assume that the delay and embedding dimension are correctly selected as a bad phase space reconstruction deteriorates the $\log C(r, n)$ versus $\log r$ plot (Kantz & Schreiber, 2004). In practice, this embedding problem can be efficiently addressed as a plethora of methods exist to select the delay and the embedding dimension (see for instance (Kantz & Schreiber, 2004), Ch. 3.3 and Ch. 9.2).

5.3 Numerical results for the radius range

Here, we visualize the meaningful range on the log-log plot of the correlation sum versus the radius. We first generate 100 series for each system (4000 points for Rössler and Lorenz attractor, 200 points for

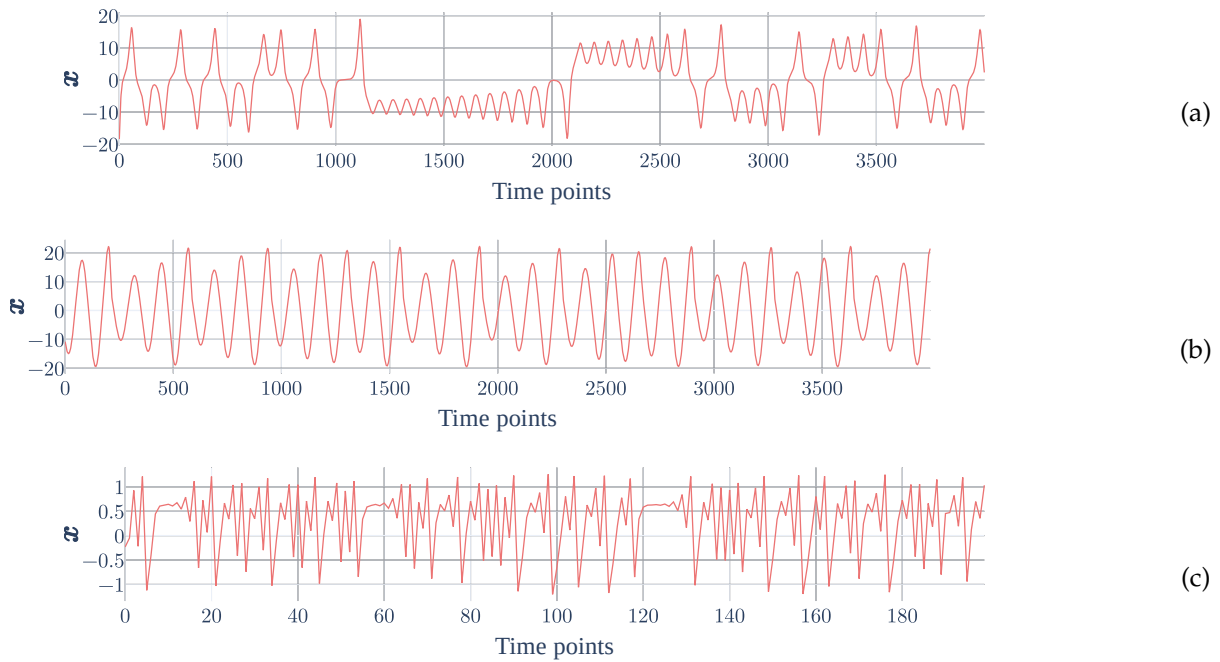


Figure 2.1: Sample series for the Lorenz attractor (a), the Rössler attractor (b) and the Hénon map (c). Series from the x coordinates were systematically used to reconstruct the trajectory using Takens delay embedding.

Hénon map, respectively), select 25 random values of radius and compute the corresponding correlation sums. We overlay the average value of r_{opt} and the ranges with arbitrary values $\beta \in \{0.01, 0.1, 0.5\}$ on the plot of $\log C(r, n)$ vs $\log r$. Results are presented in Figure 2.2. We observe that the spread of the correlation sum over the runs is low at the location of reference radius and increases when the radius is decreased. Hence, smaller values of β likely lead to higher variance estimations.

On Figure 2.2b, a knee is present around a value $\log(r_{\text{knee}}) \simeq -1$, such that the slope a_{left} in a left range $[r_0, r_{\text{knee}}]$ is higher than the slope a_{right} in right range $[r_{\text{knee}}, r_1]$. In practice, a knee may appear from the superposition of signals from non-interacting subsystems with different amplitude (Eckmann & Ruelle, 1985). In this situation, a_{left} characterizes the two subsystems while a_{right} corresponds only to the system with the largest signal amplitude. Consequently, a careful analysis of the plot of $\log C(r, n)$ vs $\log r$ might be necessary to select a range capturing the desired properties of systems under study.

5.4 Influence of the time series length

Using the procedure described in Section 5.2, we generate 100 trajectories for each length:

- (a) $N = 250, 500, 1000, 2500, 5000$ for the Lorenz system,
- (b) $N = 500, 1000, 2500, 5000, 7500$ for the Rössler system,
- (c) $N = 100, 250, 500, 1000, 2500$ for the Hénon map.

Remark 2.3. Notice that the discrepancies for the number of points used for the three systems can be justified by the resulting trajectories after time delay embedding. Indeed, when the number of points is too low, the reconstructed trajectories cannot properly reflect the dynamics nor the correct dimension of the attractor. For instance, in our experiments this was the case for time series of 100 points for the Rössler system.

We computed correlations sums for 20 values of r ranging between 10^{-8} and 2σ , where σ is the sample standard deviation. We compared the estimation using the Grassberger and Proccacia algorithm on the entire curve (the plateau on the right was omitted) with the estimation for 20 values of r in the meaningful range $(\beta r_{\text{opt}}, r_{\text{opt}})$, for values of $\beta \in \{0.01, 0.1, 0.5\}$. We show in Figure 2.3 a violin plot of

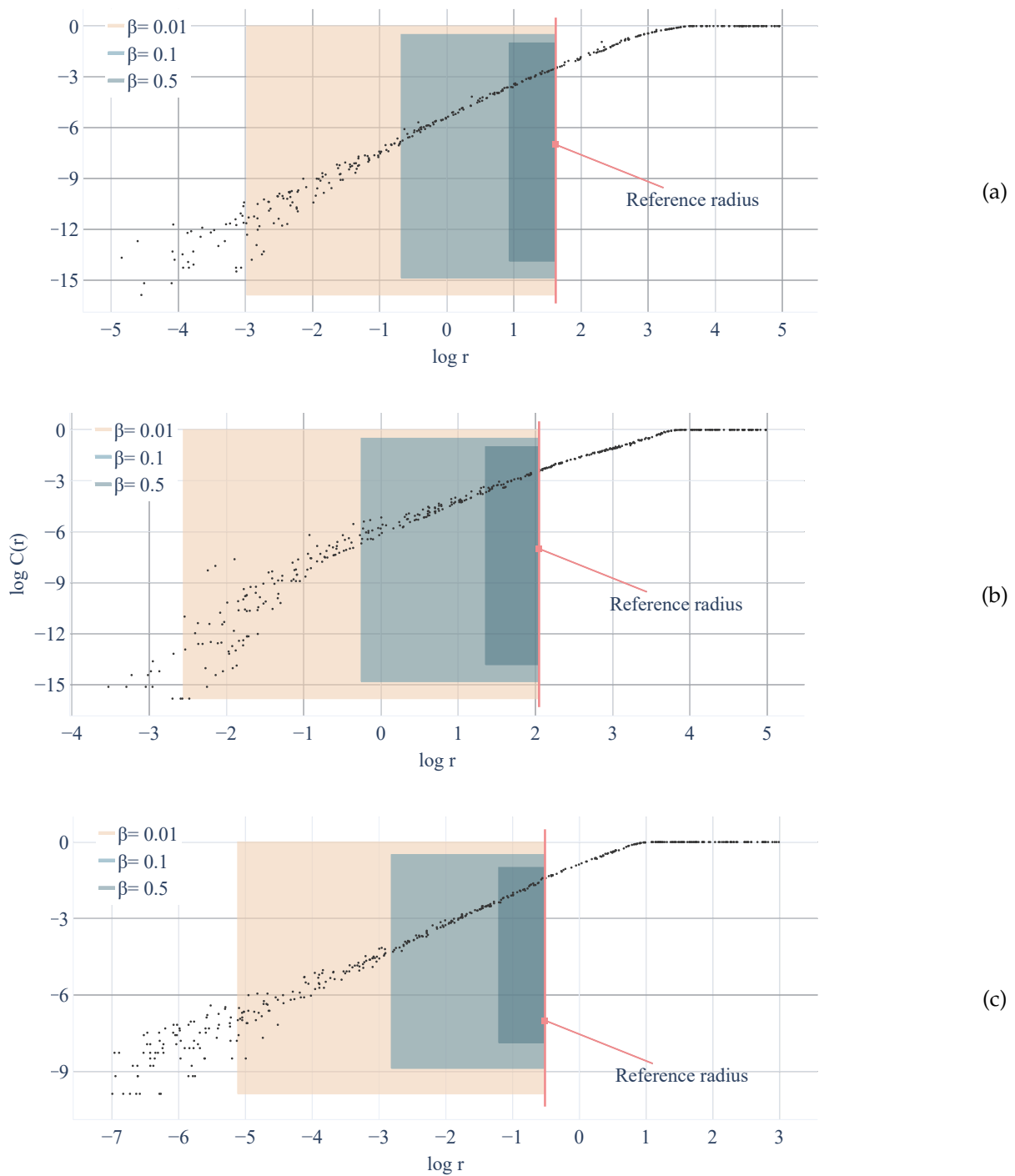


Figure 2.2: Log-log plot of correlation sums versus the radius used to estimate the correlation dimension for Lorenz (a), Rössler (b) and Hénon (c) systems. The dots correspond to estimates of the correlation sum at random values of radius for trajectories integrated from random initial states. The colored regions show different ranges defined by $[\beta r_{\text{opt}}, r_{\text{opt}}]$, with $\beta = 0.01$ (in beige), 0.1 (in light blue) or 0.5 (in dark blue).

the estimated values depending on the duration of the time series and the range used to estimate the dimension. We compare our estimations with the values of correlation dimension reported by Spratt and Rowlands (Spratt & Rowlands, 2001) for much longer series (2.049 ± 0.096 for Lorenz attractor,

1.986 ± 0.078 for Rössler attractor, 1.220 ± 0.036 for Hénon map).

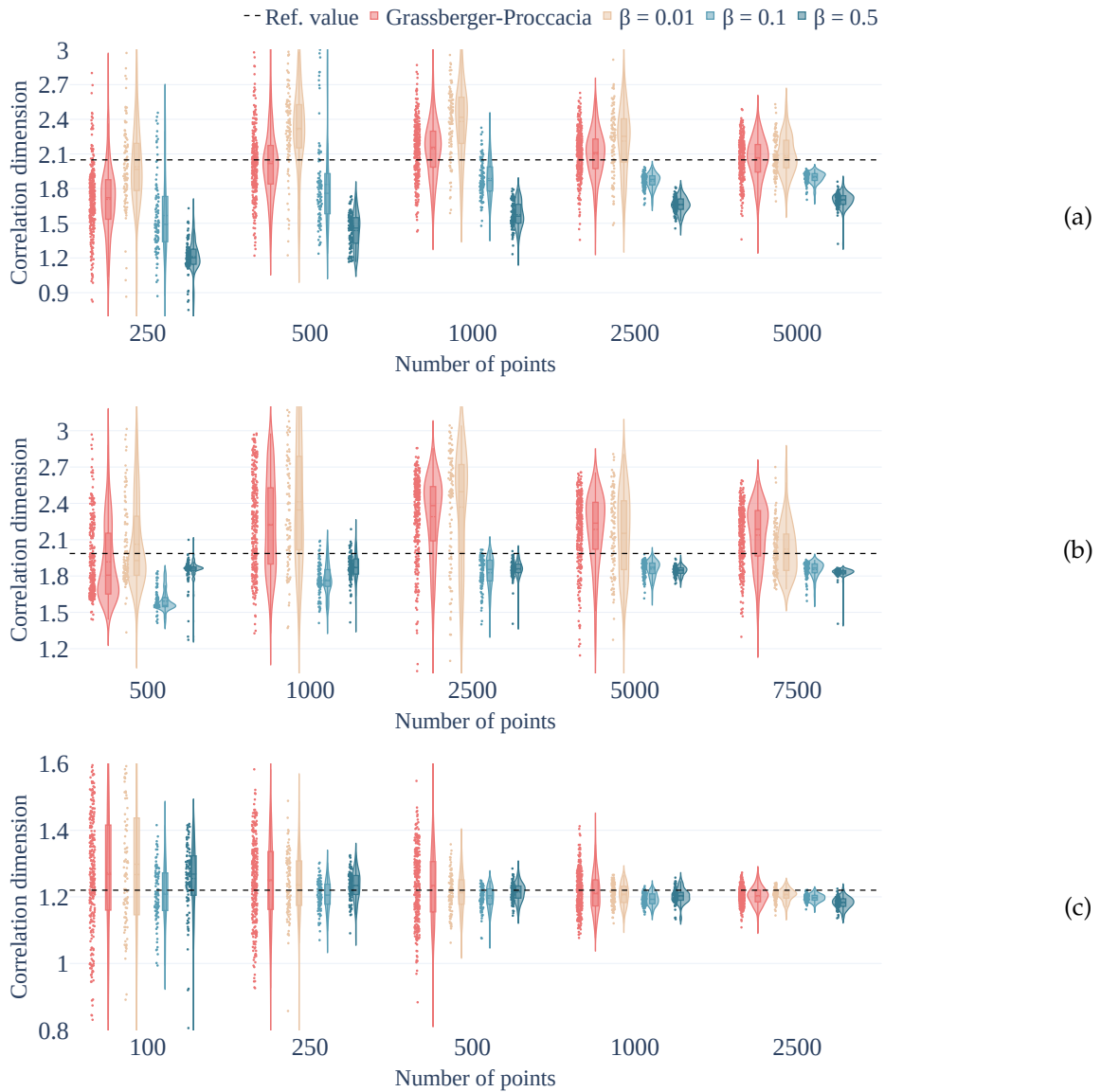


Figure 2.3: Influence of the number of points on the estimation of the correlation dimension from Lorenz (a), Rössler (b) and Hénon (c) systems. We compare the original version of the Grassberger and Proccacia algorithm (red) with an estimation of the slope in the range $[\beta r_{\text{opt}}, r_{\text{opt}}]$, with $\beta = 0.01$ (beige), $\beta = 0.1$ (light blue), $\beta = 0.5$ (dark blue).

Overall, we observe that the spread of the estimations decreases with increasing β . With $\beta = 0.01$ (beige) the result is almost similar to the original version of the Grassberger and Proccacia algorithm (red). In contrast, estimations for larger values of β are more localized, but around values of dimension further apart from the reference dimension. We observe that the number of points affects significantly the variance of the estimations for larger values of β . However, for both Rössler and Hénon attractors, the range parameter $\beta = 0.1$ (light blue) gives estimations with lower variance and bias compared to $\beta = 0.5$ (dark blue). This suggests that the range must be selected sufficiently large to provide a proper support for dimension estimation. Moreover, although the bias of the Grassberger-Proccacia algorithm is low in this setup, a single dimension estimate can be far from the true dimension. Therefore, one can favor a smaller range for r to reliably estimate a quantity slightly lower than the true dimension.

We found qualitatively similar results for Lorenz and Rössler attractors when series of different

length are obtained by downsampling an original series of fixed length (results not shown).

5.5 Influence of observational white noise

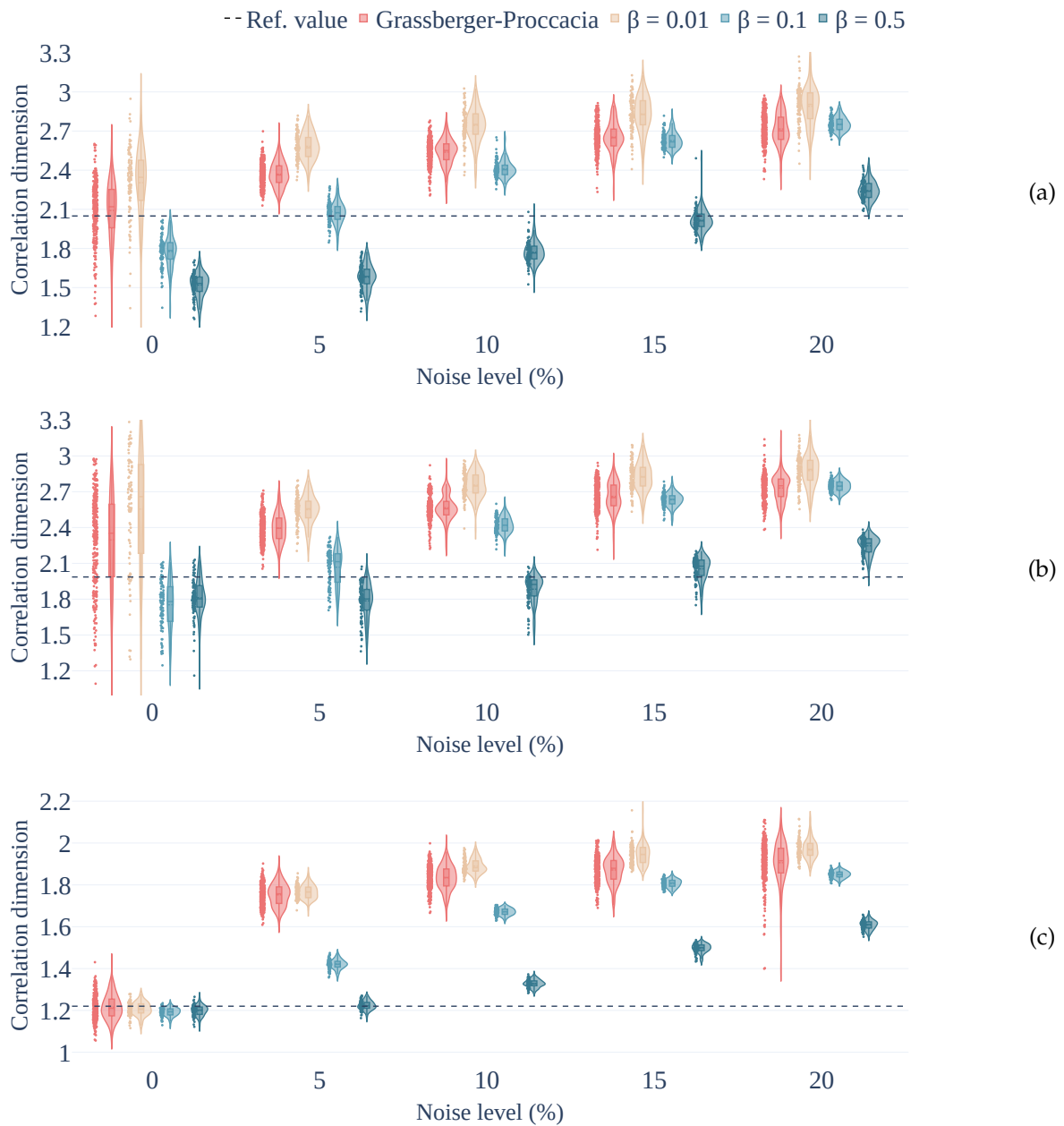


Figure 2.4: Estimation of the correlation dimension from Lorenz (a), Rössler (b) and Hénon (c) systems under different levels of additive white Gaussian noise: comparison of the original Grassberger and Proccacia algorithm (blue) with an estimation of the slope in the range $[\beta r_{\text{opt}}, r_{\text{opt}}]$, with $\beta = 0.01$ (beige), $\beta = 0.1$ (light blue), $\beta = 0.5$ (dark blue).

Finally, we investigate the influence of observational noise on the estimation of the correlation dimension in the different ranges. Observational noise is ubiquitous in practical applications and creates a knee on the plot of $\log C(r, n)$ versus $\log r$, with a dimension at the left of the knee equal to the embedding dimension (see (Eckmann & Ruelle, 1985; Grassberger & Procaccia, 2004)). Hence, the range must be selected at the right of the knee to provide good estimations of the dimension.

We generate 100 time series of 1000 points for the three systems. Each series, with standard devia-

tion σ , is corrupted with additive white Gaussian noise with standard deviation $\sigma_{\text{noise}} = k\sigma$, where k defines the noise level. As above, we compare the estimation of the original Grassberger and Proccacia algorithm with the estimation in the different ranges (the reference radius Eq. (2.14) is computed for each noise-corrupted series). We present in Figure 2.4 a violin plot for noise levels $k = 0, 0.05, 0.1, 0.15, 0.2$. For both Rössler and Lorenz attractors, we observe that a noise level of 5% is sufficient to corrupt estimations with the original version of the Grassberger and Proccacia algorithm (red) or the range $\beta = 0.01$ (beige). In contrast, larger values of β yield more consistent results under the different noise conditions. Therefore, this observation suggests that in noise conditions, the correlation dimension can be more robustly estimated from a smaller range of r .

6 Estimation of Kolmogorov-Sinai entropy using recurrence plots

In this section, we investigate the behavior of the goodness-of-fit of an estimator of a nonlinear measure with the radius parameter. We also study the reference radius inherent to Eq. (2.14) under different conditions. We use the reference radius in the construction of recurrence plots used to estimate the Kolmogorov-Sinai (KS) entropy of Hénon map and apply similar method to real electroencephalographic (EEG) signals.

6.1 Recurrence plots and Kolmogorov-Sinai entropy

6.1.a Recurrence plots

Recurrence plots (Eckmann et al., 1987) display phase-space neighbors as a 2D black-and-white image whose (i, j) element is black if trajectory points x_i and x_j are closer than a fixed radius ε . More formally, from a phase-space trajectory $\{x_i\}, 1 \leq i \leq n$, a recurrence plot $\text{RP}(\varepsilon) \in \mathbb{R}^{n \times n}$ is defined as:

$$(\text{RP}(\varepsilon))_{i,j} = \Theta(\varepsilon - \|x_i - x_j\|_p) \quad (2.23)$$

where $\Theta(\cdot)$ denotes Heaviside step function, $\|\cdot\|_p$ is a norm, usually either L_1 , L_2 , or L_∞ . The patterns in recurrence plots reflect properties of the underlying dynamical system and can be quantified using the Recurrence Quantification Analysis (RQA) framework, providing a set of powerful non-parametric visualization and characterization tools for nonlinear time series analysis. The relationship between recurrence plots (and RQA measures) and the correlation sum intuitively follows Eq. (2.23) (Grendár et al., 2013). Indeed, simple mathematical manipulations show that the *recurrence rate*, defined as the average number of recurrent points in a recurrence plot, is equal to the correlation sum (Thiel et al., 2003).

6.1.b Estimating Kolmogorov-Sinai entropy from recurrence plots

The *Kolmogorov-Sinai* (KS) or *measure-theoretic* entropy ((Kolmogorov, 1985; Sinai Ya, 1959)) measures the evolution of uncertainty with the iteration of the map of a dynamical system. The lower bound K_2 , often used as the estimate of KS entropy (Faure & Korn, 1998), is defined as (Grassberger & Procaccia, 1983b):

$$K_2 = \lim_{r \rightarrow 0} \lim_{m \rightarrow \infty} \lim_{n \rightarrow \infty} \frac{1}{\Delta t} \log \frac{C^m(r, n)}{C^{m+1}(r, n)} \quad (2.24)$$

$C^m(r, n)$ denotes the correlation sum built from a delay-reconstructed trajectory in a m -dimensional L_∞ space. While it is possible to approximate the KS entropy directly from correlation sums (Pincus, 1991; Richman & Moorman, 2000), we rather consider the method in (Faure & Korn, 1998). The latter approximates the KS entropy from the histogram of diagonal lines of length greater than m in a recurrence plot $\text{RP}(\varepsilon)$:

$$N^\varepsilon(m) = \text{card}\{(i, j) : \forall k \in \{0, \dots, m-1\}, |u_{i+k} - u_{j+k}| < \varepsilon\} \quad (2.25)$$

A diagonal of size m on a recurrence plot reflects that two trajectories stayed at a distance smaller than a threshold ε for m time-steps, or equivalently that two delay-reconstructed vectors in m -dimensional space are close under L_∞ norm. Hence, the histogram of diagonal lines, $N^\varepsilon(m)$, captures information similar to the correlation sum from delay-coordinates, $C^m(r, n)$; whereas the parameters ε and r are analogous in the two quantities. The main advantage of the Faure and Korn method is computational: while $C^m(r, n)$ is computed for several values of the embedding dimension m , the histogram $N^\varepsilon(m)$ is computed only once. Then, using the diagonal line histograms to rewrite the KS entropy Eq. (2.24) as a function of $r = \varepsilon$ gives:

$$K_2(r) = \lim_{m \rightarrow \infty} \lim_{n \rightarrow \infty} \frac{1}{\Delta t} \log \frac{N^r(m+1)}{N^r(m+2)} \quad (2.26)$$

Faure and Korn (Faure & Korn, 1998) suggest to evaluate the average slope of a $\log N^r(m)$ vs m plot for various values of r . Then, taking the limit $r \rightarrow 0$ is supposed to converge to a constant value equal to the KS entropy, K_2 , up to a scaling factor. However, selecting the smallest possible r to estimate the limit $r \rightarrow 0$ from real-world data (i.e. finite-size samples with noise) likely leads to estimations flawed by a large variance, as discussed in (Faure & Lesne, 2015). Hence, the problem is to select a value of r yielding the best possible estimations of the KS entropy. We use our reference radius (Eq. (2.14)) to compute the recurrence plot used to estimate the KS entropy. Recurrence plots and diagonal line histograms were computed using the `pyunicorn` package (Donges et al., 2015).

6.2 Numerical experiments for the Hénon map

We generate 100 time series for each length ($n = 150, 250, 500, 1500$ points) from the standard Hénon map ($a = 1.4, b = 0.3$). For each series, we use the Faure and Korn method and compute the value of $K_2(r)$, Eq. (2.26), as a function $\log r$ curve for 50 values of $\log r$ ranging from -4 to 0.5 . We then compute the reference radius (Eq. (2.14)) — using the series length n and dimension $d = 1$ — and average the values over series of same length. Results are presented in Figure 2.5.

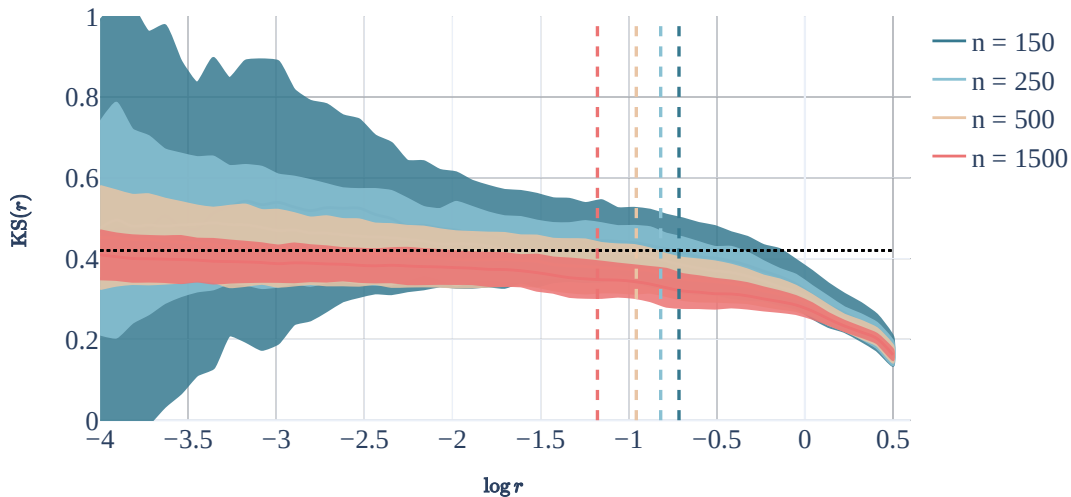


Figure 2.5: Estimation of Kolmogorov-Sinai entropy for time series from the Hénon map with different lengths n . The filled areas corresponds to the 95% (Gaussian) confidence intervals for each length. The vertical dashed lines represents the average reference radius associated to each length. The horizontal dashed line indicates the reported entropy for Hénon map, $K_2 = 0.42$.

We notice that the variance of the estimation increases for decreasing radius and decreasing number of points. This result is presumably due to a poor statistical power for small values of the radius and

short time series. However, the estimation seems to converge in average to the theoretical value ($H_{KS} = 0.42$ (Faure & Korn, 1998)) when r tends to 0. Notice that the right-most part of the plot exhibits a large bias between the estimated and theoretical entropy values. Contrary to the variance, the bias does not seem to decrease with increasing number of points. Thus this bias is more symptomatic of the radius being too high to obtain any valuable information about the Hénon map. This bias-variance trade-off is usually related to a Mean Squared Error (MSE) minimization problem.

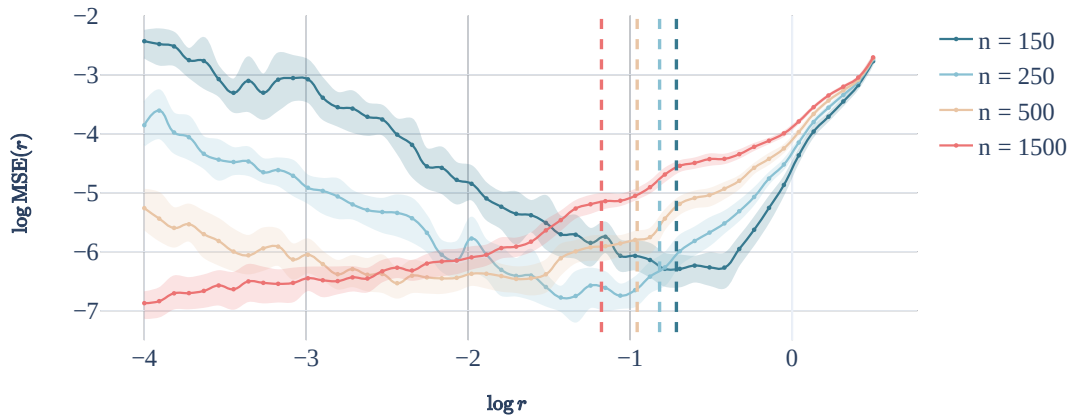


Figure 2.6: Estimation of the log-Mean Square Error of the Kolmogorov-Sinai entropy estimator as a function of the radius value (lower is better). The filled areas corresponds to the 95% bootstrap confidence interval for each length. We see that for different time series, the reference radius gives a log-MSE value between -7 and -5 .

As the MSE of an estimator quantifies the goodness-of-fit, the parameters of the estimator yielding the minimum value of MSE can be systematically selected. We numerically compute the MSE of the KS entropy estimator as a function of $\log r$ and use this plot as an objective criterion to evaluate the adequacy of our reference radius. The MSE consists in the sum of a squared bias term, measuring the difference between the theoretical value and the estimation, as well as the variance of the estimator. We use a theoretical value $K_2 = 0.42$ and all of the 100 sample series to compute the MSE, overlay the reference radius averaged over series of same length, and show the results in Figure 2.6. For short time series, we observe that the radius selected by the reference rule is systematically close to the minimum of the MSE. For longer time series, the reference radius is larger than the minimum of the curve. Nevertheless, for values of $r < r_{opt}$, the slope of the MSE curve gets flatter for increasing number of points and allows arbitrary selection of smaller radius values. We report similar observations for two other estimators of the KS entropy, the Approximate and Sample entropies (results not shown).

6.3 Application to EEG signals in the context of epilepsy

To show the viability of our approach on real-world data, we apply our radius selection procedure to estimate the KS entropy of epileptic EEG signals. A significant decrease of the EEG signal entropy at the epileptic seizure location is a common feature for automatic seizure detection (Ocak, 2008; Srinivasan et al., 2007). We use the data publicly available from the University of Bonn (Andrzejak et al., 2001), which consists in five sets of EEG data. Each set contains 100 segments of 23.6 seconds recorded at 173.61Hz (4096 points per segment), which were visually inspected for artifacts and band-pass filtered between 0.5Hz and 40Hz. Two sets contains surface EEG recorded from five healthy volunteers at rest, either with closed (set O) and opened eyes (set Z). The three other sets, consisting in signals from five epileptic patients recorded during presurgical evaluation, contain segments either from seizure-free intervals (at epileptogenic site, set F, or at the hippocampal formation of the opposite hemisphere of the brain, set

N) or during seizure (at epileptogenic site, set S).

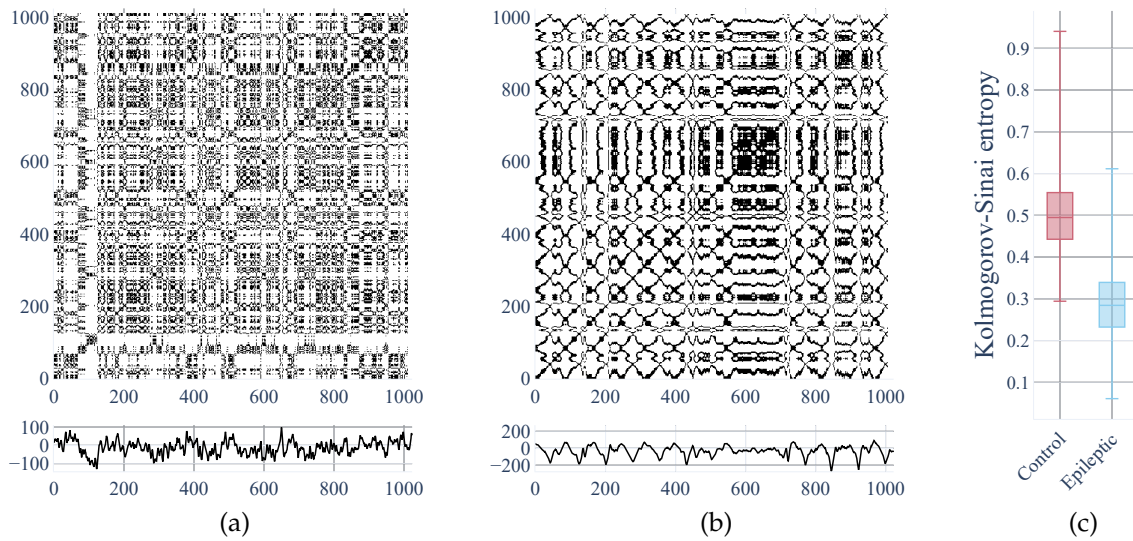


Figure 2.7: Estimation of the Kolmogorov-Sinai entropy from recurrence plots to discriminate epileptic from healthy EEG signals: (a) and (b) show sample EEG signals and recurrence plots for an healthy volunteer and an epileptic patient respectively. The value $r = 1.843 \times \hat{s} \times n^{-1/5}$ (Eq. (2.14)) is used to compute the recurrence plots from the univariate time series; (c) contains a box plot of the estimated entropies for both control and epileptic groups. As expected, the entropy values are significantly lower for the epileptic group.

Each record is divided in four segments of 1024 points. For each segment, we compute a recurrence plot with the radius set by Eq. (2.14) and estimate the KS entropy using the Faure and Korn method. Recurrence plots and signals sampled from the sets Z and F are shown in Figure 2.7a and Figure 2.7b. We present in Figure 2.7c a box plot of the KS entropy for the healthy volunteers (control group) and the epileptic patients. Our estimator gives an average KS entropy of 0.288 ± 0.005 (95% confidence interval) for the epileptic group and 0.504 ± 0.006 for the control group, which confirms an average significant decrease of the KS entropy with epilepsy, as reported in previous studies (Kannathal et al., 2005).

Finally, to compare the discrimination strength of common closed-form radius selection methods, we estimate the KS entropy with each method, perform a two-samples Z-test (epileptic versus control group) and collect the Z-score. We report a Z-score of $Z = 45.3$ (resp. $Z = 39.3$) for the $r = 0.2\sigma$ (resp. $r = 0.1\sigma$, with σ the series standard deviation) rule (Pincus, 1991), $Z = 48.9$ when the radius is set to 10% of the maximum phase space neighborhood (Zbilut & Webber Jr, 1992), $Z = 41.1$ (resp. $Z = 34.6$) when the radius is selected such that 10% (resp. 4%) of the number of points are selected as neighbors (Kraemer et al., 2018; Webber & Marwan, 2015), $Z = 54.9$ for the reference rule radius $r = 1.843 \times \hat{s} \times n^{-1/5}$ (Eq. (2.14)). Subsequently, although all methods detect significant differences between the two groups, the radius given by Eq. (2.14) gives the most statistically significant results.

7 Discussion and conclusion

We propose a new approach for selecting the radius parameter in nonlinear measures derived from the correlation sum. We first formulate a relative error function on the quantities underlying correlation sums. We show that minimizing the loss function is equivalent to minimizing the MISE of a kernel density estimator. We use the AMISE minimization method to derive a closed-form expression to select the radius. Additionally, we observe how the bias and variance of the estimator varies with the radius and derive a “meaningful” range to select a variable radius.

We investigate the behavior of the Grassberger and Proccacia algorithm for estimating the correlation dimension in radius ranges of different size. We observe that the range parameter β can be selected close to 1 for low-variance estimations, and close to 0 for low-bias estimations. However, the presence of noise in the observed signal induces typical error in the estimations and leads to favor small ranges close to the reference radius.

We then use the reference radius to construct recurrence plots for estimating the Kolmogorov-Sinai entropy from both simulated and experimental signals. In a first analysis, we reconstruct the Mean Squared Error curve of the entropy estimator for Hénon map and show that the reference radius is close to the minimum of the curve. We confirm the experimental adequacy of the method by obtaining significant results in characterizing epileptic EEG signals.

Moreover, our theoretical approach yields a reference radius that is similar to several existing radius selection methods arising from empirical or numerical experience: the radius is a fraction of the scale of the data (Pincus, 1991; Zbilut & Webber Jr, 1992) and compensates for the dimension of the data (Kraemer et al., 2018).

For the specific case of recurrence plots, (Andreadis et al., 2020) recently proposed an empirical procedure to identify an optimal radius value. They define a metric to measure the distance between recurrence plots and compute the distance between recurrence plots constructed from the same time series using increasing values of radius. The radius value is considered “optimal” when it minimizes the distance between consecutive recurrence plots, i.e. such that a slightly changing the radius has the minimal impact on the recurrence plot. The principal issues with this procedure are the computational burden of building several recurrence plots and the difficulty to reliably identify the optimum. In contrast, our method is computationally much more efficient and not restricted to recurrence plots.

Our numerical experiments suggest that the reference radius given in Eq. (2.14) can be used as a default parameter to obtain robust and significant values for a number of different nonlinear tools and measures: correlation dimension, recurrence plots, Kolmogorov-Sinai entropy. In future work, we plan to investigate the relation between our optimal radius and the embedding parameters, which play a role on the trajectories resolution in the reconstructed phase space. Additionally, we plan to use the reference radius in EEG signal processing application, notably to extract dynamical features characterizing the oscillatory dynamics of motor imagery EEG signals.

Chapter 3

Identifying statistical changes in dynamical invariants

1 Introduction

Modulation of the high-frequency components of EEG signals has been observed during movement. For instance, an increase of high frequency band power is observed in ECoG, EEG, and MEG in (Ball et al., 2008; Cheyne et al., 2008; Miller et al., 2007). Interestingly, modulation of the beta and gamma band power has been reported during walking (Seeber et al., 2014, 2015; Wagner et al., 2012), with a phase locking between the gait cycle and the power modulation. This slow modulation of fast electrophysiological signals is observed using time-frequency analysis.

Here, we claim that windowed recurrence quantification analysis (WRQA) can complement classical time-frequency analysis. Recurrence quantification analysis (RQA) refers to a set of measures that quantify dynamical properties of signals (Webber & Marwan, 2015). RQA originates from the analysis of nonlinear dynamical systems, which has been successfully applied to analysis of electrophysiological signals (Stam, 2005; Thomasson et al., 2001). The windowed version of RQA (Zbilut et al., 2002) allow to track the slow evolution of the dynamics of fast variables, where fast or slow refer to time constants being respectively lesser or greater than the window size. Therefore, WRQA is loosely the nonlinear analogous of time-frequency analysis.

We are interested in analyzing EEG during usual movement conditions. Therefore, we devised an experimental setup that consists in a simple movement task but in which several parameters are uncontrolled. Eight participants are asked to perform self-paced elbow flexion-extension movement during sessions of 23.5 seconds. Crucially, we did not specify the velocities nor the form of the movement trajectories. We collected EEG, EMG, and motion capture data while the subject is moving.

We aim at finding whether WRQA measures of EEG signals are modulated during movement. In addition, we want to investigate whether the modulation of WRQA signals depends on some parameters of movement trajectories. Besides, we are also interested in finding which type of movement parameter (e.g. position, velocity, acceleration) and which reference frame are used to encode movement in the brain. Indeed, there has been supporting evidence in favor of several hypotheses and no consensus seems to emerge (Georgopoulos et al., 1992; W. Wang et al., 2007; Wu & Hatsopoulos, 2006). Alternatively, EMG signals have been reported to correlate with EEG signals on the motor cortex and are related to force generation (Liu et al., 2019; Mima & Hallett, 1999). Therefore, investigating the relationship between EEG and EMG signals during movement contributes to question hypotheses about how the brain encodes movement.

We investigate the correlation between nonlinear measures of EEG and nonlinear measures of EMG. In other words, we try to assess whether changes in the dynamical properties of EEG signals during movement are correlated to changes in the dynamical properties of the EMG signals on the moving

arm. To assess correlation between EEG and EMG, we used a parametric approach based on statistical parametric mapping (Penny et al., 2011). Statistical parametric mapping uses a general linear model to formulate hypotheses about the presence of an effect. The statistical distribution of the model coefficients is known under a null hypothesis. Because a model is fitted at each channel, one can construct a scalp map of the statistics and identify channels where the null hypothesis is significantly violated, i.e. in our case where the EEG and EMG have correlated nonlinear measures.

The outline of this chapter is as follows. First, we present briefly recurrence plots, histograms of recurrence structures, RQA measures. Then, we introduce WRQA measures and discuss their pros and limitations. We introduce statistical testing under GLMs with SPMs, and the design matrices and contrast vectors used on our data. We then present our experimental setup, data collection, and pre-processing. Finally, we present single and group level analyses of the correlation between the nonlinear measures of EEG and EMG signals.

2 Recurrence Quantification Analysis and dynamical invariants

2.1 Recurrence plot

Let x_1, \dots, x_n be a time series of m -dimensional vectors and a threshold value $\varepsilon \in \mathbb{R}^+$. We define recurrences between two points $x_i, x_j \in \mathbb{R}^m$ as (Webber & Marwan, 2015):

$$R(i, j) = \theta(\varepsilon - \|x_i - x_j\|_p) \quad (3.1)$$

The recurrence plot is the n by n matrix R . The threshold value ε is an important parameter for constructing a recurrence plot. In the following, the threshold parameter is systematically selected using the reference rule (Equation 2.14) derived in chapter 2.

2.2 Recurrence histograms

Several measures of the recurrence quantification analysis framework can be defined from the histograms of the length of some structures: diagonal, vertical and white vertical lines (Webber & Marwan, 2015, Chapter 1). The histograms are computed by counting the occurrence of structures of length l . First, we propose the following definitions for the occurrence of structures:

Definition 3.1. Occurrence of a diagonal line of length l starting at (i, j)

$$D_{i,j}(l) = (1 - R(i-1, j-1))(1 - R(i+l, j+l)) \prod_{k=0}^{l-1} R(i+k, j+k) \quad (3.2)$$

Definition 3.2. Occurrence of a vertical line of length l starting at (i, j)

$$V_{i,j}(l) = (1 - R(i, j-1))(1 - R(i, j+l)) \prod_{k=0}^{l-1} R(i, j+k) \quad (3.3)$$

Definition 3.3. Occurrence of a white vertical line of length l starting at (i, j)

$$W_{i,j}(l) = R(i, j-1)R(i, j+l) \prod_{k=0}^{l-1} (1 - R(i, j+k)) \quad (3.4)$$

Histograms count structures on the recurrence plot (Webber & Marwan, 2015):

Definition 3.4. Histograms of diagonal, vertical, white vertical lines

$$D(l) = \sum_{i,j} D_{i,j}(l) \quad V(l) = \sum_{i,j} V_{i,j}(l) \quad W(l) = \sum_{i,j} W_{i,j}(l) \quad (3.5)$$

2.3 Recurrence quantification analysis

We define a few important RQA measures that are commonly used in the literature. These RQA measures are functionals that quantify some properties of the histograms D , V and W . In the following, we denote the histograms by h and define some useful functionals.

Definition 3.5. *Proportion of recurrent points in a structure*

$$\text{PROP}\{h\} = \frac{\sum_{k=l_{\min}}^{l-1} kh(k)}{\sum_{k=1}^{l-1} kh(k)} \quad (3.6)$$

Definition 3.6. *Average length of a structure*

$$\text{AVG}\{h\} = \frac{\sum_{k=l_{\min}}^n kh(k)}{\sum_{k=l_{\min}}^n h(k)} \quad (3.7)$$

Definition 3.7. *Entropy of the histogram of a structure*

$$\text{ENTR}\{h\} = - \sum_{k=l_{\min}}^n h(k) \log(h(k)) \quad (3.8)$$

Definition 3.8. *Maximal length of a structure*

$$\text{MAX}\{h\} = \max \{l_{\min} \leq k \leq n : h(k) > 0\} \quad (3.9)$$

We can now define common RQA measures from combining the PROP, AVG, ENTR, and MAX properties with the histograms of diagonal, vertical and white vertical lines, D , V and W .

2.4 Windowed RQA: applications, limitations, and motivations

Windowed recurrence plots and windowed RQA (WRQA) measures are recurrence plots and RQA measures computed over segments of the original time series (Zbilut et al., 2002). Given a window size κ , the recurrence plot of the segment $[t - \lfloor \kappa/2 \rfloor, t + \lfloor \kappa/2 \rfloor]$ ($\lfloor x \rfloor$ is the integer part of x) is used to compute the RQA measures of time t . This method has the advantage of being simple to implement — the RPs and RQA measures are the same but applied on a shorter time series.

Despite of their advantages, WRQA measures are possibly biased as compared to RQA measures because windowing gives a biased estimate of the time-resolved histograms. In fact, when we consider a single window of the original time series, we inevitably discard any relationship with preceding or following segments. Therefore, structures — e.g. diagonal or vertical lines — overlapping over several windows are chopped into pieces of smaller length. Hence, estimated WRQA measures are inherently biased because histograms built on WRPs overcount small structures. However, it is reasonable to assume that the bias depends mostly on the window size and thus might be considered constant for similar window size (Elbert et al., 1994). With constant bias, we can compare RQA measures between time windows because similar measures are shifted by the same bias. The constant bias assumption is discussed thoroughly in (Elbert et al., 1994, Sec.II.F.2) for some dynamical invariants. To summarize, relative changes in measures reflects important properties of the dynamics despite that windowed RQA measures do not precisely estimate RQA measures.

In fact, WRQA measures are complementary to RQA measures. WRQA provide a time-resolved information about the current dynamics of an observed system, regardless of its past and future. For instance, any nonlinear dynamical system behaves locally like a linear system when the trajectory passes close to one of its unstable fixed points¹. This phenomena can be observed in Figure 3.1 where the average length of vertical lines is significantly higher than its asymptotic value for a piece of trajectory from

¹This is a consequence of the Hartmann-Grobman theorem: dynamical systems can be linearized near their fixed points (Chicone, 1999; Guckenheimer & Holmes, 2013).

Name	Definition	Description
Determinism	$DET = PROP\{D\}$	Proportion of recurrent points involved in diagonal lines
Laminarity	$LAM = PROP\{V\}$	Proportion of recurrent points involved in vertical lines
Average diagonal length	$\langle L \rangle = AVG\{D\}$	
Trapping Time	$\langle V \rangle = TT = AVG\{V\}$	Average length of vertical lines
Mean Recurrence Time	$\langle W \rangle = MRT = AVG\{W\}$	Average length of white vertical lines
Diagonal lines entropy	$L_{ENTR} = ENTR\{D\}$	
Vertical lines entropy	$V_{ENTR} = ENTR\{V\}$	
Recurrence time entropy	$W_{ENTR} = RTE = ENTR\{W\}$	
Maximal diagonal length	$L_{MAX} = MAX\{D\}$	
Maximal vertical length	$V_{MAX} = MAX\{V\}$	
Maximal white vertical length	$W_{MAX} = MAX\{W\}$	

Table 3.1: Definition of RQA measures from functionals and structures histograms.

the Lorenz system. Another artificial example of this phenomena is presented in Figure 3.2, where the Lorenz system was initialized closely to one of the fixed points ($x_0 = 0.1 + (\sqrt{\beta(\rho - 1)}, \sqrt{\beta(\rho - 1)}, \rho - 1)$). We clearly observe that the entropy of diagonal lines, calculated WRP of 300 points, is lower for the 4000 first points. It is not surprising to find WRQA measures that differ from the global RQA measures because the Lorenz system behaves like a linear system in this region. Hence, it is reasonable to use WRQA measures to analyze the evolution of the dynamical properties of the signal.

A particularly interesting application of WRQA measures is dynamical systems where slow unobserved variables act as control parameters on the dynamics of fast observed variables. Such systems are notably considered in the field of *synergetics* (Haken, 1978) where variables called order parameters control the dynamics of the system. In particular, (Haken, 2006) argue that “the brain is conceived as a self-organizing system operating close to instabilities where its activities are governed by collective variables, the order parameters, that enslave the individual parts, i.e., the neurons”. Order parameter essentially determine the modes and characteristics of the system. Under the synergetic perspective, the dynamics of pools of neurons observed indirectly by EEG would be determined by order parameters. Importantly, order parameters may evolve in time (Haken et al., 1985). Whence, under this synergetic perspective², WRQA measures of EEG signals might be sensitive to variation of order parameters that guide neuronal activity.

²In fact, under a more general perspective the decomposition of complex systems in terms of a hierarchy of time scales provides a convenient way to approach biological systems (Kiebel et al., 2008; Lesne, 2013)

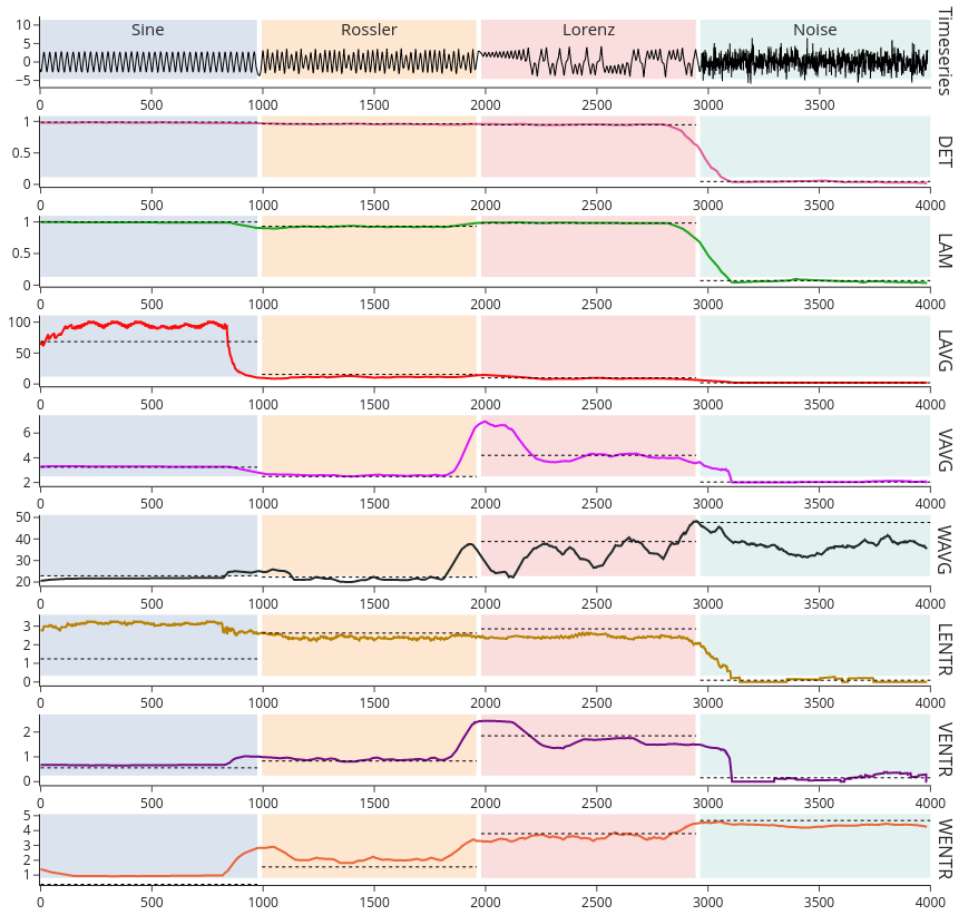


Figure 3.1: WRQA measures for 4 simulated signals (sine, Rössler, Lorenz, and Gaussian white noise). We use 3rd-order interpolation to guarantee continuity between signals. WRQA measures are computed with a window size of 300 and consecutive windows have 299 overlapping points to preserve the sampling rate of the original series. We observe that WRQA measures reflect different aspects of the signals’s time course.

3 Data collection and preprocessing

In this section, we describe our experimental setup and preprocessing steps. Aspects of acquisition and preprocessing described here do not relate to the current chapter but following chapters will refer to this section in presenting the data.

3.1 Experiment setup

We collected data from 9 healthy volunteers (among which 2 females, 1 subject left-handed). All participants gave their informed written consent before the experiment. The experimental procedure conformed the Declaration of Helsinki and was approved by the local ethics committee. None of the authors participated to the study. Subject 1 was omitted from the analysis because of an experimental problem.

Subjects were equipped with a EEG headcap, EMG sensors, and a motion capture system and asked to perform self-paced unilateral flexion/extension of the elbow. Participants were sitting in a chair and facing the screen issuing visual and auditory cues. The recording session was divided in 5 blocks of 4 minutes separated by 45-seconds break. Each block consist in a baseline collection (15 seconds) followed

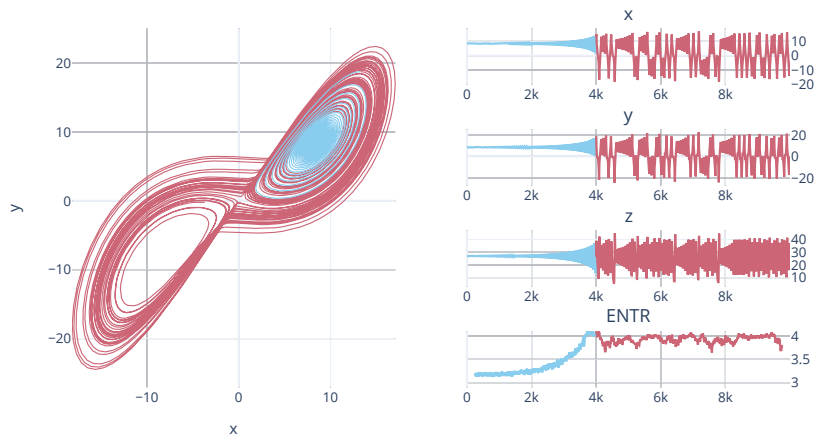


Figure 3.2: Lorenz system initialized near an unstable fixed point. We observe that the trajectory resemble to that of a linear system. The value the WRQA ENTR measure reflects this “predictability” and is therefore far from the asymptotic ENTR value.

by 8 movement trials of 23.5 seconds. The moving arm side was alternated between consecutive trials. During the pause of 4.25 seconds at the end of each trial, the subjects returned to a rest position with their hand on their knees. The beginning and end of movement were indicated by a visual and an auditory cue. 1.5 seconds before onset, countdown to movement beginning and end was printed on the screen. Stimulus was presented using the Expyriment Python package³ (Krause & Lindemann, 2014). Our experimental procedure allowed us to collect about 8 minute of movement data per arm. Graphical depiction of the experiment is shown in Figure 3.3.

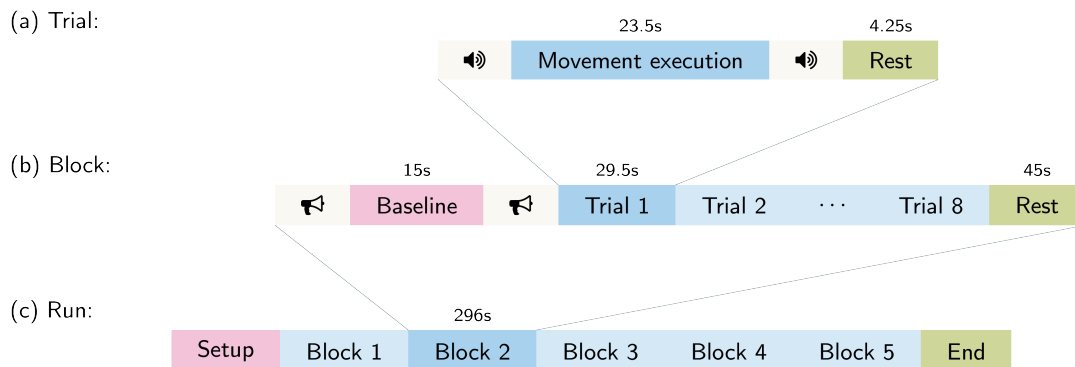


Figure 3.3: Description of the experiment

In this study, participants were free to perform the movements at their own pace. More specifically, participants were explicitly asked to perform elbow flexion and extension with varying amplitude and speed. We recommended not to move at an unreasonable speed as it may cause large motion artifacts on the EEG signals. Short movement breaks were also accepted. Our experimental design consisted in

³The poor timing precision of experiment was recently noted by (Bridges et al., 2020). On their hardware, authors report an average timing precision of 7.75ms and observe up to 100ms delay between visual and auditory cues. Although it inherently impacts the experiment, these poor performances should have minor impact on our results because our movement trials have a long duration. Moreover, (Bridges et al., 2020) report a high accuracy (< 1ms) for the onset on visual stimuli. Thus, we expect our visual onset timing to be quite accurate.

self-paced movements during long trials to reproduce naturalistic movement conditions⁴. Interestingly, we observed that participants produced heterogeneous movement trajectories.

3.2 Data collection and preprocessing

3.2.a Streaming and synchronization

Our experiment necessitates to record simultaneously several data streams: motion capture, electro-physiological signals, cues onset. These data streams have a different nature and rate: motion capture data was acquired at 60Hz, electrophysiological signals at 2000Hz, and the markers of cues onset do not have a fixed rate. We used the Lab Streaming Layer (LSL) ([kothe2022lab](https://github.com/kothe2022lab)) library to stream, collect, and synchronize the data. LSL's LabRecorder was used to generate a file containing the data with the time stamps each data point for each stream. Because of their high sampling rate, electrophysiological signals were sent by chunks of 8, thus dividing the stream rate by a factor 8. We wrote a command-line interface to LSL for a quicker setup and debugging of complex LSL setup. The command line interface is publicly available at <https://github.com/yop0/lsl-cli>.

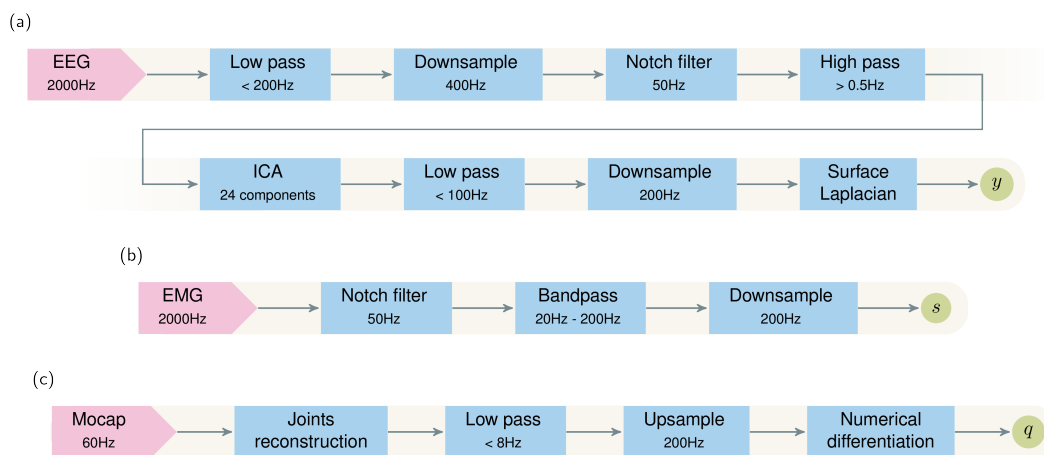


Figure 3.4: Preprocessing pipeline for EEG (a), EMG (b), and motion capture (c) signals.

3.2.b Motion capture data

We used Noitom Neuron motion capture suit to collect the data. Data is processed by the proprietary software Axis Neuron and we recorded both the skeleton configuration and the position of limbs in Cartesian space. Due to the drift of joint trajectories given by the motion capture system in the absence of whole-body motion, we preferred reconstructing the elbow angles from the Cartesian space data. Signals were collected at 60Hz. After low-pass filtering at 8Hz with a fourth-order Butterworth filter, we upsampled the time series to 200Hz. Then, we used first-order numerical differentiation to compute derivatives up to the 3rd order (jerk).

3.2.c Electrophysiological signals

We used ANT Neuro eego sports to record both EEG and EMG data. The 64-channels Waveguard Net headcap was used for EEG. The headcap uses Duke equidistant layout, as showed in Figure 3.5. EMG sensors were placed on the middle of the biceps and triceps brachii. All data were processed using the `mne-python` library ([Gramfort et al., 2013](#)).

⁴Indeed, naturalistic experiment design become increasingly popular in the neuroimaging community as they allow to observe the brain functioning under environmentally normal conditions ([Spiers & Maguire, 2007](#)).

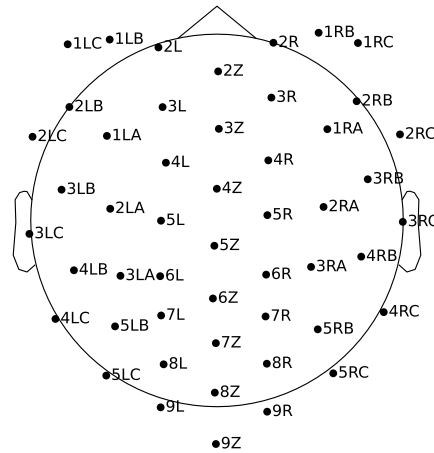


Figure 3.5: Sensor layout of the EEG headcap.

EEG We low-pass filtered EEG signals at 200Hz (fourth-order Butterworth) and downsample the signals to 400Hz to speed-up preprocessing. Then, we applied a Notch filter to attenuate the power-line noise (50Hz and harmonics). We removed low-frequency components with high-pass filter (0.5Hz, 4th-order Butterworth) and led an Independent Component Analysis using the extended infomax algorithm (T.-W. Lee et al., 1999). The 24 most prominent components were selected. Components were visually inspected for artifacts. An average of 6.3 (standard deviation 1.3) components were eliminated. As our experiment involved motion, we particularly focused on muscular artifacts. The classification of muscular artifacts is subject to debate in the literature (McMenamin et al., 2011; Olbrich et al., 2011). Following (Muthukumaraswamy, 2013), components were marked as movement artifacts due to their rich spectral content at more than 30Hz and peripheral unipolar activation⁵. 34% of artifacts components were muscular artifacts. We show some typical independent components marked as muscular artifacts in Appendix (Figure B.1). After ICA, we low-pass filtered the signals to 100Hz (fourth-order Butterworth) and downsampled to 200Hz. Finally, we applied a surface Laplacian filter to remove low spatial frequencies (Cohen, 2014).

EMG First, we applied a Notch filter (50Hz and harmonics) on EMG signals. Then, we bandpassed the signals between 20Hz and 200Hz with a fourth-order Butterworth filter. We removed frequencies below 20Hz because signals were corrupted by low-frequency artifacts due to cable motion. (De Luca et al., 2010) suggest that a 20Hz high-pass frequency is ideal to avoid motion artifacts while preserving signal information. Finally, signals were resampled to 200Hz to match the sampling rate of EEG and motion capture data.

3.2.d Computation of WRQA measures

We computed WRQA measures for both EEG and EMG signals. In addition to the preprocessing procedure described above, we high-pass filtered the signals with a fourth-order Butterworth filter with a cutoff frequency of 12Hz. This supplementary processing step is motivated by the observation made on the work of (Pitsik et al., 2020). Pitsik and colleagues analyzed the modulation of WRQA measures of EEG signals during movement, but without filtering the low frequency components of the signals. However, mu-band activity drops significantly during movement (Pfurtscheller et al., 2006). Due to the $1/f$ shape of EEG power spectrum, we can expect that a decrease in low-frequency power bands decreases the overall amplitude of the signal. Thus, the trajectory is contained in a smaller volume of

⁵In addition, the [ICLabel tutorial website](#) was particularly helpful to gain experience in telling components appart.

phase space. Whence, for a fixed threshold value as used in (Pitsik et al., 2020), points are more likely to be recurrent when low-frequency band power drops. Further studies would be necessary to understand what this increased recurrence rate implies for other WRQA measures. Hence, we deliberately filtered frequencies below mu-band activity to reduce the effect of mu-band decrease on our WRQA measures⁶.

WRQA measures were computed using the same procedure for EEG and EMG signals. We used windows of 100 points (0.5s) with 60 points overlap between consecutive windows. We did not use delay embedding. We constructed WRPs using the threshold defined by the reference rule introduced in the previous chapter (Eq. (2.14)). The number of points in Eq. (2.14) was set to 100, i.e. the window size. The data scale in Eq. (2.14) was fixed estimated for all data of each subject to avoid spurious interactions due to changing threshold value. Thus, the threshold value did not change between consecutive windows nor between trials. This is important to satisfy the constant-biased assumption discussed in Section 2.4.

3.3 Statistical parametric mapping

Statistical Parametric Maps (SPMs)⁷ is a specific combination of statistical methods for investigating relationship between physiological signals and variables of interest (K. J. Friston et al., 1994). These methods are notably used in fMRI and EEG studies (Kiebel et al., 2005). SPMs consist in a General Linear Model (GLM), contrast vectors to specify hypothesis, and a method for obtaining a significance threshold for multiple comparisons. In this section, we state the general formulation of SPMs.

We consider our experiment with $M = 8$ subjects repeating $N = 20$ trials of an experiment under $Q = 2$ conditions (right- and left-arm movement). For each WRQA measure, we want to test whether there is a linear relationship between the EEG at channel k and the EMG signal of the moving arm. Let y_{ijqt}^k be the value at t ($1 \leq t \leq T$) of EEG at channel k ($1 \leq k \leq K$) for subject i ($1 \leq i \leq M$) during trial j ($1 \leq j \leq N$) of condition $q \in \{R, L\}$. Similarly, let s_{ijqt}^l be EMG feature f for arm side $l \in \{R, L\}$. We want to identify the linear model:

$$y_{ijqt}^k = \beta_1^k s_{ijqt}^l + \epsilon_{ijqt}^k + \dots \quad (3.10)$$

where coefficients β_1^k are unique to each channel k , and arm l . Importantly, coefficients β_1^k in this model are the same for each subject i , trial j , condition q and time t . Hence, β_1^k being nonzero implies that in average – over subjects, trials, condition, and time – there is a linear relationship between the EEG at channel k and the EMG of arm l . Omitted terms in Eq. (3.10) capture the variability or offsets across subjects, trials, conditions and time. These are confounds and intercepts that compose linear transformation of the data points on the $s - y$ space and enable comparing data from different conditions.

GLM is formulated using a design matrix constructed by stacking covariates – here, EMGs s^l – with confounds and intercept. Rows of the design matrix are observations – formerly indexed by (i, j, q, t) – and columns are the values of covariates, confounds, and intercepts. Let X be the design matrix and Y obtained by stacking each y_{ijqt}^k for EEG at channel k . Then, the GLM is (Penny et al., 2011):

$$Y = X\beta + \epsilon \quad (3.11)$$

where ϵ is assumed centered Gaussian with variance σ^2 . A value for β can be obtained by solving the

⁶In general, the WRQA measures might not work as expected when the signal contains low frequency components, because the modulation of the measures that appear between windows might be due to these slow components. Thus, it is better to ensure that maximal period is greater than the window size.

⁷SPMs refer to the method to obtain voxel-wise statistics in fMRI studies and to investigate hypothesis about the relationships between regions of the brain and experimental variables. Here, we do not deal with fMRI images, thus “parametric analysis” would be a more adequate name. However, we preferred to keep the term SPM because of the combination of methods and formulation that we used.

$$\begin{pmatrix} y_{1111}^1 & \cdots & y_{1111}^K \\ \vdots & & \vdots \\ y_{111T}^1 & \cdots & y_{111T}^K \\ y_{1121}^1 & \cdots & y_{1121}^K \\ \vdots & & \vdots \\ y_{NMQT}^1 & \cdots & y_{NMQT}^K \end{pmatrix} = \begin{pmatrix} x_{1111}^1 & \cdots & x_{1111}^P \\ \vdots & & \vdots \\ x_{111T}^1 & \cdots & x_{111T}^P \\ x_{1121}^1 & \cdots & x_{1121}^P \\ \vdots & & \vdots \\ x_{NMQT}^1 & & x_{NMQT}^P \end{pmatrix} \times \underbrace{\begin{pmatrix} \beta_1^1 & \cdots & \beta_1^K \\ \vdots & \ddots & \vdots \\ \beta_P^1 & \cdots & \beta_P^K \end{pmatrix}}_{\substack{\text{Coefficients } \beta \\ \text{Covariates} \times \text{Channels}}} + \underbrace{\varepsilon}_{\text{Residuals}} \quad (3.12)$$

EEG observations Y
Design matrix X

Observations \times Channels
Observations \times Covariates

Equation 3.12: Detailed composition of the general linear model Eq. (3.11)

least-square problem:

$$\hat{\beta} = \arg \min_{\beta} \|Y - \beta X\|_2^2 \quad \Leftrightarrow \quad \hat{\beta} = (X^T X)^{-1} X^T Y \quad (3.13)$$

Let $J = NMQT$ be the number of observations, $p = \text{rank}(X)$, $e = Y - X\hat{\beta}$ the residuals and $\hat{\sigma}^2 = (e^T e)/(J - p)$ the sample variance. Under Gaussian assumption for ε , we have:

$$T = \frac{\hat{\beta} - \beta}{\sqrt{\hat{\sigma}^2 (X^T X)^{-1}}} \sim t_{J-p} \quad (3.14)$$

where t_{J-p} is Student's t-distribution with $J-p$ degrees of freedom. Therefore, testing for a significant relationship amounts simply to computing the p -value of Student's t at $\hat{\beta}/\sqrt{\hat{\sigma}^2 (X^T X)^{-1}}$. Moreover, hypotheses can be formulated as *contrast* vectors to test whether a linear combination of coefficients is equal to a specific value. To test $H_0 : c^T \beta = 0$ for contrast vector c , we use (Penny et al., 2011):

$$T = \frac{c^T \hat{\beta}}{\sqrt{\hat{\sigma}^2 c^T (X^T X)^{-1} c}} \quad (3.15)$$

Note that $\hat{\beta}$ is computed for each channel k . In fact, SPM is a mass-univariate method: linear relationship between EEG and covariates are tested separately, channel per channel. Like with other mass-univariate methods, we face a multiple-comparison problem. To do inference involving several channels — for instance, about the spatial extend of an effect — one needs to correct the threshold used in the channel-level test to guarantee the desired group-level significance. Several approaches to solve the multiple-comparison problem. Advanced methods from random field theory (Penny et al., 2011; K. J. Worsley & Friston, 1995) can be used when coefficients are correlated between channels. Here, we assume that coefficients are independent between channels and simply use Bonferroni correction. As compared with methods from random field theory, Bonferroni correction renders our tests more conservative: we are less prone to collect false positives but more likely to miss effects. However, as we filtered low spatial frequencies using Laplacian filter during preprocessing, independence between channels is a reasonable assumption.

It is important to mention that the test distribution is derived under the assumption that the residuals are Gaussian and i.i.d. The normality of the residuals is not necessary for regression but may impact the validity of the statistical analysis (Gelman & Hill, 2006). Here, we systematically check the quantile-quantile plot of normal versus empirical quantiles to visually assess the normality of the residuals. Regarding the i.i.d. assumption, we follow (Penny et al., 2011) and compute the covariance in time of

residuals. Then, the Welch-Satterthwaite approximation is used to correct the number of degrees of freedom. At the end, the value of J in the test distribution Eq. (3.14) is lower than $NMQT$ but the corrected value of J gives approximately the same statistics as if our data satisfied to the i.i.d. assumption. The problem of degrees of freedom correction for autocorrelated time series will be treated extensively in Chapter 5.

4 Results and discussion

4.1 Preliminary analysis of movement data

Before conducting more complex analysis, we compute the movement statistics for each participants. As the movement are self-paced, movement amplitude and speed change between subjects. This may imply that different “control schemes” were used by each participant and that the patterns of cortical activity are different. Hence, identifying outliers subjects in terms of movement parameters may provide a justification for these subjects being outliers in terms of EEG activity. Therefore, we need to conduct this preliminary analysis to highlight between-subject differences.

To obtain the movement statistics, we first smooth the joint trajectories with a Gaussian filter to remove spurious peaks in the signals. Then, we used `scipy`’s `find_peak` function (Virtanen et al., 2020) to identify the peaks location. We collected the mean and standard deviation of the peak-to-peak amplitude and the average number of seconds per cycles (twice the average time between two peaks). In addition, we computed the average velocity during movement. Results are shown in Figure 3.6.



Figure 3.6: Movement statistics for all subjects and group average. The first and second row are the mean and standard deviation of the peak-to-peak amplitude of the elbow motion, the third row is the average velocity, and the fourth row the number of cycles per seconds

The average amplitude of the elbow flexion-extension is 69° for the left arm and 73° for the right arm. The standard deviation of the peak-to-peak amplitude is in average 12° for the left arm and 13° for

the right arm. We see that the movements of subject 4 are less homogeneous than the other subjects. The group-averaged velocity is 60%/s for the left arm and 71%/s for the right arm. We observe that movements of subjects 5 and 7 are faster compared to the rest of the group. Finally, the average cycle duration is 2.4 seconds for the left arm and 2.3 seconds for the right arm. Subject 4 and 9 made particularly lengthy movement cycles.

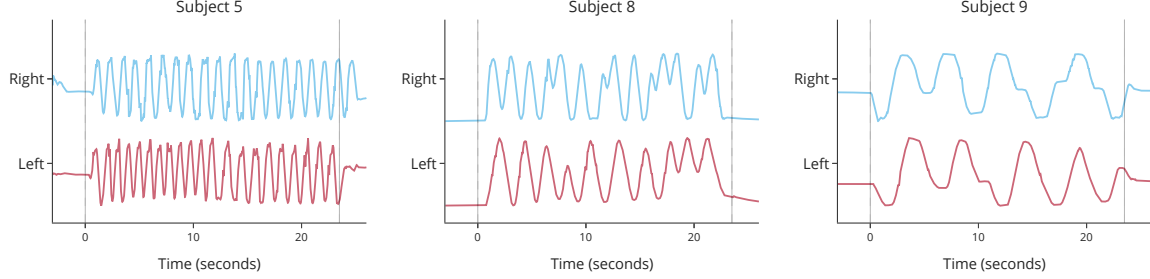


Figure 3.7: Typical movement trajectories for three representative subjects.

The movement statistics are heterogeneous between participants. Based on movement statistics, we can divide subjects in three groups. Typical joint trajectories for each group are shown in Figure 3.7. Subjects 4 and 9 performed slow movements with large amplitude and varied a lot the amplitude of their movements. In contrast, subjects 3, 5, 6, and 7 performed fast movements but did not vary much the movement amplitude. Finally, subjects 2 and 8 performed movements close to the group average.

4.2 EEG - EMG dynamical coherence in single subjects

4.2.a Single subject model

A model for the single subject is:

$$y_{jqt}^k = \underbrace{\zeta_q^k (s_{jqt} - \bar{s}_{jq\bullet})}_{\text{EMG of moving arm}} + \underbrace{\kappa_q^k (s_{j\bar{q}t} - \bar{s}_{j\bar{q}\bullet})}_{\text{EMG of steady arm}} + \underbrace{\eta^k (g_{jqt} - \bar{g}_{\bullet\bullet\bullet})}_{\text{Average scalp activity}} + \underbrace{\mu^k}_{\text{Mean}} + \underbrace{\varepsilon_{jqt}^k}_{\text{Residuals}} \quad (3.16)$$

where the notation $\bar{x}_{ij\bullet}$ is used to denote the average over a dimension, i.e. $\bar{x}_{ij\bullet} = (1/n_k) \sum_k x_{ijk}$. We review terms of Equation 3.16 one by one. First, ζ_q^k is the coefficient relating EEG with the EMG features from the moving arm. The time average of the moving arm EMG features is subtracted such that $s_{jqt} - \bar{s}_{jq\bullet}$ varies around 0. Thus, ζ_q^k is the EMG-EEG slope averaged trials and time. Then, κ_q^k is the variation of EEG features that can be attributed to the steady arm EMG feature. η^k captures change associated with mean scalp activity: g_{jqt} is the mean feature value over all channels for each trial, condition, and time. Finally, μ^k is the *per-channel* intercept. Here, the main effect is captured by ζ_q^k , while κ_q^k , η^k , and μ^k capture confounding effects. Stacking $(s_{jqt} - \bar{s}_{jq\bullet})$, $(s_{j\bar{q}t} - \bar{s}_{j\bar{q}\bullet})$ for $q \in \{\text{Right}, \text{Left}\}$, $(g_{jqt} - \bar{g}_{\bullet\bullet\bullet})$, and μ^k gives the design matrix $X_k \in \mathbb{R}^{2NT \times 6}$ presented in Figure 3.8.

We use the contrast vector $[1, 0, 0, 0, 0, 0]^T$ (resp. $[0, 1, 0, 0, 0, 0]^T$) to test the null hypothesis:

H_0 : "There is no linear correlation between the feature of EEG at channel k and the feature of EMG at the right (resp. left) arm."

or more compactly, $H_0: \zeta_R^k = 0$ (resp. $H_0: \zeta_L^k = 0$). In addition, we use the contrast vector $[1, -1, 0, 0, 0, 0]^T$ to test the hypothesis $H_0: \zeta_R^k = \zeta_L^k$, i.e. that there is no difference in correlation between the left and right arm movement.

4.2.b Results

We construct SPMs of dynamical complexity for all WRQA measures of all subjects using the model described by Eq. (3.16) and identify the channels exhibiting significant ($p < 0.005$) correlation with

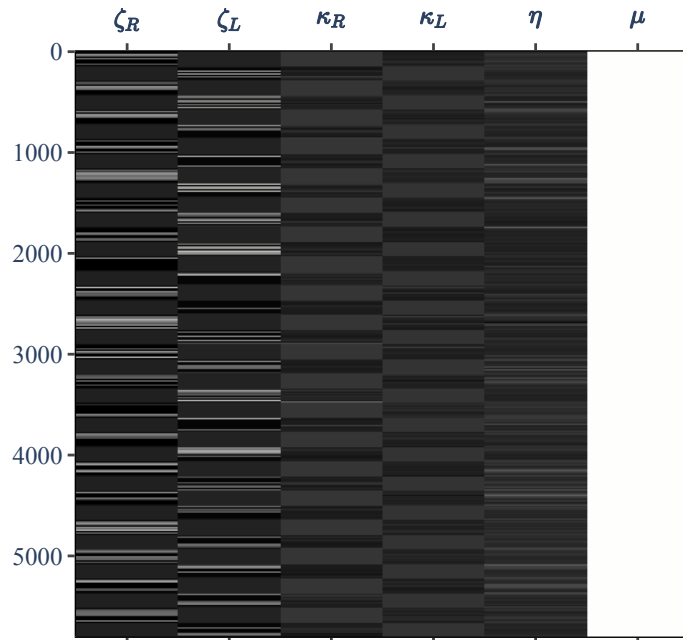


Figure 3.8: Design matrix for the single subject regression model. Values are shown in grayscale with 0 being black and 1 being white. Columns are normalized to lie between 0 and 1. Column names correspond to the coefficient the column multiplies in Equation 3.16. Rows correspond to individual observations. For more details, see Eq. (3.12).

features of EMG signals.

We first visually inspect the model residuals to assess the validity of any subsequent analysis. We show in Figure 3.9 the residuals for some selected measures for subject 3. The selected measures, respectively DET, $\langle V \rangle$, LMAX, and WENTR, each come from a different histogram operator, respectively, PROP (Def. 3.5), AVG (Def. 3.6), MAX (Def. 3.8), and ENTR (Def. 3.7)). We observe that the sample quantiles of DET and ENTR strongly follow the quantiles of the normal distribution. Indeed, we observed that this is the case for all measures deriving from the PROP and AVG operator. In the case of PROP, we argue that the approximate normality observed here is due to the values of DET and LAM being far from 1 and will not hold if the DET and LAM become too close to 1. Residuals are approximately normal, although it seems that the upper tail of the residuals distribution is longer than for the normal distribution.

We report heterogeneous results between subjects but we observe that similar patterns appear in several subjects. For instance, we report similar patterns for the SPMs for the LMAX measure for some subjects (2, 4, 5, and 7). The SPMs for the selected subjects are presented in Figure 3.10. For these subjects, the LMAX measure for channels on the left hand side of the scalp (for instance, 3L or 4L) show significant negative correlations with the LMAX measure of the right biceps and significant positive correlations with the LMAX measure of the left biceps. Similarly, channels on the right hand side of the scalp show negative correlations with the contralateral biceps and positive correlations with the ipsilateral biceps. The same result can also be observed on the difference plot. The difference is computed using the contrast vector $[1, -1, 0, 0, 0, 0]$, where the first component corresponds to the right arm. Thus, the t statistics is positive when $\zeta_R^k > \zeta_L^k$ and negative when $\zeta_R^k < \zeta_L^k$. Thus, the difference plot corroborates the previous result: there tend to be a negative correlation with the contralateral arm and positive correlations with the ipsilateral side.

Similar results are obtained for other RQA features and presented in Appendix. However, it is not clear whether the patterns that we observe illustrate a similar phenomena as they do not imply the same

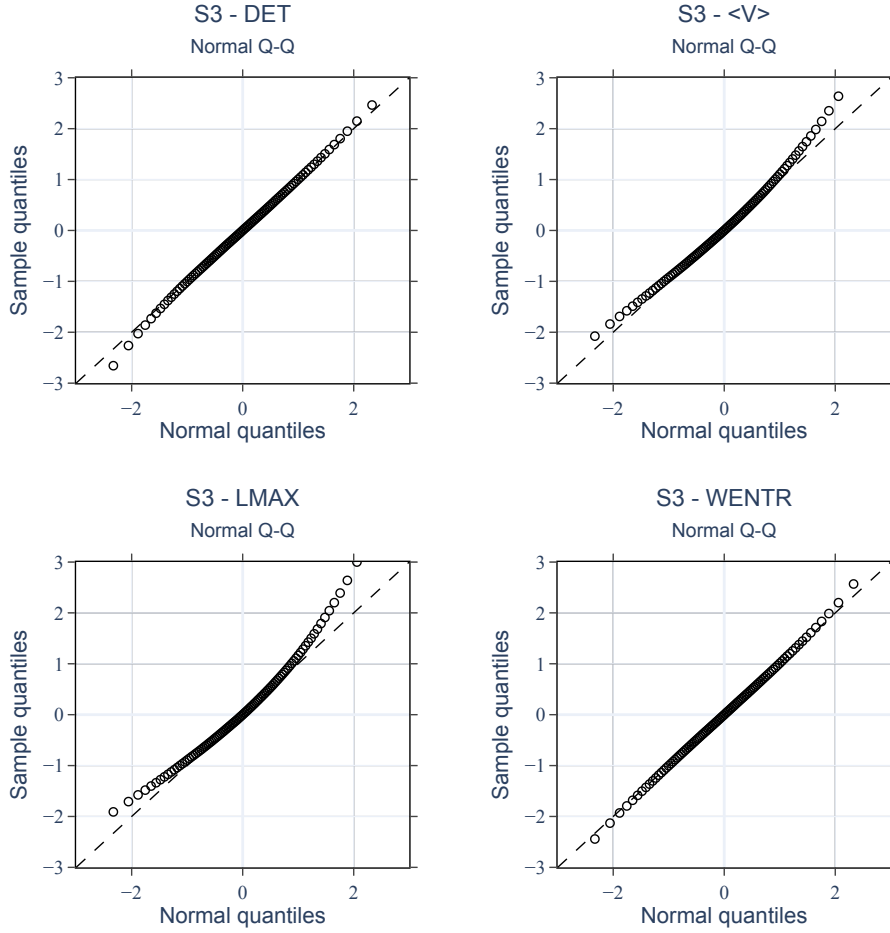


Figure 3.9: Normal Q-Q plot of the residuals of DET, $\langle V \rangle$, LMAX, WENTR for subject 3.

electrodes nor the same scalp locations. We see here a limitation of the single subject analysis: we can easily compute topographic plots for each measure and each subject but the patterns that appear may differ a lot; thus, it becomes complicated to rigorously justify their apparent similarities. Therefore, we move to multiple subjects analysis before further analyzing the results.

4.3 EEG - EMG dynamical coherence in multiple subjects

4.3.a Multiple subject model

A model for the multiple subject is:

$$\underbrace{y_{ijqt}^k}_{\text{EEG}} = \underbrace{\zeta_q^k (s_{ijqt} - \bar{s}_{ijq\bullet})}_{\text{EMG of moving arm}} + \underbrace{\kappa_q^k (s_{ijqt} - \bar{s}_{ijq\bullet})}_{\text{EMG of steady arm}} + \underbrace{\eta_i^k (g_{ijqt} - \bar{g}_{i\bullet\bullet\bullet})}_{\text{Average scalp activity}} + \underbrace{\mu_i^k}_{\text{Mean}} + \underbrace{\varepsilon_{ijqt}^k}_{\text{Residuals}} \quad (3.17)$$

Similarly to the single subject model, the two first terms of multiple subject model represent the linear coefficient scaling EEG features at channel k with EMGs features at the moving and steady arm (ζ_q^k and κ_q^k). These coefficients are common to all subjects, meaning that they capture an average effect over subjects. In contrast, both scalp activity coefficient η_i^k and intercept μ_i^k are indexed by subject index i and thus may capture a different effect for each subject. Stacking ζ_q^k and κ_q^k for each condition and η_i^k and μ_i^k for each subject gives the design matrix $X_k \in \mathbb{R}^{\sum_i N_i T \times 20}$ showed in Figure 3.11.

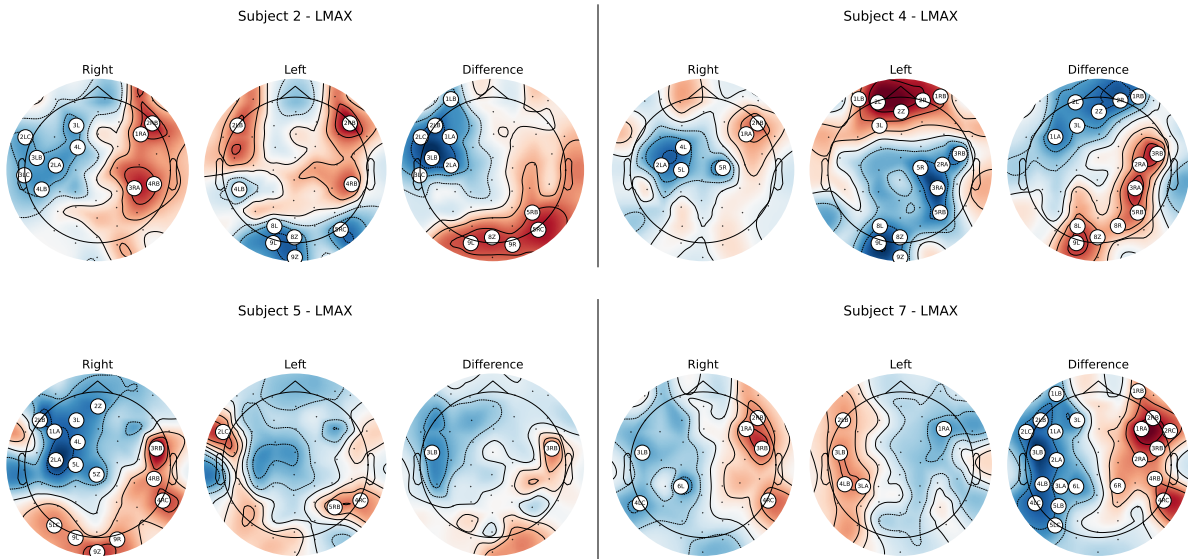


Figure 3.10: Topographic maps of the LMAX measure for some subjects. The color map (blue to red) indicates the value of the t -statistics (negative to positive). Significant channels are in white circles ($p < 0.005$, Bonferroni correction). For “right” and “left” plots, this corresponds to accepting $H_a: “\zeta_q^k < 0”$ (significant negative correlations) in blue regions and $H_a: “\zeta_q^k > 0”$ (significant positive correlations) in red regions. For the difference plot, the accepted hypothesis is $H_a: “\zeta_R^k > \zeta_L^k”$ (larger correlation with right arm) in blue regions and $H_a: “\zeta_R^k < \zeta_L^k”$ (larger correlation with left arm) in red regions.

4.3.b Results

We compute the SPMs with the model from Eq. (3.17). Now, the results corresponds to a correlation which appear as significant for the group (this does not necessarily corresponds to an effect that is significant for each subject). The model residuals for some measures are shown in Figure D.1 and strongly match to the normal distribution. In light of the observation made for the single subject analysis, we test the one-sided hypothesis of significant negative correlation with the contralateral arm. The contrast vector the negative of the contrast in the single subject analysis, i.e. $[-1, 0, 0, 0, 0, 0]^T$ and $[0, -1, 0, 0, 0, 0]^T$. Hence, the colors on the topographic map are inverted as compared to 3.10. Results for some WRQA measures are presented in Figure 3.13 (figures for remaining WRQA measures are presented in Appendix).

We observe that most of the electrodes showing strong negative correlations are located in the central part of the scalp. The channel 4Z (which is roughly equivalent to FCz in the standard 20-20 system) systematically shows significant correlations. Surrounding channels are also often significant. We also observe an asymmetry between the scalp map in the left and the right condition. In the plots of RR, DET, $\langle W \rangle$, WENTR, we observe that more channels from the contralateral hemisphere show significant correlations. This is clear in the WENTR plot: the column of channels from 2L to 6L and from 1LA to 3LA (left part of the brain) show high negative correlation with the WENTR of the right biceps EMG. Oppositely, channels from 3R to 6R and 2RA, 3RA (right part of the brain) show high negative correlation with the left biceps.

So far, our results indicate that the “dynamical complexity” (as quantified by RQA measures) of EEG signals is negatively correlated with that of the EMG of the contralateral biceps. These results seems unexpected as we know that primate arms are controlled by the contralateral side of the motor cortex (Bear et al., 2020). Thus, we may expect the dynamic features of neural activity to be positively correlated with that of motor neurons activity. However, it is important to notice that we do not measure directly the neural activity nor the activity of motor neurons and that we are working with dynamical

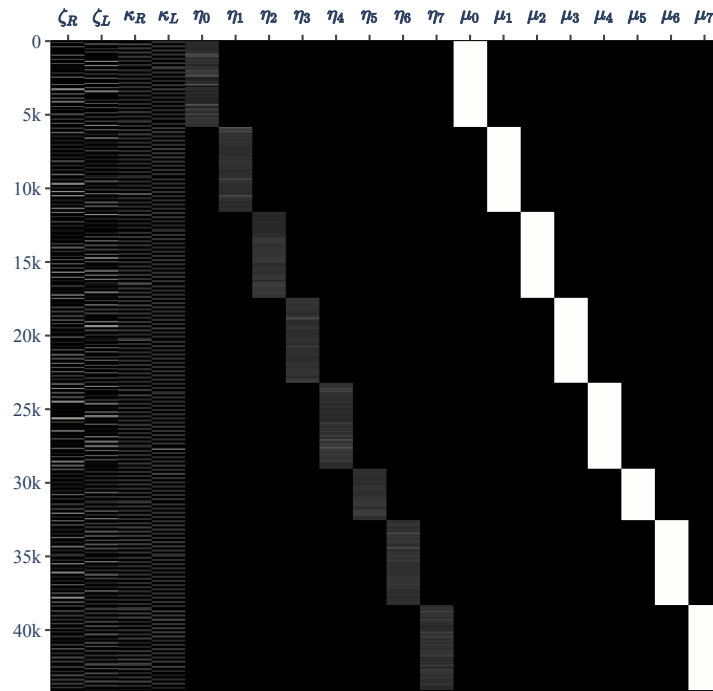


Figure 3.11: Design matrix for the multiple subject regression model. Values are shown in grayscale with 0 being black and 1 being white. Columns are normalized to lie between 0 and 1. Column names correspond to the coefficient the column multiplies in Equation 3.17. Rows correspond to individual observations. For more details, see Eq. (3.12).

complexity measures. These measures are well-defined when dealing with autonomous dynamical systems, but may provide surprising results in the case of stochastic processes and non-autonomous dynamical systems. Hence, we look directly to the signals in the next section and show that our results are indeed not surprising nor unprecedented in the literature.

4.4 Decreased EEG complexity with movement

4.4.a Related work

We previously observed that the dynamical complexity of EEG signals in the central part of the scalp is negatively correlated to that of the EMG signals in the biceps, with a preference for contralateral negative correlation. We start by mentioning that similar results have been reported by (Pitsik et al., 2020), with different methods. In their work, (Pitsik et al., 2020) created three hybrid three-dimensional dynamical systems. For each system, the dimensions corresponded to the EEG activity at three channels selected on the longitudinal axis of the brain, for instance, CPz, Cz, and FCz. The trajectory of the dynamical system is created from the signals of the three channels that compose the dimensions of the system. The participants of the study were equipped with EEG and EMG and asked to perform simple unilateral hand-closing movements after hearing a cue. The authors normalized the WRQA measures with respect to resting state measures (a few seconds before movement onset) and noticed that DET increased during movement while the WENTR diminished. Importantly, when the subjects closed one hand, author noticed that the WRQA measures from the contralateral side of the brain departs further its resting state value than the WRQA measures from the ipsilateral side of the brain.

Similarly to (Pitsik et al., 2020), we have WRQA measures during our movement trials. We compute the “background activity” by averaging the value of the measures between 2.5 and 0.5 seconds prior to movement onset and 0.5 to 2.5 seconds after movement end. Then, we subtract the background

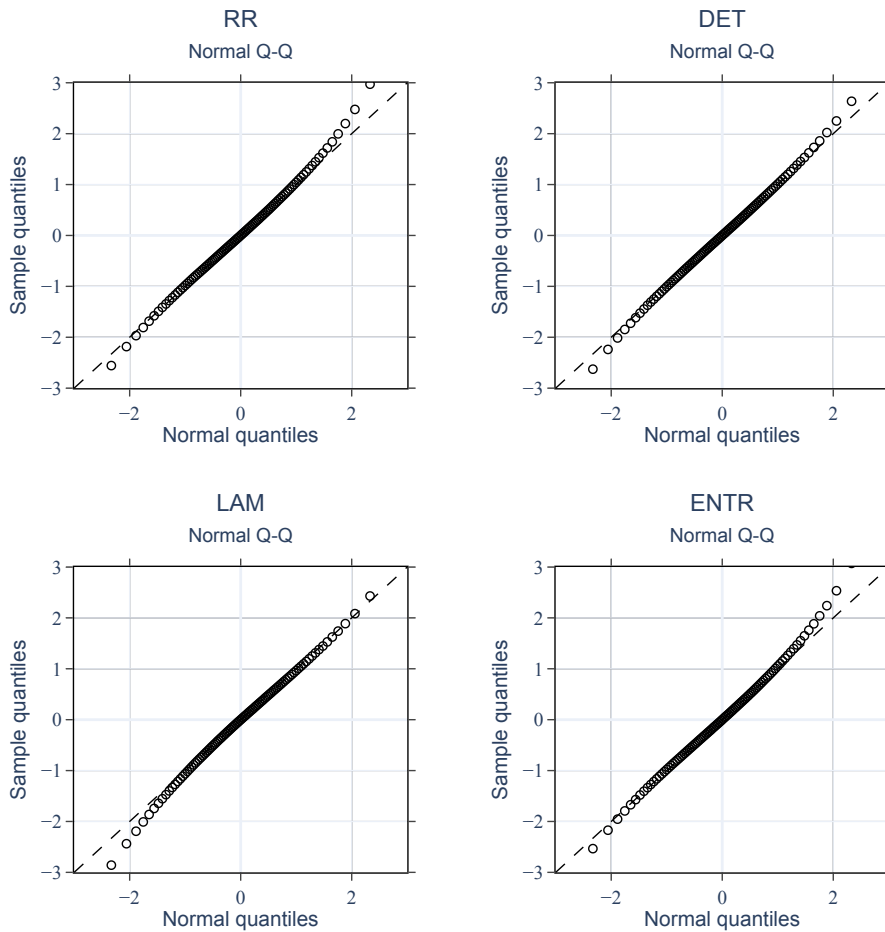


Figure 3.12: Normal Q-Q plot of the LMAX residuals for RR, DET, LAM, and ENTR for the multiple subjects model.

activity to the time course of the measures.

4.4.b Results

On Figure 3.14, we present group-averaged results for 3 EEG channels located over the primary motor cortex (3LB, 4Z, and 3RB) and for biceps EMG of both arms. The results shown here cover the measures presented in (Pitsik et al., 2020) (DET and WENTR) but also several other WRQA measures. The plate containing all WRQA measures are shown in Appendix.

The first observation is that measures related to black structures (DET, LAM, $\langle L \rangle$, $\langle V \rangle$, LMAX, VMAX, ENTR, and VENTR) of EEG signals increase after movement onset and only decrease at movement end. In contrast, both recurrence time entropy (WENTR) of EEG signals decrease at movement onset and until movement end. The joint decrease of recurrence time entropy and increase of measures related to black structures (diagonal and vertical) is an indicator of reduced signal complexity. Hence, we observe a decrease complexity in EEG signals from contralateral motor cortex, similarly to (Pitsik et al., 2020).

Second, measures from EMG signals have an opposite behavior to EEG measures: when a measure increases (resp. decreases) for EEG, it decreases (resp. increases) for EMG signal of the moving arm biceps. This antitonic relationship between EEG and EMG measures is observed for all WRQA measures. This observation implies that EMG signal complexity decreases during movement. The result is consistent with related studies (Farina et al., 2002; Zhang & Zhou, 2012).

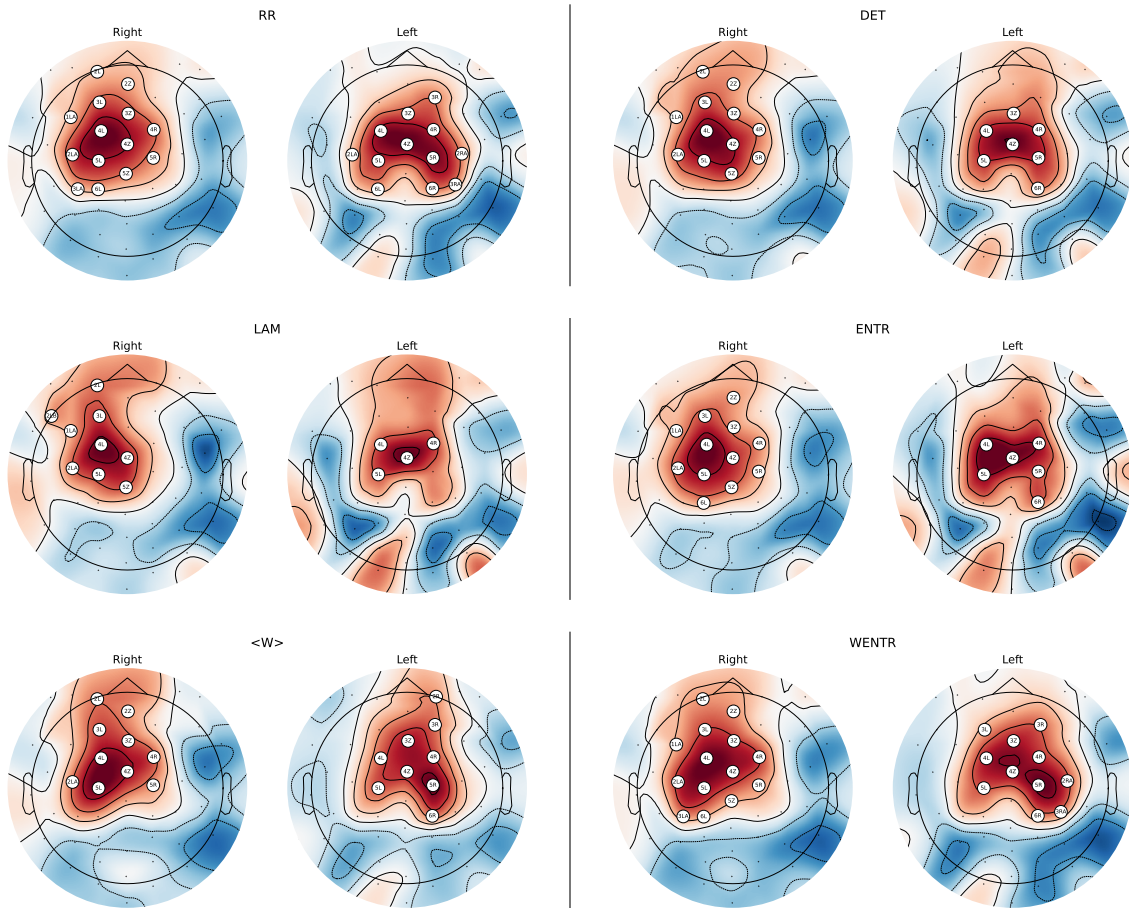


Figure 3.13: Multiple subject SPMs for several nonlinear complexity measures. The color map (from red to blue) shows the value of the t statistics in scalp space (from lower to higher values). Sensors with white circles show significant negative correlation with the EMG features. This correspond to accepting H_a : “ $\zeta_q^k < 0$ ” (significant negative correlation) at $p < 0.005$ with Bonferroni correction.

Our third observation is that measures from 3LB depart further appart from their mean than 3RB during right hand movement. Similarly, it appears that 3RB is more affected by left hand movement than 3LB. We show in Figure 3.15 the relative changes from baseline value. In the case of right arm movements, measures from 3LB depart further from baseline than 4Z and 3RB. In contrast, absolute relative changes are higher for 3RB during left arm movements. This result is consistent with the existing literature: the contralateral side of the brain is more modulated during unilateral movement (Bear et al., 2020).

The fact that EEG and EMG are modulated in opposite directions can be understood. In fact, this result is partially due to the adaptive radius that is used to compute the WRQA measures. At resting state, EMG signals contain only noise, thus the measured dynamical complexity is high. When movement starts, the amplitude of EMG signal increases; however, the radius fits to the standard deviation of the signal and also increases. During movement, the EMG signal is “complex” but less than white noise. Whence the dynamical complexity measured from EMG signals decreases during movement and this is mostly due to a change in the nature of the signal. This is observed by large variation of the dynamical complexity measures of EMG signal during movement. In contrast the nature of EEG signals does not vary much before and during movement and the order of change of the measures compared to baseline is much smaller than for EMG.

In the light of our results, we understand that the large changes of the measures around movement

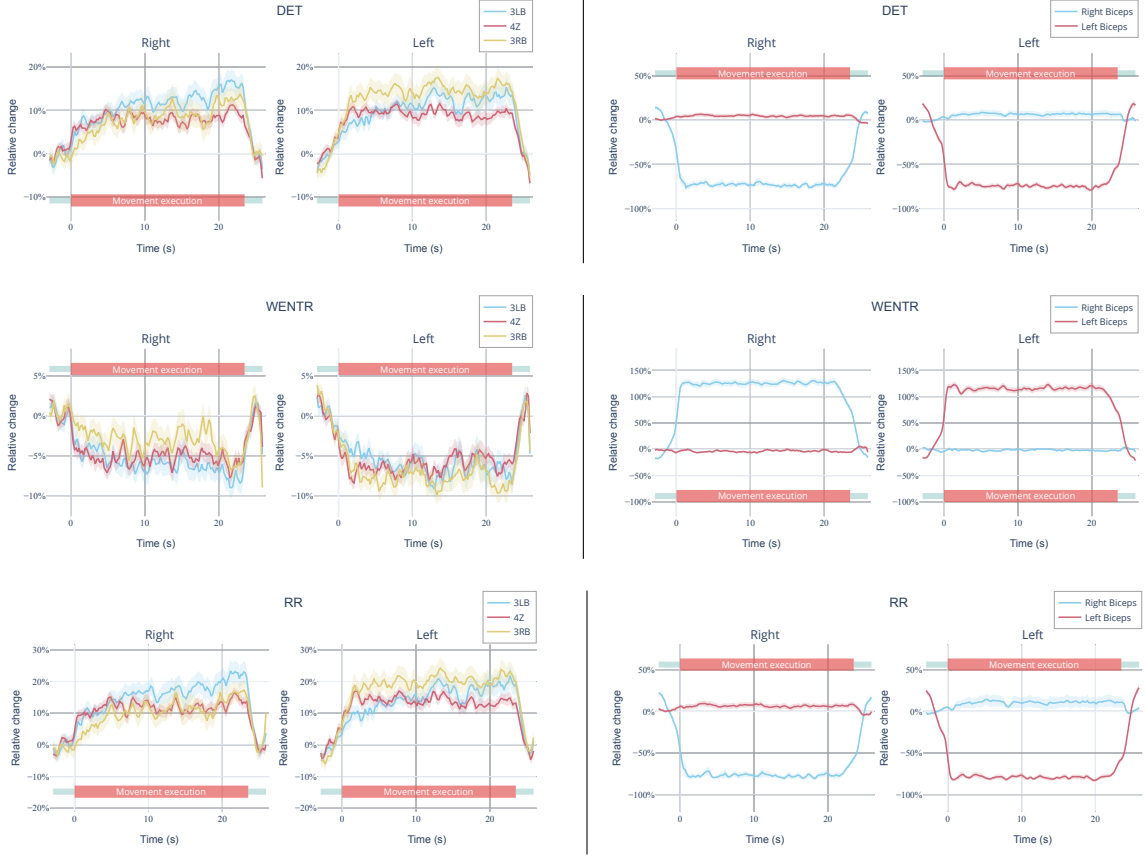


Figure 3.14: DET and WENTR of EEG and biceps EMG signals during right and left arm movements. Colorbands indicates standard error.

onset and movement end are responsible for the significant correlation found in the multiple subject SPMs from the previous section. In contrast to the work of (Pitsik et al., 2020), we have here continuous data and long movement sessions. Hence, it is interesting to isolate the transient effects due to onsets and to investigate whether dynamical coherence exists during movement.

4.5 Analysis of EEG-EMG dynamical coherence during continuous movement

4.5.a Multiple subject model

We extend the model for multiple subjects Eq. (3.17) to integrate a confound with the rest condition. Moreover, we divide the columns containing EMG activity between movement and rest. We define the movement as the times between 2 seconds after onset and 2 seconds before movement end. Rest is 1 second before movement onset and 1 second after movement rest. Time points not included in the rest or movement condition were removed from the analysis. We let θ_t^{mov} (resp. θ_t^{rest}) be the indicator of movement (resp. rest), i.e. $\theta_t^{\text{mov}} = 1$ iff t is in the movement time range and similarly for θ_t^{rest} . The model is

$$\underbrace{y_{ijqt}^k}_{\text{EEG}} = \theta_t^{\text{mov}} \underbrace{\zeta_q^k(s_{ijqt} - \bar{s}_{ijq\bullet})}_{\text{EMG of moving arm during movement}} + \underbrace{\kappa_q^k(s_{ij\dot{q}t} - \bar{s}_{ij\dot{q}\bullet})}_{\text{EMG of steady arm}} + \theta_t^{\text{rest}} \underbrace{\gamma_q^k(s_{ijqt} - \bar{s}_{ijq\bullet})}_{\text{EMG of steady arm during rest}} + \underbrace{\eta_i^k(\bar{g}_{ijqt} - \bar{g}_{i\bullet\bullet})}_{\text{Average scalp activity}} + \underbrace{\mu_i^k}_{\text{Mean}} + \underbrace{\epsilon_{ijqt}^k}_{\text{Residuals}}$$
(3.18)

The first term represent the linear coefficient between EEG features at channel k and EMGs features of the moving arm limited during movement (ζ_q^k). κ_q^k is the steady arm confound. γ_q^k captures the

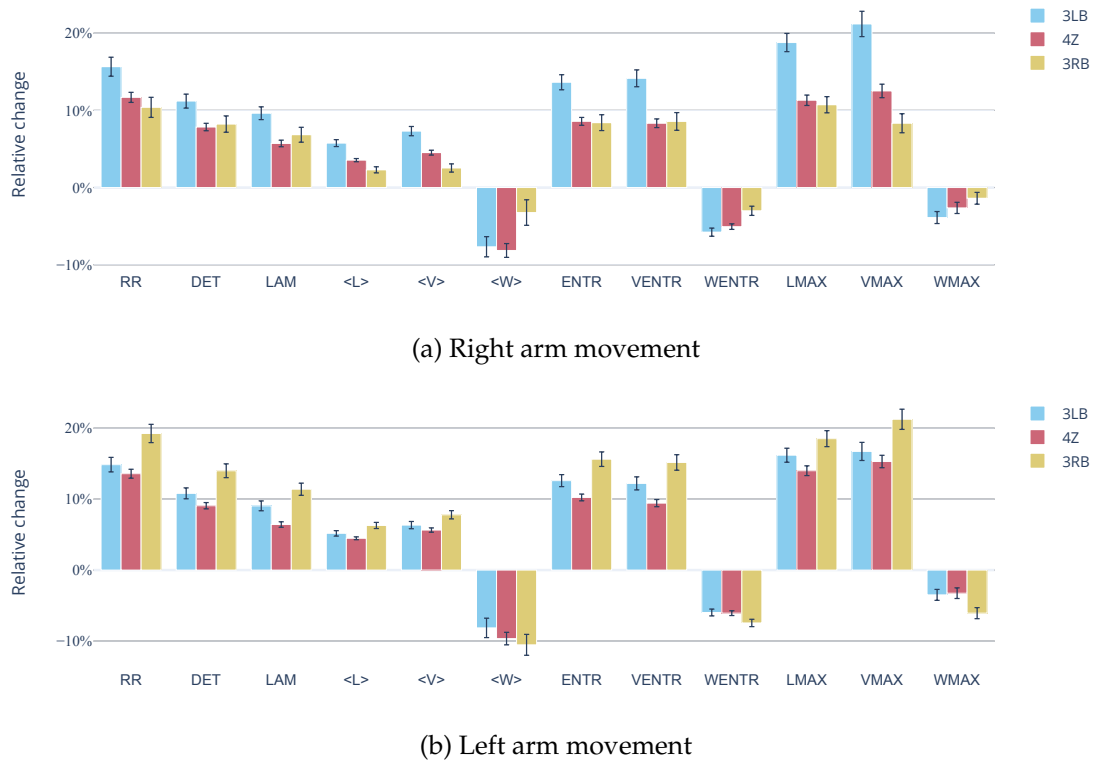


Figure 3.15: Bar plots of relative change from baseline for 3RB, 4Z, and 3LB during right and left hand movements. Error bar indicates the 99% confidence interval of the mean. We observe that absolute change is larger for 3LB during right hand movements and for 3RB during left hand movements.

correlation of the moving arm during the resting phase. Other terms are similar to the previous multiple subject models Eq. (3.17). The design matrix corresponding to this model is shown in Figure 3.16. Here, we use the contrast vectors $(1, 0, \dots)$ and $(0, 1, \dots)$ to test for significant correlation with the right and left arm and the vector $(1, -1, 0, \dots)$ to test for the preference of a channel for a side, i.e. $\zeta_R^k < \zeta_L^k$ or $\zeta_R^k > \zeta_L^k$.

4.5.b Results

We show in Figure 3.17 the SPMs testing for correlation of the EEG measures with EMG measures of the right and left biceps, after removing the data points close to the movement onset and movement end. A first observation is that there is several channels that show significant correlation but are not located on the central regions of the scalp. This is different from the previous multisubject analysis where all significant channels were located in the center of the scalp. Here, we see that some occipital channels (7L, 8L, 9L, 5LC, 5LB) show significant positive correlation with measures from both biceps. Due to the extreme location of the channels, we argue that the correlation is due to a muscular artifact from neck muscle. This is not necessarily an effect that is common to the group but may result from a single subject having particularly strong artifacts in this location.

For both RR and DET, we observe that there is a negative correlation of the dynamical complexity of the EEG signals with the EMG signals of the contralateral biceps. Oppositely, there is a positive correlation with the ipsilateral arm. The results are less strong for LAM and ENTR, but the trend is similar.

The results for the difference between the left and the right conditions are shown for some measures

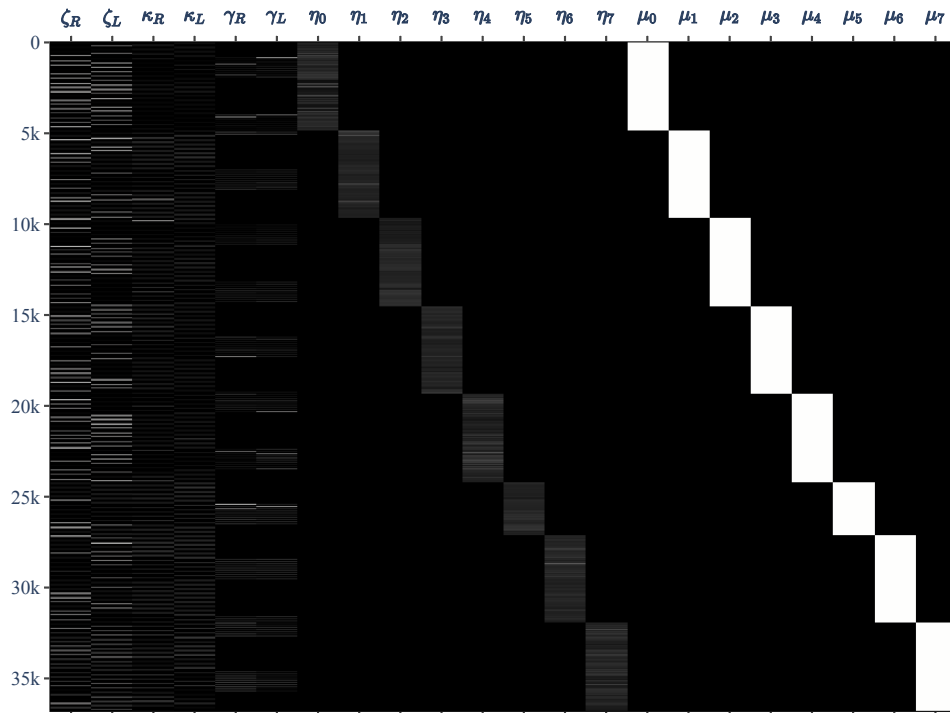


Figure 3.16: Design matrix for the multiple subject regression model. Values are shown in gray scale with 0 being black and 1 being white. Columns are normalized to lie between 0 and 1. Column names correspond to the coefficient the column multiplies in Equation 3.18.

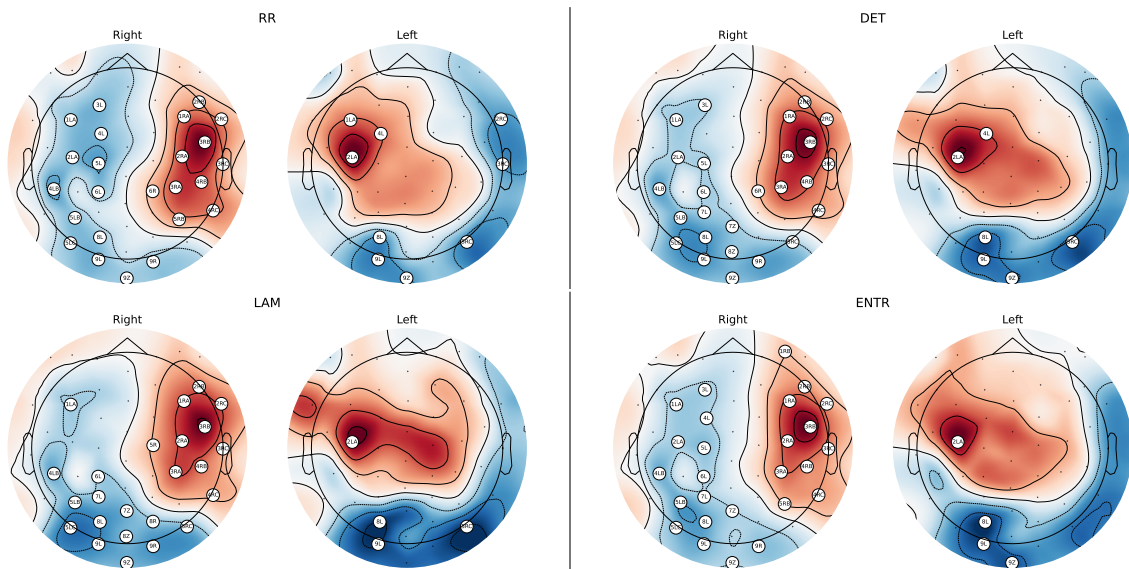


Figure 3.17: Multiple subject SPMs for several nonlinear complexity measures. The color map (from blue to red) shows the value of the t statistics in scalp space (from lower to higher values). Channels with significant t ($p < 0.005$, Bonferroni corrected) are shown in white circles. Significant channels correspond to $H_a: \zeta_q^k < 0$ (significant negative correlation) in blue regions and $H_a: \zeta_q^k > 0$ (significant positive correlation) in red regions.

in Figure 3.18. The topographic maps corresponds to the null hypothesis $H_0: \zeta_R^k - \zeta_L^k = 0$. We clearly see that on channels on the left hand side of the scalp the null hypothesis is violated by strongly negative t statistics. Oppositely, channels on the right hand side of the scalp, the null hypothesis is violated by strongly positive t statistics. We can conclude that $\zeta_R^k < \zeta_L^k$ in the central left region and that $\zeta_R^k > \zeta_L^k$ in the central right region.

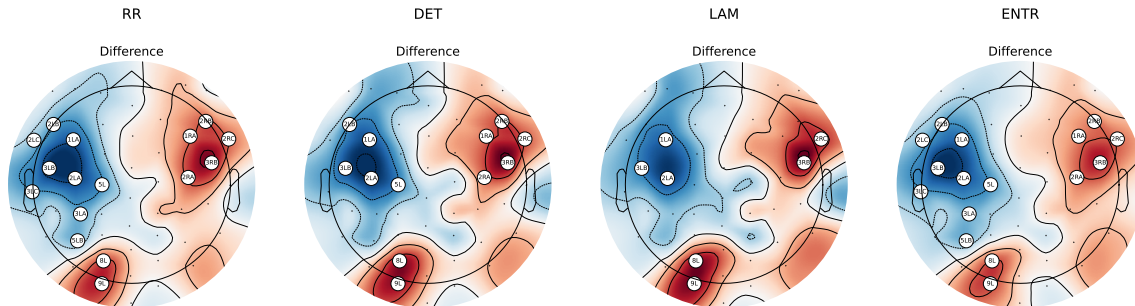


Figure 3.18: Multiple subject SPMs for several nonlinear complexity measures. The color map (from red to blue) shows the value of the t statistics in scalp space (from lower to higher values). Sensors with white circles show significant negative correlation with the EMG features ($p < 0.005$, Bonferroni correction). Significant channels correspond to $H_a: \zeta_R^k < \zeta_L^k$ (larger correlation with left arm) in blue regions and $H_a: \zeta_R^k > \zeta_L^k$ (larger correlation with right arm) in red regions.

5 Conclusion

In this chapter, we investigated the correlation between the dynamical complexity of EEG signals and EMG signals. The dynamical complexity was evaluated using several measures from the recurrence quantification analysis framework. These measures capture important properties of complex dynamical systems. Here, we needed a windowed version of RQA and justified its adequacy to obtain time-resolved estimation of dynamical features of time series. We then introduced the statistical parametric framework which incorporate several well-known methods to construct and test statistical hypotheses in a simple manner. As our objective was to use WRQA with SPM, we justified that our data lead to approximately Gaussian residuals.

We collected EEG, EMG, and motion capture data from several subject performing unilateral elbow flexion-extension. After preprocessing the data, we computed the WRQA measures from the EEG and EMG time series. We first constructed SPM on single and multiple subjects to identify EEG channels where the dynamical complexity of the signal exhibited significant correlation with the dynamical complexity of the EMG of the biceps of the moving arm. For each arm, we observed that several WRQA measures showed negatively correlation with the contralateral side of the scalp.

Then, we analyzed more in detail the time course of several WRQA measures during movement. In particular, we selected three EEG channels located on the left, center, and right of the scalp. For all WRQA measures, we observed significant changes in both EEG and EMG at the beginning and at the end of the movement. Interestingly, we report the same antitonic relationship that was reported in the literature. We also noticed that the channel contralateral to the moving arm deviated more from its resting state value than the other channels.

Finally, we removed signals close to the beginning or to the end of the movement trial and computed new group-level SPMs. Our results suggest that the negative correlation between WRQA measures of EEG in central lateral regions and EMG of the contralateral arm is maintained during movement.

Chapter 4

On degrees of freedom correction for the correlation coefficient of time series

1 Introduction

In this chapter, we consider the problem of finding the number of “effective degrees of freedoms” of time series. We are concerned with testing for significant correlation between movement trajectories. A classical approach is to compute Pearson’s correlation coefficient between the series. However, the test distribution of the Pearson correlation coefficient is limited to pairwise-independent samples. As movement trajectories vary slowly with respect to the sampling rate of motion capture systems, consecutive observations are strongly dependent. Hence, time series cannot be used with the classical test distribution of Pearson’s correlation coefficient. A solution to this problem is to assume that the test statistics with dependent observations is distributed like the test statistics with a lower number of independent observations. Thus, this number of “effective degrees of freedom” (e.d.f.) is the size of an independent sample that would produce the same test statistics. It allows to test against a null-hypothesis derived under the assumption of independent samples, even when the actual samples are not independent.

Bartlett (M. Bartlett, 1935) was the first to investigate the number of *e.d.f.* of the Pearson correlation coefficient of dependent series. His approach was latter extended by (M. S. Bartlett, 1946) and works of Bayley and Hammersley (Bayley & Hammersley, 1946) and Quenouille (Quenouille, 1947). All these approaches were derived under the null hypothesis that the two time series are uncorrelated. (Pyper & Peterman, 1998) discusses other methods from the oceanographic field which are derived from (M. S. Bartlett, 1946; Bayley & Hammersley, 1946). More recently, (Afyouni et al., 2019) proposed a more general approach which accommodates nonzero correlation between the series. Their approach reduces to the expression proposed by Bayley and Hammersley in the case of zero correlation.

The accuracy of the number of *e.d.f.* yielded by the methods presented above depends on a good estimation of the autocorrelation function (Afyouni et al., 2019). In fact, the number of *e.d.f.* depends on the sum-of-squares of the autocorrelation function. Bias is introduced by summing up the square of spurious autocorrelation terms in the the autocorrelation function tail. Regularization methods are usually used to restrict the summation to a smaller interval of the autocorrelation function and thus limit the bias by omitting spurious autocorrelation terms (Pyper & Peterman, 1998). When the series are short and the autocorrelation decreases slowly, the mode of the regularized autocorrelation function contribute largely to the d.f. correction term. Hence, we propose to construct a parametric estimate of the number of *e.d.f.* by fitting the the autocorrelation function mode with the autocorrelation of a known stochastic process.

In a first time, we observe that the method on which rely the work of Bartlett and others is exactly

the Welch-Satterthwaite approximation, which gives the number of *e.d.f.* for a weighted sum of chi-square random variables. The Welch-Satterthwaite approximation can be written as the ratio of traces of matrices (Penny et al., 2011). When the matrices are symmetric Toeplitz matrices – such as the autocorrelation matrices for dependent samples – the Welch-Satterthwaite approximation reduces to the formula given by Bayley and Hammersley (Bayley & Hammersley, 1946) and Quenouille (Quenouille, 1947).

Using work on Toeplitz matrices (Gray et al., 2006), asymptotic expressions of the Welch-Satterthwaite approximation can be derived. Moreover, the expression can be further simplified using a Gaussian (Laplace) approximation of autocorrelation functions with finite second-order derivatives. The final expression depends on the second spectral moment of the process, which is defined as second-order derivatives of the autocorrelation function at its mode. The second spectral moment is a measure of the roughness of the underlying process and relates to several of its statistical properties (Cox & Miller, 2017). Moreover, the second spectral moment can be simply estimated from the variance of the first-order derivatives of the series, as shown in (Cox & Miller, 2017) for stochastic processes and in (K. J. Worsley & Friston, 1995; K. Worsley, 1996) and (Adler, 2010; Rosenblatt, 2012) for general random fields. The main result of this chapter is two simple expressions for correcting the number of degrees of freedom for stochastic processes. For a series $x = \{x_1, \dots, x_n\}$, the number of effective degrees of freedoms ν is asymptotically:

$$\nu = n \sqrt{\text{var}\{\dot{x}\} / \pi} \quad (4.1)$$

which is also related, by Rice’s formula (Rice, 1944), to the number of zero-crossings N_0 of the series:

$$\nu = \sqrt{\pi} N_0 \quad (4.2)$$

We show numerically that using Eq. (4.1) in the exact test distribution of the Pearson correlation coefficient gives the appropriate false positive rate and enables testing for correlation between dependent samples. We observe that the approach can also be used with Spearman’s correlation coefficient. We use the proposed d.f. correction method with real motion capture data in two different applications. In the first example, we show how the corrected p -values can be used to identify in-phase continuous movements. We present quantile-quantile plot to compare our method with the literature. In a second example, we show that our approach is adequate to evaluate the performance of models decoding joint movements from EEG signals.

2 Problem statement

We conduct some numerical trials to reveal problems that arise when testing for a nonzero correlation coefficient from series of dependent samples. To generate series of dependent observations, we convolve series of independent observations with a Gaussian kernel. The size of the kernel is parameterized by its standard deviation λ which we refer to as the “smoothness” of the series. Importantly, we compute the correlation coefficient between pairs of series that are generated independently. Therefore, the correlation coefficient computed from pairs of series with the same smoothness follows the true distribution of the null hypothesis of zero cross-correlation. The objective is to illustrate how the test distribution of Pearson’s correlation coefficient, which relies on independence, degenerates when the independence assumption is violated.

First, we generate some random i.i.d. normally distributed samples with zero mean and unit variance. We create normally distributed dependent samples by convolving the i.i.d. samples with a normalized Gaussian kernel parameterized by a standard deviation λ . For 30 values of λ distributed between 0.1 and 10, we generate 65536 independent series of 1024 dependent observations. Because of the convolution with the Gaussian kernel, each series has a Gaussian autocorrelation. We show in Figure 4.1 the mean and the 95% confidence interval for the correlation coefficient as a function of λ . We see

that the smoothness has no impact on the average correlation: independent samples have in average a correlation coefficient of zero. However, the spread of the CC largely increases with smoothness.

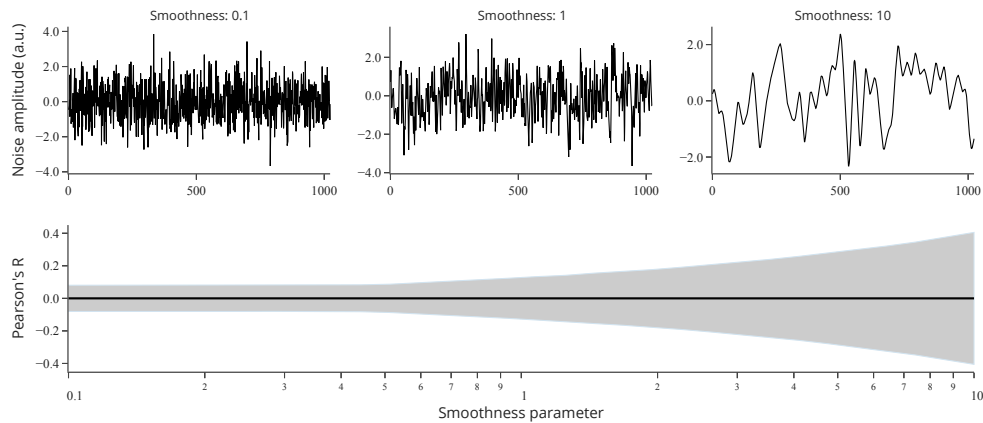


Figure 4.1: Pearson correlation coefficient computed from stochastic processes with Gaussian autocorrelation. The upper row shows sample random series with different degrees of “smoothness”, where the smoothness is understood as the standard deviation of the Gaussian kernel used to produce the series. The lower row illustrates the distribution of the correlation coefficient as a function of the series smoothness. The shaded area corresponds to the 95% interval under normal assumptions. This is indeed the distribution of the Pearson correlation coefficient under the null hypothesis of zero correlation. The problem highlighted here is that even if the mean of the correlation coefficient is zero, its standard deviation increases with smoothness. Hence, smoother series are more likely to show high correlations.

Now, we consider what happens when testing against the zero-correlation hypothesis with dependent samples. Here, we use the Python package `scipy` (Virtanen et al., 2020) which relies on exact test distribution of the Pearson’s R under the null hypothesis (Hotelling, 1953)

$$f(r) = \frac{(1 - r^2)^{\frac{n}{2} - 2}}{B\left(\frac{1}{2}, \frac{1}{2}(n - 2)\right)} \quad (4.3)$$

where n is the sample size and B is the Beta function. Note that both Matlab’s `corr` (`corr2022matlab`) and R’s `cor` (stats package, (R Core Team, 2022)) use the Studentized version of the test, which is exact for Gaussian samples (Teukolsky et al., 1992) and should produce the same results as presented here. Another test statistics for correlation is built on Fisher’s z -transformation, $z = \text{atanh}(r)$, which approximately follows a normal distribution with standard error $1/\sqrt{n-3}$ (Fisher, 1915, 1921). Interestingly, we can also use Fisher’s z -transformation with Spearman’s rank correlation coefficient, replacing the standard error with $\sqrt{1.06/(n-3)}$ (Fieller et al., 1957). Spearman’s rank correlation coefficient (Spearman, 1904) is the Pearson’s correlation coefficient applied to the rank of samples and thus can be applied to non-Gaussian data.

For different α levels and varying level of smoothness, we measure the false positive rate, i.e. the percentage of points that are counted as significantly correlated. By definition, this percentage should be close to the α -level. Results are presented in Figure 4.2 with 99% binomial confidence intervals. We observe that the false positive rate leaves the α -level when the smoothness is greater than 0.4. This illustrates the risk of testing for correlation from dependent samples; for instance, when testing at a

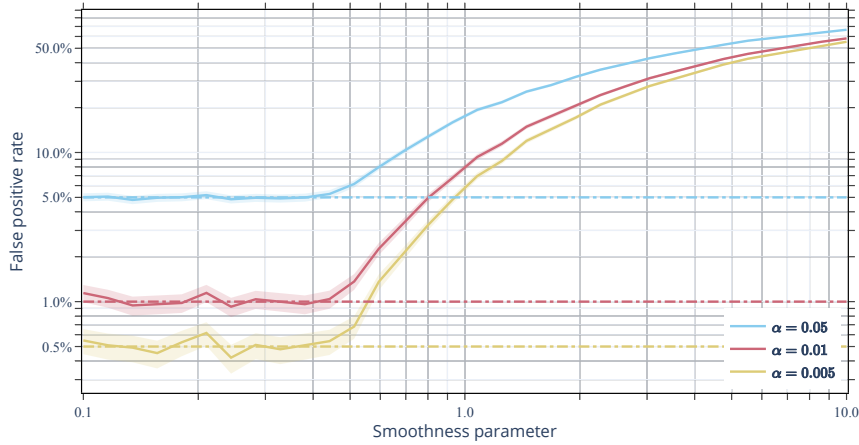


Figure 4.2: False positive rate of the Pearson correlation test applied to stochastic processes with Gaussian autocorrelation. Notice that process smoothness corrupts the test distribution. Hence, smooth signals should not be used to test for correlation without correction.

significance level $\alpha = 5\%$ with a smoothness of 2, the false-positive rate is about 30%, 6 times the desired p -value. Therefore, correction for the test statistics is necessary.

3 Related work

3.1 Preamble

The problem of finding *e.d.f.* for time series have been approached several times since the seminal work of Bartlett (M. Bartlett, 1935). The general approach is to consider two random variables X, Y with zero mean and variance σ_x and σ_y . Given a sample of dependent observations $\{x_1, \dots, x_n\}$ and $\{y_1, \dots, y_n\}$ with autocorrelation ρ_k and γ_k , the estimator for the cross-correlation is $\frac{1}{n}(\sum_{k=1}^n x_k y_k)$, and has mean

$$E \left\{ \frac{1}{n} \sum_k x_k y_k \right\} = \frac{1}{n} \sum_k E \{ x_k y_k \} = \frac{1}{n} \sum_k E \{ x_k \} \cdot E \{ y_k \} = 0 \quad (4.4)$$

and variance

$$\begin{aligned} E \left\{ \frac{1}{n^2} \left(\sum_k x_k y_k \right)^2 \right\} &= \frac{1}{n^2} E \left\{ \sum_k x_k^2 y_k^2 \right\} + \frac{2}{n^2} E \left\{ \sum_i \sum_{j>i} x_i y_i x_j y_j \right\} \\ &= \frac{\sigma_x^2 \sigma_y^2}{n} \left(\rho_0 \gamma_0 + 2 \sum_{k=1}^{n-1} \frac{(n-k)}{n} \rho_k \gamma_k \right) \end{aligned} \quad (4.5)$$

Now, let \tilde{x}_k and \tilde{y}_k , $1 \leq k \leq N$, be a sample of independent observations from X and Y . Then, the cross-covariance $\frac{1}{N} \sum_k \tilde{x}_k \tilde{y}_k$ has zero mean and variance

$$E \left\{ \frac{1}{N^2} \left(\sum_k \tilde{x}_k \tilde{y}_k \right)^2 \right\} = \frac{\sigma_x^2 \sigma_y^2}{N} \quad (4.6)$$

Comparing Eq. (4.6) and Eq. (4.5), we see that

$$N = n \left(\rho_0 \gamma_0 + 2 \sum_{k=1}^{n-1} \frac{(n-k)}{n} \rho_k \gamma_k \right)^{-1} \quad (4.7)$$

When it is reasonable to assume that the estimator in the dependent case is distributed as the estimator in the independent case, then we can consider that the estimator from dependent samples is roughly distributed as an estimator with N d.f. and we say that $\frac{1}{n}(\sum_{k=1}^n x_k y_k)$ has N effective degrees of freedom.

3.2 Methods for finding the number of e.d.f.

Bartlett (M. Bartlett, 1935) considered first-order autoregressive processes with autocorrelation ρ and proposed to approximate Eq. (4.7) with

$$v_{Ba} = n \left(\frac{1 + \rho^2}{1 - \rho^2} \right) \quad (4.8)$$

A few years latter, Bartlett published a novel treatment of the problem (M. S. Bartlett, 1946). Then, Bayley and Hammersley (Bayley & Hammersley, 1946) proposed to use directly the expression from Eq. (4.7):

$$v_{BH} = n \left(\rho_0 \gamma_0 + 2 \sum_{k=1}^{n-1} \frac{(n-k)}{n} \rho_k \gamma_k \right)^{-1} \quad (4.9)$$

and Quenouille (Quenouille, 1947) used the expression

$$v_{Qu} = n \left(\sum_{k=-\infty}^{+\infty} \rho_k \gamma_k \right)^{-1} \quad (4.10)$$

The expressions proposed above are derived under the null hypothesis of zero correlation between x and y . More recently, (Afyouni et al., 2019) proposed a novel expression which accommodates the case of nonzero correlation. Under the null hypothesis, their expression reduces to Eq. (4.9). Hence, as we are interested in finding *e.d.f.* for the test distribution under the null hypothesis, the expression proposed by (Afyouni et al., 2019) is not considered here.

3.3 Link with Welch-Satterthwaite approximation

We show that the number of *e.d.f.* given by Bayley and Hammersley Eq. (4.9) and Quenouille Eq. (4.10) is equivalent to the well-known Welch-Satterthwaite approximation (Satterthwaite, 1946; Welch, 1947) in the case of samples with the same autocorrelation $\gamma_k = \rho_k$. Let X a random vector of size n with zero mean, unit variance and a covariance matrix Σ ; the Welch-Satterthwaite approximation is

$$v_{WS} = \frac{\text{tr}(\Sigma)^2}{\text{tr}(\Sigma\Sigma)} \quad (4.11)$$

Now, if the covariance between elements of X is given by a symmetric function $\text{Cov}(X_i, X_j) = \rho_{|i-j|}$, then Σ is a symmetric Toeplitz matrix, i.e.

$$\Sigma = \begin{pmatrix} \rho_0 & \rho_1 & \cdots & \rho_{n-1} \\ \rho_1 & \rho_0 & \cdots & \rho_{n-2} \\ \vdots & \vdots & \ddots & \vdots \\ \rho_{n-1} & \rho_{n-2} & \cdots & \rho_0 \end{pmatrix}$$

or more compactly, $\Sigma_{ij} = \rho_{|i-j|}$. Toeplitz covariance matrices represent the autocorrelation matrices of stochastic processes (Gray et al., 2006). In that case, the numerator of Eq. (4.14) becomes

$$\text{tr}(\Sigma)^2 = n^2 \rho_0^2 \quad (4.12)$$

and the denominator is

$$\begin{aligned} \text{tr}(\Sigma\Sigma) &= \sum_i \sum_{j=1}^n \Sigma_{ij}\Sigma_{ji} = \sum_i \sum_{j=1}^n \rho_{|i-j|}^2 = \sum_i \left(\rho_0^2 + \sum_{k=1}^{n-i} \rho_k^2 + \sum_{k=1}^{i-1} \rho_k^2 \right) \\ &= n\rho_0^2 + 2 \sum_{k=1}^{n-1} (n-k)\rho_k^2 \end{aligned} \quad (4.13)$$

Whence the number of degrees of freedom given by the Welch-Satterthwaite approximation is similar to Eq. (4.9)

$$\nu_{WS} = n \left(\rho_0^2 + 2 \sum_{k=1}^{n-1} \frac{(n-k)}{n} \rho_k^2 \right)^{-1} \quad (4.14)$$

3.4 Problem with current approaches

The methods mentioned above rely on estimating the autocorrelation function of the process and using the sum of squares to correct the number of *d.f.* This formulation has the benefit of being quite generic as it does not require any assumption on the underlying process. However, we shall show that this methods systematically underestimates the number of *e.d.f.* Let $\hat{\rho}_k$ be the unbiased estimator of the k -th term ρ_k of the autocorrelation function

$$\hat{\rho}_k = \frac{1}{n-k} \sum_{i=1}^{n-k} x_i x_{i+k} \quad (4.15)$$

From the definition of the variance, we have

$$E\{\hat{\rho}_k^2\} = \rho_k^2 + \text{var}(\hat{\rho}_k^2) \quad (4.16)$$

and thus

$$E\left\{ \sum_k \hat{\rho}_k^2 \right\} = \sum_k \rho_k^2 + \sum_k \text{var}(\hat{\rho}_k^2) \quad (4.17)$$

Thus, if we estimate the number of *e.d.f.* given by Eq. (4.9) using Eq. (4.17), then the bias

$$E\{\hat{\nu} - \nu\} = n E\left\{ \frac{1}{\sum_k \hat{\rho}_k^2} - \frac{1}{\sum_k \rho_k^2} \right\} = \frac{n}{\sum_k \rho_k^2} E\left\{ \frac{\sum_k (\hat{\rho}_k^2 - \rho_k^2)}{\sum_k \hat{\rho}_k^2} \right\} \quad (4.18)$$

$$= -\nu E\left\{ \frac{1}{\sum_k \hat{\rho}_k^2} \sum_k \text{var}(\hat{\rho}_k) \right\} \quad (4.19)$$

From which

$$E\{\hat{\nu}\} = \left(1 - E\left\{ \frac{1}{\sum_k \hat{\rho}_k^2} \sum_k \text{var}(\hat{\rho}_k) \right\} \right) \nu \quad (4.20)$$

Hence, directly computing the *d.f.* correction from an unbiased estimator of the autocorrelation function yields biased results. In particular, the variance of the estimator $\text{var}(\hat{\rho}_k)$ is expected to increase with k because the estimation is carried over decreasing number of points $n - k$ (see the bounds of the summation in Eq. (4.15)). In contrast, as the autocorrelation decreases, the contribution of terms $\hat{\rho}_k^2$ to the sum $E\{1/\sum_k \hat{\rho}_k^2\}$ decreases with k . Therefore, zeroing the tails of the autocorrelation function is expected to decrease the bias. This is the core idea of regularization methods. Several methods exist for regularizing the autocorrelation function. Because our approach does not require to estimate the autocorrelation function, we mention only the approach from (Pyper & Peterman, 1998) which is used in our numerical experiments, similarly to (Afyouni et al., 2019). (Pyper & Peterman, 1998) proposed to truncate after the $n/5$ first lags of the autocorrelation function. The interested reader can refer to (Afyouni et al., 2019) for a more thorough review of regularization methods.

4 A parametric approach to estimate the effective degrees of freedom for time series

4.1 Asymptotic effective degrees of freedoms

We observed that existing methods for degrees of freedoms are related to the Welch-Satterthwaite approximation. Thus, it is worth taking a closer look in the terms of Eq. (4.14) in the case of 1-dimensional series. We derive here the Welch-Satterthwaite for asymptotically large Toeplitz matrices. We give an explanation here and a simple proof in Appendix C. For a more general treatment, see e.g. (Ginovyan & Sahakyan, 2013; Gray et al., 2006).

The numerator in the expression of the Welch-Satterthwaite approximation is the trace of a Toeplitz matrix and is therefore $n\rho(0)$, where n is the size of the matrix and $\rho(0)$ is the diagonal element. The denominator is the trace of product of two Toeplitz matrix – which is not a Toeplitz matrix. Toeplitz matrices represent a convolution operation; whereas the columns of the product matrix represents the convolution the autocorrelation function with the columns of Σ . By construction, the j -th column of Σ is the autocorrelation function shifted by t_j , thus

$$(\Sigma\Sigma)_{ij} = \sum_k \rho(t_k - t_i)\rho(t_j - t_k)$$

We see that most diagonal elements of the product matrix correspond to the timestep where the mode of the two convolved functions coincide. As the autocorrelation function is symmetric, this gives

$$(\Sigma\Sigma)_{ii} = \sum_k (\rho(t_k - t_i))^2$$

Although it is in general not true on the edges (i close to 1 or n), the impact of these terms on the trace of the entire matrix becomes negligible when the matrix size increases. Thus, if we consider large matrices and decreasing autocorrelation, then most of the diagonal elements represent the sum of squares of the autocorrelation terms. Dividing by n and taking the limit of the Riemann sum yields

$$\frac{1}{n}\text{tr}(\Sigma\Sigma) = \frac{1}{n} \sum_i \sum_j (\rho(t_j - t_i))^2 \xrightarrow{n \rightarrow +\infty} \int_{-\infty}^{+\infty} (\rho(\tau))^2 d\tau$$

Thus, the Welch-Satterthwaite approximation is asymptotically

$$v \approx \frac{n\rho(0)^2}{\int_{-\infty}^{+\infty} (\rho(\tau))^2 d\tau} \quad (4.21)$$

For processes with known autocorrelation function, we can directly evaluate Eq. (4.21). Examples for common autocorrelation function are presented in Table 4.1.

4.2 Laplace approximation of the autocorrelation function

Let ρ be the autocorrelation function of a stationary process. We assume that ρ has finite second-order derivatives. The second-order expansion of ρ around its mode at $\tau = 0$ is

$$\rho(\tau) = \rho(0) - \rho''(0)\frac{\tau^2}{2} + \dots$$

and is similar (up to second-order) to a process with autocorrelation

$$r(\tau) = e^{-\tau^2/2\lambda^2}$$

where

$$\lambda^2 = \frac{1}{-\rho''(0)}$$

Autocorrelation	<i>e.d.f.</i>
δ_τ (white noise)	n
$e^{-\tau^2/2\lambda^2}$	$n/\sqrt{\pi\lambda^2}$
$(2\sigma^2/\theta)e^{-\theta \tau }$ (Ornstein-Uhlenbeck process)	$n\theta^3/\sigma^4$
ϕ^τ (first-order autoregressive process)	$-n \log \phi$
$\sin(\alpha\tau)/(\alpha\tau)$	$n\alpha/\pi$
$\sin^2(\alpha\tau)/(\alpha\tau)^2$	$n3\alpha/2\pi$

Table 4.1: Empirical degrees of freedoms for some common autocorrelation functions

This second-order approximation at the mode is known as the Laplace approximation (Bishop & Nasrabadi, 2006). The term $\rho''(0)$ that acts as a precision (inverse variance) in the Laplace approximation is the second spectral moment of the process. For the approximating autocorrelation function, we have

$$\int_{-\infty}^{\infty} (r(\tau))^2 d\tau = \int_{-\infty}^{\infty} e^{-\tau^2/\lambda^2} d\tau = \sqrt{\pi} \lambda = \sqrt{\frac{\pi}{-\rho''(0)}} \quad (4.22)$$

Plugin Eq. (4.22) in Eq. (4.21), we find that the number of *e.d.f.* for a process with second spectral moment $\rho''(0)$ is approximately

$$v = \frac{n}{\sqrt{\pi}\lambda} = n\sqrt{\frac{-\rho''(0)}{\pi}} \quad (4.23)$$

Remark 4.1. The second spectral moment is a universal measure of “roughness” in the literature of stochastic processes (Cox & Miller, 2017; K. J. Friston et al., 2008). In fact, the second spectral moment is related to the average number of zero-crossings N_0 by Rice’s formula (Rice, 1944) (for derivation, see (Cox & Miller, 2017, Ch. 7.4, Example 7.9)):

$$N_0 = n\sqrt{-\rho''(0)}/\pi \quad (4.24)$$

Using Rice’s formula, we can derive a simple way to quickly estimate the number of *e.d.f.* v for an empirical time series with N_0 zero-crossings

$$v = \sqrt{\pi}N_0 \quad (4.25)$$

In Figure 4.3, we plot the correlation factor v/n as a function of the smoothness parameter λ . We see that the number of *e.d.f.* decreases with the second spectral moment. The interpretation is the same as for other approaches: smoother processes have less degrees of freedom. We see that when $\lambda < 1/\sqrt{\pi}$, i.e. $-\rho''(0) > \pi$, Eq. (4.23) yields more *e.d.f.* than the number of points in the series. Interestingly, the critical point $\sqrt{\pi}$ corresponds to having $N_0 = n$ zero-crossings in the series of n points.

4.3 An unbiased estimator of smoothness

We give a sketch of proof that the variance of the first-order derivatives is an unbiased estimator of the second spectral moment. For convenience, we use a Gaussian process, and let the reader refer to e.g. (Cox & Miller, 2017, Ch 7.4), (Adler, 2010, Theorem 2.2.2.), (K. Worsley, 1996) for general cases.

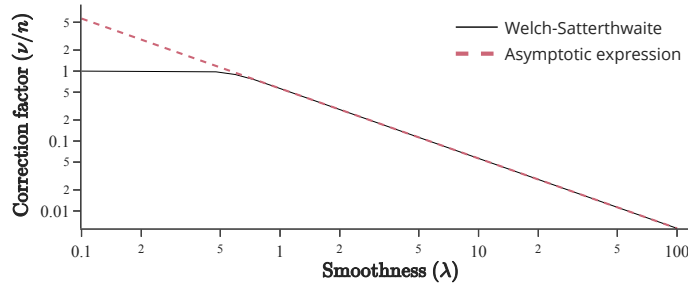


Figure 4.3: Correction factor, defined as the number of *e.d.f.* divided by the number of points, as a function of the smoothness parameter. We see that the correction factor is greater than 1 when the smoothness is $1/\sqrt{\pi} \approx 0.56$ and converges to the correction factor given by the Welch-Satterthwaite approximation (Eq. (4.14)) for higher smoothness.

Let $X = (x_1, \dots, x_n)^T$ be a series of Gaussian random vectors with mean μ_x , unit variance, and a Toeplitz covariance matrix $\Sigma_{ij} = \text{Cov}(X_i, X_j) = \rho_{|i-j|}$. Assuming the series has time resolution δ , we introduce the forward finite difference operator

$$D = \frac{1}{\delta} \begin{pmatrix} -1 & 1 & 0 & & \\ 0 & -1 & 1 & \ddots & \\ & \ddots & \ddots & \ddots & 0 \\ & & & 0 & -1 & 1 \end{pmatrix} \quad (4.26)$$

and observe that the series of first-order forward finite differences is given by

$$\dot{X} \stackrel{\text{def}}{=} \left(\frac{x_2 - x_1}{\delta}, \dots, \frac{x_n - x_{n-1}}{\delta} \right)^T = DX$$

From the properties of the multivariate normal distribution, we have

$$\dot{X} \sim \mathcal{N}(0, \Lambda) \quad (4.27)$$

where $\Lambda = D\Sigma D^T$ is the symmetric Toeplitz matrix with elements

$$(\Lambda)_{ij} = \frac{2\rho_{|i-j|} - \rho_{|i-j+1|} - \rho_{|i-j-1|}}{\delta^2}$$

Interestingly, the elements of Λ are the second-order finite differences of ρ , i.e.

$$(\Lambda)_{ij} = -\ddot{\rho}_{|i-j|} \quad (4.28)$$

Let $\frac{1}{n} \sum_k \dot{x}_k^2$ be the sample variance of the first-order finite differences $\dot{x}_k = (x_{k+1} - x_k)/\delta$. We observe that

$$E \left\{ \frac{1}{n} \sum_k \dot{x}_k^2 \right\} = \frac{1}{n} \sum_k E \{ \dot{x}_k^2 \} = \frac{1}{n} \text{tr}(\Lambda) = -\ddot{\rho}_0 \quad (4.29)$$

Thus,

$$\lim_{\delta \rightarrow 0} \frac{1}{n} \sum_k E \{ \dot{x}_k^2 \} = -\rho''(0) \quad (4.30)$$

Whence, the sample variance of the first-order derivatives is an unbiased estimator of the process roughness. Replacing in Eq. (4.23) leads to the expression Eq. (4.1) presented in introduction

$$e.d.f. = n \sqrt{\frac{1/n \sum \dot{x}_k^2}{\pi}} \quad (4.31)$$

4.4 Relationship with resolution elements in neuroimaging

In the neuroimaging literature, the concept of *resolution elements* (resels) is closely related to the number of *e.d.f.* (Penny et al., 2011). The FWHM is widely used in imaging problems. It naturally arises when considering to the problem of finding the minimum separation distance that allow to distinguish two features on an image (Logothetis, 2002) (see Figure 4.4). The FWHM criterion is one of the solutions, with e.g. the Raileigh criterion, the Sparrow criterion (Cheng, 2009). The number of resels can thus be interpreted as the maximal number of independent features we can distinguish in an image. The number of resels is found by assuming that the images have been smoothed by a Gaussian kernel with a certain width. The width of the smoothing kernel is parameterized in terms of *Full-Width at Half-Height*, which is the distance between the points where the kernel reaches half of its peak value. It is related to the standard deviation of the Gaussian kernel by the formula (Kiebel et al., 1999)

$$\text{FWHM} = \sqrt{8 \log 2} \lambda \quad (4.32)$$

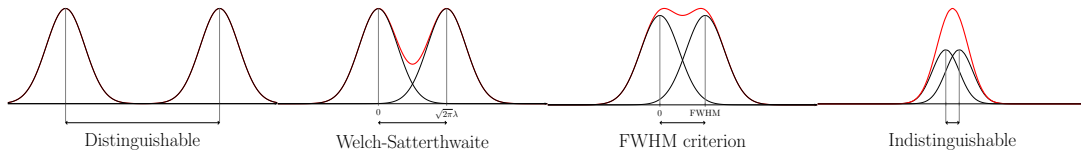


Figure 4.4: Distinguishing features on an image. The x -axis represents the sensor space and the y -axis is the source intensity. Gaussian functions in black represent the spread of the original sources on the sensor and the red curve is the perceived intensity. When the two sources are separated from more than the FWHM, the perceived intensity allow to distinguish between them. However, distinction is not possible when the separation becomes smaller. FWHM is one of the criterions characterizing the minimal distinguishable distance and can be interpreted as the inverse of the maximal sampling rate.

In the 1-dimensional case, the formula giving the number of resels ν for a number of n voxels reduces to (Penny et al., 2011):

$$\text{Resels} = n / \text{FWHM} \quad (4.33)$$

The FWHM in fMRI studies is computed using the variance of the first-order derivatives, which is an estimator of the smoothness of the random field (Kiebel et al., 1999; Penny et al., 2011; K. Worsley, 1996). Thus, resels have a similar interpretation to *e.d.f.* and are based on the same mathematical tools used to derive Eq. (4.1). Whence, it is interesting to compare the number of resels with the number of *e.d.f.* given by Eq. (4.1). Let $z = \{z_1, \dots, z_n\}$ be a series of independent observations of a random variable (i.e., white noise). We define the Gaussian kernel

$$\kappa(t) = C e^{-t^2/2\lambda^2} \quad (4.34)$$

where C is a normalizing constant such that $C^2 = 1$. The autocorrelation of the filtered signal $x = \kappa * z$ is

$$r(\tau) = (\kappa * \kappa)(\tau) = e^{-\tau^2/4\lambda^2} \quad (4.35)$$

which has roughness

$$r''(0) = -\frac{1}{2\lambda^2} = -\frac{4 \log 2}{\text{FWHM}^2} \quad (4.36)$$

where the last equality comes from Eq. (4.32). Plugin in Eq. (4.23) yields

$$v = \frac{n}{\text{FWHM}} \sqrt{\frac{4 \log 2}{\pi}} \approx 0.939 \times \text{Resels} \quad (4.37)$$

Thus, the number of e.d.f. is quite close to the number of resolution elements, although it is a little bit lower.

5 Numerical experiments

5.1 False positive rate for Gaussian processes with known smoothness

We use the procedure described in Section 2 to generate series with Gaussian autocorrelation. We evaluate the Pearson correlation coefficient for series of 2048 points with smoothness (kernel width) ranging between 0.1 and 100. We repeat 65,536 independent experiments. As before, we use the exact test distribution of the Pearson correlation coefficient under the null hypothesis of uncorrelated samples. However, we use here the number of *e.d.f.* to parameterize the test distribution. Eq. (4.23) is used to obtain the number of e.d.f., replacing n with the length of the series and λ with the standard deviation of Gaussian autocorrelation. Note that we did not estimate the smoothness from the series but used the exact analytical value to disentangle the problems of smoothness estimation and *d.f.* correction. Hence, this corresponds to the case of known smoothness and yields results similar to the methods of Bayley-Hammersley, Quenouille, and Welch-Satterthwaite.

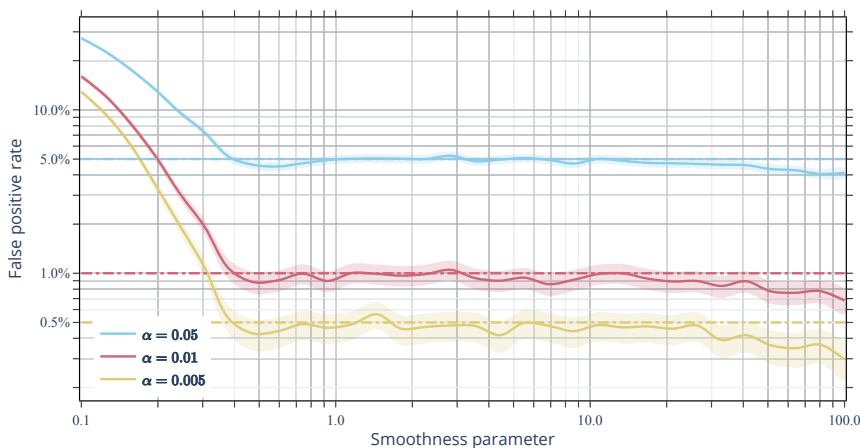


Figure 4.5: False Positive Rate of the Pearson correlation test with the correction of the number of degrees of freedom.

We present the False Positive Rate as a function of kernel smoothness in Figure 4.5. As we did not specify a maximal number of e.d.f., we observe that the False Positive Rate is far from the test level when the process roughness is greater than π . This corresponds to a kernel smoothness of $1/\sqrt{2\pi} \approx 0.399$, yielding a number of *e.d.f.* greater than the series length. Then, the 99% confidence interval of the FPR contains the target α level up to a kernel smoothness of 30. This corresponds to an autocorrelation taking about 42 points to decrease by a factor $1/e$. For our series of 2048 points, this represents about 27 *e.d.f.* Hence, there seems to be a limitation when the number of *e.d.f.* is too low – roughly 1% of the length of the series.

5.2 False positive rate for Gaussian processes with unknown smoothness

We repeat the same procedure as in the previous section to generate random series with a Gaussian autocorrelation. Similarly to before, we use series of 2048 points with smoothness between 0.1 and 100, and repeat the experiment 2^{16} times. However, we estimate the correction factor directly from the series instead of using the theoretical value. Therefore, we shall expect differences between the number of degrees of freedoms given by the Welch-Satterthwaite approximation and by our approach. This difference is due to the different estimation approach for the number of *e.d.f.* To compute the Welch-Satterthwaite approximation, we use Eq. (4.9) where ρ_k is obtained with the unbiased estimator from Eq. (4.15). Following (Pyper & Peterman, 1998), we truncate autocorrelation terms at lags greater than $n/5 = 410$. Our approach uses Eq. (4.31) based of the variance of the first-order derivative of the normalized series.

As in the problem statement (Section 2), we plot the false positive rate as a function of the smoothness parameter for three test levels, $\alpha = 0.05$, $\alpha = 0.01$, $\alpha = 0.005$. Results are shown in Figure 4.6. For the Welch-Satterthwaite approximation, we see that the false positive rate is systematically lower than the test level, thus the test is systematically too conservative. This is due to accumulating the square of non-zero terms in the sample autocorrelation, as mentioned in Section 3.4. For the proposed approach, the test level remain in the confidence interval for smoothness between 1 and 50. For low values of smoothness, the false positive rate obtained with the estimator is different from the theoretical one (Figure 4.5). This is a natural limitation of estimating the roughness from the variance of first-order derivatives: when consecutive samples with unit variance become independent, their finite differences have variance 2, which limits the estimated roughness. In that case, the estimated number of *e.d.f.* is wrong and the false positive rate is below the test level. For high values of smoothness, the false positive rate drops for the same reason as mentioned in the previous section.

6 Application to movement trajectories

6.1 Detecting synchronous movements from motion capture data

Here, we analyze motion capture data that has been recorded during the preliminary study of an electrophysiological experiment. Three (3) subjects were asked to perform self-paced elbow flexion/extension movement. Movement phases lasted for 23.5 seconds and elbow flexion was measured using XSens Awinda suit at a 60Hz rate, low-pass filtered, and upsampled to 200Hz. For an exploratory analysis of the neuronal events accompanying movement, we want to isolate sessions during which the movement of both arms were synchronized (in phase or anti-phase) from sessions with no apparent synchronization. A simple approach is to compute the Pearson correlation coefficient between right-arm and left-arm movement and to separate the sessions with significant correlation from the others. However, the *p*-value associated with the Pearson correlation coefficient is unreasonably high: about 90% of trials are significantly correlated with very low level of synchronization. Using the *e.d.f.* correction proposed here, we separate synchronized movement from others.

We show some sample trajectories on Figure 4.7. The trajectories analyzed here have extremely low roughness (≈ 0.0003) and hence very low number of *e.d.f.*. We evaluated the number of *e.d.f.* to 45.3 ± 3.0 for the right arm and 38.3 ± 2.2 for the left arm ($p < 0.05$). Hence, we are in the extreme case mentioned in the previous section: the number of *e.d.f.* is roughly 1% of size of the series. Trajectories on the first row are significantly correlated according to the uncorrected *p*-value but correspond to a very low correlation coefficient. Indeed, once we take into account the degrees of freedom reduction due to autocorrelation, the *p*-value increases drastically and samples are not considered as significantly correlated. Trajectories presented on the second row are considered as significantly correlated, both from the corrected and uncorrected *p*-values.

In addition, we use bootstrapping to generate samples from the null-distribution and compare the *p*-values given by our approach with the *p*-values given by the bootstrap method. We use the phase-

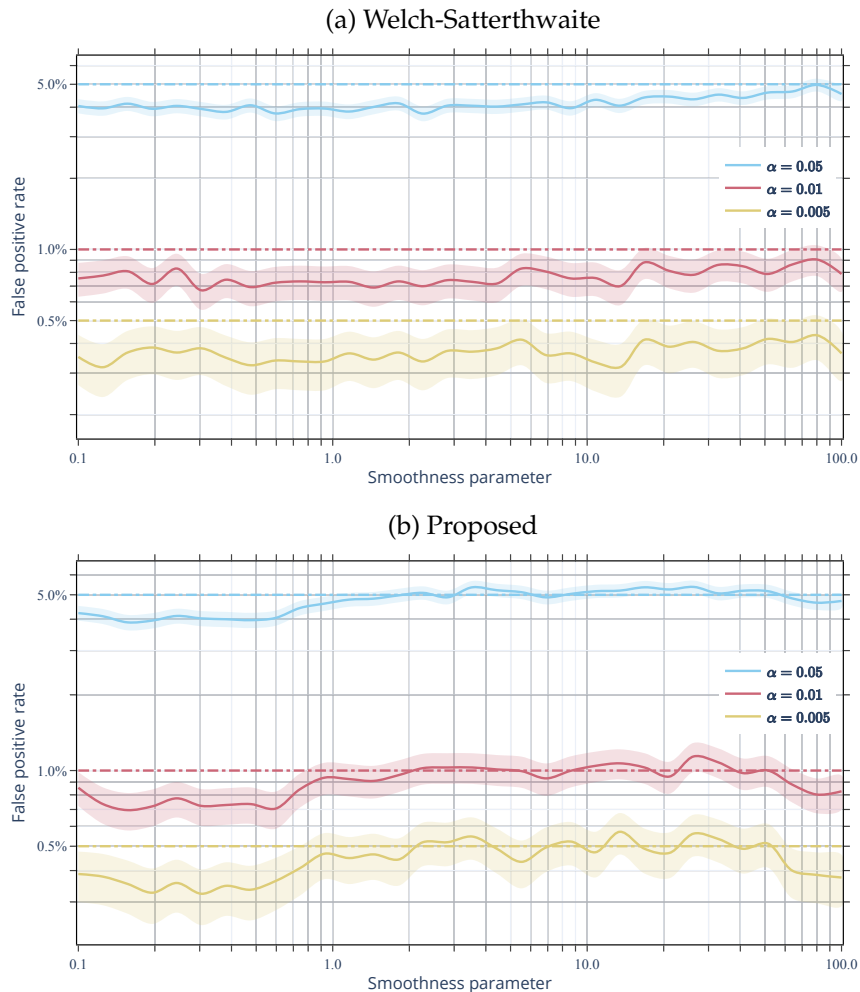


Figure 4.6: False positive rate of the correlation test with the *e.d.f.* correction proposed by Bayley and Hammersley (a) and our approach (b). Continuous error bands represent the 99% binomial confidence interval.

randomized surrogate method (Schreiber & Schmitz, 1996) to construct random samples having the same power spectral density, and thus the same autocorrelation, as the recorded trajectories. Phase-randomized surrogates are created by adding to the signal a random phase uniformly distributed between $-\pi$ and π . We compute 256 surrogates for each trajectory and compute the Pearson and Spearman correlation coefficients between pairs of surrogates. We evaluate the p -values uncorrected and corrected using Welch-Satterthwaite and the proposed approach. Results are presented as probability-probability plots in Figure 4.8.

Interestingly, we observe the effect of the bias in the Welch-Satterthwaite approximation (Eq. (4.20)): as the estimated number of *e.d.f.* is lower than the real value, the test distribution is less sharp, thus the p -value estimated for extreme correlation coefficient is lower. In contrast, the test distribution that comes from our approach relies on the assumption that the autocorrelation is Gaussian. Hence, we neglect some of the long-range correlations in the signal. Thus, we overestimate the number of *e.d.f.*, our test distribution is sharper than it should be, and we have more extreme p -values than bootstrapped.

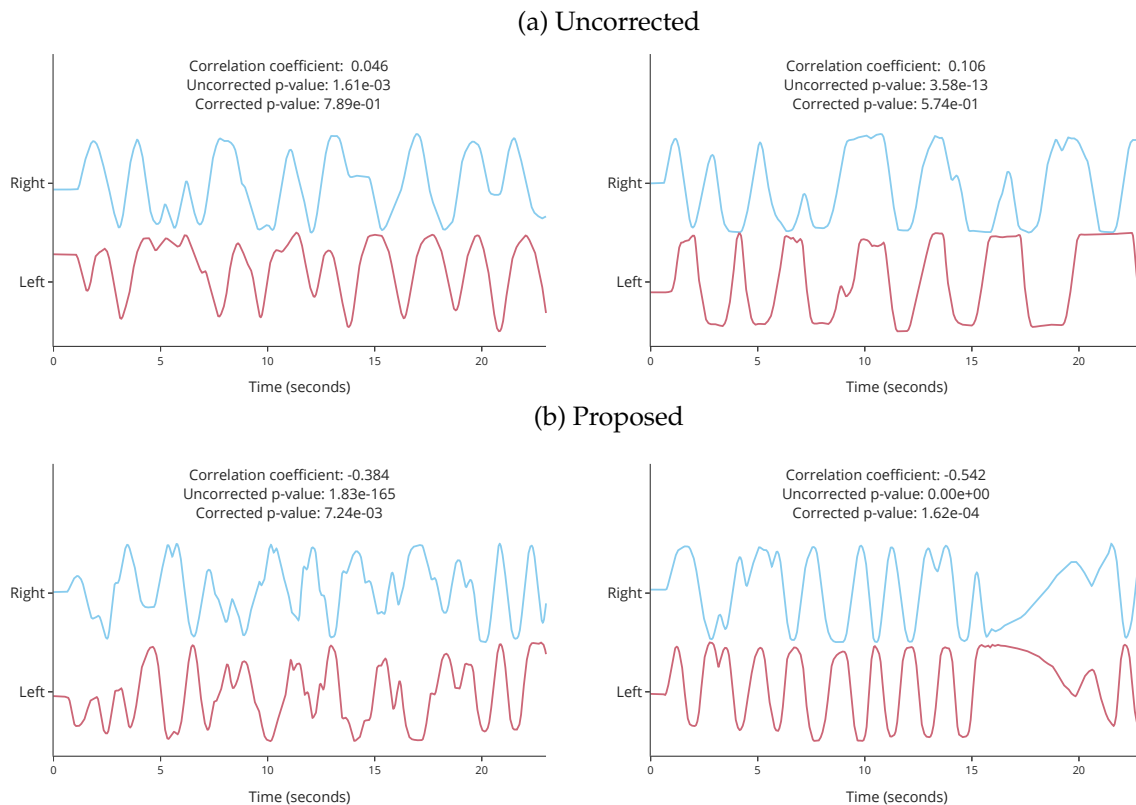


Figure 4.7: Sample movement trajectories showing significant correlation according to the Pearson coefficient. Series in the first row show significant correlation ($p < 0.01$, no correction) according to the uncorrected test distribution. Series in the second row show significant correlation ($p < 0.01$, *e.d.f.* correction) with the corrected test distribution. We see that trajectories with low correlation coefficient may be marked as significantly correlated with the uncorrected test distribution may not be significantly correlated when we take autocorrelation into account.

6.2 Accuracy of models reconstructing movement trajectories from EEG signals

In this section, we address the problem of evaluating the accuracy of models reconstructing movement trajectories from EEG signals. In the literature, reconstruction methods have been evaluated on a variety of movement types. To our best knowledge, these work systematically report the correlation coefficient between executed and reconstructed movement trajectories. In Table 4.2, we show an overview of movement types and performance metrics used in related works. We observe that the correlation coefficient is systematically reported and that the scale of the coefficient varies greatly. In particular, we see that some works report very low correlation coefficients which may be insignificant if the autocorrelation of the series is taken into account.

We are interested in evaluating the significance of the performance of some reconstruction methods. In addition, we investigate interactions between movement parameters and decoding accuracy. We use the data collected during our experiment on elbow movement. A complete description of our experimental procedure is given in Section 3.2. To summarize, 8 subjects were asked to perform self-paced, continuous, unilateral elbow flexion/extension during 23.5s-trials. Participants alternated between right- and left-arm movement. Participants were free to vary the speed and amplitude of the movements and produced movement trajectories with heterogeneous statistical properties, as observed

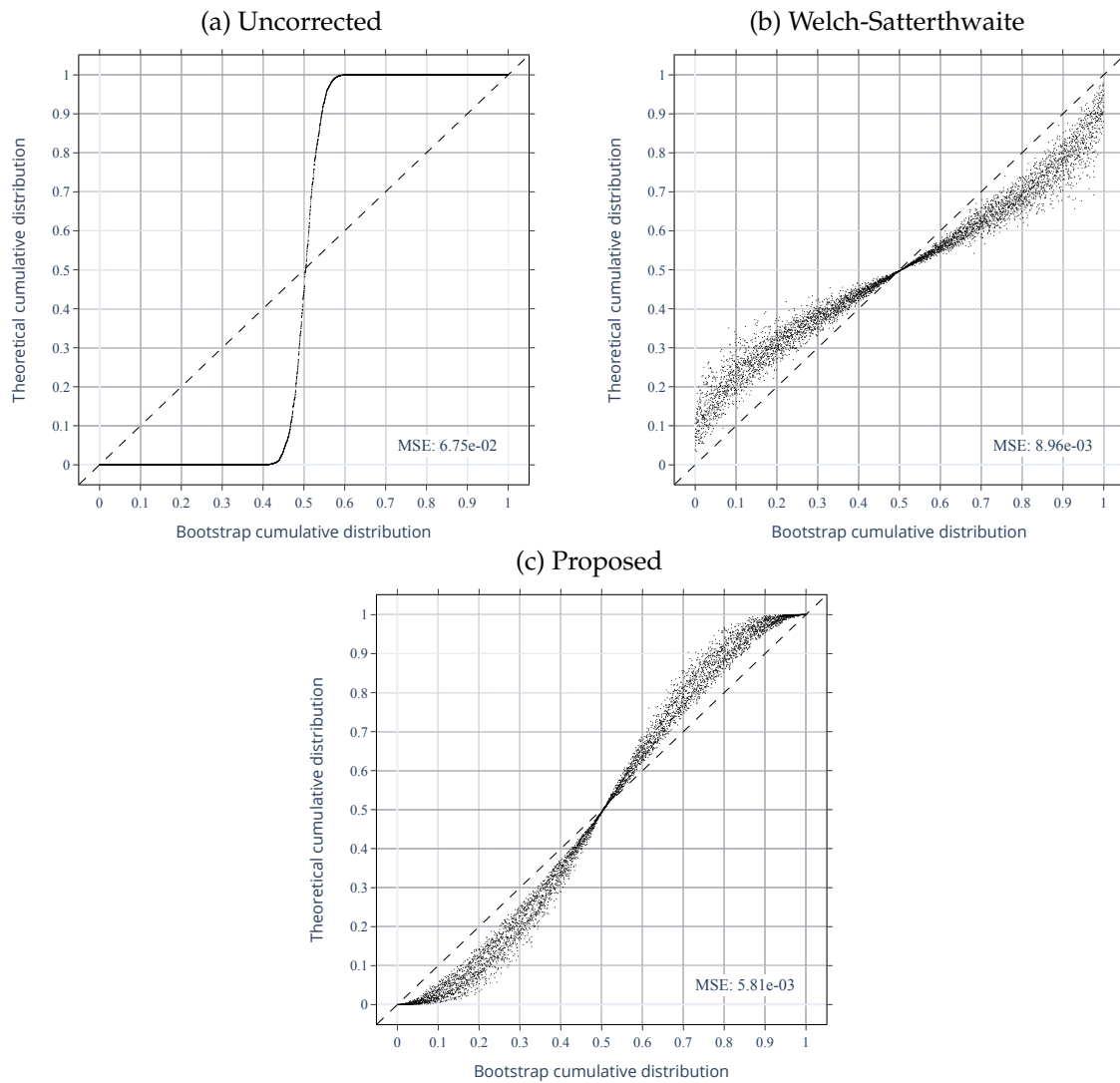


Figure 4.8: Probability-probability plots of the bootstrap versus theoretical p -values. Shown p -values are uncorrected (a), corrected with the Welch-Satterthwaite method (b), and corrected with our approach (c). The mean-squared error are indicated to quantify the deviation from the line of identity.

in Section 4.1.

We focus on methods based on slow-cortical potentials (SCPs), i.e. EEG signals at low frequencies, to reconstruct joint trajectories from EEG signals. SCPs-based methods have been introduced first and extensively studied in the literature (e.g. (Antelis et al., 2013; Bradberry et al., 2010; Kim et al., 2014; Ofner & Müller-Putz, 2012)). To obtain SCPs, we filter EEG signals between 0.5 and 4Hz with a fourth-order Butterworth filter. Two reconstruction models are evaluated. The first model is a simple linear model, as proposed in (Ofner & Müller-Putz, 2012). This model is a Wiener filter which reconstructs each point of the movement trajectory from EEG signals at different lags. We used a number of lags of 10 (Bradberry et al., 2010) and a lag of 10ms (Ofner & Müller-Putz, 2012). The second model is a Kalman filter. All parameters of the models are identified using the expectation-maximization algorithm (Ghahramani & Hinton, 1996). The mathematical aspect of these models is not treated here, but a quick introduction to Kalman filtering is given in Appendix.

We compute Spearman’s correlation coefficient for each trial of each subject. Visual inspection of

the histograms of the trajectories indicated that our data is non-normal, which motivates our choice of using Spearman’s correlation coefficient. Scores are computed using leave-one-out cross-validation: models are trained on all the trials of the subject except the trial for which the score is computed. For instance, scores for trial 1 of subject 3’s left-arm movements is computed with a model trained on trials 2 to 20 of subject 3’s left-arm movements. In addition, we compute the two-sided p -value associated with Spearman’s r using the Fisher z -transformation method, as presented in Section 2. We estimate the number of $e.d.f.$ using Eq. (4.31). Importantly, the variance of the series was estimated from the executed trajectories, to preclude any effect from our reconstruction model on the number of $e.d.f.$

6.2.a Results and discussion

First, we evaluate for our two reconstruction models the average reconstruction score for each subject. Results are presented in Figure 4.9. For right arm movements, the group median of reconstruction scores are 0.09 for the linear model and 0.05 for the Kalman filter. For left arm movement, the group median of reconstruction scores 0.09 for the linear model and 0.07 for the Kalman filter. Results are heterogeneous across subjects. For both arms, the median score of subject 3 and subject 7 is higher than the group median. Poor performance are systematically obtained for subjects 4 and 9 and for left arm movements for subject 8. Interestingly, during the preliminary analysis of movement data (Section 4.1), we observed that subjects 4 and 9 performed slow movements with large amplitude and varied a lot the amplitude of their movements. Hence, this might indicate that the parameters of movement trajectories influence the reconstruction performance.

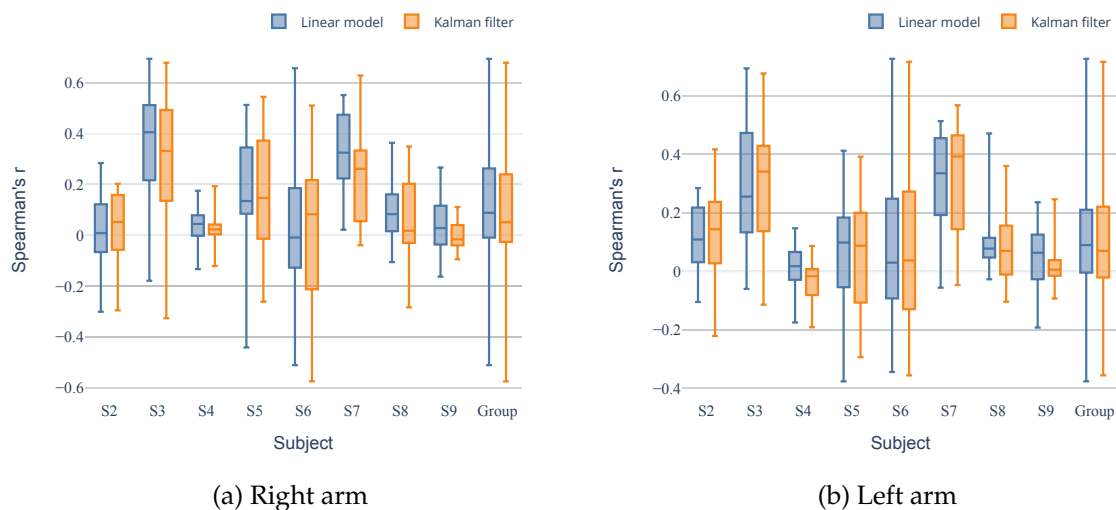


Figure 4.9: Per-subject reconstruction score for right- and left-arm movements.

To confirm that reconstruction performance is related to movement parameters, we show executed and reconstructed movement trajectories with correlation coefficient associated with low and high p -values. This corresponds to movement trajectories that were well or badly reconstructed. Results are presented in Figure 4.10 for the linear model. Results are similar for Kalman filter and shown in Appendix 2 (Figure C.1). We observe that movement trajectories that are well reconstructed “oscillate” more quickly than movement trajectories that are badly reconstructed. For instance, 18 cycles were realized during the trial 19 of left-arm movements of subject 6 (Figure 4.10, upper-right quadrant). The movement trajectory was fairly well reconstructed from EEG signals, with a correlation coefficient of 0.73 (corrected $p = 7.6 \times 10^{-14}$). In contrast, only 5 complete cycles were realized during the trial 18 of right-arm movements of subject 4 (Figure 4.10, lower-left quadrant). The movement trajectory was badly reconstructed with a correlation coefficient of 0.01 (corrected $p = 0.86$).

To illustrate the strong interdependence between movement parameters and reconstruction accu-

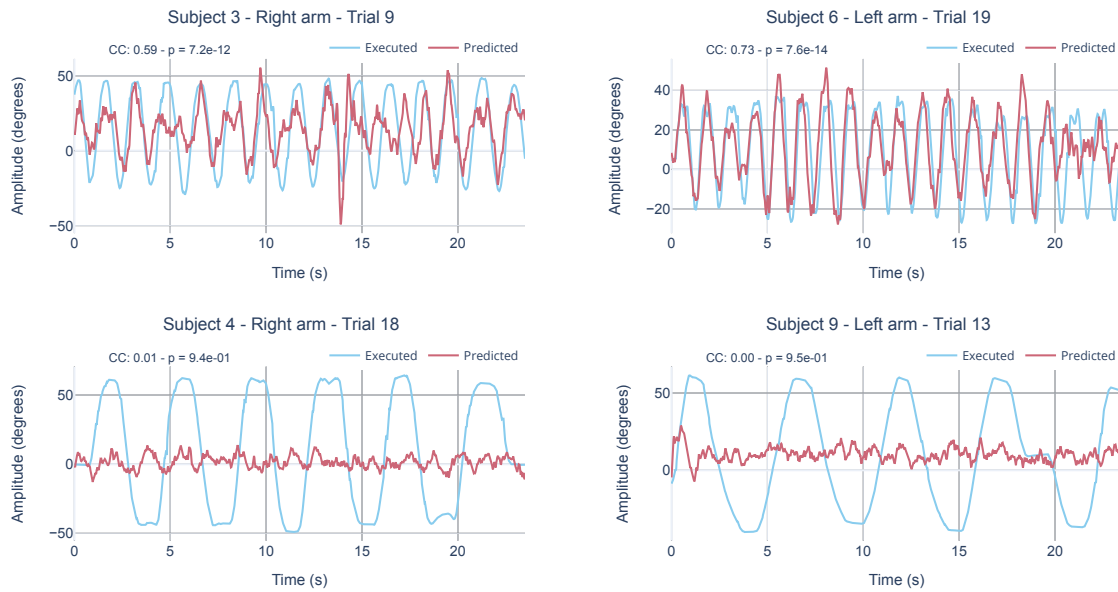


Figure 4.10: Sample executed and reconstructed movement trajectories, associated with low p -values (first row) and high p value (second row). Trajectories are reconstructed with the linear model.

rary, we present scatter plots of the p -value associated with the reconstruction score against the mean and standard deviation of movement cycles. Results are shown in Figure 4.11 for the linear model and in Appendix 2, Figure C.2 for the Kalman filter. We observe that low p -values are systematically obtained for movement trajectories with a low cycle duration. Equivalently, trajectories with long mean cycle duration are systematically badly reconstructed. In addition, low p -values are exclusively associated with trajectories with little variation in their cycle duration. In summary, trajectories consisting in fast and precise cycles are well reconstructed while trajectories with slow or variable cycles are badly reconstructed. In the case of precise cycles, the correlation coefficient might be unadequate because the trajectory is closer to a periodic function with noise than to a stochastic process.

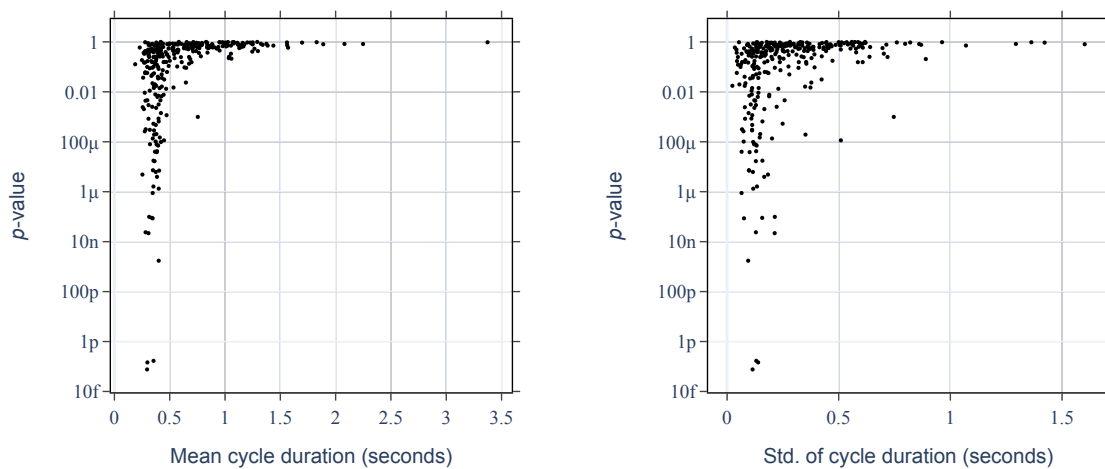


Figure 4.11: p -value of the decoding accuracy of the linear decoding model versus of mean and standard deviation of movement cycles. Each marker represent the value obtained for a single trial of a single subject.

Finally, we illustrate and discuss an interesting observation that occurred during our analysis. In some situations, two trajectories with a similar reconstruction score differed greatly in terms of p value. This phenomena is illustrated in Figure 4.12. We observe that the two trajectories have similar reconstruction score but the significance of these scores differ by an order 10^2 . In fact, this phenomena is partly due to a difference in the number of *e.d.f.* of the two series. In the trajectory of trial 9 of right arm movements for subject 5, we can count 38 zero-crossings. Using Eq. (4.2), we can estimate that the trajectories has $38\sqrt{\pi} \approx 67$ *e.d.f.*. In contrast, the trajectory of the fourth trial of right arm movement by subject 8 has 18 zero-crossings which result in $18\sqrt{\pi} \approx 32$ *e.d.f.*. Equivalently, the statistics of the first series are virtually produced with twice more independent samples than the statistics of the second series. Whence, differences in p -values are unsurprising. This result implies that we must interpret the correlation coefficient conditionally to the “smoothness” of the series. In particular, operations such as averaging correlation coefficients might produce unexpected results because the distribution of individual coefficients might differ strongly.

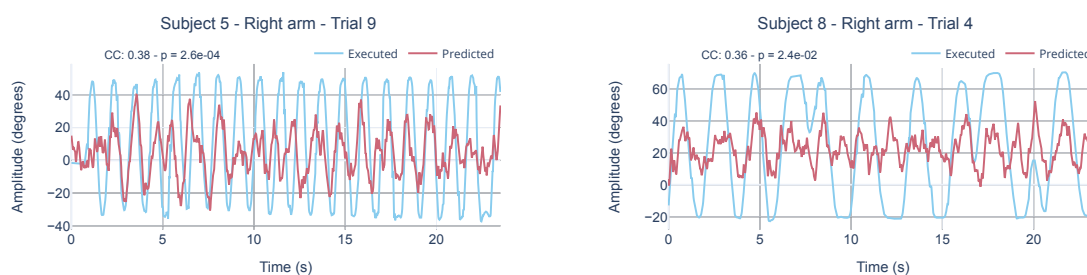


Figure 4.12: Two sample trajectories with similar correlation coefficient. The p -values associated to the correlation coefficient differ by an order 10^2 because of the differences in the smoothness of the series.

7 Conclusion

In this work, we considered the problem of testing for significant correlation from autocorrelated series. Several works have proposed to find the number of *e.d.f.* of the series. The number of *e.d.f.* correspond to the size of a sample of independent observations that would produce the same statistics. The number of *e.d.f.* can then be used in the test distribution of the correlation coefficient even if the distribution relies on an independence assumption. Related methods require to estimate the autocorrelation function, which can be problematic when testing correlation between two unique and smooth series.

Here, we show that works in the literature are indeed related to the well-known Welch-Satterthwaite approximation with particular Toeplitz matrices. We propose to use the asymptotic extension of the approximation in an integral form. Using a Laplace approximation of the autocorrelation function, we derive a simple formula giving the number of *e.d.f.* of stochastic processes having an autocorrelation with finite second-order derivatives. The expression depends on the second-order derivatives of the autocorrelation function at its mode, which is a measure of the roughness of the process and relates to several of its statistical properties. Works on random field have highlighted that roughness can be easily estimated from the variance of the first-order time derivatives of the process. We use these results to propose a new estimator for the number of *e.d.f.*. In addition, we use Rice’s formula to derive an estimator of *e.d.f.* based on the number of zero-crossings. We confirm the adequacy of our approach on random series. We use bootstrapping to compute the false positive rate of our approach as a function of the smoothness of the signal. We also highlight problems in current approaches due to a wrong estimation of the autocorrelation function.

Finally, we use our approach on real motion capture data from a neurophysiological experiments. First, we use the Spearman correlation coefficient to separate synchronous and asynchronous move-

ment trajectories. In addition, we create phase-randomized surrogates to construct quantile-quantile plots of the p -values yielded by the different *e.d.f.* correction methods. We observe that our approach give adequate results, despite the fact that the data are extremely smooth. Second, we use our approach to obtain corrected p -values for the Spearman correlation coefficient between executed movement trajectories and trajectories reconstructed from EEG signals. We reproduce well-known methods from the literature and apply them to our movement data. We interpret our results in the light of the *e.d.f.*

Overall, our results indicate that Pearson and Spearman correlation coefficients can be applied to time series and even used for significance testing. However, as the “smoothness” of individual series impacts their test distribution, further work is required to assess whether group-level statistics can be produced from individual coefficients.

Reference	Movement type	Subj.	Metrics	CC
(Bradberry et al., 2010)	Reaching	5	CC	0.2 to 0.35
(Ofner & Müller-Putz, 2012)	Self-paced	5	CC	0.23 to 0.35
(Antelis et al., 2013)	Reaching	7	CC, NRMSE	0.15 to 0.37
(Kim et al., 2014)	Loop	10	CC, NRMSE	0.35 to 0.65
(Robinson et al., 2015)	Reaching	7	CC	0.6
(Korik et al., 2016)	Reaching	4	CC	0.2 to 0.5
(Úbeda et al., 2018)	Loop (lower limb)	4	CC, others	0.35 to 0.55
(Korik et al., 2018)	Reaching	12	CC	0.4
(Veslin et al., 2019)	Reaching (elbow flexion)	6	CC, MSE	0.33 to 0.98
(Jeong et al., 2019)	Reaching	5	CC	0.8
(Kobler, Almeida, et al., 2020)	Loop	12	CC	0.5 to 0.85
(Mondini et al., 2020)	Pursuit	10	CC	0.28
(Kobler, Sburlea, et al., 2020)	Pursuit	15	CC	0.8
(Martínez-Cagigal et al., 2020)	Pursuit	5	CC	0.35 to 0.48
(Müller-Putz et al., 2021)	Pursuit	1	CC, amplitude	0.23 to 0.36

Table 4.2: Related work on decoding movement trajectories from EEG signals. The abbreviations are MSE for Mean Squared Error, NRMSE for Normalized Root Mean Squared Error. We report group-averaged values when possible, otherwise minimum and maximum scores. The objective of reported values is to indicate the scale of the scores. The interested reader should refer to the related references to properly assess the performance of a method.

Chapter 5

Modelling the movement and the brain: perspectives and challenges

1 Introduction

In this chapter, we are interested in devising and estimating a simplified model of elbow movements. Our thoughts in favor of this approach follow from the fact that the task is relatively simple and might be well captured by a biologically-plausible model, guided by physical evidence.

A simple musculoskeletal model could suffice because our task is relatively simple: participants realized movements with one degree of freedom joint. The approximate dynamics of the arm can be obtained with rigid body dynamics. The combined forces from the pair of antagonist muscles, the *biceps* and *triceps brachii*, determine the exogenous joint torque. The modeling of muscular forces has been well-studied in the 20th century and resulted, for instance, in Hill's muscle model (Hill, 1938). Therefore, by combining Hill's muscle models of both biceps and triceps with the rigid body dynamics of the arm, we obtain a simple musculoskeletal model.

Modeling the cortical activity and its coupling to muscle motoneurons activity is less straightforward but yet feasible. A model of the spinal cord is necessary to incorporate cortical activity with the muscle motoneurons activity that enter Hill's muscle models. The circuitry of the spinal cord is responsible for closed-loop modulation of muscle forces that pervades reflex arcs (Bear et al., 2020). In order to model this circuitry, we must equip our muscle models with afferent neurons that give a feedback on the muscle configuration. Fortunately, simplified models of both afferents neurons and of the spinal cord are found in the literature (Hao et al., 2013; Li et al., 2015; Teka et al., 2017). Finally, we can use one of the numerous models of the cortical activity as measured in electrophysiology. To summarize, building a simplified model of the cortical activity and corticospinal tracts may also be feasible.

Because we only measure a subset of the variables of our model, we need an advanced Bayesian estimation scheme. During the movement task, only joint angle, EMG signals, and EEG signals are measured. It is important to notice that there are many aspects of our model that we are hidden to our measurement setup. For instance, we may only guess the timecourse of the spinal neurons activities, the time constants of the excitatory populations in cortical columns, or the noise variance of the motion capture system. In general, the literature gives us prior ideas on the distribution of parameter values. These prior distributions can be used to weight the likelihood of the measurements under our model and thus refined from the measurements. In other word, we may use Bayes rule to obtain the posterior distributions of states (i.e. the variables varying in time), parameters (i.e. the variables fixed in time) and hyperparameters (i.e. the variables configuring the shapes of distributions). Because our model contains nonlinear mappings, we need an advanced Bayesian scheme to solve this triple estimation problem.

Here, we use a variational Bayesian estimation scheme called DEM (K. J. Friston et al., 2008). The

go-to method to solve triple-estimation problems is to use a nonlinear variant of Kalman filter with the Expectation-Maximization algorithm; however, the strongly-nonlinear nature of the problem at hand precludes this solution. In contrast, the DEM algorithm has been constructed to work well on nonlinear problems. DEM is an instance of *variational* or *approximate* Bayes methods, which refers to a group of methods that transform the ill-defined problem of estimating a posterior distribution into an optimization problem (Bishop & Nasrabadi, 2006). The optimization problem is to minimize the variational free energy (VFE), which is the divergence between the approximate and true posterior plus the model evidence, i.e., the log-probability of the measurements under our model. While the divergence and model evidence are individually intractable, the VFE can be evaluated. In other words, our Bayesian triple-estimation problem reduces to minimizing a single, global quantity. Under this perspective, the DEM algorithm solves the problem quite straightforwardly: it minimizes the VFE with respect to the states, parameters, and hyperparameters, using gradient descent for each of these three quantities.

So far, we briefly presented a set of models that can be assembled to build a neuromusculoskeletal model. In addition, we introduced a powerful estimation scheme that can be used with such model. Trying to use the model and the estimation scheme together allowed us to discover technical problems. Thus, our objective in this chapter is to highlight some challenges that need to be tackled to enable inverting such kind of model on real data. The rest of the chapter is organized as follows. First, after briefly introducing the Kalman filter, we extensively present the DEM algorithm. In particular, we provide a numerical comparison of the two methods, based on our own Python implementation of DEM – the code to reproduce the results is available online. Then, we present our results and discussion. In the result and discussion section, we build up the neuromusculoskeletal model from the arm model to the neural masses. At each stage, we present some generated trajectories and, where possible, some inversion on real movement data. In addition, we show the problems that may arise at that stage and discuss possible ways to resolve them. In a last section, we give a brief summary and discussion.

2 Bayesian inversion of nonlinear dynamical systems

2.1 Kalman Filtering and generalization

Since the seminal paper of R.E. Kalman in 1960 (Kalman, 1960), the Kalman filter has been extensively used in research and industrial application. The Kalman filter solves the Bayesian filtering problem in the case of linear dynamic models with additive white Gaussian noise. Given a series of measurements and a probabilistic generative model (that is, a dynamical model with a description of the statistical properties of the noise), the Kalman filter finds the most likely state of the system at present time.

The Kalman filter is originally limited to linear systems but may be extended to nonlinear ones. Nonlinear systems are problematic because the predictive density originates from a nonlinear function and thus do not generally take a convenient form. In that case, three natural solutions arise. First, we can use a set of random samples (*particles*) to model our state distribution. The moments of the distribution of the state variables is not explicitly modeled, but can be retrieved at any time from the particles. This method is known as particle filtering and will not be further treated here. Second, we can assume that nonlinear functions are relatively smooth with respect to the spread of our data, and linearize the function around the mean to get the variance of the projected data. More precisely, let f be the nonlinear function with Jacobian J_f and X a normal random vector such as $X \sim \mathcal{N}(\mu, \Sigma)$, we have

$$f(X) \approx Y \sim \mathcal{N}\left(f(\mu), J_f(\mu)\Sigma J_f^T(\mu)\right)$$

Using the linearization, we construct a reasonable approximation to the transformed distribution when the function is sufficiently smooth. Kalman filter using this transform are known as Extended Kalman filters (EKF). The third approach to overcome nonlinear functions takes ideas from both EKF and particle filtering. Similarly to the EKF, we will try to identify the moments of the distribution after applying the function. And similarly to the particle filters, we will use a set of samples points that we will project

independently. However, the points are not randomly sampled but are rather important points of the normal distribution. Basically, these points relates to moments of the distribution, thus we project them using the nonlinear function and then fit the normal distribution that has the same points. The transformation is known as unscented transform and is used in the Unscented Kalman filter (UKF).

Using Kalman filter and generalization, we can perform a Bayesian inversion and identify the most likely sequence of hidden states that produced our observations, given a probabilistic model. However, in some applications, we do not have an exact model or have only a partial knowledge of some aspects of the model. Thus, we may want to identify unknowns from the data. Our partial knowledge may comprise some priors on the distribution of some parameters but also some priors on the probabilistic model — hyperparameters, typically, the distribution of the covariance matrices. The expectation-maximization (EM) algorithm can be used to estimate parameters and hyperparameters. The typical estimation scheme for dynamical models is the following. First, we specify a probabilistic model and some priors. We initialize the model using the expectations of the prior. Then, we run the filter on a set of data to produce filtered state estimate. This step is important, because it allows us to create sample trajectories for the system states, even though we did not observe them. Then¹, we can directly find the maximum-a-posteriori (MAP) values for each parameter and hyperparameter. This is the most crucial step of EM: given a first guess on model parameters, we create some plausible trajectories for the hidden states that we use directly in the equations as if the real trajectories of the hidden states were observed. By repeating this scheme, we are guaranteed to converge to a local minima.

EM with Kalman filtering form a powerful scheme to solve triple inversion problems — estimating states, parameters, hyperparameters — in a Bayesian way. However, this inversion scheme becomes greatly limited on highly nonlinear models such as biophysical models. A major limitation comes from the inability of the Kalman filter and of its nonlinear generalization to track robustly hidden states. In the next section, we introduce another inversion scheme that comprises Kalman filter and EM as a particular case: the Dynamic Expectation Maximization.

2.2 Dynamic Expectation Maximization

In this section, we give a brief introduction to Dynamic Expectation Maximization (DEM) and illustrate on numerical examples its difference with the Kalman filtering approach. As the scheme incorporates a large number of new ideas, a thorough presentation of DEM is incompatible with brevity. Therefore, although an effort is made to explain essential ideas and reproduce important figures, many technical details have been omitted and we let the reader refer to the original paper (K. J. Friston et al., 2008) for any supplementary details.

2.2.a Hierarchical dynamic model

We assume here that we deal with nonlinear hierarchical dynamic model, i.e. a cascade of models

$$v_L = \eta_v + z_{L+1} \quad (5.1)$$

$$\begin{cases} \dot{x}_L &= f_L(x_L, v_L; \theta) + w_L \\ v_{L-1} &= g_L(x_L, v_L; \theta) + z_L \end{cases} \quad (5.2)$$

...

$$\begin{cases} \dot{x}_2 &= f_2(x_2, v_2; \theta) + w_2 \\ v_1 &= g_2(x_2, v_2; \theta) + z_2 \end{cases} \quad (5.3)$$

$$\begin{cases} \dot{x}_1 &= f_1(x_1, v_1; \theta) + w_1 \\ y &= g_1(x_1, v_1; \theta) + z_1 \end{cases} \quad (5.4)$$

¹A supplementary step is to use a smoother (roughly, a backward filter) to produce state estimates that also integrate subsequent observations. However, this is out of the scope of this treatment and was omitted for brevity.

We see that the input of the model at each level is the output of the model that is directly above. The terms $w = (w_1, \dots, w_L)^T$ and $z = (z_1, \dots, z_{L+1})^T$ are Gaussian innovations with zero mean and covariance matrices Σ_w and Σ_z . These covariance matrices are random variables governed by some hyperparameters λ with mean μ_λ and covariance Σ_λ^2 . The term η_v gives the mean of the input at the highest hierarchical level. Functions may have some parameters to estimate, in that case they are parameterized by the general vector θ , which contains the parameters of all functions. θ is also a normal random variable with mean μ_θ and covariance Σ_θ . The values of μ_θ and Σ_θ are used to formulate our priors on the distribution of the parameters. For instance, we can formulate that the typical value of the maximal force produced by the Biceps Brachii is 2300N and that we expect the exact value to differ between individuals.

2.2.b Condensed notation

As the hierarchical model presented before is not very convenient to deal with, we simplify the notation. We stack all states derivative $\dot{x}_1, \dots, \dot{x}_L$ in a column vector

$$\dot{x} = (\dot{x}_1, \dots, \dot{x}_L)^T \quad (5.5)$$

Note that each \dot{x}_i is itself a vector of size n_i^x and thus the size of \dot{x} is $\sum_{i=1}^L n_i^x$. We proceed similarly for the outputs

$$v = (y, v_1, \dots, v_L)^T \quad (5.6)$$

We see that \dot{x} and v are two random variables with a multivariate normal distribution

$$\dot{x} \sim \mathcal{N}(f, \Sigma_w) \quad v \sim \mathcal{N}(g, \Sigma_z) \quad (5.7)$$

where f and g are the mean of the states and outputs, i.e.

$$f = (f_1(x_1, v_1; \theta), \dots, f_L(x_L, v_L; \theta))^T \quad (5.8)$$

$$g = (g_1(x_1, v_1; \theta), \dots, g_L(x_L, v_L; \theta), \eta_v)^T \quad (5.9)$$

In addition, we will stack the time-varying variables a random variable

$$u = (\dot{x}, v)^T \quad (5.10)$$

The distribution of u follows from that of x and v

$$u \sim \mathcal{N}(\mu_u, \Sigma_u) \quad (5.11)$$

where

$$\mu_u = \begin{pmatrix} f \\ g \end{pmatrix} \quad \Sigma_u = \begin{pmatrix} \Sigma_w & 0 \\ 0 & \Sigma_z \end{pmatrix} \quad (5.12)$$

2.2.c Variational Free Energy

We will now introduce the cost function that is optimized by the DEM algorithm. Given observed data y , we want to obtain the posterior distribution $p(u, \theta, \lambda | y)$ of the states u , parameters θ , and hyperparameters λ . Let $Z = \{u, \theta, \lambda\}$ be the set of these hidden variables. The posterior distribution is

$$p(Z|y) = \frac{p(y|Z)p(Z)}{p(y)} = \frac{p(y|Z)p(Z)}{\int p(y, Z)dZ} \quad (5.13)$$

²We will not cover how covariance matrices are formed from the hyperparameters because it falls beyond the scope of this chapter.

We see that the denominator in Eq. (5.13) is an integral over hidden variables, which implies integrating over all possible trajectory, under each possible value of parameter and hyperparameter. Naturally, this renders the problem intractable. DEM, as other Variational Bayes methods, proposes to approximate the posterior with a function q . For any choice of q , we can measure its distance to the true posterior $p(Z|y)$ using the Kullback-Leibler (KL) divergence:

$$D_{\text{KL}}(q(Z) || p(Z|y)) = \int q(Z) \log \frac{q(Z)}{p(Z|y)} dZ = F + \log p(y) \quad (5.14)$$

F is the *Variational Free-Energy* (VFE, also known as the negative *evidence-lower bound*)

$$F = - \int q(Z) \log \frac{p(y, Z)}{q(Z)} dZ = E_q\{-\log p(Z, y)\} + H\{q\} \quad (5.15)$$

where $H[q]$ is the entropy of the distribution q and the term $E_q\{-\log p(Z, y)\}$ is the expectation of the complete-data likelihood when the hidden variables are sampled from the approximating distribution. Finally, noticing that the term $\log p(y)$ in Eq. (5.14) is independent of q yields the important result of this section: minimizing the free-energy minimizes the distance between the approximating distribution q and the true posterior distribution.

2.2.d Mean-field approximation

We did not make any assumption on q to derive the previous results. Hence, we are free to choose q in a form that renders the variational free-energy easy to compute. This is the motivation for the particular form of the hierarchical dynamic model that was introduced before (Eq. (5.1)): using Gaussian distributions, we only need to estimate two sufficient statistics – the mean and the covariance. To furthermore simplify the problem, we force our approximating distribution q to factorize over states u , parameters θ , and hyperparameters λ . In other words, the function q for our hierarchical dynamic model is

$$q(u, \theta, \lambda) = q_u(u)q_\theta(\theta)q_\lambda(\lambda) \quad (5.16)$$

where q_u (resp., q_θ, q_λ) is Gaussian, parameterized by its mean μ_u (resp., μ_θ, μ_λ) and its covariance Σ_u (resp., $\Sigma_\theta, \Sigma_\lambda$). Note that some of these distribution parameters depends on each other, for instance, the mean of the states μ_u is a function of the parameters θ . To make Eq. (5.16) operate, we need to make a mean-field approximation, i.e. assume that the distribution of one variable (e.g. u) is obtained at the mean of the other variables (e.g. $\mu_u(\theta) \equiv \mu_u(\mu_\theta)$). The mean-field approximation make some terms appear in the expression of the free-energy, but these terms will be omitted here for simplicity.

2.2.e Inversion scheme

We can now explain the DEM inversion scheme. The general idea behind the DEM algorithm is to estimate states, parameters, and hyperparameters such that they minimize the VFE. As we mentioned before, minimizing the VFE renders our approximating density close to the true posterior density. DEM solves this optimization problem with a gradient descent on the VFE. However, as we have to deal with both time-varying and static quantities, there are some technical details to consider.

First, let us reintroduce time, which was deliberately kept out of the equations for simplicity. Here, the time varying quantity is $u \equiv u(t)$ which comprises the states and outputs of each system. Both the parameters θ and the hyperparameters λ are kept static³. DEM scheme consist in two steps that deal with dynamic and static quantities. The first step is analogous of the filtering step in the EM algorithm: the D-step of DEM estimates the posterior distribution of the state variables. The posterior is obtained by using a gradient descent on the free-energy. Because the system evolution is dictated by differential

³Alternatively, *generalized filtering* could be used to estimate of time-varying parameters (K. Friston et al., 2010).

equations, the gradient descent scheme takes the form of a flow $-\partial_u F$ acting on the system. This results in a new set of differential equations that can be integrated using any integration scheme – here, a local linearization scheme (Ozaki, 1992). This step allows to obtain the mean of the approximate posterior for the next time point. Then, the covariance of the approximate posterior is given by the Hessian of the VFE evaluated at the posterior mean⁴. To summarize, at each timestep, we use the “variational flow” to obtain the sufficient statistics of a Gaussian distribution that best approximate the posterior distribution of each state.

When the entire sequence has been processed, we can use the sequence of means of the state distribution to compute the gradients of the VFE with respect to the parameters and hyperparameters. Because of the mean field approximation, the VFE used to update the parameters and hyperparameters is different from that used to update the states. Parameters and hyperparameters are updated using a “static” VFE, usually termed *variational free-action* (VFA). While the VFE is evaluated at each timestep and represent an instantaneous quantity, the VFA is static and contains the time integral of the VFE evaluated at the mean of approximate states posterior. In other words, the parameters and hyperparameters are updated to minimize the *path integral* of the VFE — whence the term *free-action*. This gradient descent of the VFA with respect to the parameters and hyperparameters constitutes the E- and M-steps.

2.2.f Generalized coordinates

Generalized coordinates is a crucial aspect of DEM that enable filtering on nonlinear systems. So far, we deliberately ignored generalized coordinates to keep the notation uncluttered. In fact, to introduce generalize coordinates, we need to replace all time-varying quantities u by

$$\tilde{u} = (u, u', u'', \dots)^T \quad (5.17)$$

which contains derivatives of u up to order n . Interestingly, the vector of generalized coordinates \tilde{u} is sufficient to obtain a local expansion of the trajectory around u . Hence, filtering now takes also place at the level of the derivatives. The mean of the generalized states \tilde{u} , $\tilde{f} = (f, f', f'', \dots)^T$ and $\tilde{g} = (g, g', g'', \dots)^T$, are expressed from the generalized coordinates:

$$\begin{array}{ll} f' = \partial_x f x' + \partial_v f v' & g' = \partial_x g x' + \partial_v g v' \\ f'' = \partial_x f x'' + \partial_v f v'' & g'' = \partial_x g x'' + \partial_v g v'' \\ \dots & \dots \end{array}$$

where $\partial_x f \equiv \partial f / \partial x$. To use generalized coordinates, we also need to formulate how the noise w and z impact higher-order derivatives. In DEM, the noise is assumed to have a Gaussian autocorrelation parameterized by the roughness parameter (see Chapter 4 for more details). Therefore, the covariance matrix in generalized coordinates can be explicitly calculated. Because the random innovations propagates in the generalized coordinates, we have some uncertainty about the derivatives of the states. Hence, during the D-step, the flow of the VFE acts on the generalized coordinates. Therefore, in contrast to Kalman filter, the filtering step of DEM does not simply estimate the mean and covariance of the state at a particular time, but estimates a stochastic process which locally approximates the piece of trajectory.

A claim of the (K. J. Friston et al., 2008) is that the DEM algorithm can be applied to chaotic systems because of the generalized coordinates. In fact, this statement can furthermore extended: when applied to dynamical systems with a strange attractor and a smooth observation function, using generalized coordinates enable filtering on an embedding of the original attractor. We give in Appendix 1 a simple proof that generalized coordinates, as defined in DEM, can be used to embed a strange attractor. This

⁴This can be shown very simply, by writing down the VFE of the Gaussian distribution and solving $\partial_{\Sigma_u} F = 0$, see (Zeidman et al., 2022).

result is proved for more general cases by a (less famous) theorem in Takens' work (see (Takens, 1981, Theorem 3)). This embedding theorem for generalized coordinates supports the adequacy of using generalized coordinates to filter chaotic dynamical systems.

2.3 Implementation details

Results presented in this chapter come from our Python implementation of the DEM algorithm. Our implementation is extensively based on the original Matlab implementation in the SPM software but differs in some aspects. The commented pseudo-code of the algorithm is given in Algorithm 1. Crucially, we replaced the numerical differentiation scheme by symbolic differentiation based on Sympy and Symengine. This allows to use analytical derivatives automatically derived from the analytical expressions of the dynamic and observation functions. We validated our implementation by reproducing some examples of the original DEM paper. The code is available at <https://github.com/yop0/dempy>. In addition, the code for reproducing the results of this chapter is available at <https://github.com/yop0/nms-model>.

2.4 Comparison of the extended Kalman filter with DEM filtering

In this section, we present some numerical results reproduced from the original DEM paper and relevant for our application⁵. In particular, one of the claim of (K. J. Friston et al., 2008) is that the DEM algorithm uncovers the true state-space trajectories of chaotic system. In contrast, authors argue that conventional filters such as the Extended Kalman Filter (EKF) are unable to converge to the true trajectory and "succumb to the system's attractor" (K. J. Friston et al., 2008). Here, we analyze more in depth the behavior of both inversion schemes in the case of chaotic systems. In chaotic systems, even a perfect knowledge of the equations of the system is not sufficient: knowledge of the initial state is necessary to track the evolution of the system because of the sensitivity to initial conditions.

To highlight this phenomena, (K. J. Friston et al., 2008) proposed to consider the Lorenz system in the case where the sum of the three states is observed with additive noise. The parameters are assumed known but the initial state is unknown. This example is used to illustrate the differences between DEM and EKF on chaotic systems. The parameters are found DEM_demo_lorenz.m in the DEM toolbox of SPM12. The equations for the Lorenz systems used here are:

$$\begin{aligned}\dot{x} &= 18y - 18x, \\ \dot{y} &= 46.94x - 2xz - y, \\ \dot{z} &= 4xy - 4z, \\ v &= x + y + z.\end{aligned}$$

The variance of the state noise is assumed very low (e^{-16}) and the output noise on v has unit variance. The equations are integrated with a local linearization scheme (Ozaki, 1992) with a timestep⁶ $dt = 1/128$. We generated a series of 1024 observations by integrating the system from the initial state $(x_0, y_0, z_0) = (0.9, 0.8, 30)$. We then inverted the model, i.e. estimated the executed trajectories from the generated observations, using another initial state $(x_0, y_0, z_0) = (1, 1, 16)$. For the DEM algorithm, we used generalized coordinates up to order 8. For the EKF, we additionally used a backwards pass with the Rauch-Tung-Striebel (RTS) smoother (Rauch et al., 1965). Thus, in contrast to DEM and EKF, the "EKF with smoother" (EKF-RTS) algorithm is noncausal. More specifically, both EKF and DEM estimate the state distribution from past and present observations whereas EKF-RTS additionally uses future observations. This difference must be kept in mind when comparing EKF-RTS with DEM or EKF. Results of the inversion for the EKF, EKF-RTS and the DEM algorithm are shown in Figure 5.1. The fig-

⁵We also present in Appendix the figures for the linear convolution model with the parameters found in the DEM_demo_convolution_LAP.m file from the DEM toolbox of SPM12

⁶We used a smaller timestep than the original paper to obtain smoother time series.

Algorithm 1: Pseudo-code of the (simplified) DEM algorithm**Data:** models, priors, input series m , output observations y , number of steps n_E, n_M, n_T **Result:** approximate posterior distribution of states, parameters, and hyperparameters

```

for  $1 \leq i \leq n_E$  do
   $A \leftarrow 0$  // reset the VFE accumulator

  /* D-step: update states distribution */
  for  $1 \leq t \leq n_T$  do
     $(\tilde{x}, \tilde{v}) \leftarrow \tilde{\mu}_u$  // unpack current states

     $\tilde{v}_l = \tilde{\eta}_v + \tilde{m}(t)$  // initialize top-level input
    for  $1 \leq l \leq L$  do // propagate predictions through the hierarchy
       $\dot{x}_l = f_l(x_l, v_l, \mu_\theta)$  // compute dynamics at level  $l$ 
       $v_{l-1} = g_l(x_l, v_l, \mu_\theta)$  // compute output at level  $l$ 

       $\dot{x}_l = \partial_x f_l x'_l + \partial_v f_l v'_l$  // compute derivatives of dynamics
       $\dot{v}_{l-1} = \partial_x g_l x'_l + \partial_v g_l v'_l$  // compute derivatives of output
      ... // ... up to a defined order
    end

     $\tilde{x} = (\dot{x}, \ddot{x}, \dots)^T$  // define generalized coordinates of states
     $\tilde{v} = (v, \dot{v}, \dots)^T$  // define generalized coordinates of causes

     $F(t) \leftarrow F(\tilde{x}, \tilde{v}, \tilde{y}(t); \mu_\theta, \Sigma_z(\mu_\lambda), \Sigma_w(\mu_\lambda))$  // compute the VFE for timestep  $t$ 
     $A \leftarrow A - F(t)$  // accumulate VFE over time

     $\tilde{u}' = (\dot{x}, \ddot{x}, \dots, \dot{v}, \ddot{v}, \dots)^T$  // define derivatives of the generalized states
     $\tilde{u}' \leftarrow \tilde{u}' - \partial_{\tilde{u}} F(t)$  // compute the dynamics of the generalized states
     $\tilde{\mu}_u(t) \leftarrow \text{INTEGRATE}(\tilde{u}, \tilde{u}')$  // update the mean of generalized states
     $\tilde{\Sigma}_u(t) \leftarrow \partial_{\tilde{u}\tilde{u}} F(t)$  // compute the covariance of generalized states
  end

  /* M-step: update hyperparameters distribution */
  for  $1 \leq j \leq n_M$  do
     $\mu_\lambda \leftarrow \mu_\lambda - \partial_\lambda A$  // update the mean of hyperparameters
     $\Sigma_\lambda \leftarrow \partial_{\lambda\lambda} A$  // compute the covariance matrix of hyperparameters
  end

  /* E-step: update parameters distribution */
   $\mu_\theta \leftarrow \mu_\theta - \partial_\theta A$  // update the mean of parameters
   $\Sigma_\theta \leftarrow \partial_{\theta\theta} A$  // compute the covariance matrix of parameters
end

```

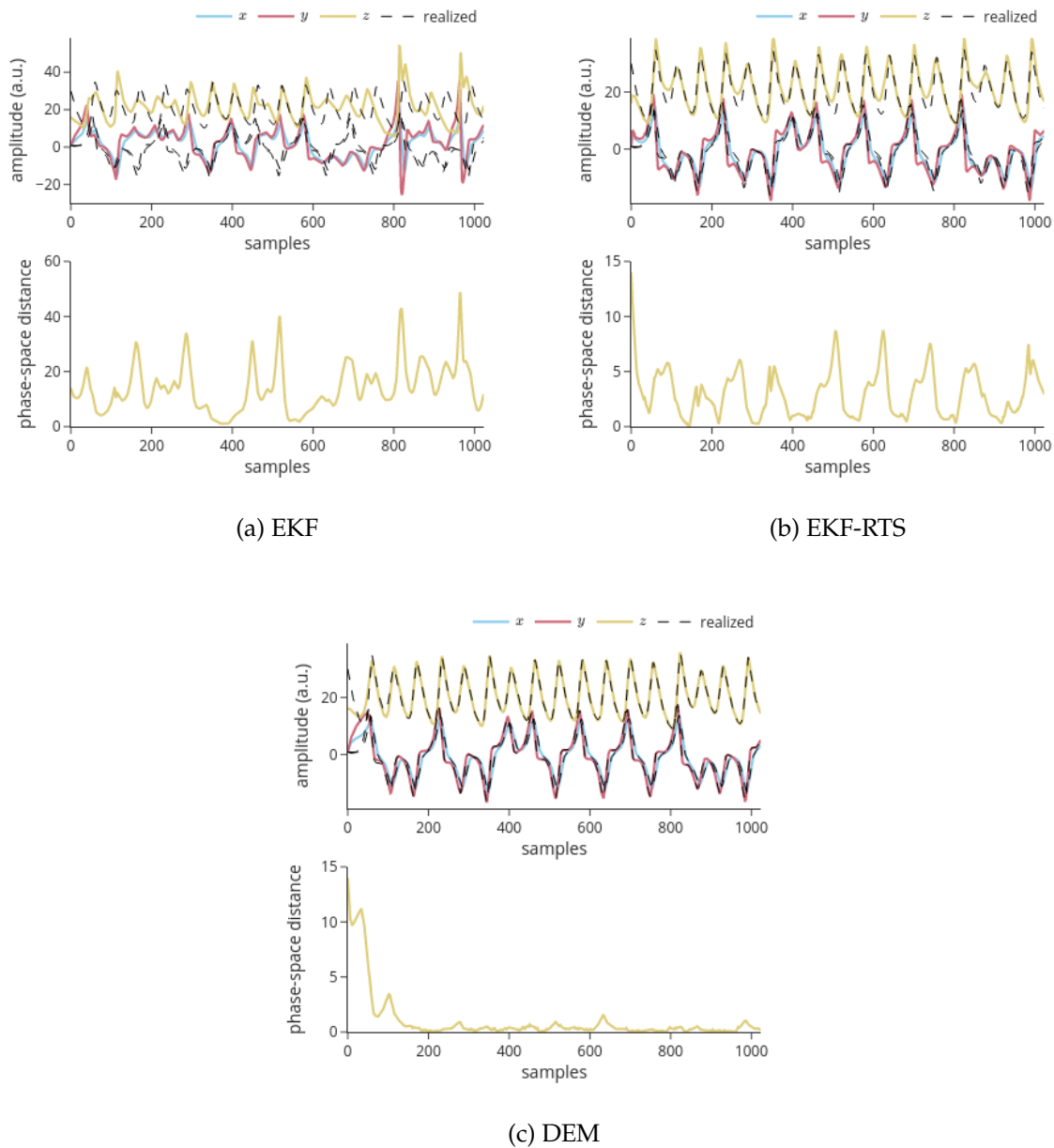


Figure 5.1: Comparison of EKF (a), EKF-RTS (b), and DEM algorithm (c) to invert the Lorenz system with unknown initial state. Figures on the upper row show the estimated and realized (unobserved) trajectories. Figures on the lower row show the Euclidean distance in phase-space between the estimated and realized trajectories. We see that phase-space error for the EKF-RTS is bounded below 10, while the error for the DEM algorithm is bounded below 2. The phase-space error for the EKF does not seem to converge: the system “succumb to the attractor”. Thus, the DEM algorithm provides a powerful alternative to conventional EKF or EKF-RTS schemes.

ure also shows the course of the phase-space distance between the realized and estimated trajectories. In the case of the EKF, the reconstructed trajectory is qualitatively different from the realized trajectory, i.e. peaks and cycles do not appear at the same location (see for instance between timestep 100 and 300). The EKF-RTS gives better estimates than the EKF alone and the reconstructed trajectory is qualitatively

similar to the original trajectory. However, the phase space distance is clearly higher than for the DEM algorithm. Indeed, this example provide striking evidence motivating to use the DEM algorithm to invert chaotic or highly nonlinear systems: in a single forward pass, the DEM algorithm uncovers the realized trajectory with a satisfying precision. The difference in precision between DEM and EKF-RTS is clearly visible when observing the trajectories in phase-space. In Figure 5.2, we show the realized and reconstructed trajectories projected on (x, y) and (x, z) planes for both EKF-RTS and DEM. We clearly see that the trajectory reconstructed by the EKF-RTS does not match the realized trajectory, whereas only minor errors appear on the trajectory reconstructed by the DEM algorithm.

3 On modelling the arm

3.1 Dynamic model of the arm

We present a simple model of a two dimensional arm with two degrees of freedom. Shoulder joint is only modeled to modulate the influence of gravity on motion. We consider the antagonist muscles for elbow flexion/extension: *biceps* and *triceps brachii*. The force exerted by the two muscles determines the stiffness of the joint. The center of mass of the upper-arm and forearm is considered centered on each limb segment. Prior distribution of the masses and segment dimensions are derived from the physiological tables in (Drillis et al., 1964). All parameters values are given in Appendix 2.

The elbow flexion angle is actuated by both biceps and triceps. Muscle insertions represent the distance between the elbow joint and the muscle connection to the forearm. Values of muscle insertions are set to 2cm for both biceps and triceps to obtain moment arms similar to (Murray et al., 1995). From muscle insertions and dimension of the upper arm, we can derive the moment arm formula using the muscle excursion method (An et al., 1984). Let \vec{l}_b and \vec{l}_t be muscle vectors pointing towards the shoulder, \vec{d}_b and \vec{d}_t insertion vectors from elbow joint towards muscle insertion and \vec{L} the humerus vector pointing towards the shoulder. These quantities follow the equality:

$$\vec{L} = \vec{d}_b + \vec{l}_b = \vec{d}_t + \vec{l}_t \quad (5.18)$$

Using position of muscles insertions, we can compute the muscle lengths:

$$l_b \stackrel{\text{def}}{=} \|\vec{l}_b\| = \sqrt{d_b^2 + L^2 - 2d_bL \cos q} \quad l_t \stackrel{\text{def}}{=} \|\vec{l}_t\| = \sqrt{d_t^2 + L^2 + 2d_tL \cos q} \quad (5.19)$$

The length of the muscle can then be used to compute the biceps and triceps moment arms r_b and r_t (An et al., 1984; Sherman et al., 2013):

$$r_b \stackrel{\text{def}}{=} \frac{dl_b}{dq} = \frac{d_b L \sin q}{\sqrt{d_b^2 + L^2 - 2d_bL \cos q}} \quad r_t \stackrel{\text{def}}{=} \frac{dl_t}{dq} = \frac{-d_t L \sin q}{\sqrt{d_t^2 + L^2 + 2d_tL \cos q}} \quad (5.20)$$

In order to avoid singularities, we clip the minimum values of muscles moment arms to 0.01. The torque from the gravity is given by $\tau_g = l_1 \sin(q - q^S) m_1 g$, where q^S is the shoulder angle. We model maximal flexion and extension bounds as viscoelastic moments, $\tau_{\text{bounds}} \equiv \tau_{\text{bounds}}(q, \dot{q})$. The total torque generated by the muscles is $\tau_{\text{muscles}} = -r_b F_b - r_t F_t$. The angular acceleration results from the sum of torques:

$$\ddot{q} = \frac{1}{mL^2} (\tau_g + \tau_{\text{muscles}} + \tau_{\text{bounds}}) = f(q, \dot{q}, F_b, F_t) \quad (5.21)$$

As the dynamics is defined by a second-order differential equation, we must transform the model into a couple of first order differential equations:

$$\begin{cases} \dot{q} &= v + w_v \\ \dot{v} &= f(q, \omega, q^S, F_b, F_t) + w_a \end{cases} \quad (5.22)$$

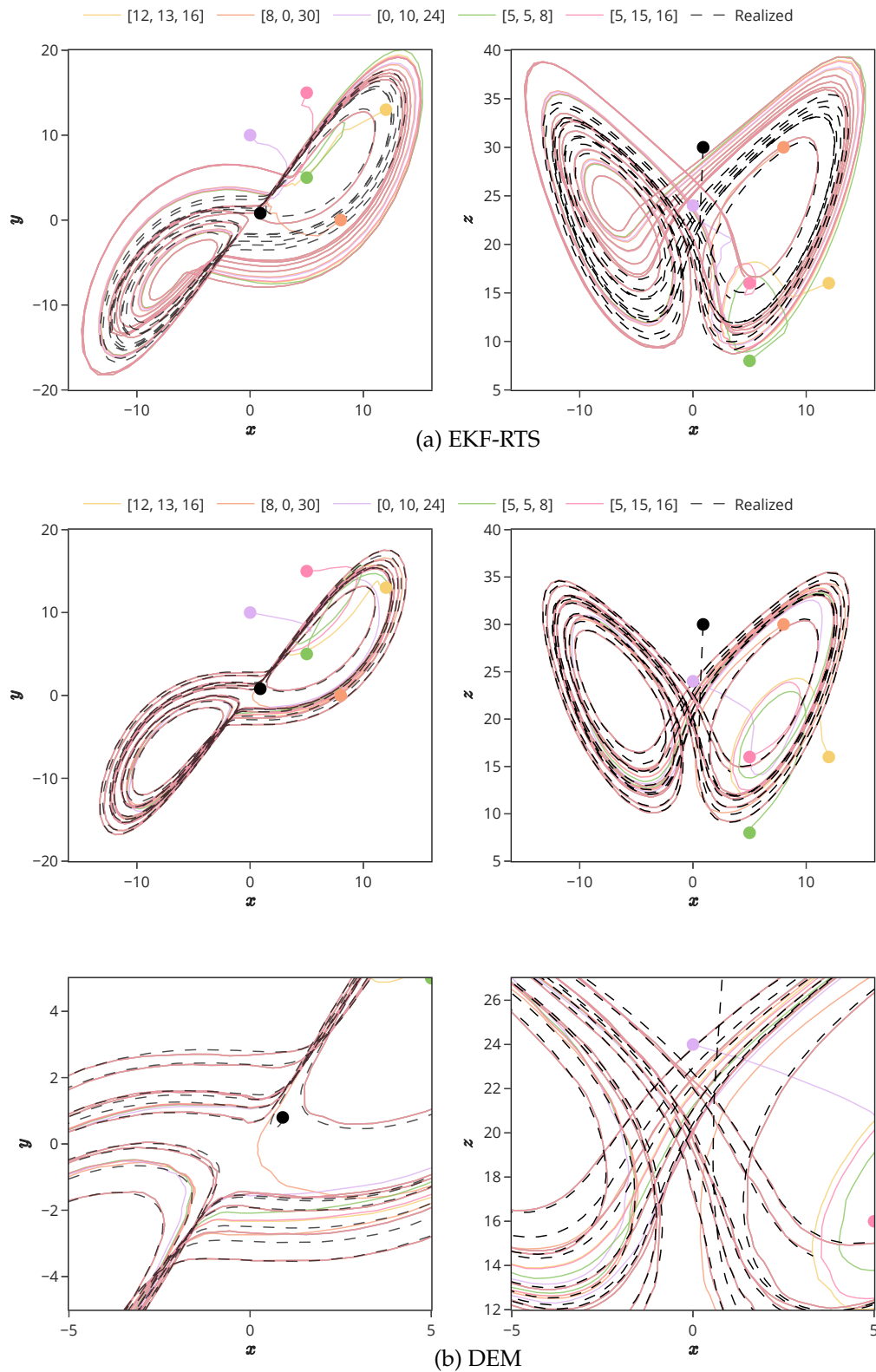


Figure 5.2: Realized phase-space trajectories for the Lorenz system and reconstructions by the EKF-RTS (a) and DEM algorithm (b). The first column shows projection on the (x, y) plane and the second column shows projection on the (x, z) plane. For the DEM, the second row shows zooms on the central part of the attractor.

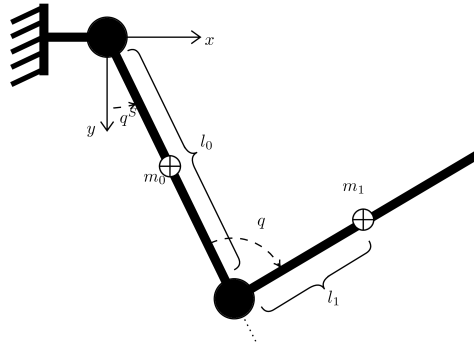


Figure 5.3: Schematic of 2-d arm model.

where q and v are the model states and q^S , F_b , and F_t are the model inputs. w_v and w_a are the dynamic noise, where w_v has a very small variance ($\sigma_v^2 \approx 0$) and w_a has a variance σ_a . Having noise in the equation of \dot{q} is surprising but reflects the fact that all variables are random variables in DEM. We discuss this issue in detail thereafter. Finally, we assume that we measure directly the joint angle with observation noise:

$$y = q + z_y \quad (5.23)$$

where z_y has variance σ_y^2 .

3.2 Face validity: generating and inverting some movement trajectories

To evaluate the face validity of our model, we generate some movement trajectories. We input a cosine torque in our arm model

$$\tau_{\text{muscles}}(t) = \alpha + \beta \cos(\gamma t)$$

where α , β , and γ are randomly drawn ($\alpha \sim \mathcal{N}(-1, 0.25)$, $\beta \sim \mathcal{N}(0.7, 1)$, $\alpha \sim \mathcal{N}(0.25, 0.01)$). We generate series of 1024 points with a integration step $\delta t = 0.01$. Some sample trajectories are shown in Figure 5.4.

We observe that the inversion scheme successfully recovers the input torque. However, we also see that the state representing the mean velocity does not always match the derivative of the mean position. This can be observed on second figure of the states trajectories, where the orange curve, representing the mean velocity, is sometimes negative while the position, on the blue curve, is increasing (see for instance at $t = 6s$). This is surprising because, mathematically, the expectation and derivation operator commutes, thus the mean velocity should be the time derivative of the mean position. Hence, the DEM algorithm can yield inconsistent trajectories. Indeed, we show in the next section that this problem is not specific to our model but might be expected for most systems governed by classical mechanics.

3.3 Second-order models from classical mechanics, generalized coordinates, and generalized fluctuations

Our simple dynamical model of the arm is based on rigid body dynamics which follows from classical mechanics. We explain here why a particular care is necessary when using systems driven by classical mechanics with generalized coordinates.

3.3.a Random fluctuations in rigid body systems

In classical mechanics, the total energy of closed systems is distributed between their position and momentum, and exchanges between these two quantities and with the environment are described by the equations of motion (Goldstein, 1980). Crucially, distinct closed systems interact through changes

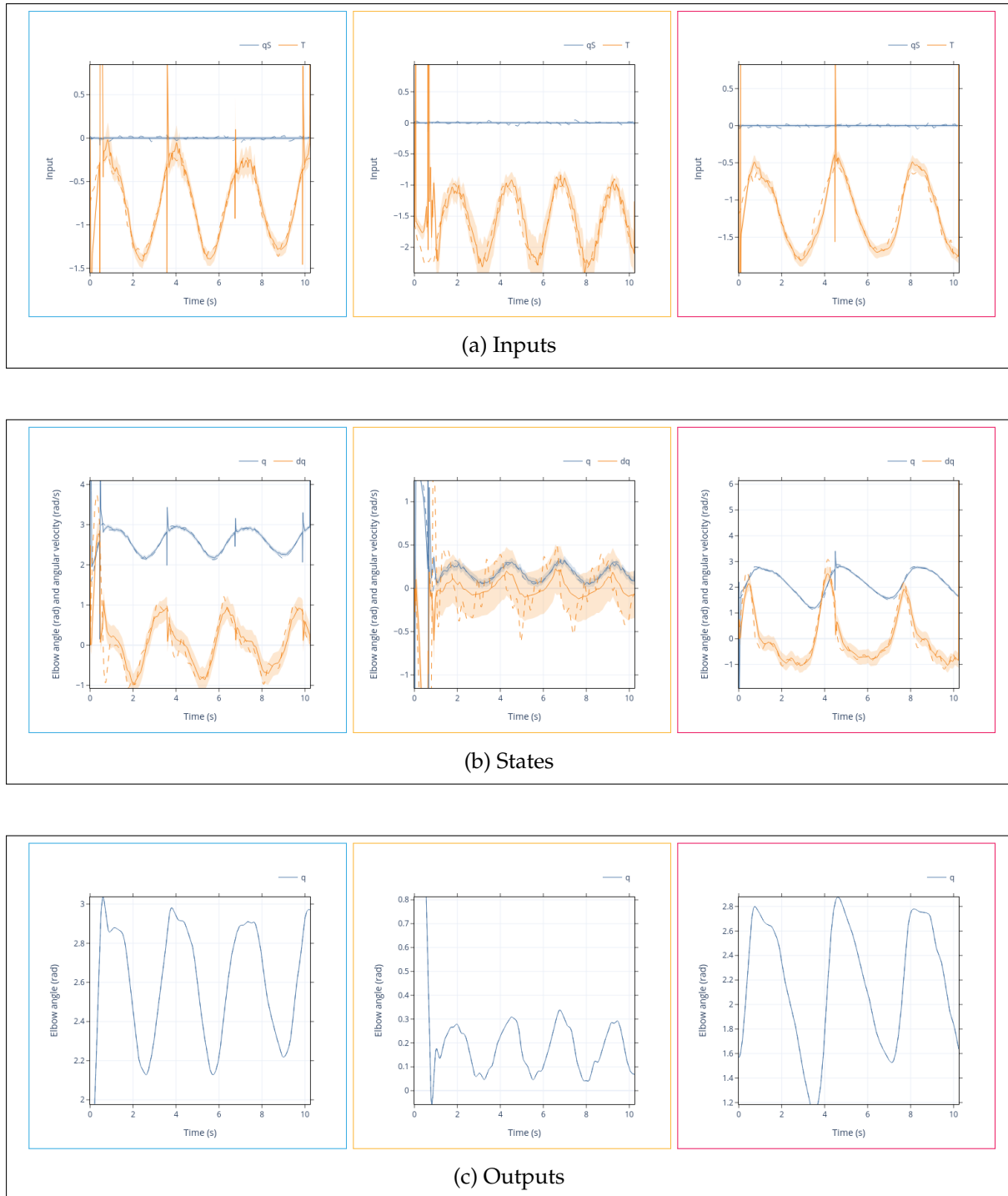


Figure 5.4: Sample generated and inverted trajectories of the arm model in response to a cosine torque. Generated input and state trajectories are in dashed strokes. The mean of the inverted trajectories are in plain strokes. Color bands indicate the posterior standard deviation. Rows corresponds to inputs (a), states (b), and outputs (c) trajectories. The inputs are the shoulder angle (q_S , radians) and the muscle torque (T , N.m). The states are the elbow angle (q , radians) and the elbow angular velocity (dq , rad/s). The output is the elbow angle. The samples are generated using $T = \alpha + \beta \cos(\gamma t)$ where (α, β, γ) is approximately $(-0.75, 0.56, 0.31)$ for the blue boxes, $(-1.61, -0.65, 0.40)$ for the yellow boxes, and $(-1.17, 0.57, 0.27)$ for the red boxes.

of momentum, i.e. forces. Consequently, the random fluctuations in the environment of mechanical systems act as random forces (Kerr & Graham, 2000). In other words, the environmental noise causes random accelerations (random fluctuation in momentum, assuming constant mass) (K. Friston, 2019; K. Friston & Ao, 2012). Therefore, introducing noise in a second-order system gives:

$$\ddot{q} = f(q, \dot{q}, u) + w_a \quad (5.24)$$

where u represents the system input (that enter through muscle forces) and w_a represents random fluctuation in acceleration⁷. For second-order systems, the initial value problem is solved by transforming systems in first-order systems with twice more state variables, thus, Eq. (5.24) is transformed in:

$$\begin{cases} \dot{v} = f(q, v, u) + w_a \\ \dot{q} = v + w_v \end{cases} \quad (5.25)$$

where the system states are its position q and velocity v . Crucially, the random fluctuations in velocity w_v have zero variance because random fluctuations enter the system as random accelerations exclusively. This is important because in the DEM algorithm all states are treated as random variables.

3.3.b Problem statement

Using the DEM algorithm with our arm model, or with any other system, requires that we embed the model in generalized coordinates. Using two generalized coordinates is sufficient to highlight our problem. With two generalized coordinates, the model from Eq. (5.25) is described by nine equations:

$$\begin{array}{lll} y = q + z_y & \dot{q} = v + w_v & \dot{v} = f(q, v, u) + w_a \\ y' = q' + z'_y & \dot{q}' = v' + w'_v & \dot{v}' = \partial_q f q' + \partial_v f v' + w'_a \\ y'' = q'' + z''_y & \dot{q}'' = v'' + w''_v & \dot{v}'' = \partial_q f q'' + \partial_v f v'' + w''_a \end{array}$$

These nine equations describe the conditional part of our generative model (the other part being the priors). The first column corresponds to the model output in generalized coordinates. The second and third column gives the evolution of the position and the velocity in our (generalized) model. The notation might appear surprising and reads as follows. Using q' as an example, \dot{q}' defines a stochastic differential equation which models the distribution of the first generalized derivative q' of the position q conditioned on the velocity v . The stochastic part of the equation is w'_v , which is the first derivative of the noise process w_v .

The VFE of the model is the expectation of the complete data likelihood under our approximate posterior density plus the entropy of our approximate posterior. Because we work under Gaussian assumption, the entropy depends on the covariance only. Similarly, the complete data likelihood can be divided in a part depending only on the covariances and another part depending on the means. We are interested in a problem which concerns the means so we group all other terms under a single constant. Let μ_q, μ'_q, μ''_q be the posterior means of the generalized position, μ_v, μ'_v, μ''_v the posterior means of the generalized velocity, and let $\bar{f}, \bar{f}', \bar{f}''$ be the generalized accelerations computed by our model at the current mean position and velocity (i.e. $\bar{f} \equiv f(\mu_q, \mu_v, 0)$). We can use these posterior means to evaluate

⁷Note that the environmental noise (with standard deviation σ) enters the equation weighted by the inertia of the system (i.e. the standard deviation of η_q is $\sigma/(mL^2)$)

the VFE:

$$\begin{aligned}
F(t) = & \frac{1}{2} \frac{(y - \mu_q)^2}{\sigma_z^2} + \frac{1}{2} \frac{(y' - \mu'_q)^2}{\alpha_1 \sigma_z^2} + \frac{1}{2} \frac{(y'' - \mu''_q)^2}{\alpha_2 \sigma_z^2} \\
& + \frac{1}{2} \frac{(\mu'_q - \mu_v)^2}{\sigma_v^2} + \frac{1}{2} \frac{(\mu''_q - \mu'_v)^2}{\beta_1 \sigma_v^2} \\
& + \frac{1}{2} \frac{(\mu'_v - \bar{f})^2}{\sigma_a^2} + \frac{1}{2} \frac{(\mu''_v - \bar{f}')^2}{\gamma_1 \sigma_a^2} \\
& + \text{const}
\end{aligned} \tag{5.26}$$

where the important terms for our problem are on the second line of the VFE (Eq. (5.26)). The evolution of the states in the DEM scheme follow a gradient descent on the VFE, which means that the differential equations that are effectively integrated during the D-step are of the form

$$\frac{d}{dt} \mu_x = \mu'_x - \partial_{\mu_x} F \tag{5.27}$$

Taking the mean velocity μ_v as an example, its evolution through the inversion scheme is governed by the differential equation:

$$\frac{d}{dt} \mu_v = \mu'_v - \partial_{\mu_v} F = \mu'_v + \frac{\partial f}{\partial v} \frac{\mu'_v - \bar{f}}{\sigma_a^2} + \frac{\mu'_q - \mu_v}{\sigma_v^2} \tag{5.28}$$

Here, we see that the consistency of having the mean velocity μ_v being the first derivative of the mean position μ'_q appears as a ‘‘target’’ that is tracked with a time constant σ_v^2 . This is not a problem if we can guarantee that μ_v converges quickly to μ'_q . Therefore, if we want the solution to remain consistent over time, we need to have $\sigma_v^2 \ll \sigma_a^2$. Similarly, for the equation of μ'_q :

$$\frac{d}{dt} \mu'_q = \mu''_q - \partial_{\mu'_q} F = \mu''_q + \frac{y' - \mu'_q}{\alpha_1 \sigma_y^2} + \frac{\partial f}{\partial q} \frac{\mu''_v - \bar{f}'}{\gamma_1 \sigma_a^2} - \frac{\mu'_q - \mu_v}{\sigma_v^2} \tag{5.29}$$

There, we have to guarantee that $\sigma_v^2 \ll \gamma_1 \sigma_a^2$ and $\sigma_v^2 \ll \alpha_1 \sigma_y$. There are technical reasons that make this solution undesirable. When working with systems under classical mechanics, we have generally a good confidence in the state equations and would assume that a great part of the observed unexplained variability comes from the inputs (for instance, the muscle forces in our model). Thus, we will generally have σ_a^2 greatly smaller than the input variance. This results in another inequality to satisfy and implies that σ_v^2 would need to be extremely small. This leads to a numerically unstable problem because σ_v^2 appears both as a denominator and in logarithms in the VFE. Even in the case where σ_a^2 is not small, we still need to make sure that σ_v^2 is small with respect to all other variances of the model to ensure that μ_v converges quickly to μ'_q . It is important to remember that some variances may need to be estimated during the M-step. Therefore, guaranteeing at all time the internal consistency of the solutions is far from being trivial.

Now, let's highlight a second problem that appear with second-order systems. Let assume that the current posterior means are consistent, i.e. $\mu_v = \mu'_q, \mu'_v = \mu''_q$. Plugin in Eq. (5.28) yields:

$$\frac{d}{dt} \mu_v = \mu'_v + \frac{\partial f}{\partial v} \frac{\mu'_v - \bar{f}}{\sigma_a^2} \tag{5.30}$$

Similarly, replacing in Eq. (5.29) gives:

$$\frac{d}{dt} \mu'_q = \mu'_v + \frac{y' - \mu_v}{\alpha_1 \sigma_y^2} + \frac{\partial f}{\partial q} \frac{\mu''_v - \bar{f}'}{\gamma_1 \sigma_a^2} \tag{5.31}$$

Subtracting the two equations gives:

$$\frac{d}{dt} (\mu'_q - \mu_v) = \frac{y' - \mu_v}{\alpha_1 \sigma_y^2} + \frac{\partial f}{\partial q} \frac{\mu''_v - \bar{f}'}{\gamma_1 \sigma_a^2} - \frac{\partial f}{\partial v} \frac{\mu'_v - \bar{f}}{\sigma_a^2} \tag{5.32}$$

$$= \frac{y' - \mu_v}{\alpha_1 \sigma_y^2} + \frac{\partial f}{\partial q} \frac{\partial F}{\partial f'} - \frac{\partial f}{\partial v} \frac{\partial F}{\partial f} \tag{5.33}$$

We see that the derivative is not necessarily zero, thus having a consistent estimate is not sufficient for the estimates to remain consistent. Importantly, we observe that first term is due to the fact that the mean velocity μ_v is not involved in predicting the first derivative of the observation y' , whereas the first derivative of the mean position μ'_q is. In the following, we use this observation to present a simple workaround that partly address the consistency problem.

3.3.c Workaround and perspectives

To summarize, the DEM scheme as introduced in (K. J. Friston et al., 2008) does not provide consistent solutions for dynamical systems of the second (and higher) order. This phenomena is especially problematic in the case of systems derived from classical mechanics for which the random fluctuations create random accelerations only. The inconsistency of the solutions partly due to the fact that intermediate states are considered as random variables. The intuitive solution of setting their variance to a very small value is not sufficient to guarantee the consistency of the scheme. Finding a systematic way to guarantee the consistency of the solutions for second order dynamical systems could be an interesting update to the DEM algorithm⁸. We believe that this may be done analytically by using the two first generalized coordinates (μ_q and μ'_q) to predict the acceleration.

We propose a simple workaround for this problem. The idea is to artificially augment the observation y with a fake observation of its velocity y' with a variance $\alpha_1\sigma_y^2$. This solution makes the term $(y' - \mu_v)/(\alpha_1\sigma_y^2)$ cancel in Eq. (5.33), so the derivative of the internal consistency error is simply

$$\frac{d}{dt}(\mu'_q - \mu_v) = \frac{\partial f}{\partial q} \frac{\partial F}{\partial f'} - \frac{\partial f}{\partial v} \frac{\partial F}{\partial f}$$

which we assume to be small⁹. This solution does not require any modification to the DEM algorithm.

To validate experimentally our proposed solution, we generate samples trajectories using a cosine input torque and estimate the mean state trajectories, with and without the virtual velocity observation. The velocity is computed using finite differences on the position trajectories. The output variance of the velocity is set to the variance of the position scaled by a factor $1/(2s^2)$, where s is the smoothness of the output noise process (here, $1/8$). This follows from the variance of the velocity of a process with Gaussian autocorrelation (see (K. J. Friston et al., 2008), Eq. 53). 8 samples of 1024 points are generated for 8 cosine frequencies between 0.5Hz and 2Hz. For each sample, we compute the mean squared error between the first generalized coordinate of the mean position μ'_q and the mean velocity μ_v . Results are presented in Figure 5.5. We see that the adding a velocity observation scales down the mean squared internal consistency error by a factor 10^{-5} . In addition, it appear that the correction decreases the effect of the frequency of the input cosine on the consistency error.

We emphasize that the proposed workaround does not completely solve the consistency problem. Our concern is that the filtering equations of the D-step that appear in DEM are indeed found in both generalized filtering (K. Friston et al., 2010) and active inference (Parr et al., 2022). Finding an analytical solution to this problem is beyond the scope of this research work but is an important question that remains to be solved.

⁸Indeed, the equations of the D-step are also governing the filtering schemes in generalized filtering (K. Friston et al., 2010) and active inference (Parr et al., 2022), thus this problem also appears in these frameworks.

⁹Reducing the term $\frac{\partial f}{\partial q} \frac{\partial F}{\partial f'} - \frac{\partial f}{\partial v} \frac{\partial F}{\partial f}$ is not trivial, although its symmetry reminds us of Lie brackets. It seems to quantify the degree of noncommutativity of the position and velocity in computing the VFE flow with respect to the velocity. Tools from differential topology might be helpful in analyzing this term.

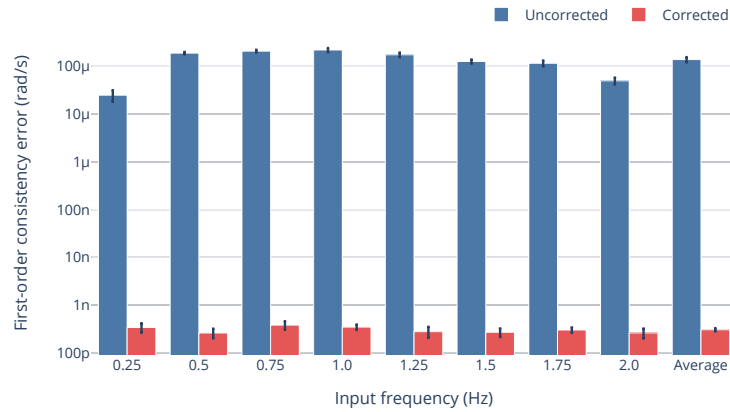


Figure 5.5: Mean squared error between the first derivative of the position in generalized coordinates and the mean velocity. “Uncorrected” bars corresponds to using the DEM algorithm with observed position only. “Corrected” bars corresponds to solution with observed position and velocity.

4 On modelling musculo-spinal loops

4.1 Modelling the muscles

We use Hill’s muscle model (Hill, 1938) to model both biceps and triceps. The formulation used here derives from (Desplenter & Trejos, 2018). Hill’s muscle model is composed of a contractile element and a elastic elements. The force is given by:

$$F_{RTE} = (F_{MCE} + F_{MEE}) \cos\left(\frac{l_0 \sin(\phi_0)}{l}\right) \quad (5.34)$$

where the force of the muscle contractile element F_{MCE} depends on muscle activation, length, and velocity:

$$F_{MCE} = aF_{\max}f_l(l)f_v(v) \quad (5.35)$$

The functions f_l and f_v correspond to force-length and force-velocity relationships:

$$f_l(l) = \exp\left(-\frac{(l-l_0)^2}{(Wl_0)^2}\right) \quad f_v(v) = \begin{cases} \frac{v_{\max} + v}{v_{\max} - \frac{v}{A}} & \text{if } v < 0 \\ \frac{g_{\max}v + c_d}{v + c_d} & \text{otherwise.} \end{cases} \quad c_d = \frac{v_{\max}A(g_{\max} - 1)}{A + 1} \quad (5.36)$$

where l_0 is the optimal muscle length, W is a shape parameter, v_{\max} is the maximal velocity, A and c_d are shape parameters, and g_{\max} is the maximal eccentric concentric force. The force of the muscle elastic element F_{MEE} is given by:

$$F_{MEE} = \begin{cases} k_1(l - l_{\text{slack}}) & \text{if } l < l_{\text{slack}} \\ k_1(l - l_{\text{slack}}) + k_2(l - l_{\text{slack}})^2 & \text{otherwise.} \end{cases} \quad (5.37)$$

where l_{slack} is the slack length of the muscle, and k_1 and k_2 configure the slack elastic response. Note that the model *per se* is not dynamic: we can directly compute the force from the length and linear velocity of the muscle and the motoneuron activity. However, the rising time of the motoneurons activity is usually modeled with a linear differential equation with time constant τ_{act} .

4.2 Modelling the spinal control loops

4.2.a Type Ia and Ib afferents model

Muscle afferents provide sensory feedback on the muscle configuration (Bear et al., 2020). We use the model of afferents given by (Teka et al., 2017) and adapted from (Prochazka, 1999). The firing rate of afferents sensory fibers is modeled by two linear models. Type Ia afferents capture the strain of the muscle spindles located inside the muscle and provide feedback on several muscular states, in particular the muscle length (Bear et al., 2020, Ch. 13). The dynamics of muscle spindles is neglected here. The firing rate of type I_a afferents depends on muscle length and velocity and on motoneurons activity (Teka et al., 2017):

$$I_a = k_v \frac{v}{v_{\max}} + k_l \frac{l - 0.2l_0}{l_0} + k_a a + \text{const} \quad (5.38)$$

Type I_b afferents capture the strain in the Golgi tendon organs located at the muscle extremities and provide feedback on the muscle force (Bear et al., 2020, Ch. 13). Their firing rate is proportional to the muscle force (Prochazka, 1999), and modeled by the linear relationship (Teka et al., 2017):

$$I_b = k_F \frac{F - 0.1F_{\max}}{F_{\max}} \quad (5.39)$$

4.2.b A model of the spinal cord

Using a model of the spinal cord is crucial for a neuromusculoskeletal model because it incorporates several important neuronal connections that are necessary to generate natural movements (Li et al., 2015). For instance, the activity of type Ib afferents (related to force) inhibits the alpha motoneurons that causes muscle contraction (Bear et al., 2020, Ch. 13, Fig. 13.24). This feedback loop naturally constrains the muscle force. Another example is the gamma loop which enables length-control. The activation of alpha motoneurons causes contraction of muscle fibers which reduces the length of the muscle spindle and therefore deactivate the type Ia afferents. This causes the activation of gamma motoneurons because type Ia afferents have inhibitory connection to gamma motoneurons in the spinal cord (Bear et al., 2020, Ch. 13, Fig. 13.23). The spinal cord is also responsible for the *reciprocal inhibition* of antagonist muscles: contraction of a muscle (e.g. the *biceps brachii*) causes the relaxation of the antagonist muscle (e.g. the *triceps brachii*). This is due to the presence of an inhibitory interneuron between type Ia afferents and alpha motoneurons of the antagonist muscle (Bear et al., 2020, Ch. 13, Fig. 13.25).

We use here a model based on the model of the spinal cord proposed in (Hao et al., 2013; Li et al., 2015) and depicted in Figure 5.6. The model is appealing because most of the spinal circuitry is described with simple relationships between normalized neuronal activations. The model inputs are normalized neuronal activities descending from the motor cortex and divided in six variables: $\alpha_d, \alpha_{st}, \alpha_{sb}, \gamma_d, \gamma_{st}, \gamma_{sb}$. The α and γ variables respectively target *alpha* and *gamma* motoneurons. The activities are assumed to configure either the *static* configuration (subscript *s*) or the *dynamic* state (subscript *d*). The static activities target either the *biceps brachii* muscle (subscript *b*) or the *triceps brachii* muscle (subscript *t*). In contrast to static variables, dynamic variables are described only with two variables because of the equality constraints $\alpha_d = \alpha_{db} = \alpha_{dt}$ and $\gamma_d = \gamma_{dt} = 1 - \gamma_{db}$. Our model is slightly different from (Li et al., 2015). First, we remove the dynamics of the pool of α motoneuron because it already features in our muscle model. Second, we did remove the noise input to the pool of α motoneuron because we are working directly with distribution. The resulting model gives the normalized activities of the triceps and biceps motoneuron pools (resp. Y_{MNt} and Y_{MNb}). It uses directly the afferents activity

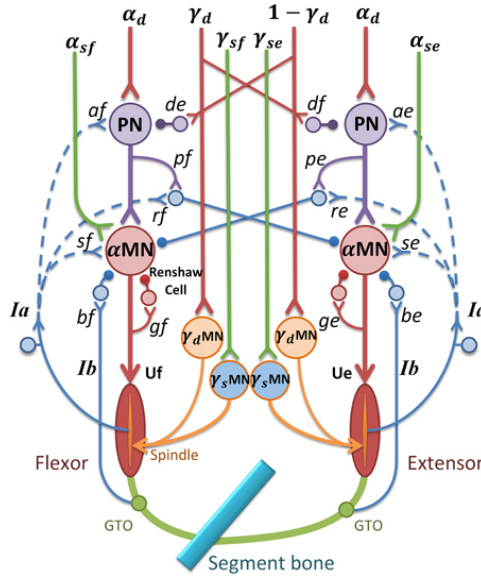


Figure 5.6: A model of the spinal cord. Reproduced with permission from (Li et al., 2015).

I_a^{tr} , I_b^{tr} (from triceps) and I_a^{bi} , I_b^{bi} (from biceps).

$$\text{propriospinal neurons activity} \begin{cases} Y_{PNt} &= \alpha_d - d_t \gamma_d + a_t I_a^{\text{tr}} \\ Y_{PNb} &= \alpha_d - d_b (1 - \gamma_d) + a_b I_b^{\text{bi}} \end{cases} \quad (5.40)$$

$$\begin{cases} m_t &= \frac{\alpha_{st} + Y_{PNt}}{1 + g_t (\alpha_{st} + Y_{PNt})} \\ m_b &= \frac{\alpha_{sb} + Y_{PNb}}{1 + g_b (\alpha_{sb} + Y_{PNb})} \end{cases} \quad (5.41)$$

$$\alpha \text{ motoneurons activity} \begin{cases} Y_{\alpha MNt} &= (1 + s_t I_a^{\text{tr}} - r_t I_b^{\text{bi}} - b_t I_b^{\text{tr}}) m_t \\ Y_{\alpha MNb} &= (1 + s_b I_a^{\text{bi}} - r_b I_a^{\text{tr}} - b_b I_b^{\text{bi}}) m_b \end{cases} \quad (5.42)$$

The terms d_t and d_b configure the gain of the dynamic γ_d input to the propriospinal neural pools.

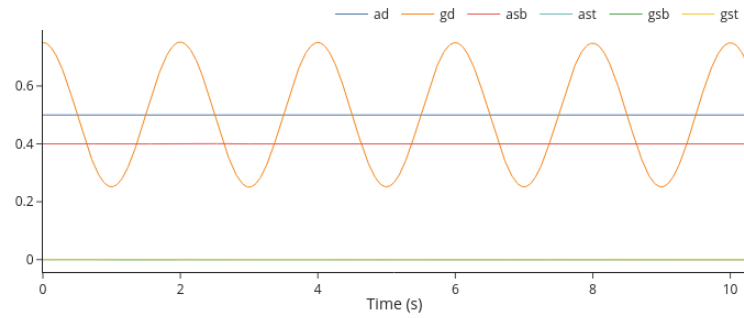
4.3 Face validity

We generate some data with the model of the spinal cord, two Hill's muscles, and the arm dynamics. The four models are integrated in a single level of the hierarchical model, as discussed more in depth thereafter. At the second level, we used the pendulum equations to simulate a value of γ_d oscillating around 0.5. Thus, omitting noise terms, γ_d follows the equation:

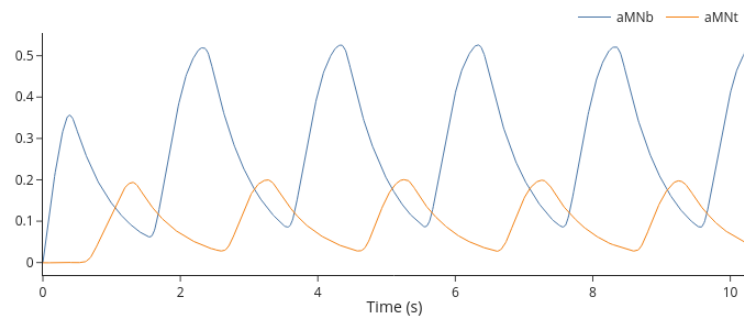
$$\gamma_d(t) = 0.5 + u \cos(2\pi ft)$$

where the parameters $u = 0.3$ and $f = 0.5$ were introduced to model the amplitude and frequency of the oscillations. Other model parameters are presented in Appendix 2. We also use parameters to set the static values of γ_{sb} , γ_{st} , α_{sb} , α_{st} . These parameters were tuned manually. Alternatively, one could configure the static "resting pose" for the arm and use DEM to invert the model and estimate the necessary values of the static parameters.

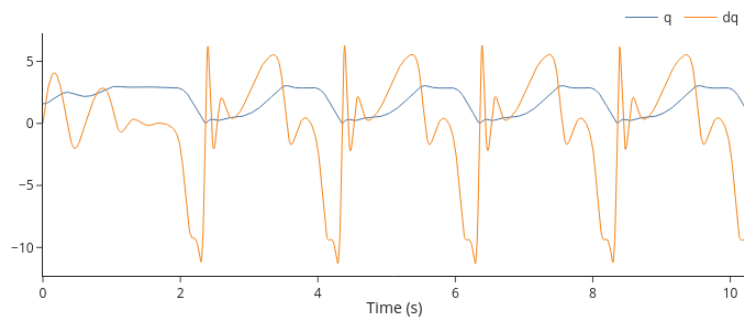
We generate a trial of 1024 points (10.24s). Results are presented in Figure 5.7. We observe that varying the value of γ_d is sufficient to generate movement. In particular, we see that the normalized activations of the biceps α motoneurons and triceps α motoneurons are conversely modulated. This is the expected behavior: the spinal circuitry handles the reciprocal inhibition of antagonist muscles.



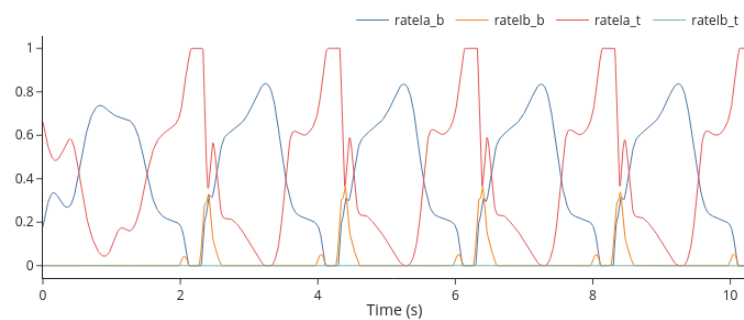
(a) Spinal cord inputs



(b) Motoneurons



(c) Elbow



(d) Afferents

Figure 5.7: Sample trajectories for the spino-musculo-skeletal model. The first row represent the variables of the spinal model, where $a \equiv \alpha$ and $g \equiv \gamma$. On the second row are the a_{MN} activities. The third row contains the model output, i.e. the angle and angular velocity of the elbow joint. On fourth row are the afferents variables.

4.4 Closing the loop: the problem with hierarchical models

When introducing the functions of the spinal cord, we indicated that several control loops underpinning reflex arcs were implemented by the spinal circuitry. In particular, we mentioned that muscle afferents were particularly useful in enabling closed-loop control of some muscular variables such as force or length. In this section, we emphasize problems due to closed loops.

DEM is essentially built on hierarchical models. The directed acyclic nature of hierarchical models make the predictions flow from higher-hierarchical levels to lower-hierarchical levels. In other words, propagating through the hierarchy is sufficient to evaluate or to invert the model. The hierarchical structure is convenient to work with because it breaks down a complex generative model into a chain of simpler ones. In addition, it allows to investigate the properties of each subsystem independently from the others. In other words, we can estimate the first level variables from the data, and then use the posterior of the first level to estimate the second level, and repeat this process throughout the hierarchy (K. J. Friston et al., 2016). Thus, we can estimate each model individually and do not need to re-estimate the lower level models. In particular, we can investigate hypothesis about higher-level models (e.g. the functional form of the cortico-spinal connections) without having to re-estimate the lower-level model parameters (e.g. the weight or length of the forearm)¹⁰. In other words, hierarchical structure is important from a computational and practical perspective because it allows to decompose the problem of inverting complex models constructed under different hypotheses.

The limitation is that closed-loop mechanisms, which pervades biological systems, do not fit to the directed structure of hierarchical models. For instance, we used a single “spino-musculo-skeletal” model because the musculospinal loop links the spinal and muscle models and the muscles length and velocity depend on the elbow angle and velocity. In addition, if we were to model sensorimotor cortical loops, then we would need to formulate a single “cortico-spino-musculo-skeletal” model. In summary, although hierarchical models allow to break down complex systems in simpler components, we need to use them on systems which do not comply to their structure. This stands as an inherent limitation of using hierarchical models for complex systems.

5 On modelling cortical columns

5.1 Time-resolved inversion of neural mass models

Neural mass models can be used to model the electric potentials measured in electrophysiology (Jansen & Rit, 1995). Neural masses have been used to model EEG signals during epilepsy (Grimbert & Faugeras, 2006) but also evoked electrophysiological responses to stimuli (David & Friston, 2003). In the later case, the response is mostly governed by a large change in the deterministic input. In the general case, the input of the neural mass model is noise that represents unmodeled background activity from other cortical areas. In that case, the evolution of neural mass models is essentially driven by noise. When noise drive the system, we cannot directly use the equations of a neural model model as equations of a dynamic model in DEM. Indeed, trying to do so would imply to estimate the timecourse of the input noise, which is unreasonable. Therefore, the problem of inverting the electrophysiological response must be formulated differently.

We describe a simple approach to the problem based on (Jafarian et al., 2021; R. Moran, 2015; R. J. Moran et al., 2007). The core idea is to decouple the dynamics of fast neuronal variables from the dynamics of the slow physiological parameters. It is assumed that the slow parameters govern the fixed points of the fast variables. Following from the center manifold theorem, the dynamics of the fast variables is linearized at the fixed points. Because the fast variables are linearized, we can compute their response function in the operational domain and thus compute the spectral representation of the output

¹⁰This is due to recent advances on parametric empirical Bayes: when generative models differ only by their priors, we only need to invert the model once, and we can then reuse the model to compute the VFE under a different set of priors (see (K. J. Friston et al., 2016), Eq. 10).

from the spectrum of the input. Hence, we can compute a complex multivariate normal distribution in the spectral domain which is parameterized by the slow variables. The complex multivariate normal distribution is taken as the conditional distribution of a windowed Fourier transform of the EEG signal, and used to compute a VFE. (Jafarian et al., 2021) proposes to test hypotheses about the evolution of parameters through time using parametric empirical Bayes. A model of spectral responses is inverted for each time window, which yields a series of posterior distribution of parameters. Modeling of the between-window evolution of slow variables is performed from the series of posterior distributions.

In modeling arm movements, we have to deal with a dynamical model of the arm and muscles. Therefore, although it is acceptable to assume that the neuronal responses are fast compared to the dynamic of the (spino-)musculoskeletal model, we cannot divide the measurement time series in independent windows. A possible approach is to specify a model of the slow variables dynamics in DEM. The observation function of the system is the response function of the fast variables. We describe our model more in details in the next section.

5.2 Neural mass model of spectral responses

We used here the neural mass model of spectral responses presented in (R. J. Moran et al., 2007) and adapted for DEM. The model is obtained by linearizing a model of cortical columns found in (David et al., 2006). The model is essentially similar to the classical Jansen-Rit model (Jansen & Rit, 1995) but features additional populations that enable richer spectral output (in particular high-frequency activity, see (David et al., 2006) for details). The fast variables (x) are governed by a set of linear equations which depend on the slow variables (r):

$$\begin{cases} \dot{x} &= A(r)x + B(r)u \\ y &= C(r)x \end{cases} \quad (5.43)$$

where the matrices A , B , and C are given in 3.1. Transforming the system to the operational domain using Laplace transform results in the following pair of equations

$$\begin{cases} sX &= A(r)X + B(r)U \\ Y &= C(r)X \end{cases} \quad (5.44)$$

where $s = j2\pi f$. The response function $H(r, s)$ is given by

$$H(r, s) = \frac{Y}{U} = C(r)(s\mathbb{I} - A(r))^{-1}B(r) \quad (5.45)$$

In practice, we select a set of specific frequencies (f_0, f_1, \dots) at which we want to evaluate the model (here, 25 frequencies linearly spaced between 1 and 50Hz). We use the relationship $s = j2\pi f$ to compute the response at each frequency in function of input of each frequency (i.e. $Y(j2\pi f) = H(r, j2\pi f)U(j2\pi f)$). Thus, our observation model is $h(r, u) \equiv (H(r, j2\pi f_0)U(j2\pi f_0), H(r, j2\pi f_1)U(j2\pi f_1), \dots)$. Finally, the total response model is

$$\begin{cases} \dot{r} &= f(r, u) \\ Y &= h(r, u) \end{cases} \quad (5.46)$$

The vector of slow variables contains the classical parameters of the neural mass models, such as the time constants of the excitatory and inhibitory population (τ_e and τ_i), their gain He and Hi , the between population couplings C_i . To show the influence of each parameter on the response spectra, the transfer function plots from (R. J. Moran et al., 2007, Fig. 7) were reproduced with our implementation and are presented in 3.2. In addition, we construct a simple example to show how this model can be used with DEM. We let the dynamics of the slow variables be a simple exponential decay from twice their default value to half their default value. We generate an input spectra with three frequency bands (resp.

10Hz, 36Hz, 70Hz) and modulated the amplitudes of each band with a sinus with different frequencies (resp. 0.1Hz, 0.2Hz, 0.3Hz). Complex spectra is obtained by multiplying the spectral amplitude with a random phase (Schreiber & Schmitz, 1996). Hence, the model input was a complex time-frequency spectra with 128 time points and 10 frequency points, as shown in Figure 5.8. As expected, we observe that the spectral response change with time and tends to attenuate high frequency inputs. Therefore, using the slow-fast decomposition approach should enable evaluating hypotheses on the continuous changes in the parameters of neural mass models.

6 Conclusion and future work

In this chapter, we attempted to use a neuromusculoskeletal model with an advanced DEM scheme. This challenging task allowed us to highlight some limitations of the DEM algorithm. While some limitations are due to the numerical solvability of the problem, others are inherent to the problem of modeling complex, multiscale systems.

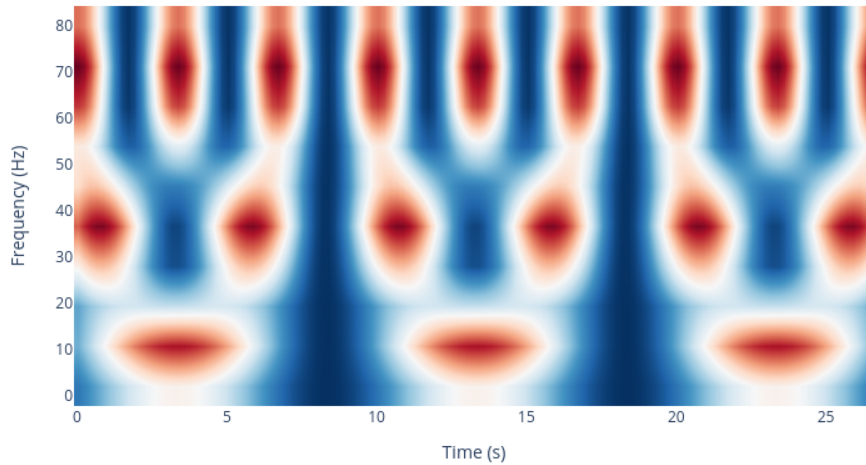
In a first part of the chapter, we introduced the DEM algorithm as an extension of the Kalman filter. We gave an overview of the algorithm, its pseudo-code, and a Python implementation. In addition, we provided mathematical evidence supporting some claims made by the authors of the algorithm. The authors claimed that filtering chaotic system in DEM was possible because of the introduction of generalized coordinates, that represent a trajectory using its value and its derivatives up to a defined order. We show that the generalized coordinates formed indeed an embedding for the observed trajectory from a strange attractor, as shown by a theorem by Takens (Takens, 1981). This motivate to use DEM with nonlinear or chaotic systems.

In a second part of the chapter, we introduced subsets of our neuromusculoskeletal model and use them to highlight and discuss issues of the DEM algorithm. We first introduced an arm model with two degrees of freedom based on rigid body dynamics. In these models, the random fluctuations act only as random forces and do not impact directly the velocity. Unfortunately, this is not feasible in DEM which represents all variables as random quantities. We showed that setting the variance of random fluctuations in velocity to a low value was not sufficient to guarantee the consistency of the solutions. A workaround for this issue is to augment the observations with an observation of the velocity.

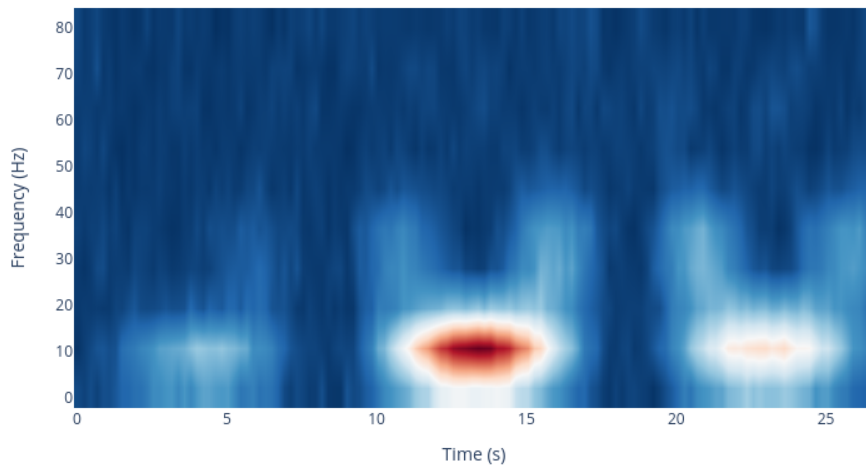
We then introduced a model of arm muscles and of the spinal cord. Control loops in the spinal cord are responsible for important features of naturalistic movement. However, modeling these control loops cannot be done using the hierarchical structure used in DEM. This is an inevitable issue because the process that is modeled is not hierarchical. We think that nonhierarchical systems pervades biological processes and that although quite convenient, the framework of hierarchical dynamical systems will rarely be usable.

Third, we discussed the problem of modeling systems with different temporal scales. In the case of modeling the brain activity during arm movement, we have dynamics at different scales: the cortical activity evolve quickly with respect to arm movement. We presented an interesting approach based on decoupling the slow and fast variables. More specifically, the dynamics of the fast variables is linearized around fixed points determined by slow variables. This allow to compute the (linear) response function of the fast system and to perform filtering in the spectral domain.

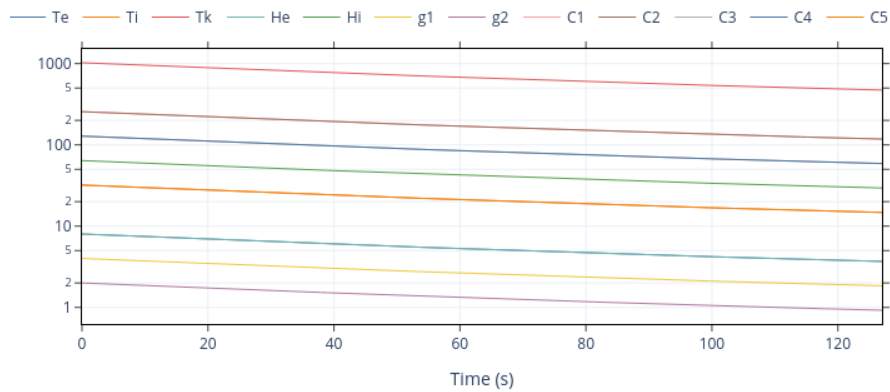
Although we identified some challenges in using complex model with the DEM algorithm, we do not report any major limitations. In other words, a workaround or solution can be found for all the issues that we encountered. Future work may leverage these results and focus on modeling of neuro-spinal connections, identifying adequate priors, and inverting the complete model of elbow movements from real data.



(a) Input spectra



(b) Output spectra



(c) Slow variables

Figure 5.8: Continuous changes in slow variables inducing changes in the spectral response of a neural mass model. Parameters (c) follow an exponential decay. Parameters variation changes the spectral response of the neural mass model (b), which attributes different weights to different input frequencies.

Chapter 6

Discussion and conclusion

In this concluding chapter, we discuss more in depth some of the themes developed in this thesis.

1 Towards naturalistic experiments

When introducing the experimental setup used to collect arm motion data from our participants, we mentioned that our setup aimed at reproducing “naturalistic” movement conditions. These movement conditions were initially motivated by a specifically challenging application. We wanted to build a BCI for whole-body human tracking that can later be used for BCI humanoid robot control. This application inherently features a substantial environmental noise as compared to well-controlled neuroscience experiments. Thus, reproducing movement conditions essentially aimed at building a reconstruction model that remains useful outside of the laboratory setup. Succeeding in constructing such a model would have implied finding robust features that distinguish clearly despite environmental perturbation. This constitutes indeed a complex neuroimaging task!

During the two last decades, there has been an increasing research interest in studying the brain in its natural environment (Maguire, 2012). Indeed, neuroscience has for long focused on studying responses elicited by controlled stimuli. This has been criticized because the truth is that our environment features rich and complex stimuli (Nastase et al., 2020). Therefore, an increasing amount of works are investigating the brain responses in ecologically plausible environments. For instance, neuroscientists studied the brain during driving (Spiers & Maguire, 2006), free recall (Polyn et al., 2005), movie watching (Hasson et al., 2004; Nishimoto et al., 2011) — which is incidentally at the seed of an exciting emerging field, neurocinematics (Hasson et al., 2008).

Methods to investigate hypotheses from neuroimaging data of brain responses have been thoroughly studied in the case of simple stimuli. However, methods for studying the brain responses in ecologically-plausible situations are still in their infancy. This is due to mainly three reasons. First, natural stimuli are multimodal; thus, they are complicated to model and elicit multimodal responses. Second, subjects are actors in natural situations, meaning that they do not only respond to stimuli but also behave (Krakauer et al., 2017). Third, naturalistic stimuli evolve in time; hence, we must consider entangled responses to different stimuli. Therefore, studying the brain in natural situations is a quite challenging.

A systematic, statistically-valid approach is still to be identified to evaluate hypotheses during naturalistic experiments. In particular, the nature of measured signals may sometimes preclude classical analysis and lead to misinterpretations of the results. For instance, some works used correlation coefficients to assess the possibility of reconstructing movement from EEG signals, e.g., citebradberry2010reconstructing,ofner2012decoding. This approach is appealing because theoretically simple. However, we showed in Chapter 4 that the distribution of the correlation coefficient degenerates for autocorrelated time series. Importantly, we also showed that the correlation coefficient must be interpreted conditionally to the smoothness of the series. The corollary is that reporting a correlation

coefficient alone might lead to a wrong interpretation on its significance. In addition, further researches are required to evaluate whether averaging correlation coefficients from series with different smoothness is well defined. To sum-up, despite their ease of use, evaluating hypotheses with simple statistical tools requires a particular care with the kind of series found in naturalistic experiments. Therefore, using more advanced and more robust statistical methods might be a good alternative to ensure the statistical validity of the results.

From first principles, a systematic way of evaluating hypotheses is to model the subject responses under the different hypotheses. The Neyman-Pearson lemma ensures us that the strongest statistical test is always to compare models on their ability to predict our observations (Neyman & Pearson, 1933). Therefore, we can claim that investigating hypotheses about physiological responses to natural stimuli requires to build generative models of the responses under the different hypotheses.

In Chapter 5, we have tried to model subject responses in a non-constrained movement task. Our results suggest promising perspective to modeling multimodal responses in non-conditioned settings. However, although our movement task is simple, as compared to everyday tasks, we yet faced important problems in modeling it. In particular, we showed that even using an advanced Bayesian method, there remain challenges in inverting complicated models. While some of these problem concern technical issues and might be solved rapidly, for instance inverting models from classical mechanics, other are more fundamental and require to cope with the nature of the modeled phenomena, for instance circular causality and multiscale properties (Breakspear, 2017; D'Angelo & Jirsa, 2022; Haken, 2006).

2 Modeling multiscale systems

The multiscale properties are pervasive in complex systems such as biological systems (Lesne, 2013), and the brain is no exception (D'Angelo & Jirsa, 2022). These multiscale properties are characterized by a complex evolution at mixed scales of both temporal and spatial dimensions. Importantly, the mean field argument, which arises from statistical physics and allows to “zoom-out” by averaging interactions, might fail to capture the circular dependence between different scales (Lesne, 2013). Even under mean field assumptions, modeling multiscale problems remains complicated.

Approaches based on phase transitions proved to be a useful tool in modeling the temporal multiscale nature of the brain (Haken, 2006). As we mentioned during the introduction, (Haken et al., 1985) proposed to model hand synchronization as stable modes of a fast dynamics controlled by slow parameters. More recently, Jirsa and colleagues (Jirsa et al., 2014) introduced the Epileptor, a multiscale model of seizure dynamics based on the concept of phase transitions governed by slow dynamical variables. These methods provide an interesting approach to multiscale modeling. However, because natural stimuli elicit multimodal responses, it is plausible that part of the physiological response is driven by unmodeled exogenous variables, i.e., noise.

In Chapter 5, we saw that when timescale decoupling can be assumed, approaches based on the center manifold theorem could prove to be useful to model multiscale electrophysiological responses, even when the response is partially driven by noise. In particular, we saw that the response of the fast variables could be used as the observation function for a state-space model of the dynamics of slow variables. We showed that this enables to model continuous changes in slow variables while keeping the rich spectral content due to the fast dynamics.

A perspective for the slow-fast decoupling approach is to replace or extend the spectral output with statistical measures of the dynamical complexity. In Chapter 3, we emphasized that statistical measures of dynamical complexity could complete the spectral analysis for nonlinear dynamical systems. Particularly, this motivated the use of windowed recurrence quantification analysis (WRQA). The results obtained on Chapter 3 show that WRQA might be appealing to follow the evolution of parameters governing the dynamics of fast variables. In addition, we showed in Chapter 2 that RQA measures could be robustly estimated under practical conditions. More generally, we argue that using windowed estimates of some sufficient statistics of dynamical complexity might improve the reconstruction of the

trajectories of slow variables.

RQA measures might be a step towards these sufficient statistics. However, RQA measures are intercorrelated (Webber & Marwan, 2015) and it is therefore complicated to understand how changes in the dynamics impact each measure. This shortcoming could be addressed by constructing analytically the measures for models of the system under study. In other words, if we can relate the value of RQA measures to some parameters of the system's model, then we do not need to understand changes in RQA measures because we can directly work with changes in the parameters.

An effort has been made to develop parametric approaches to RQA (Ramdani et al., 2016; Ramdani et al., 2018), with successful applications to electroencephalographic data (Ramdani et al., 2021). We think that generalizing this approach to more advanced biophysical systems such as neural mass models is a promising perspective. In fact, the approach taken by spectral neural mass models, i.e., linearizing the dynamics and deriving the spectral response to the noise spectrum, might be leveraged by building models of the RQA measures of neural masses.

3 A systematic approach to behavior modeling

Beyond the complexity of dealing with multiscale properties, we need a systematic approach to model the behavioral aspect of subject responses to natural stimuli. Indeed, we actively seek for information in unconditioned settings. An example can be found in vision, the gaze of subjects actively parses its environment (Parr, 2019). Similarly, during our movement task, we might assume that the subject actively tried to follow a virtual target. Our motivation might be to investigate whether different “control schemes” may explain the variability of the movement trajectories, as reported in Chapter 3. For instance, we may want to evaluate the hypothesis that subjects performing fast, cycle movements used a different control strategy than those performing slow, discontinuous movements. Evaluating this hypothesis requires to model the subject proactive behavior in tracking its virtual target.

Fortunately, a general theory of behavior has started to gain interest in the scientific community. During the last decade, the free-energy principle (K. Friston, 2009) and active inference (Parr et al., 2022) were considered as possible explanations for sentient behavior. The free-energy principle states that pertaining systems, such as the living ones, use their internal states to minimize their variational free energy and thus build a model of the hidden causes of their perceptions (K. Friston, 2010). In addition, under this principle, living systems also use their active states – that is, states that have an influence on the environment – to reduce their uncertainty about the world. These concepts have been both acclaimed and criticized by the scientific community (see, e.g., (Aguilera et al., 2021) and the numerous related responses).

Regardless whether biological systems actually comply to it, the free-energy principle provides an appealing framework to build models of behavior (Parr et al., 2022). More specifically, the free-energy principle and active inference are interesting from a neuroimaging perspective because they provide a systematic way to obtain generative models of behavior. This property has been used to build generative models for active vision (Parr, 2019; Parr et al., 2021). In addition, the authors used their models to evaluate different hypotheses about the connectivity between regions of the brain during active vision (Parr et al., 2019).

We believe that the active inference framework will allow to derive behavioral models of free movements under different hypothesized motor control schemes. Evaluating hypotheses will be possible using Bayesian model comparison (K. J. Friston et al., 2016). Importantly, behavioral models derived in the active inference framework will feature the limitations discussed in Chapter 5, in particular circular causality and multiscale properties. Circular causality underpins motor control loops. Movement construction involves several brain regions and ultimately project on a few neurons in the spinal cord (Bear et al., 2020); therefore, movement production involves multiple spatial scales. In addition, movement and neuronal activity span different time scales. We showed that modeling these properties is not trivial. Therefore, active inference gives promising tracks for the future of neuroimaging, but important

questions related to modeling complex systems are yet to be solved.

Appendix

Appendix A

Mathematical derivation of the optimal radius

1 Volume of generalized balls

Let $B_r^{p,d}(x)$ be an open d -ball of size r in an L_p space, i.e. $B_r^{p,d}(x) = \{y \in \mathbb{R}^d : \|x - y\|_p < r\}$. We write $\tau_{p,d} = \lambda(B_1^{p,d})$ the volume of the generalized unit ball, where λ is the Lebesgue measure. The volume of a generalized ball of radius r is $\lambda(B_r^{p,d}) = \tau_{p,d}r^d$. The general formula for the volume of a generalized unit ball is ((X. Wang, 2005)):

$$\tau_{p,d} = \frac{(2\Gamma(\frac{1}{p} + 1))^d}{\Gamma(\frac{d}{p} + 1)} \quad (\text{A.1})$$

which can be simplified for common L_p spaces:

$$\tau_{1,d} = \frac{2^d}{d!} \quad \tau_{2,d} = \frac{\pi^{\frac{d}{2}}}{\Gamma(\frac{d}{2} + 1)} \quad \tau_{\infty,d} = 2^d \quad (\text{A.2})$$

Γ denotes Euler's gamma function with the property $\Gamma(z + 1) = z\Gamma(z)$.

2 Derivation of a reference rule for the uniform kernel

The expression of the bandwidth minimizing the Asymptotic Mean Integrated Squared Error is ((Silverman, 1986), Eq. 4.14 and 4.15):

$$h_{\text{AMISE}} = \left[\frac{W_1(K) \cdot d}{n \cdot [W_2(K)]^2 \cdot W_1(\nabla^2 f)} \right]^{1/(d+4)} \quad (\text{A.3})$$

where W_i are the functionals $W_1(g) = \int_{\mathbb{R}^d} g^2(u) du$ and $W_2(g) = \int_{\mathbb{R}^d} u_1^2 g(u) du$, where u_1 is the first component of $u \in \mathbb{R}^d$ (as the kernel is symmetric, it is sufficient to consider only u_1 in W_2). We compute W_1 for the uniform kernel:

$$W_1(K) = \int_{\mathbb{R}^d} K^2(u) du = \int_{B_1^{p,d}(0)} \left(\frac{1}{\tau_{p,d}} \right)^2 du = \frac{1}{\tau_{p,d}} \quad (\text{A.4})$$

$W_1(\nabla^2 \rho)$ for a d -dimensional Gaussian reference distribution ϕ is given in (Silverman, 1986, Eq. 4.13):

$$W_1(\nabla^2 \rho) \approx W_1(\nabla^2 \phi) = (2\sqrt{\pi})^{-d} \left(d/2 + d^2/4 \right) \quad (\text{A.5})$$

Then, W_2 in the 1-dimensional case:

$$W_2(K) = \int_{\mathbb{R}} u^2 K(u) du = \int_{-1}^1 \frac{u^2}{\tau_{p,1}} du = \frac{1}{3} \quad (\text{A.6})$$

For $d \geq 2$, using u_i to denote the i -th coordinate of $u \in \mathbb{R}^d$:

$$\begin{aligned} W_2(K) &= \int_{\mathbb{R}^d} u_1^2 K(u) du \\ &= \frac{1}{\tau_{p,d}} \int_{\mathbb{R}} u_1^2 \left(\int_{\mathbb{R}^{d-1}} \Theta(1 - (|u_1|^p + \sum_{i=2}^d |u_i|^p)^{1/p}) du_d \dots du_2 \right) du_1 \end{aligned}$$

Changing to spherical coordinates $\vec{u}_{2:d} = (\eta, \vec{\zeta})$ with an orientation vector $\vec{\zeta}$ and a radius $\eta = (\sum_{i=2}^d |u_i|^p)^{1/p}$ and :

$$\begin{aligned} W_2(K) &= \frac{1}{\tau_{p,d}} \int_{\mathbb{R}} u_1^2 \int_{\eta=0}^{\infty} \int_{\mathbb{R}^{d-2}} \Theta(1 - (|u_1|^p + \eta^p)^{1/p}) d\vec{\zeta} d\eta du_1 \\ &= \frac{\tau_{p,d-1}}{\tau_{p,d}} \int_{\mathbb{R}} u_1^2 \int_{\eta=0}^{\infty} (d-1) \eta^{d-2} \Theta(1 - (|u_1|^p + \eta^p)^{1/p}) d\eta du_1 \\ &= \frac{\tau_{p,d-1}}{\tau_{p,d}} \int_{u_1=-1}^1 u_1^2 \int_{\eta=0}^{(1-|u_1|^p)^{1/p}} (d-1) \eta^{d-2} d\eta du_1 \\ &= \frac{\tau_{p,d-1}}{\tau_{p,d}} \int_{u_1=-1}^1 u_1^2 \left((1 - |u_1|^p)^{1/p} \right)^{(d-1)} du_1 \\ &= \frac{\tau_{p,d-1}}{\tau_{p,d}} \frac{2}{3} {}_2F_1 \left(\frac{3}{p}, \frac{1-d}{p}; \frac{3+p}{p}; 1 \right) \end{aligned}$$

where ${}_2F_1(a, b; c; z)$ is the Gaussian hypergeometric function. Finally, using the fact that $\frac{\tau_{p,d-1}}{\tau_{p,d}} = \frac{\Gamma(\frac{d}{p}+1)}{2\Gamma(\frac{1}{p}+1)\Gamma(\frac{d-1}{p}+1)}$ (see Appendix A.1) and the expansion of ${}_2F_1$ at $z = 1$ (Olver et al., 2020, Eq. 15.4.20), we can further simplify:

$$W_2(K) = \frac{\tau_{p,d-1}}{\tau_{p,d}} \frac{2\Gamma\left(1 + \frac{3}{p}\right) \Gamma\left(\frac{d-1}{p} + 1\right)}{3\Gamma\left(\frac{d+2}{p} + 1\right)} = \frac{\Gamma\left(\frac{d}{p} + 1\right) \Gamma\left(1 + \frac{3}{p}\right)}{3\Gamma\left(\frac{d+2}{p} + 1\right) \Gamma\left(\frac{1}{p} + 1\right)} \quad (\text{A.7})$$

We then derive the reference rule by plugging the appropriate values in Eq. (A.3). First, we derive the expression in the simple 1 dimensional case, which is independent from p :

$$r_{\text{opt}} = [12\sqrt{\pi}]^{1/5} \cdot \hat{s} \cdot n^{-1/5} \approx 1.843 \cdot \hat{s} \cdot n^{-1/5} \quad (\text{A.8})$$

The general formula for $d \geq 2$ is more complex:

$$\begin{aligned} r_{\text{opt}} &= \left[\frac{4d(2\sqrt{\pi})^2}{\tau_{p,d} d(d+2)} \times \frac{\left(3\Gamma\left(\frac{d+2}{p} + 1\right) \Gamma\left(\frac{1}{p} + 1\right)\right)^2}{\left(\Gamma\left(\frac{d}{p} + 1\right) \Gamma\left(1 + \frac{3}{p}\right)\right)^2} \right]^{1/(d+4)} \cdot \hat{s} \cdot n^{-1/(d+4)} \\ &= \left[\frac{4(2\sqrt{\pi})^d \left(3\Gamma\left(\frac{d+2}{p} + 1\right) \Gamma\left(\frac{1}{p} + 1\right)\right)^2}{\tau_{p,d} (d+2) \left(\Gamma\left(\frac{d}{p} + 1\right) \Gamma\left(1 + \frac{3}{p}\right)\right)^2} \right]^{1/(d+4)} \cdot \hat{s} \cdot n^{-1/(d+4)} \quad (\text{A.9}) \end{aligned}$$

3 Simplification of the reference rule for common norms

We address the case $p = 1$:

$$\begin{aligned} r_{\text{opt}} &= \left[\frac{4(2\sqrt{\pi})^d (3\Gamma(d+3)\Gamma(2))^2}{\tau_{p,d}(d+2)(\Gamma(d+1)\Gamma(4))^2} \right]^{1/(d+4)} \cdot \hat{s} \cdot n^{-1/(d+4)} \\ &= \left((\sqrt{\pi})^d (d+1)(d+2)! \right)^{1/(d+4)} \cdot \hat{s} \cdot n^{-1/(d+4)} \end{aligned} \quad (\text{A.10})$$

Then, the limiting case $p \rightarrow \infty$:

$$\begin{aligned} r_{\text{opt}} &= \left[\frac{4(2\sqrt{\pi})^d (3\Gamma(1)\Gamma(1))^2}{\tau_{p,d}(d+2)(\Gamma(1)\Gamma(1))^2} \right]^{1/(d+4)} \cdot \hat{s} \cdot n^{-1/(d+4)} \\ &= \left[\frac{36(\sqrt{\pi})^d}{d+2} \right]^{1/(d+4)} \cdot \hat{s} \cdot n^{-1/(d+4)} \end{aligned} \quad (\text{A.11})$$

Finally the case $p = 2$:

$$\begin{aligned} r_{\text{opt}} &= \left[\frac{4(2\sqrt{\pi})^d \left(3\Gamma\left(\frac{d+2}{2}+1\right)\Gamma\left(\frac{1}{2}+1\right) \right)^2}{\tau_{2,d}(d+2)\left(\Gamma\left(\frac{d}{2}+1\right)\Gamma\left(1+\frac{3}{2}\right)\right)^2} \right]^{1/(d+4)} \cdot \hat{s} \cdot n^{-1/(d+4)} \\ &= \left[\frac{2^{d+2}\Gamma\left(\frac{d}{2}+1\right)\left(3\Gamma\left(\frac{d}{2}+1\right)\left(\frac{d}{2}+1\right)\Gamma\left(\frac{1}{2}+1\right)\right)^2}{(d+2)\left(\Gamma\left(\frac{d}{2}+1\right)\Gamma\left(1+\frac{1}{2}\right)\left(1+\frac{1}{2}\right)\right)^2} \right]^{1/(d+4)} \cdot \hat{s} \cdot n^{-1/(d+4)} \\ &= \left[2^{d+2}\Gamma\left(\frac{d}{2}+1\right)(d+2) \right]^{1/(d+4)} \cdot \hat{s} \cdot n^{-1/(d+4)} \\ &= 2 \left[\frac{\Gamma\left(\frac{d}{2}+1\right)}{2} \right]^{1/(d+4)} \cdot \hat{s} \cdot n^{-1/(d+4)} \end{aligned} \quad (\text{A.12})$$

Appendix B

Additional figures for Chapter 3

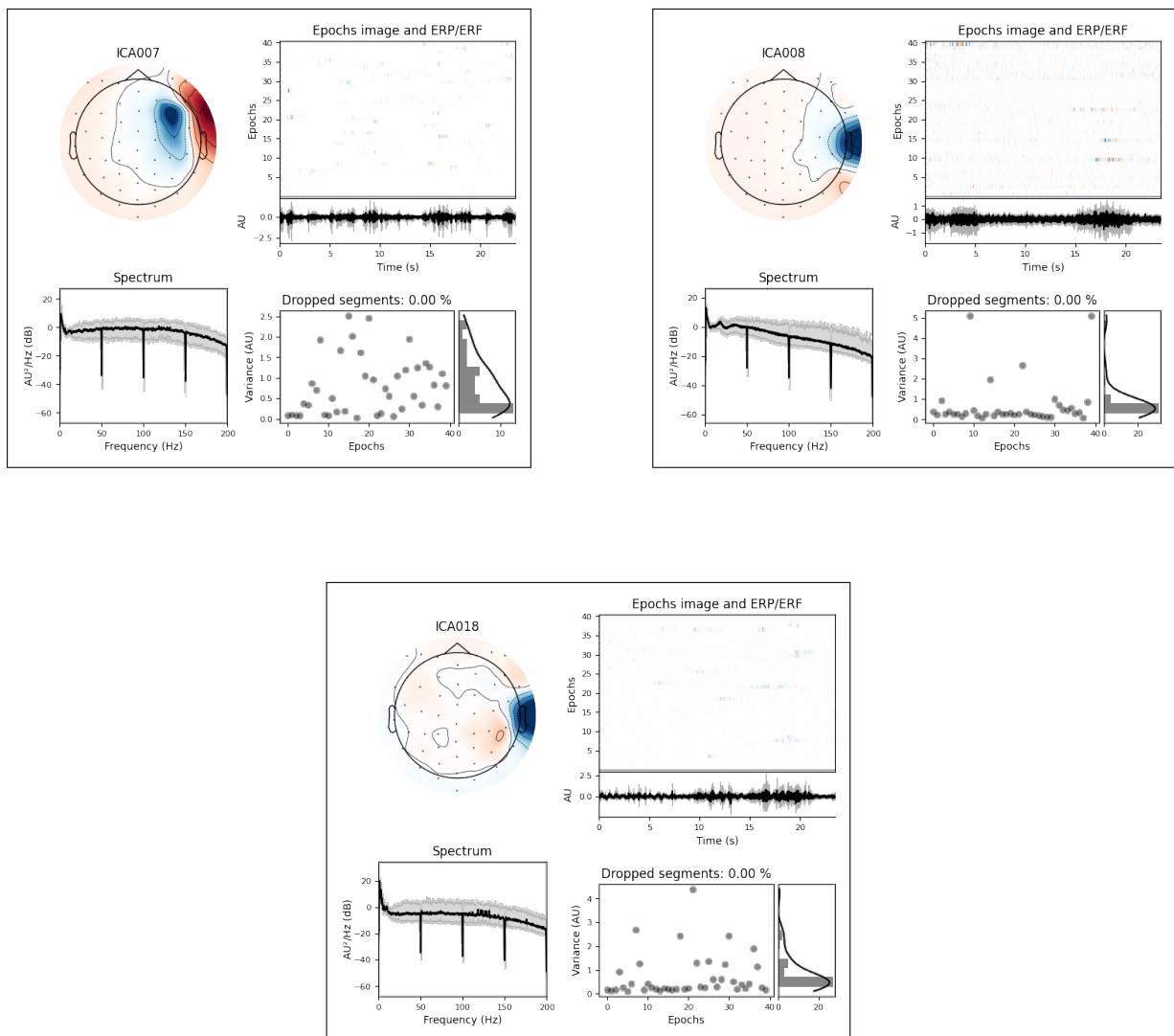


Figure B.1: Typical independent components marked as muscular artifacts (from subject 2, 5, and 6).

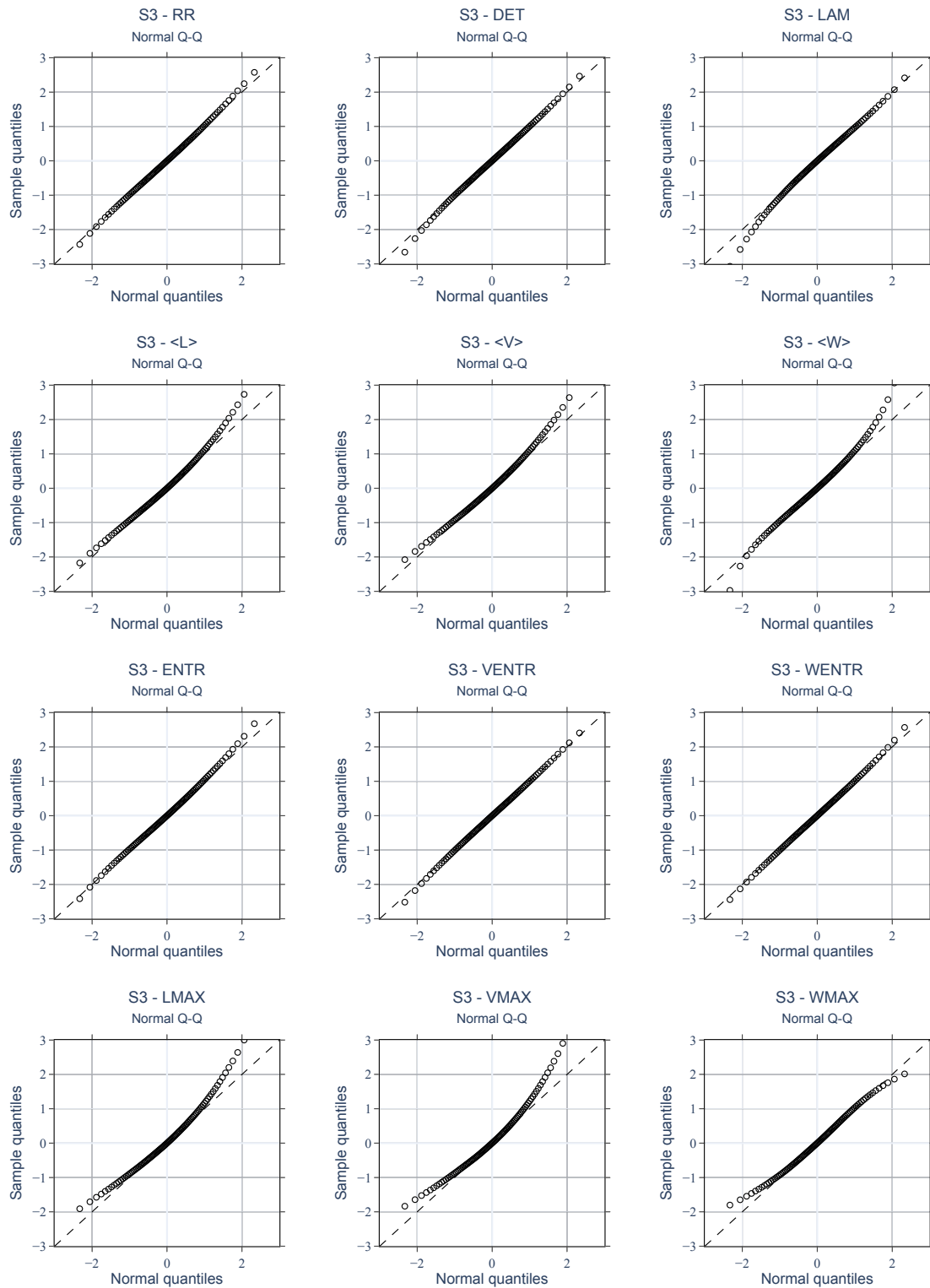


Figure B.2: Normal Q-Q plot of the LMAX residuals for the multiple subjects model.

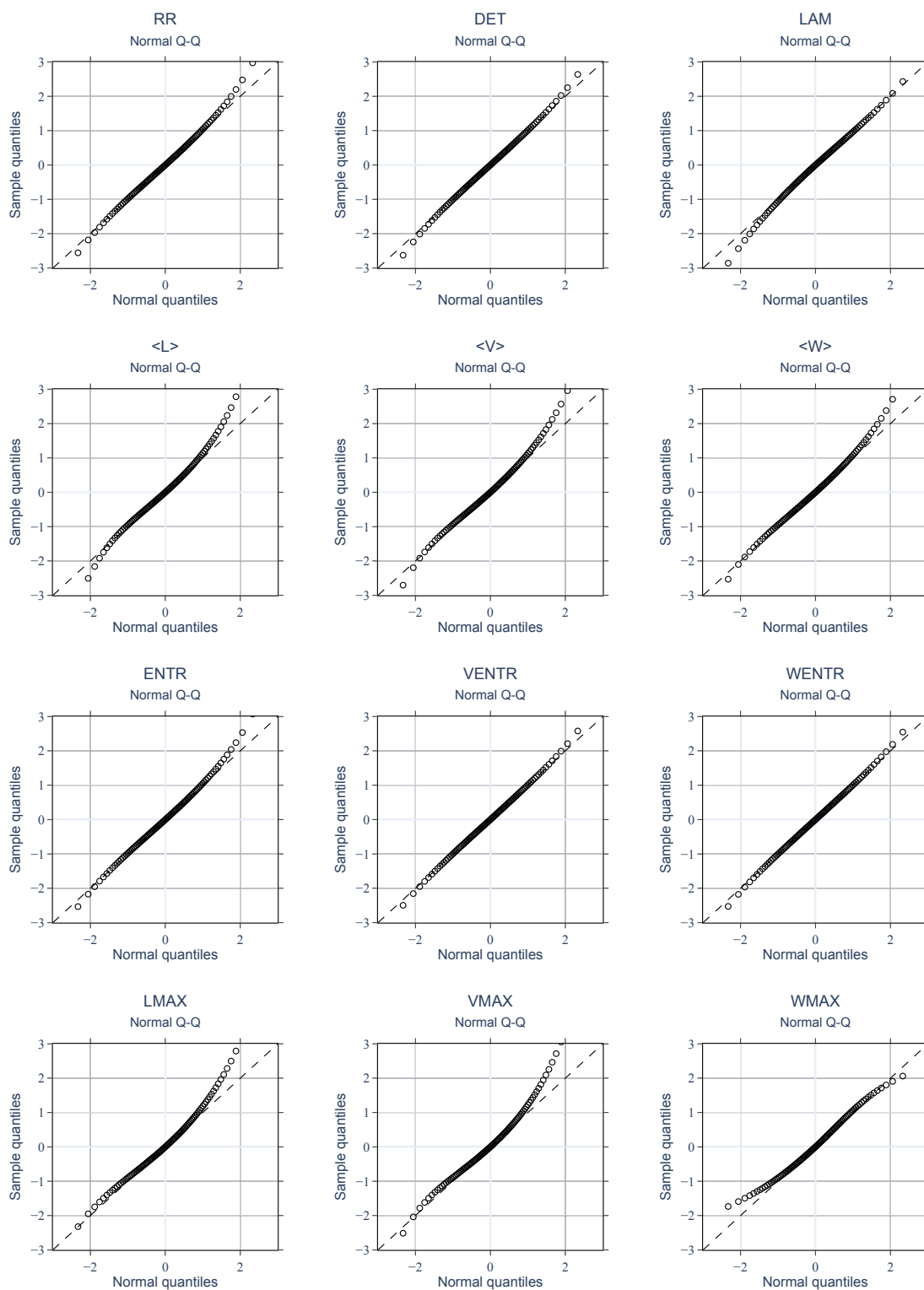


Figure B.3: Normal Q-Q plot of the LMAX residuals for the multiple subjects model.

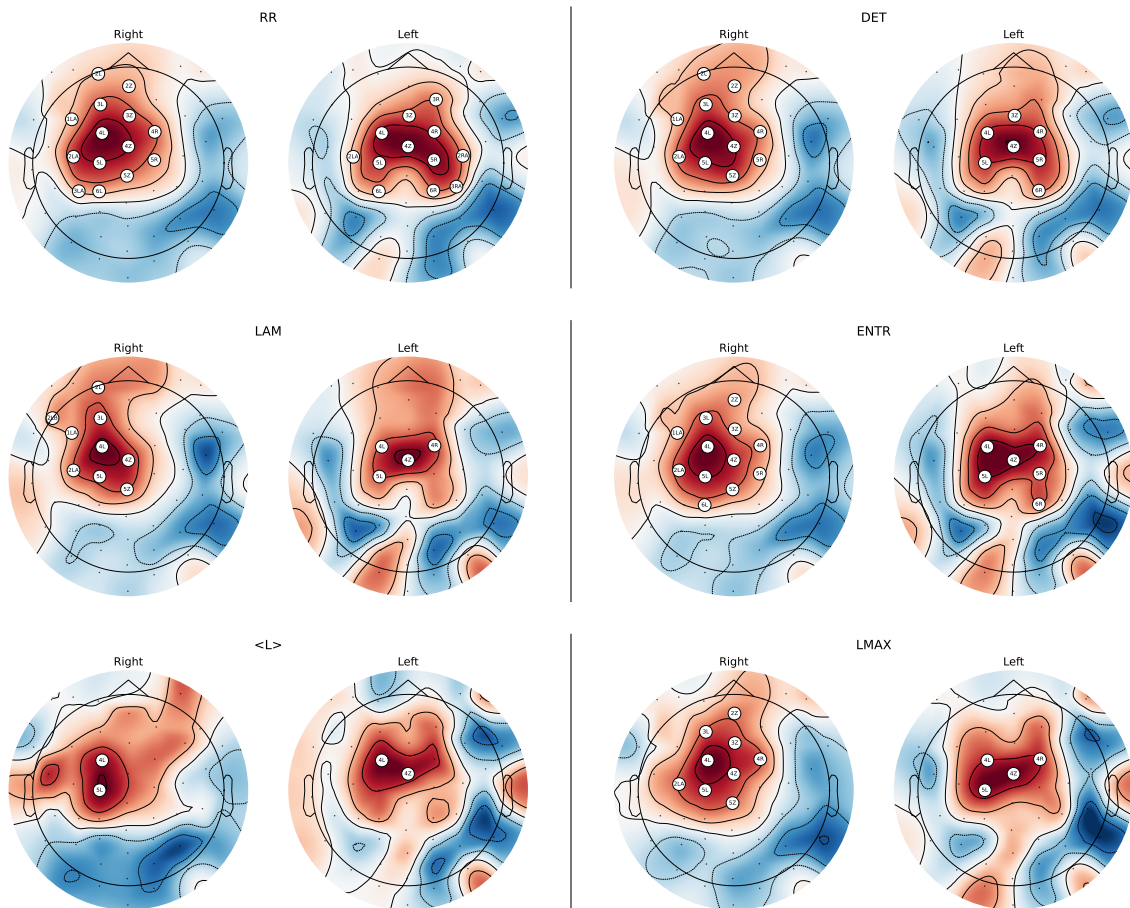


Figure B.4: Multiple subject SPMs for several nonlinear complexity measures. Colormap shows the value of the T statistics in scalp space (arbitrary units). Sensors with white circles show significant negative correlation with the EMG features ($p < 0.01$, Bonferroni corrected).

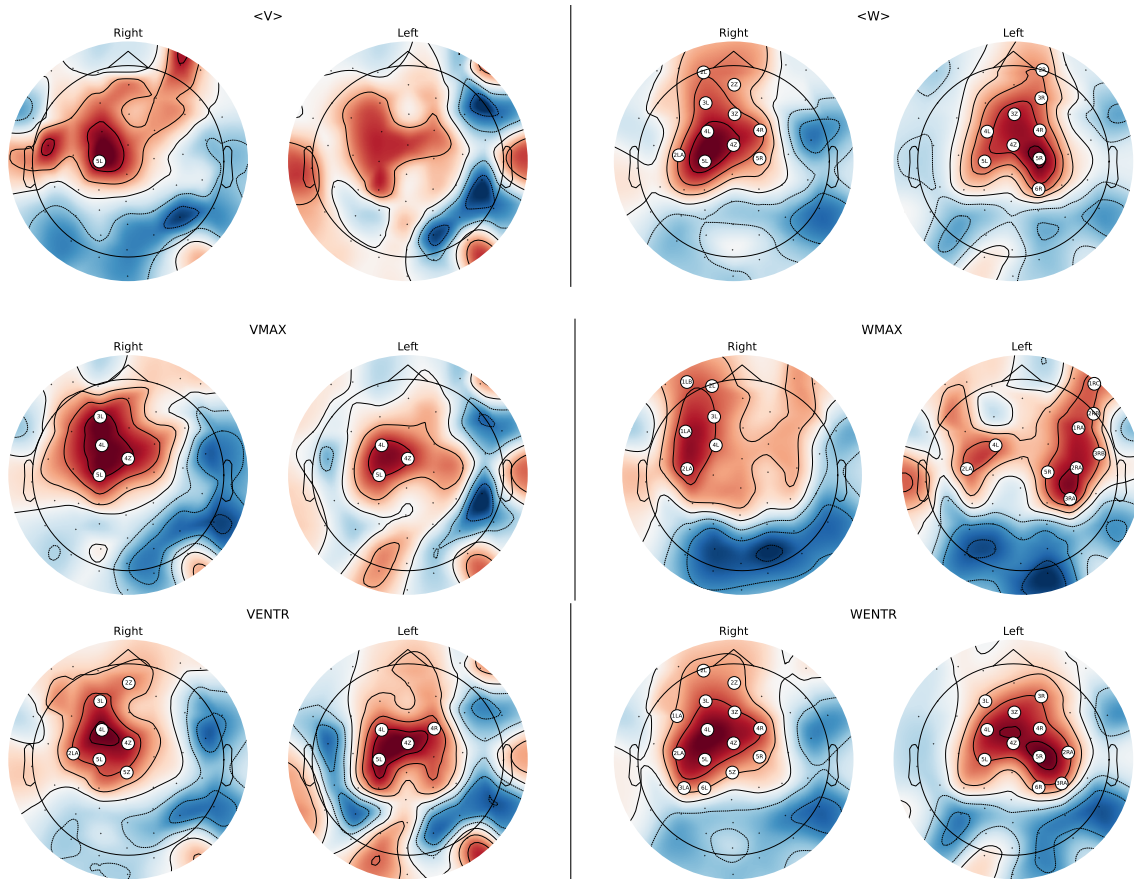


Figure B.4: Multiple subject SPMs for several nonlinear complexity measures. Colormap shows the value of the T statistics in scalp space (arbitrary units). Sensors with white circles show significant negative correlation with the EMG features ($p < 0.01$, Bonferroni corrected).

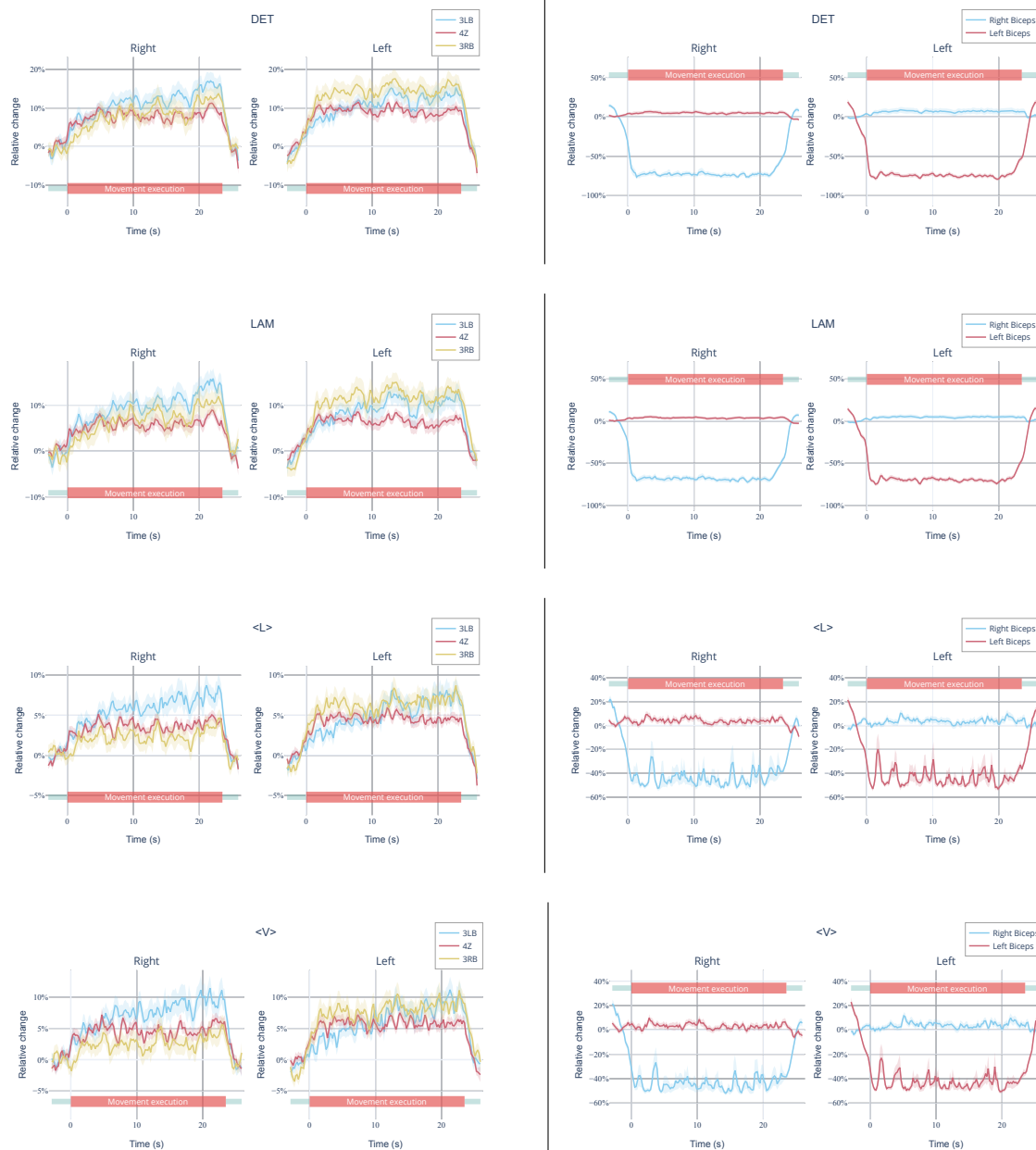
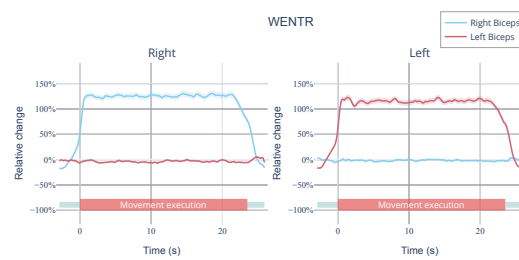
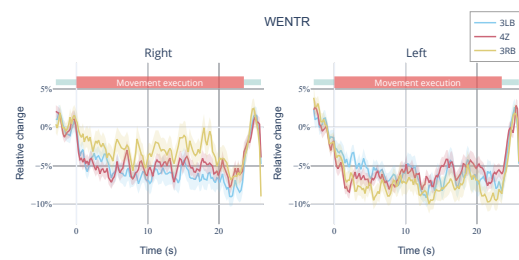
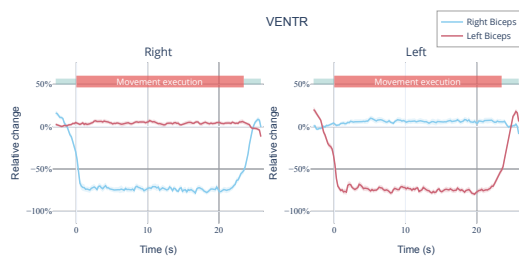
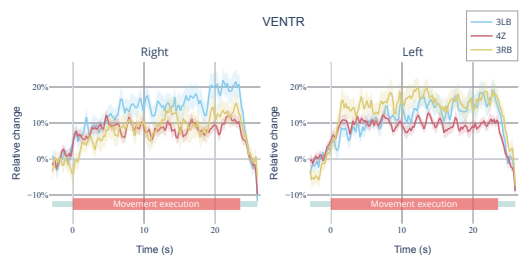
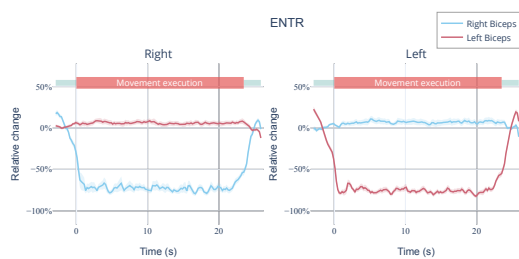
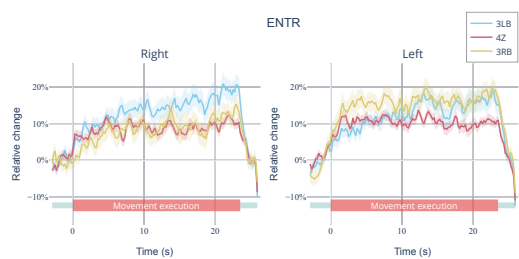
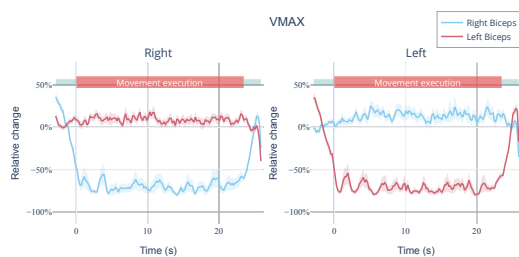
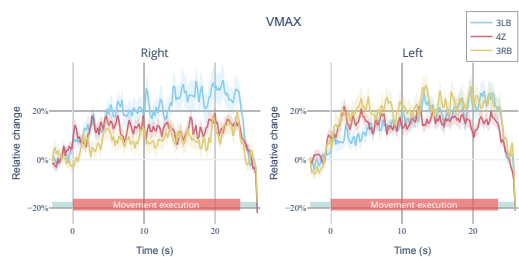
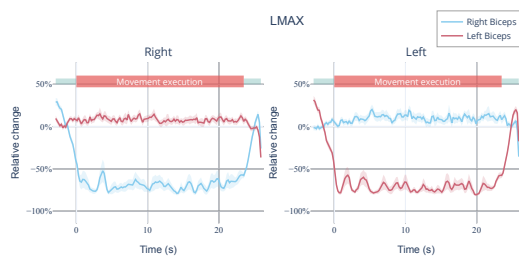
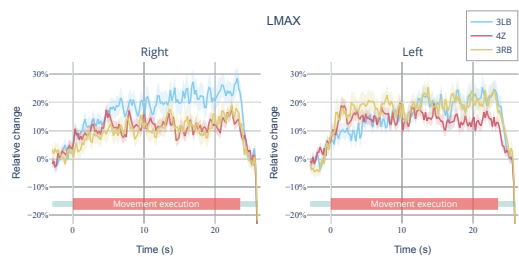


Figure B.5: RQA measures and Sampen of EEG and biceps EMG signals during right and left arm movements. Colorbands indicates standard error. We observe a systematic contravariant evolution of EEG and EMG signals: when a nonlinear measure of the moving arm EMG signal increases (resp. decrease), the measure of the EEG signal on the primary motor cortex decreases (resp. increases). In addition, we see that movement is associated with increased complexity of the moving arm EMG signal (e.g. DET decreases, SAMPEN increases). In contrast, movement is associated with decreased signal complexity of the EEG signal.



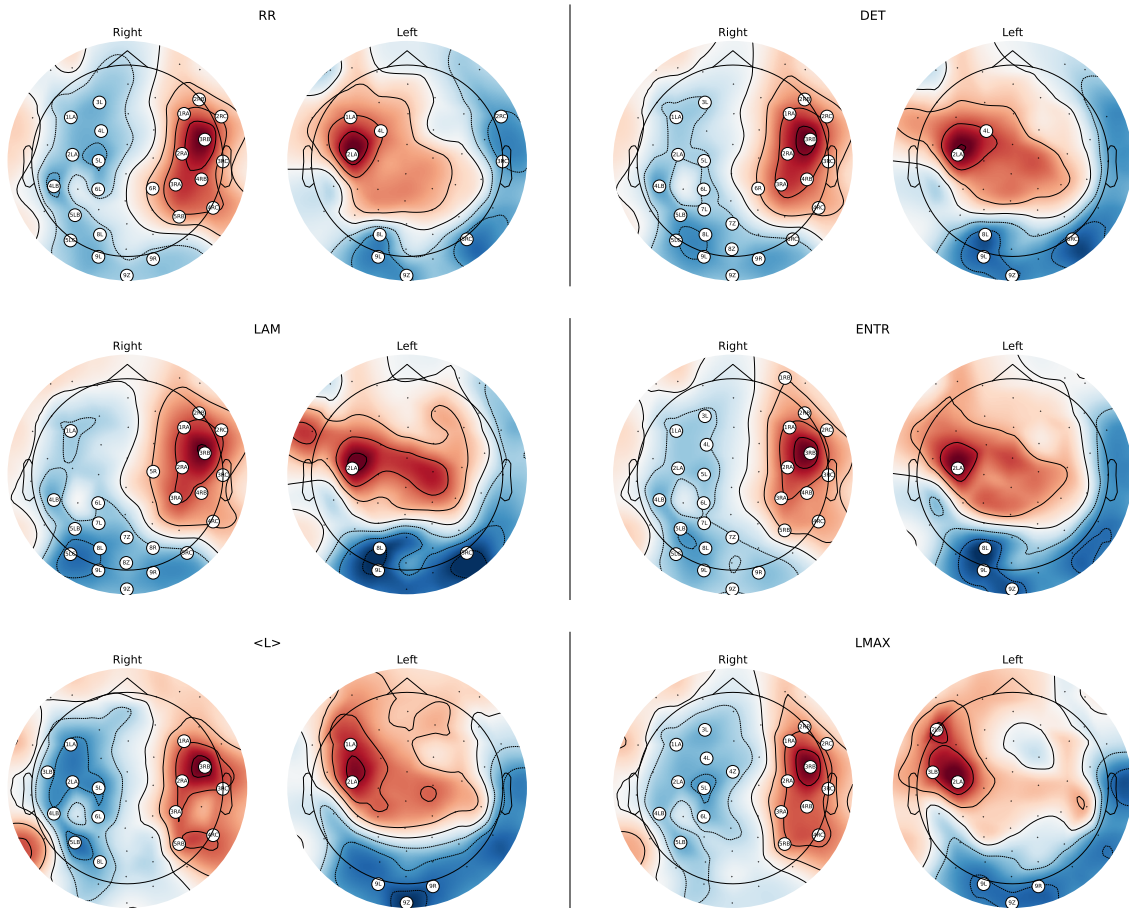


Figure B.6: Multiple subject SPMs for several nonlinear complexity measures. Colormap shows the value of the T statistics in scalp space (arbitrary units). Sensors with white circles show significant negative correlation with the EMG features ($p < 0.01$, Bonferroni corrected).

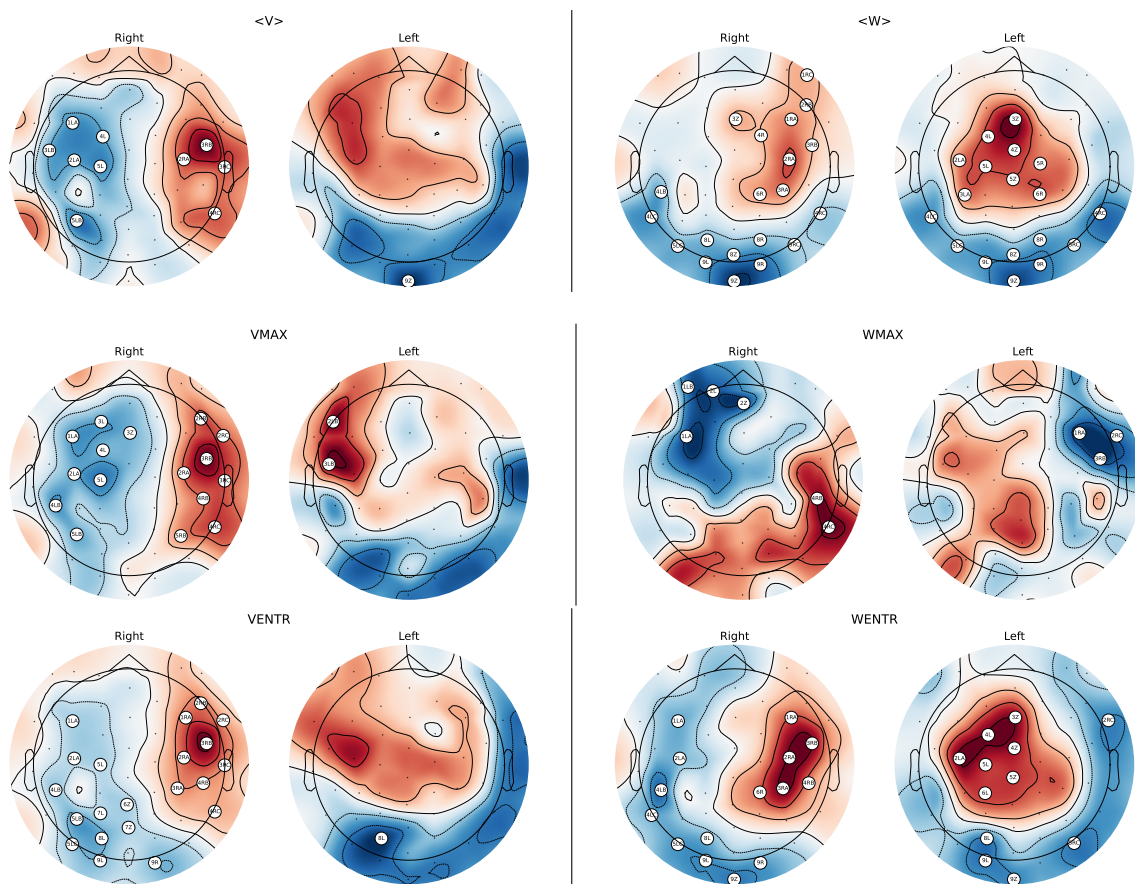


Figure B.6: Multiple subject SPMs for several nonlinear complexity measures. Colormap shows the value of the T statistics in scalp space (arbitrary units). Sensors with white circles show significant negative correlation with the EMG features ($p < 0.01$, Bonferroni corrected).

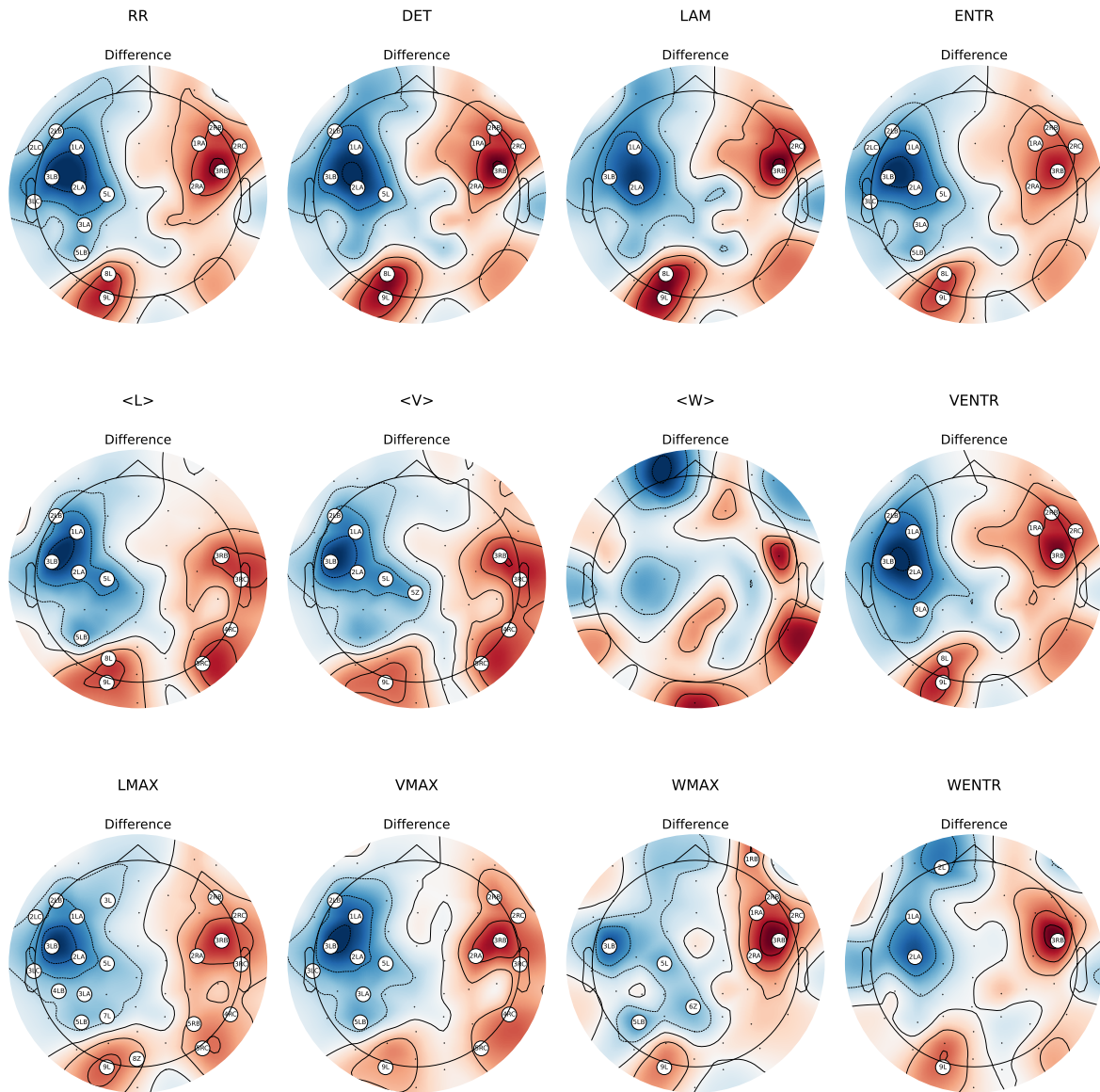


Figure B.7: Multiple subject SPMs for several nonlinear complexity measures. Colormap shows the value of the T statistics in scalp space (arbitrary units). Sensors with white circles show significant negative correlation with the EMG features ($p < 0.01$, Bonferroni corrected).

Appendix C

Supplementary material for Chapter 4

1 Derivation of Welch-Satterthwaite approximation of some stationary processes

Consider a stationary process with absolutely decreasing autocorrelation ρ . We discretize ρ as $\rho_k = \rho(k\epsilon)$ with $\epsilon > 0$ and $1 \leq k \leq n$. Let Σ be the $n \times n$ Toeplitz matrix generated by ρ , i.e. $\Sigma_{ij} = \rho_{|i-j|}$. The number of e.d.f.s given by the Welch-Satterthwaite approximation is

$$e.d.f. = \frac{\text{tr}(\Sigma)^2}{\text{tr}(\Sigma\Sigma)} \quad (\text{C.1})$$

First, we observe that

$$\text{tr}(\Sigma)^2 = \left(\sum_{i=1}^n \rho_0 \right)^2 = n^2 \rho_0^2 \quad (\text{C.2})$$

and

$$\text{tr}(\Sigma\Sigma) = \sum_{i=1}^n \left(\rho_0^2 + \sum_{k=1}^{n-i} \rho_k^2 + \sum_{k=1}^{i-1} \rho_k^2 \right) \quad (\text{C.3})$$

We shall prove that

$$\frac{1}{n} \text{tr}(\Sigma\Sigma) \approx \int_{-\infty}^{+\infty} (\rho(\tau))^2 d\tau$$

The idea of the proof is to assume some order of decrease for the autocorrelation such that the contribution of tail part of the autocorrelation becomes insignificant. In that case, most terms in $\text{tr}(\Sigma\Sigma)$ Let $s = \lfloor n^{1/\gamma} \rfloor$ with $\gamma > 1$ and $\lfloor x \rfloor$ is the integer part of x . We further assume that $|\rho_k| \leq \alpha k^{-\beta}$ with $\alpha > 0$ and $\beta > \gamma/2$. We write

$$S_i = \rho_0^2 + \sum_{k=1}^{n-i} \rho_k^2 + \sum_{k=1}^{i-1} \rho_k^2$$

and

$$M_s = \rho_0^2 + 2 \sum_{k=1}^s \rho_k^2$$

the sum appearing in Eq. (C.3). For $s \leq i \leq n - s$, we have

$$M_s \leq S_i < M_s + \sum_{k=s+1}^i \rho_s^2$$

For $0 \leq i < s$ and $n - s < i \leq n$, we simply notice that

$$0 \leq S_i < s\rho_0^2$$

Thus, using

$$\frac{1}{n} \text{tr}(\Sigma\Sigma) = \frac{1}{n} \sum_{i=1}^n S_i$$

we have

$$\frac{n-s}{n} M_s \leq \frac{1}{n} \text{tr}(\Sigma\Sigma) < \frac{n-s}{n} M_s + \frac{s}{n} \rho_0^2 + \frac{(n-2s+1)(n-2s+2)}{2n} \rho_s^2$$

where

$$\frac{(n-2s+1)(n-2s+2)}{2n} \rho_s^2 \propto n^{1-2\beta/\gamma}$$

Observing that $1 - 2\beta/\gamma < 0$, we have

$$\lim_{n \rightarrow +\infty} \frac{1}{n} \text{tr}(\Sigma\Sigma) = \rho(0) + 2 \sum_{k=1}^{+\infty} \rho(k\varepsilon) \quad (\text{C.4})$$

which leads to the desired result

$$\lim_{\varepsilon \rightarrow 0} \lim_{n \rightarrow +\infty} \frac{1}{n} \text{tr}(\Sigma\Sigma) = \int_{-\infty}^{+\infty} (\rho(\tau))^2 d\tau \quad (\text{C.5})$$

Finally, replacing in Eq. (C.1) yields Eq. (4.21):

$$v_{WS} = \frac{\text{tr}(\Sigma)^2}{\text{tr}(\Sigma\Sigma)} = \frac{n^2 \rho_0^2}{\text{tr}(\Sigma\Sigma)} \approx \frac{n \rho_0^2}{\int_{-\infty}^{+\infty} (\rho(\tau))^2 d\tau} \quad (\text{C.6})$$

2 Additional figures

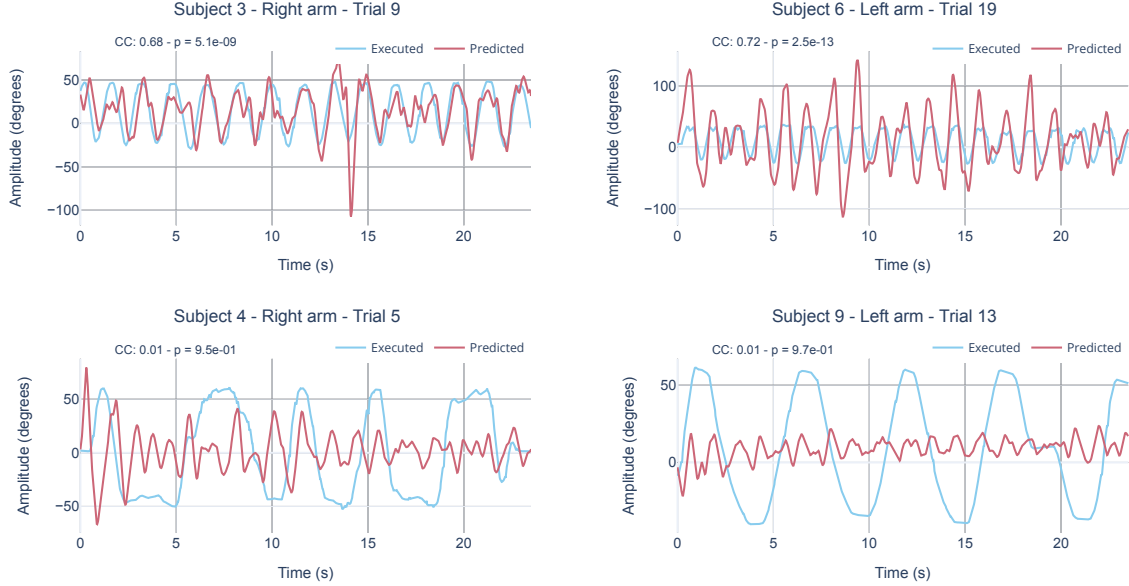


Figure C.1: Sample executed and reconstructed movement trajectories, associated with low p -values (first row) and high p value (second row). Trajectories are reconstructed with the Kalman filter model.

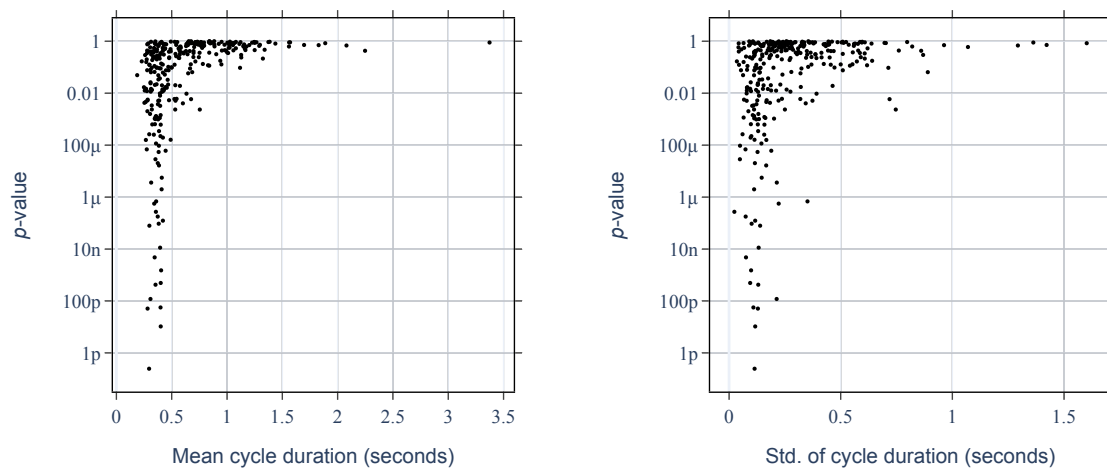


Figure C.2: p -value of the decoding accuracy of the Kalman filter model versus of mean and standard deviation of movement cycles.

Appendix D

Supplementary material for Chapter 5

1 Proof of the embedding theorem for generalized coordinates

Generalized coordinates of order p of a time series x are:

$$\tilde{x}(t) = \begin{pmatrix} x(t) \\ x'(t) \\ x''(t) \\ x'''(t) \\ \dots \end{pmatrix} = \lim_{dt \rightarrow 0} \begin{pmatrix} x(t) \\ (x(t) - x(t-dt))/dt \\ (x(t) - 2x(t-dt) + x(t-2dt))/dt^2 \\ (x(t) - 3x(t-dt) + 3x(t-2dt) - x(t-3dt))/dt^3 \\ \vdots \end{pmatrix} \quad (\text{D.1})$$

$$= \lim_{dt \rightarrow 0} \text{diag} \left\{ \begin{pmatrix} 1 \\ 1/dt \\ 1/dt^2 \\ 1/dt^3 \\ \vdots \end{pmatrix} \right\} \cdot \begin{pmatrix} 1 & & & & \\ 1 & 1 & & & \\ 1 & 2 & 1 & & \\ 1 & 3 & 3 & 1 & \\ \vdots & & & & \ddots \end{pmatrix} \cdot \text{diag} \left\{ \begin{pmatrix} 1 \\ -1 \\ 1 \\ -1 \\ \vdots \end{pmatrix} \right\} \cdot \begin{pmatrix} x(t) \\ x(t-dt) \\ x(t-2dt) \\ x(t-3dt) \\ \vdots \end{pmatrix} \quad (\text{D.2})$$

Whence, generalized coordinates with order p are obtained by a linear transformation of the vector $(x(t), \dots, x(t-pdt))$. The linear transformation has full rank as the product of two diagonal matrix and a lower Pascal matrix (the determinant of a lower Pascal matrix is 1, see [\(Brawer & Pirovino, 1992\)](#)). As the (linear) map from delay coordinates to generalized coordinates is invertible, it is a smooth diffeomorphism [\(J. M. Lee, 2013\)](#). Now, if x is the observation through a smooth map of the trajectory of a dynamical system with a strange attractor with dimension n , then, from Takens theorem, an embedding of the attractor can be constructed from delayed coordinates $(x(t-2ndt), \dots, x(t))$ [\(Sauer et al., 1991\)](#). Therefore, by composition, the attractor in generalized coordinates is an embedding of the original attractor when $p \geq 2n$.

2 Parameter tables

Name	Value	Ref.
Body height	1.75	
Relative forearm size	0.1648	(Drillis et al., 1964, Table I)
Relative upper arm size	0.1959	(Drillis et al., 1964, Table I)
Relative hand size	0.11465	(Drillis et al., 1964, Table I)
Relative humerus size	0.8	
Body weight	70	
Relative forearm weight	0.00762	(Drillis et al., 1964, Table II)
Relative upper arm weight	0.01373	(Drillis et al., 1964, Table II)
Relative hand weight	0.00361	(Drillis et al., 1964, Table II)
Constraints: Max elbow flexion	0.523599	
Constraints: Max elbow extension	2.827433	
g	9.81	

Table D.1: Parameters of the skeletal model. All parameters with a dimension are in SI units.

Name	Value	Name	Value
Biceps insertion	0.02	Triceps insertion	0.02
Biceps tendon length	0.145	Triceps tendon length	0.155
Biceps muscle - F_{\max}	2874.67	Triceps muscle - F_{\max}	2397.12
Biceps muscle - l_0	0.13	Triceps muscle - l_0	0.15
Biceps muscle - ϕ_0	0.0	Triceps muscle - ϕ_0	0.2094
Biceps muscle - W	0.56	Triceps muscle - W	0.56
Biceps muscle - v_{\max}	1.3	Triceps muscle - v_{\max}	1.3
Biceps muscle - A	0.25	Triceps muscle - A	0.25
Biceps muscle - g_{\max}	1.5	Triceps muscle - g_{\max}	1.5
Biceps muscle - l_{slack}	0.18	Triceps muscle - l_{slack}	0.21
Biceps muscle - k_1	10.0	Triceps muscle - k_1	10.0
Biceps muscle - k_2	10000.0	Triceps muscle - k_2	10000.0
Biceps muscle - τ_{act}	0.625	Triceps muscle - τ_{act}	0.625

Table D.2: Parameters of muscle models. Muscle parameters are from (Desplenter & Trejos, 2018). Insertion and tendon length have been selected manually. All parameters with a dimension are in SI units.

Name	Value	Name	Value
Biceps gain - a_b	0.1	Triceps gain - a_t	0.1
Biceps gain - d_b	1.0	Triceps gain - d_t	1.0
Biceps gain - p_b	0.0	Triceps gain - p_t	0.0
Biceps gain - r_b	0.1	Triceps gain - r_t	0.1
Biceps gain - s_b	0.2	Triceps gain - s_t	0.2
Biceps gain - g_b	0.2	Triceps gain - g_t	0.2
Biceps gain - b_b	0.1	Triceps gain - b_t	0.1

Table D.3: Parameters of the spinal cord model, from (Li et al., 2015).

3 Spectral neural mass model

3.1 Equations

We put here the equations of the linearized neural mass model. The fast variables are driven by the system

$$\dot{x} = Ax + Bu \quad (\text{D.3})$$

$$y = Cx \quad (\text{D.4})$$

where

$$A = \begin{pmatrix} 0 & 0 & 0 & 1 & 0 & 0 & 0 & 0 & 0 & 0 & 0 & 0 & 0 \\ 0 & 0 & 0 & 0 & 1 & 0 & 0 & 0 & 0 & 0 & 0 & 0 & 0 \\ 0 & 0 & 0 & 0 & 0 & 1 & 0 & 0 & 0 & 0 & 0 & 0 & 0 \\ -\kappa_e^2 & 0 & 0 & -2\kappa_e & 0 & 0 & 0 & 0 & \kappa_e H_e \gamma_1 g & 0 & 0 & 0 & 0 \\ \kappa_e H_e \gamma_i g & -\kappa_e^2 & 0 & 0 & -2\kappa_e & 0 & 0 & 0 & 0 & 0 & 0 & 0 & 0 \\ 0 & 0 & -\kappa_i^2 & 0 & 0 & -2\kappa_i & 0 & 0 & 0 & 0 & 0 & 0 & \kappa_i H_i \gamma_4 g \\ 0 & 0 & 0 & 0 & 0 & 0 & 0 & 1 & 0 & 0 & 0 & 0 & 0 \\ 0 & 0 & 0 & 0 & 0 & 0 & -\kappa_e^2 & -2\kappa_e & \kappa_e H_e \gamma_3 g & 0 & 0 & 0 & 0 \\ 0 & 0 & 0 & 0 & 1 & -1 & 0 & 0 & 0 & 0 & 0 & 0 & 0 \\ 0 & 0 & 0 & 0 & 0 & 0 & 0 & 0 & 0 & 0 & 0 & 1 & 0 \\ 0 & 0 & 0 & 0 & 0 & 0 & 0 & 0 & 0 & 0 & -\kappa_i^2 & -2\kappa_i & \kappa_i H_i \gamma_5 g \\ 0 & 0 & 0 & 0 & 0 & 0 & 0 & 0 & 1 & 0 & 0 & 0 & -1 & 0 \end{pmatrix} \quad (\text{D.5})$$

$$B^T = \begin{pmatrix} 0 & 0 & 0 & \kappa_e H_e & 0 & 0 & 0 & 0 & 0 & 0 & 0 & 0 & 0 & 0 \end{pmatrix} \quad (\text{D.6})$$

$$C = \begin{pmatrix} 0 & 0 & 0 & 0 & 0 & 0 & 0 & 0 & 0 & 1 & 0 & 0 & 0 & 0 \end{pmatrix} \quad (\text{D.7})$$

3.2 Transfer functions

We present here the reproduction of the results for the neural mass model of spectral responses, introduced in (R. J. Moran et al., 2007). Similarly to the original article ((R. J. Moran et al., 2007, Fig. 7)), we varied the parameters one by one, the other ones set to their default values, and plot the frequency responses of the linearized model.

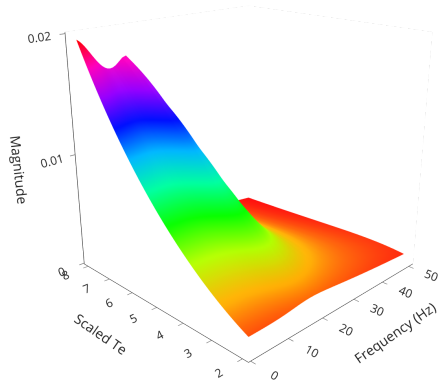
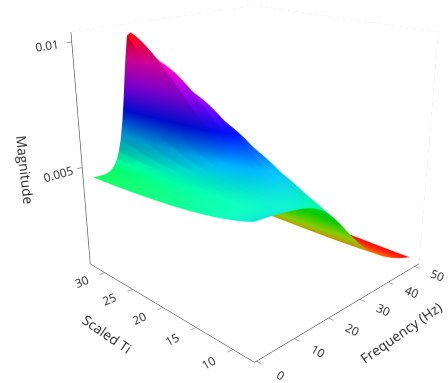
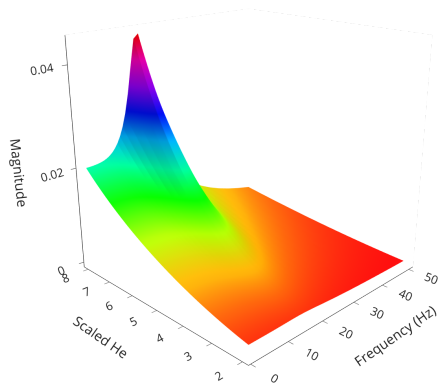
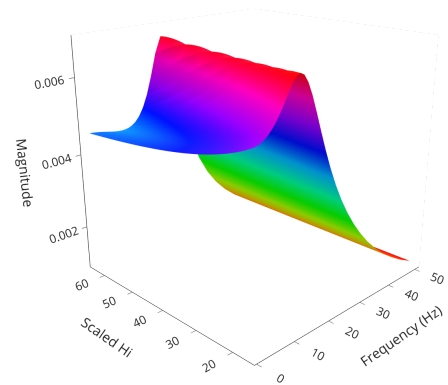
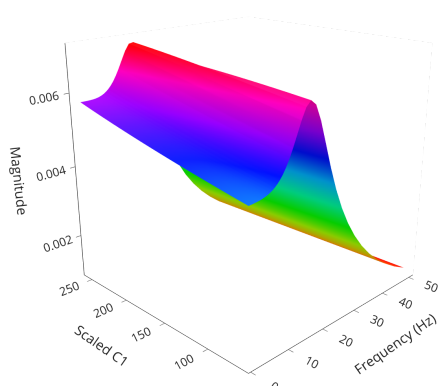
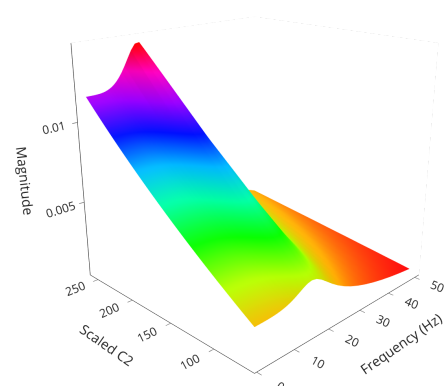
(a) Excitatory time constant τ_e (ms)(b) Inhibitory time constant τ_i (ms)(c) Excitatory maximum depolarization H_e (mV)(d) Inhibitory maximum depolarization H_i (mV)(e) First coupling C_1 (f) Second coupling $2 C_2$

Figure D.1: Change in spectral content with model parameters.

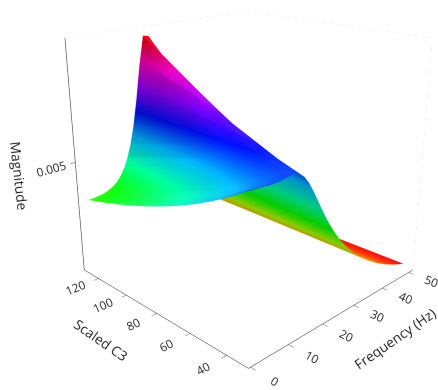
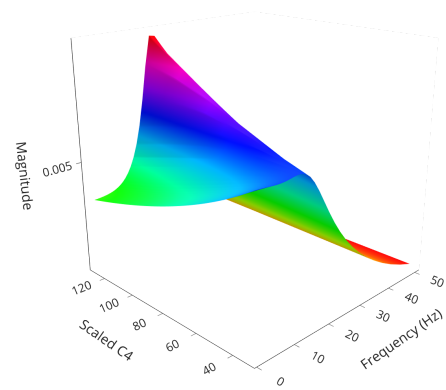
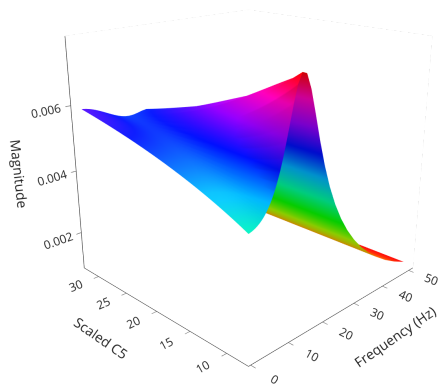
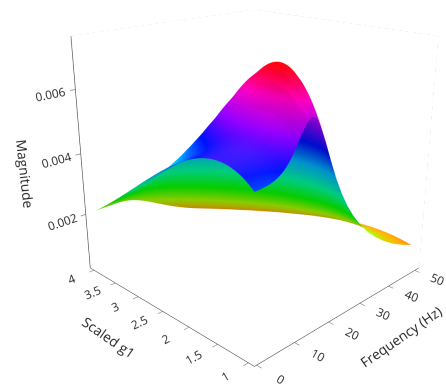
(g) Third coupling $3 C_3$ (h) Fourth coupling $4 C_4$ (i) Fifth coupling $5 C_5$ (j) Rate to voltage gain ρ_1

Figure D.1: Change in spectral content with model parameters.

Bibliography

- Adler, R. J. (2010). *The geometry of random fields*. SIAM. (Cit. on pp. 48, 54).
- Afyouni, S., Smith, S. M., & Nichols, T. E. (2019). Effective degrees of freedom of the pearson's correlation coefficient under autocorrelation. *NeuroImage*, 199, 609–625. <https://doi.org/10.1016/j.neuroimage.2019.05.011> (cit. on pp. 5, 47, 51, 52, ix)
- Aguilera, M., Millidge, B., Tschantz, A., & Buckley, C. L. (2021). How particular is the physics of the free energy principle? *Physics of Life Reviews*. <https://doi.org/10.1016/j.pprev.2021.11.001> (cit. on p. 93)
- An, K., Takahashi, K., Harrigan, T., & Chao, E. (1984). Determination of muscle orientations and moment arms. *Journal of biomechanical engineering*, 106(3), 280–282. <https://doi.org/10.1115/1.3138494> (cit. on p. 76)
- Andreadis, I., Fragkou, A. D., & Karakasidis, T. E. (2020). On a topological criterion to select a recurrence threshold. *Chaos: An Interdisciplinary Journal of Nonlinear Science*, 30(1), 013124. <https://doi.org/10.1063/1.5116766> (cit. on p. 24)
- Andrzejak, R. G., Lehnertz, K., Mormann, F., Rieke, C., David, P., & Elger, C. E. (2001). Indications of nonlinear deterministic and finite-dimensional structures in time series of brain electrical activity: Dependence on recording region and brain state. *Physical Review E*, 64(6), 061907. <https://doi.org/10.1103/PhysRevE.64.061907> (cit. on p. 22)
- Antelis, J. M., Montesano, L., Ramos-Murguialday, A., Birbaumer, N., & Minguetz, J. (2013). On the usage of linear regression models to reconstruct limb kinematics from low frequency eeg signals. *PloS one*, 8(4), e61976. <https://doi.org/10.1371/journal.pone.0061976> (cit. on pp. 61, 66)
- Aymerich-Franch, L., Petit, D., Ganesh, G., & Kheddar, A. (2016). The second me: Seeing the real body during humanoid robot embodiment produces an illusion of bi-location. *Consciousness and cognition*, 46, 99–109. <https://doi.org/10.1016/j.concog.2016.09.017> (cit. on pp. 3, vii)
- Baker, S., Olivier, E., & Lemon, R. (1997). Coherent oscillations in monkey motor cortex and hand muscle emg show task-dependent modulation. *The Journal of physiology*, 501(Pt 1), 225. <https://doi.org/10.1111/j.1469-7793.1997.225bo.x> (cit. on pp. 4, viii)

- Ball, T., Demandt, E., Mutschler, I., Neitzel, E., Mehring, C., Vogt, K., Aertsen, A., & Schulze-Bonhage, A. (2008). Movement related activity in the high gamma range of the human eeg. *Neuroimage*, 41(2), 302–310. <https://doi.org/10.1016/j.neuroimage.2008.02.032> (cit. on pp. 4, 25, vii)
- Bartlett, M. S. (1946). On the theoretical specification and sampling properties of autocorrelated time-series. *Supplement to the Journal of the Royal Statistical Society*, 8(1), 27–41. <https://doi.org/10.2307/2983611> (cit. on pp. 47, 51)
- Bartlett, M. (1935). Some aspects of the time-correlation problem in regard to tests of significance. *Journal of the Royal Statistical Society*, 98(3), 536–543. <https://doi.org/10.2307/2342284> (cit. on pp. 5, 47, 50, 51, ix)
- Bayley, G., & Hammersley, J. (1946). The "effective" number of independent observations in an autocorrelated time series. *Supplement to the Journal of the Royal Statistical Society*, 8(2), 184–197. <https://doi.org/10.2307/2983560> (cit. on pp. 47, 48, 51)
- Bear, M., Connors, B., & Paradiso, M. A. (2020). *Neuroscience: Exploring the brain, enhanced edition: Exploring the brain*. Jones & Bartlett Learning. (Cit. on pp. 4, 7, 39, 42, 67, 84, 93, viii, x).
- Bishop, C. M., & Nasrabadi, N. M. (2006). *Pattern recognition and machine learning* (Vol. 4). Springer. <https://doi.org/10.5555/1162264>. (Cit. on pp. 3, 54, 68, vi)
- Bradberry, T. J., Gentili, R. J., & Contreras-Vidal, J. L. (2010). Reconstructing three-dimensional hand movements from noninvasive electroencephalographic signals. *Journal of neuroscience*, 30(9), 3432–3437. <https://doi.org/10.1523/jneurosci.6107-09.2010> (cit. on pp. 3, 5, 61, 66, vii, ix)
- Brawer, R., & Pirovino, M. (1992). The linear algebra of the pascal matrix. *Linear Algebra and Its Applications*, 174, 13–23. [https://doi.org/10.1016/0024-3795\(92\)90038-c](https://doi.org/10.1016/0024-3795(92)90038-c) (cit. on p. 115)
- Breakspear, M. (2017). Dynamic models of large-scale brain activity. *Nature Neuroscience* 2017 20:3, 20, 340–352. <https://doi.org/10.1038/nn.4497> (cit. on p. 92)
- Bridges, D., Pitiot, A., MacAskill, M. R., & Peirce, J. W. (2020). The timing mega-study: Comparing a range of experiment generators, both lab-based and online. *PeerJ*, 8, e9414. <https://doi.org/10.7717/peerj.9414> (cit. on p. 30)
- Cao, L. (1997). Practical method for determining the minimum embedding dimension of a scalar time series. *Physica D: Nonlinear Phenomena*, 110(1-2), 43–50. [https://doi.org/10.1016/s0167-2789\(97\)00118-8](https://doi.org/10.1016/s0167-2789(97)00118-8) (cit. on pp. 2, v)
- Chapin, J. K., Moxon, K. A., Markowitz, R. S., & Nicolelis, M. A. (1999). Real-time control of a robot arm using simultaneously recorded neurons in the motor cortex. *Nature neuroscience*, 2(7), 664–670. <https://doi.org/10.1038/10223> (cit. on pp. 3, vii)
- Cheney, P. D., & Fetz, E. E. (1980). Functional classes of primate corticomotoneuronal cells and their relation to active force. *Journal of neurophysiology*, 44(4), 773–791. <https://doi.org/10.1152/jn.1980.44.4.773> (cit. on pp. 4, viii)

- Cheng, J. (2009). *The principles of astronomical telescope design* (Vol. 360). Springer. <https://doi.org/10.1007/b105475>. (Cit. on p. 56)
- Cheyne, D., Bells, S., Ferrari, P., Gaetz, W., & Bostan, A. C. (2008). Self-paced movements induce high-frequency gamma oscillations in primary motor cortex. *Neuroimage*, *42*(1), 332–342. <https://doi.org/10.1016/j.neuroimage.2008.04.178> (cit. on pp. 4, 25, vii)
- Chicone, C. (1999). *Ordinary differential equations with applications*, Springer. (Cit. on p. 27).
- Churchland, M. M., Santhanam, G., & Shenoy, K. V. (2006). Preparatory activity in premotor and motor cortex reflects the speed of the upcoming reach. *Journal of neurophysiology*, *96*(6), 3130–3146. <https://doi.org/10.1152/jn.00307.2006> (cit. on pp. 4, viii)
- Cohen, M. X. (2014). *Analyzing neural time series data: Theory and practice*. MIT press. (Cit. on pp. 1, 32, v).
- Conway, B., Halliday, D., Farmer, S., Shahani, U., Maas, P., Weir, A., & Rosenberg, J. (1995). Synchronization between motor cortex and spinal motoneuronal pool during the performance of a maintained motor task in man. *The Journal of physiology*, *489*(3), 917–924. <https://doi.org/10.1113/jphysiol.1995.sp021104> (cit. on pp. 4, viii)
- Cooray, G. K., Sengupta, B., Douglas, P. K., & Friston, K. (2016). Dynamic causal modelling of electrographic seizure activity using bayesian belief updating. *NeuroImage*, *125*, 1142–1154. <https://doi.org/10.1016/J.NEUROIMAGE.2015.07.063> (cit. on pp. 6, x)
- Cox, D. R., & Miller, H. D. (2017). *The theory of stochastic processes*. Routledge. (Cit. on pp. 6, 48, 54, ix).
- D'Angelo, E., & Jirsa, V. (2022). The quest for multiscale brain modeling. *Trends in Neurosciences*. <https://doi.org/10.1016/J.TINS.2022.06.007> (cit. on pp. 3, 92, vii)
- David, O., & Friston, K. J. (2003). A neural mass model for meg/eeg:: Coupling and neuronal dynamics. *NeuroImage*, *20*(3), 1743–1755. <https://doi.org/10.1016/j.neuroimage.2003.07.015> (cit. on pp. 7, 87, x)
- David, O., Kiebel, S. J., Harrison, L. M., Mattout, J., Kilner, J. M., & Friston, K. J. (2006). Dynamic causal modeling of evoked responses in eeg and meg. *NeuroImage*, *30*(4), 1255–1272. <https://doi.org/10.1016/j.neuroimage.2005.10.045> (cit. on p. 88)
- De Luca, C. J., Gilmore, L. D., Kuznetsov, M., & Roy, S. H. (2010). Filtering the surface emg signal: Movement artifact and baseline noise contamination. *Journal of biomechanics*, *43*(8), 1573–1579. <https://doi.org/10.1016/j.jbiomech.2010.01.027> (cit. on p. 32)
- Desplenter, T., & Trejos, A. L. (2018). Evaluating muscle activation models for elbow motion estimation. *Sensors*, *18*(4), 1004. <https://doi.org/10.3390/s18041004> (cit. on pp. 83, 117)
- Olver, F. W. J., Daalhuis, A. B. O., Lozier, D. W., Schneider, B. I., Boisvert, R. F., Clark, C. W., B. R. Mille and, B. V. S., Cohl, H. S., & M. A. McClain, e. (2020). Nist Digital Library of Mathematical Functions. <http://dlmf.nist.gov/>. (Cit. on p. 98)
- Donges, J. F., Heitzig, J., Beronov, B., Wiedermann, M., Runge, J., Feng, Q. Y., Tupikina, L., Stolbova, V., Donner, R. V., Marwan, N., Et al. (2015). Unified functional network and nonlinear time series analysis for complex systems science: The pyunicorn package.

- Chaos: An Interdisciplinary Journal of Nonlinear Science*, 25(11), 113101. <https://doi.org/10.1063/1.4934554> (cit. on p. 21)
- Drillis, R., Contini, R., & Bluestein, M. (1964). Body segment parameters. *Artificial limbs*, 8(1), 44–66. <https://doi.org/10.5040/9781492595809.ch-003> (cit. on pp. 76, 116)
- Eckmann, J.-P., Kamphorst, S. O., & Ruelle, D. (1987). Recurrence plots of dynamical systems. *EPL (Europhysics Letters)*, 4(9), 973. <https://doi.org/10.1209/0295-5075/4/9/004> (cit. on pp. 10, 20)
- Eckmann, J.-P., & Ruelle, D. (1985). Ergodic theory of chaos and strange attractors. In *The theory of chaotic attractors* (pp. 273–312). Springer. https://doi.org/10.1007/978-0-387-21830-4_17. (Cit. on pp. 10, 12, 14, 16, 19)
- Elbert, T., Ray, W. J., Kowalik, Z. J., Skinner, J. E., Graf, K. E., & Birbaumer, N. (1994). Chaos and physiology: Deterministic chaos in excitable cell assemblies. *Physiological reviews*, 74(1), 1–47. <https://doi.org/10.1152/physrev.1994.74.1.1> (cit. on p. 27)
- Erdogmus, D., & Principe, J. C. (2006). From linear adaptive filtering to nonlinear information processing—the design and analysis of information processing systems. *IEEE Signal Processing Magazine*, 23(6), 14–33. <https://doi.org/10.1109/SP-M.2006.248709> (cit. on p. 10)
- Farina, D., Fattorini, L., Felici, F., & Filligoi, G. (2002). Nonlinear surface emg analysis to detect changes of motor unit conduction velocity and synchronization. *Journal of Applied Physiology*, 93(5), 1753–1763. <https://doi.org/10.1152/jappphysiol.00314.2002> (cit. on p. 41)
- Faure, P., & Korn, H. (1998). A new method to estimate the Kolmogorov entropy from recurrence plots: Its application to neuronal signals. *Physica D: Nonlinear Phenomena*, 122(1-4), 265–279. [https://doi.org/10.1016/s0167-2789\(98\)00177-8](https://doi.org/10.1016/s0167-2789(98)00177-8) (cit. on pp. 10, 20–22)
- Faure, P., & Korn, H. (2001). Is there chaos in the brain? I. Concepts of nonlinear dynamics and methods of investigation. *Comptes Rendus de l'Académie des Sciences-Series III-Sciences de la Vie*, 324(9), 773–793. [https://doi.org/10.1016/S0764-4469\(01\)01377-4](https://doi.org/10.1016/S0764-4469(01)01377-4) (cit. on p. 9)
- Faure, P., & Lesne, A. (2015). Estimating Kolmogorov entropy from recurrence plots. In *Recurrence quantification analysis* (pp. 45–63). Springer. https://doi.org/10.1007/978-3-319-07155-8_2. (Cit. on p. 21)
- Fieller, E. C., Hartley, H. O., & Pearson, E. S. (1957). Tests for rank correlation coefficients. i. *Biometrika*, 44(3/4), 470–481. <https://doi.org/10.2307/2332878> (cit. on p. 49)
- Fisher, R. A. (1915). Frequency distribution of the values of the correlation coefficient in samples from an indefinitely large population. *Biometrika*, 10(4), 507–521. <https://doi.org/10.2307/2331838> (cit. on p. 49)
- Fisher, R. A. (1921). On the 'probable error' of a coefficient of correlation deduced from a small sample. *Metron*, 1, 1–32. <https://doi.org/10.2307/2331798> (cit. on p. 49)

- Fraser, A. M., & Swinney, H. L. (1986). Independent coordinates for strange attractors from mutual information. *Physical review A*, 33(2), 1134. <https://doi.org/10.1103/physreva.33.1134> (cit. on pp. 2, 15, vi)
- Freeman, W. J. (2003). Evidence from human scalp electroencephalograms of global chaotic itinerancy. *Chaos: An Interdisciplinary Journal of Nonlinear Science*, 13(3), 1067–1077. <https://doi.org/10.1063/1.1596553> (cit. on p. 9)
- Friston, K. (2009). The free-energy principle: A rough guide to the brain? *Trends in Cognitive Sciences*, 13, 293–301. <https://doi.org/10.1016/j.tics.2009.04.005> (cit. on p. 93)
- Friston, K. (2010). The free-energy principle: A unified brain theory? *Nature reviews neuroscience*, 11(2), 127–138. <https://doi.org/10.1038/nrn2787> (cit. on p. 93)
- Friston, K. (2019). A free energy principle for a particular physics. *arXiv preprint arXiv:1906.10184*. <https://doi.org/10.48550/arXiv.1906.10184> (cit. on p. 80)
- Friston, K., & Ao, P. (2012). Free energy, value, and attractors. *Computational and mathematical methods in medicine*, 2012. <https://doi.org/10.1155/2012/937860> (cit. on p. 80)
- Friston, K., Stephan, K., Li, B., & Daunizeau, J. (2010). Generalised filtering. *Mathematical Problems in Engineering*, 2010. <https://doi.org/10.1155/2010/621670> (cit. on pp. 71, 82)
- Friston, K. J. (2011). Functional and effective connectivity: A review. *Brain connectivity*, 1(1), 13–36. <https://doi.org/10.1089/brain.2011.0008> (cit. on pp. 7, x)
- Friston, K. J., Holmes, A. P., Worsley, K. J., Poline, J.-P., Frith, C. D., & Frackowiak, R. S. (1994). Statistical parametric maps in functional imaging: A general linear approach. *Human brain mapping*, 2(4), 189–210. <https://doi.org/10.1002/hbm.460020402> (cit. on p. 33)
- Friston, K. J., Litvak, V., Oswal, A., Razi, A., Stephan, K. E., Van Wijk, B. C., Ziegler, G., & Zeidman, P. (2016). Bayesian model reduction and empirical bayes for group (dcm) studies. *Neuroimage*, 128, 413–431. <https://doi.org/10.1016/j.neuroimage.2015.11.015> (cit. on pp. 87, 93)
- Friston, K. J., Trujillo-Barreto, N., & Daunizeau, J. (2008). Dem: A variational treatment of dynamic systems. *Neuroimage*, 41(3), 849–885. <https://doi.org/10.1016/j.neuroimage.2008.02.054> (cit. on pp. 7, 54, 67, 69, 72, 73, 82, xi)
- Gelman, A., & Hill, J. (2006). *Data analysis using regression and multilevel/hierarchical models*. Cambridge university press. (Cit. on p. 34).
- Georgopoulos, A. P., Ashe, J., Smyrnis, N., & Taira, M. (1992). The motor cortex and the coding of force. *Science*, 256(5064), 1692–1695. <https://doi.org/10.1126/science.256.5064.1692> (cit. on pp. 4, 25, viii)
- Georgopoulos, A. P., Langheim, F. J., Leuthold, A. C., & Merkle, A. N. (2005). Magnetoencephalographic signals predict movement trajectory in space. *Experimental brain research*, 167(1), 132–135. <https://doi.org/10.1007/s00221-005-0028-8> (cit. on pp. 3, vii)

- Georgopoulos, A. P., Schwartz, A. B., & Kettner, R. E. (1986). Neuronal population coding of movement direction. *Science*, 233(4771), 1416–1419. <https://doi.org/10.1126/science.3749885> (cit. on pp. 3, vii)
- Gergondet, P., Druon, S., Kheddar, A., Hintermüller, C., Guger, C., & Slater, M. (2011). Using brain-computer interface to steer a humanoid robot, In *2011 IEEE International Conference on Robotics and Biomimetics*. IEEE. <https://doi.org/10.1109/robio.2011.6181284>. (Cit. on pp. 3, vii)
- Ghahramani, Z., & Hinton, G. E. (1996). Parameter estimation for linear dynamical systems (cit. on p. 61).
- Ghil, M., Chekroun, M. D., & Simonnet, E. (2008). Climate dynamics and fluid mechanics: Natural variability and related uncertainties. *Physica D: Nonlinear Phenomena*, 237(14-17), 2111–2126. <https://doi.org/10.1016/j.physd.2008.03.036> (cit. on p. 9)
- Ginovyan, M. S., & Sahakyan, A. A. (2013). On the trace approximations of products of Toeplitz matrices. *Statistics & Probability Letters*, 83(3), 753–760. <https://doi.org/10.1016/j.spl.2012.11.019> (cit. on p. 53)
- Goldstein, H. (1980). *Classical mechanics*. Addison-Wesley. <https://doi.org/10.1002/0471654817.ch3>. (Cit. on p. 78)
- Gramfort, A., Luessi, M., Larson, E., Engemann, D. A., Strohmeier, D., Brodbeck, C., Goj, R., Jas, M., Brooks, T., Parkkonen, L., & Hämäläinen, M. S. (2013). MEG and EEG data analysis with MNE-Python. *Frontiers in Neuroscience*, 7(267), 1–13. <https://doi.org/10.3389/fnins.2013.00267> (cit. on p. 31)
- Grassberger, P., & Procaccia, I. (1983a). Characterization of strange attractors. *Physical review letters*, 50(5), 346. <https://doi.org/10.1007/bfb0091924> (cit. on pp. 10, 11, 15)
- Grassberger, P., & Procaccia, I. (1983b). Estimation of the Kolmogorov entropy from a chaotic signal. *Physical review A*, 28(4), 2591. <https://doi.org/10.1103/physreva.28.2591> (cit. on pp. 10, 20)
- Grassberger, P., & Procaccia, I. (2004). Measuring the strangeness of strange attractors. In *The theory of chaotic attractors* (pp. 170–189). Springer. https://doi.org/10.1007/978-0-387-21830-4_12. (Cit. on p. 19)
- Gray, R. M. Et al. (2006). Toeplitz and circulant matrices: A review. *Foundations and Trends® in Communications and Information Theory*, 2(3), 155–239. <https://doi.org/10.1561/9781933019680> (cit. on pp. 48, 52, 53)
- Grendár, M., Majerová, J., & Špitalský, V. (2013). Strong laws for recurrence quantification analysis. *International Journal of Bifurcation and Chaos*, 23(08), 1350147. <https://doi.org/10.1142/s0218127413501472> (cit. on pp. 10, 20)
- Grimbert, F., & Faugeras, O. (2006). *Analysis of jansen's model of a single cortical column* (Doctoral dissertation). INRIA. (Cit. on p. 87).
- Guckenheimer, J., & Holmes, P. (2013). *Nonlinear oscillations, dynamical systems, and bifurcations of vector fields* (Vol. 42). Springer Science & Business Media. (Cit. on p. 27).

- Gunduz, A., & Principe, J. C. (2009). Correntropy as a novel measure for nonlinearity tests. *Signal Processing*, 89(1), 14–23. <https://doi.org/10.1016/j.sigpro.2008.07.005> (cit. on p. 10)
- Haken, H. (1978). *Synergetics: Self-organization and clinical psychology*. Springer. <https://doi.org/10.1007/978-3-642-96469-5>. (Cit. on pp. 3, 28, vii)
- Haken, H. (2006). Synergetics of brain function. *International journal of psychophysiology*, 60(2), 110–124. <https://doi.org/10.1016/j.ijpsycho.2005.12.006> (cit. on pp. 3, 28, 92, vii)
- Haken, H. (2013). *Principles of brain functioning: A synergetic approach to brain activity, behavior and cognition* (Vol. 67). Springer Science & Business Media. (Cit. on pp. 3, vii).
- Haken, H., Kelso, J. S., & Bunz, H. (1985). A theoretical model of phase transitions in human hand movements. *Biological cybernetics*, 51(5), 347–356. <https://doi.org/10.1007/bf00336922> (cit. on pp. 3, 28, 92, vii)
- Hang, H., Steinwart, I., Feng, Y., & Suykens, J. A. (2018). Kernel density estimation for dynamical systems. *The Journal of Machine Learning Research*, 19(1), 1260–1308. <https://doi.org/10.5555/3291125.3291160> (cit. on pp. 10, 11)
- Hao, M., He, X., Xiao, Q., Alstermark, B., & Lan, N. (2013). Corticomuscular transmission of tremor signals by propriospinal neurons in parkinson's disease. <https://doi.org/10.1371/journal.pone.0079829> (cit. on pp. 67, 84)
- Hasson, U., Landesman, O., Knappmeyer, B., Vallines, I., Rubin, N., & Heeger, D. J. (2008). Neurocinematics: The neuroscience of film. *Projections*, 2, 1–26. <https://doi.org/10.3167/PROJ.2008.020102> (cit. on p. 91)
- Hasson, U., Nir, Y., Levy, I., Fuhrmann, G., & Malach, R. (2004). Intersubject synchronization of cortical activity during natural vision. *science*, 303(5664), 1634–1640. <https://doi.org/10.1126/science.1089506> (cit. on p. 91)
- Hénon, M. (1976). A two-dimensional mapping with a strange attractor. In *The theory of chaotic attractors* (pp. 94–102). Springer. https://doi.org/10.1007/978-0-387-21830-4_8. (Cit. on p. 15)
- Hill, A. V. (1938). The heat of shortening and the dynamic constants of muscle. *Proceedings of the Royal Society of London. Series B-Biological Sciences*, 126(843), 136–195. <https://doi.org/10.1098/rspb.1938.0050> (cit. on pp. 7, 67, 83, x)
- Hotelling, H. (1953). New light on the correlation coefficient and its transforms. *Journal of the Royal Statistical Society. Series B (Methodological)*, 15(2), 193–232. <https://doi.org/10.1111/j.2517-6161.1953.tb00135.x> (cit. on p. 49)
- Jafarian, A., Zeidman, P., Wykes, R. C., Walker, M., & Friston, K. J. (2021). Adiabatic dynamic causal modelling. *NeuroImage*, 238, 118243. <https://doi.org/10.1016/j.neuroimage.2021.118243> (cit. on pp. 87, 88)
- Jansen, B. H., & Rit, V. G. (1995). Electroencephalogram and visual evoked potential generation in a mathematical model of coupled cortical columns. *Biological cybernetics*, 73(4), 357–366. <https://doi.org/10.1007/bf00199471> (cit. on pp. 87, 88)

- Jeong, J.-H., Shim, K.-H., Kim, D.-J., & Lee, S.-W. (2019). Trajectory decoding of arm reaching movement imageries for brain-controlled robot arm system, In *2019 41st annual international conference of the IEEE engineering in medicine and biology society (embc)*. IEEE. <https://doi.org/10.1109/embc.2019.8856312>. (Cit. on p. 66)
- Jirsa, V. K., Stacey, W. C., Quilichini, P. P., Ivanov, A. I., & Bernard, C. (2014). On the nature of seizure dynamics. *Brain*, *137*, 2210–2230. <https://doi.org/10.1093/BRAIN/AWU133> (cit. on pp. 6, 92, x)
- Jones, M. C., Marron, J. S., & Sheather, S. J. (1996). A brief survey of bandwidth selection for density estimation. *Journal of the American statistical association*, *91*(433), 401–407. <https://doi.org/10.1080/01621459.1996.10476701> (cit. on pp. 10, 11)
- Takei, S., Hoffman, D. S., & Strick, P. L. (1999). Muscle and movement representations in the primary motor cortex. *Science*, *285*(5436), 2136–2139. <https://doi.org/10.1126/science.285.5436.2136> (cit. on pp. 4, viii)
- Takei, S., Hoffman, D. S., & Strick, P. L. (2001). Direction of action is represented in the ventral premotor cortex. *Nature neuroscience*, *4*(10), 1020–1025. <https://doi.org/10.1038/nn726> (cit. on pp. 4, viii)
- Kalman, R. E. (1960). A new approach to linear filtering and prediction problems. *Transactions of the ASME—Journal of Basic Engineering*, *82*(Series D), 35–45 (cit. on p. 68).
- Kannathal, N., Choo, M. L., Acharya, U. R., & Sadasivan, P. (2005). Entropies for detection of epilepsy in eeg. *Computer methods and programs in biomedicine*, *80*(3), 187–194. <https://doi.org/10.1016/j.cmpb.2005.06.012> (cit. on p. 23)
- Kantz, H., & Schreiber, T. (2004). *Nonlinear time series analysis* (Vol. 7). Cambridge university press. https://doi.org/10.1007/springerreference_205493. (Cit. on p. 15)
- Kaplan, D., & Glass, L. (1997). *Understanding nonlinear dynamics*. Springer Science & Business Media. (Cit. on pp. 1, v).
- Kerr, W. C., & Graham, A. (2000). Generalized phase space version of langevin equations and associated fokker-planck equations. *The European Physical Journal B-Condensed Matter and Complex Systems*, *15*(2), 305–311. <https://doi.org/10.1007/s100510051129> (cit. on p. 80)
- Kiebel, S. J., Daunizeau, J., & Friston, K. J. (2008). A hierarchy of time-scales and the brain. *PLoS computational biology*, *4*(11), e1000209. <https://doi.org/10.1371/journal.pcbi.1000209> (cit. on pp. 3, 28, vii)
- Kiebel, S. J., Poline, J.-B., Friston, K. J., Holmes, A. P., & Worsley, K. J. (1999). Robust smoothness estimation in statistical parametric maps using standardized residuals from the general linear model. *Neuroimage*, *10*(6), 756–766. <https://doi.org/10.1006/nimg.1999.0508> (cit. on p. 56)
- Kiebel, S. J., Tallon-Baudry, C., & Friston, K. J. (2005). Parametric analysis of oscillatory activity as measured with eeg/meg. *Human brain mapping*, *26*(3), 170–177. <https://doi.org/10.1002/hbm.20153> (cit. on p. 33)

- Kim, J.-H., Bießmann, F., & Lee, S.-W. (2014). Decoding three-dimensional trajectory of executed and imagined arm movements from electroencephalogram signals. *IEEE Transactions on Neural Systems and Rehabilitation Engineering*, 23(5), 867–876. <https://doi.org/10.1109/tnsre.2014.2375879> (cit. on pp. 61, 66)
- Kobler, R. J., Almeida, I., Sburlea, A. I., & Müller-Putz, G. R. (2020). Using machine learning to reveal the population vector from eeg signals. *Journal of Neural Engineering*, 17(2), 026002. <https://doi.org/10.1088/1741-2552/ab7490> (cit. on p. 66)
- Kobler, R. J., Sburlea, A. I., Mondini, V., Hirata, M., & Müller-Putz, G. R. (2020). Distance-and speed-informed kinematics decoding improves m/eeg based upper-limb movement decoder accuracy. *Journal of Neural Engineering*, 17(5), 056027. <https://doi.org/10.1088/1741-2552/abb3b3> (cit. on p. 66)
- Kolmogorov, A. N. (1985). A new metric invariant of transitive dynamical systems and automorphisms of Lebesgue spaces. *Trudy Matematicheskogo Instituta imeni VA Steklova*, 169, 94–98 (cit. on p. 20).
- Korik, A., Sosnik, R., Siddique, N., & Coyle, D. (2016). Imagined 3d hand movement trajectory decoding from sensorimotor eeg rhythms, In *2016 IEEE International Conference on Systems, Man, and Cybernetics (SMC)*. IEEE. <https://doi.org/10.1109/smc.2016.7844955>. (Cit. on p. 66)
- Korik, A., Sosnik, R., Siddique, N., & Coyle, D. (2018). Decoding imagined 3d hand movement trajectories from eeg: Evidence to support the use of mu, beta, and low gamma oscillations. *Frontiers in neuroscience*, 12, 130 (cit. on p. 66).
- Korn, H., & Faure, P. (2003). Is there chaos in the brain? ii. experimental evidence and related models. *Comptes rendus biologiques*, 326(9), 787–840. <https://doi.org/10.1016/j.crv.2003.09.011> (cit. on pp. 1, v)
- Kraemer, K. H., Donner, R. V., Heitzig, J., & Marwan, N. (2018). Recurrence threshold selection for obtaining robust recurrence characteristics in different embedding dimensions. *Chaos: An Interdisciplinary Journal of Nonlinear Science*, 28(8), 085720. <https://doi.org/10.1063/1.5024914> (cit. on pp. 23, 24)
- Krakauer, J. W., Ghazanfar, A. A., Gomez-Marin, A., MacIver, M. A., & Poeppel, D. (2017). Neuroscience needs behavior: Correcting a reductionist bias. *Neuron*, 93, 480–490. <https://doi.org/10.1016/j.neuron.2016.12.041> (cit. on p. 91)
- Krause, F., & Lindemann, O. (2014). Expyriment: A python library for cognitive and neuroscientific experiments. *Behavior Research Methods*, 46(2), 416–428. <https://doi.org/10.3758/s13428-013-0390-6> (cit. on p. 30)
- Lee, J. M. (2013). Smooth maps. In *Introduction to smooth manifolds* (pp. 32–49). Springer. https://doi.org/10.1007/0-387-22739-3_6. (Cit. on p. 115)
- Lee, T.-W., Girolami, M., & Sejnowski, T. J. (1999). Independent component analysis using an extended infomax algorithm for mixed subgaussian and supergaussian sources. *Neural computation*, 11(2), 417–441. <https://doi.org/10.1162/089976699300016719> (cit. on p. 32)

- Lehnertz, K. (1999). Non-linear time series analysis of intracranial eeg recordings in patients with epilepsy—an overview. *International Journal of Psychophysiology*, 34(1), 45–52. [https://doi.org/10.1016/s0167-8760\(99\)00043-4](https://doi.org/10.1016/s0167-8760(99)00043-4) (cit. on pp. 1, v)
- Lesne, A. (2013). Multiscale analysis of biological systems. *Acta Biotheoretica*, 61(1), 3–19. <https://doi.org/10.1007/s10441-013-9170-z> (cit. on pp. 3, 28, 92, vii)
- Li, S., Zhuang, C., Hao, M., He, X., Marquez, J. C., Niu, C. M., & Lan, N. (2015). Coordinated alpha and gamma control of muscles and spindles in movement and posture. *Frontiers in Computational Neuroscience*, 9. <https://doi.org/10.3389/FNCOM.2015.00122> (cit. on pp. 7, 67, 84, 85, 118, x)
- Liu, J., Sheng, Y., & Liu, H. (2019). Corticomuscular coherence and its applications: A review. *Frontiers in human neuroscience*, 13, 100. <https://doi.org/10.3389/fnhum.2019.00100> (cit. on p. 25)
- Logothetis, N. K. (2002). The neural basis of the blood–oxygen–level–dependent functional magnetic resonance imaging signal. *Philosophical Transactions of the Royal Society of London. Series B: Biological Sciences*, 357(1424), 1003–1037. <https://doi.org/10.1098/rstb.2002.1114> (cit. on p. 56)
- Lorenz, E. N. (1963). Deterministic nonperiodic flow. *Journal of the atmospheric sciences*, 20(2), 130–141. <https://doi.org/10.1201/9780203734636-38> (cit. on p. 15)
- Maguire, E. A. (2012). Studying the freely-behaving brain with fmri. *NeuroImage*, 62, 1170–1176. <https://doi.org/10.1016/J.NEUROIMAGE.2012.01.009> (cit. on p. 91)
- Martínez-Cagigal, V., Kobler, R. J., Mondini, V., Hornero, R., & Muller-Putz, G. R. (2020). Non-linear online low-frequency eeg decoding of arm movements during a pursuit tracking task, In *2020 42nd annual international conference of the ieee engineering in medicine & biology society (embc)*. IEEE. <https://doi.org/10.1109/embc44109.2020.9175723>. (Cit. on p. 66)
- Marwan, N., Romano, M. C., Thiel, M., & Kurths, J. (2007). Recurrence plots for the analysis of complex systems. *Physics reports*, 438(5-6), 237–329. <https://doi.org/10.1016/j.physrep.2006.11.001> (cit. on p. 10)
- McMenamin, B. W., Shackman, A. J., Greischar, L. L., & Davidson, R. J. (2011). Electromyogenic artifacts and electroencephalographic inferences revisited. *NeuroImage*, 54(1), 4–9. <https://doi.org/10.1016/j.neuroimage.2010.07.057> (cit. on p. 32)
- Medrano, J., Kheddar, A., Lesne, A., & Ramdani, S. (2021). Radius selection using kernel density estimation for the computation of nonlinear measures. *Chaos: An Interdisciplinary Journal of Nonlinear Science*, 31(8), 083131. <https://doi.org/10.1063/5.0055797> (cit. on p. 9)
- Miller, K. J., Leuthardt, E. C., Schalk, G., Rao, R. P., Anderson, N. R., Moran, D. W., Miller, J. W., & Ojemann, J. G. (2007). Spectral changes in cortical surface potentials during motor movement. *Journal of Neuroscience*, 27(9), 2424–2432. <https://doi.org/10.1523/jneurosci.3886-06.2007> (cit. on p. 25)

- Mima, T., & Hallett, M. (1999). Corticomuscular coherence: A review. *Journal of clinical neurophysiology*, 16(6), 501. <https://doi.org/10.1097/00004691-199911000-00002> (cit. on pp. 4, 25, viii)
- Mondini, V., Kobler, R. J., Sburlea, A. I., & Müller-Putz, G. R. (2020). Continuous low-frequency eeg decoding of arm movement for closed-loop, natural control of a robotic arm. *Journal of Neural Engineering*, 17(4), 046031. <https://doi.org/10.1088/1741-2552/aba6f7> (cit. on p. 66)
- Moon, Y.-I., Rajagopalan, B., & Lall, U. (1995). Estimation of mutual information using kernel density estimators. *Phys. Rev. E*, 52, 2318–2321. <https://doi.org/10.1103/PhysRevE.52.2318> (cit. on p. 10)
- Moran, R. (2015). State space models and their spectral decomposition in dynamic causal modeling. *Advanced State Space Methods for Neural and Clinical Data*, 114. <https://doi.org/10.1017/cbo9781139941433.006> (cit. on p. 87)
- Moran, R. J., Kiebel, S. J., Stephan, K. E., Reilly, R. B., Daunizeau, J., & Friston, K. J. (2007). A neural mass model of spectral responses in electrophysiology. *NeuroImage*, 37(3), 706–720. <https://doi.org/10.1016/j.neuroimage.2007.05.032> (cit. on pp. 87, 88, 119)
- Müller-Putz, G. R., Mondini, V., Martíñez-Cagigal, V., Kobler, R. J., Pereira, J., Dias, C. L., Hehenberger, L., & Sburlea, A. I. (2021). Decoding of continuous movement attempt in 2-dimensions from non-invasive low frequency brain signals, In *2021 10th international ieee/embs conference on neural engineering (ner)*. IEEE. <https://doi.org/10.1109/ner49283.2021.9441346>. (Cit. on p. 66)
- Murray, W. M., Delp, S. L., & Buchanan, T. S. (1995). Variation of muscle moment arms with elbow and forearm position. *Journal of biomechanics*, 28(5), 513–525. [https://doi.org/10.1016/0021-9290\(94\)00114-j](https://doi.org/10.1016/0021-9290(94)00114-j) (cit. on p. 76)
- Muthukumaraswamy, S. D. (2013). High-frequency brain activity and muscle artifacts in meg/eeg: A review and recommendations. *Frontiers in human neuroscience*, 7, 138. <https://doi.org/10.3389/fnhum.2013.00138> (cit. on p. 32)
- Nastase, S. A., Goldstein, A., & Hasson, U. (2020). Keep it real: Rethinking the primacy of experimental control in cognitive neuroscience. *NeuroImage*, 222, 117254. <https://doi.org/10.31234/osf.io/whn6d> (cit. on p. 91)
- Neyman, J., & Pearson, E. S. (1933). IX. on the problem of the most efficient tests of statistical hypotheses. *Philosophical Transactions of the Royal Society of London. Series A, Containing Papers of a Mathematical or Physical Character*, 231(694-706), 289–337. <https://doi.org/10.1098/rsta.1933.0009> (cit. on p. 92)
- Nishimoto, S., Vu, A. T., Naselaris, T., Benjamini, Y., Yu, B., & Gallant, J. L. (2011). Reconstructing visual experiences from brain activity evoked by natural movies. *Current biology*, 21(19), 1641–1646. <https://doi.org/10.1016/j.cub.2011.08.031> (cit. on p. 91)
- Ocak, H. (2008). Optimal classification of epileptic seizures in EEG using wavelet analysis and genetic algorithm. *Signal processing*, 88(7), 1858–1867. <https://doi.org/10.1016/j.sigpro.2008.01.026> (cit. on p. 22)

- Ocak, H. (2009). Automatic detection of epileptic seizures in eeg using discrete wavelet transform and approximate entropy. *Expert Systems with Applications*, 36(2), 2027–2036. <https://doi.org/10.1016/j.eswa.2007.12.065> (cit. on pp. 2, vi)
- Ofner, P., & Müller-Putz, G. R. (2012). Decoding of velocities and positions of 3d arm movement from eeg, In *2012 annual international conference of the ieee engineering in medicine and biology society*. IEEE. <https://doi.org/10.1109/embc.2012.6347460>. (Cit. on pp. 5, 6, 61, 66, ix, x)
- Olbrich, S., Jödicke, J., Sander, C., Himmerich, H., & Hegerl, U. (2011). Ica-based muscle artefact correction of eeg data: What is muscle and what is brain?: Comment on mcme-namin et al. *Neuroimage*, 54(1), 1–3. <https://doi.org/10.1016/j.neuroimage.2010.04.256> (cit. on p. 32)
- Ott, E. (2002). *Chaos in dynamical systems*. Cambridge university press. <https://doi.org/10.1017/cbo9780511803260>. (Cit. on pp. 9, 11, 14, 15)
- Ozaki, T. (1992). A bridge between nonlinear time series models and nonlinear stochastic dynamical systems: A local linearization approach. *Statistica Sinica*, 113–135 (cit. on pp. 72, 73).
- Papadopoulou, M., Leite, M., van Mierlo, P., Vonck, K., Lemieux, L., Friston, K., & Marinazzo, D. (2015). Tracking slow modulations in synaptic gain using dynamic causal modelling: Validation in epilepsy. *NeuroImage*, 107, 117–126. <https://doi.org/10.1016/J.NEUROIMAGE.2014.12.007> (cit. on pp. 6, x)
- Parr, T. (2019). *The computational neurology of active vision* (Doctoral dissertation). UCL (University College London). (Cit. on p. 93).
- Parr, T., Mirza, M. B., Cagnan, H., & Friston, K. J. (2019). Dynamic causal modelling of active vision. *Journal of Neuroscience*, 39(32), 6265–6275. <https://doi.org/10.1523/jneurosci.2459-18.2019> (cit. on p. 93)
- Parr, T., Pezzulo, G., & Friston, K. J. (2022). *Active inference: The free energy principle in mind, brain, and behavior*. MIT Press. (Cit. on pp. 82, 93).
- Parr, T., Sajid, N., Da Costa, L., Mirza, M. B., & Friston, K. J. (2021). Generative models for active vision. *Frontiers in Neurobotics*, 15, 34. <https://doi.org/10.3389/fnbot.2021.651432> (cit. on p. 93)
- Penny, W. D., Friston, K. J., Ashburner, J. T., Kiebel, S. J., & Nichols, T. E. (2011). *Statistical parametric mapping: The analysis of functional brain images*. Elsevier. (Cit. on pp. 6, 26, 33, 34, 48, 56, x).
- Pesin, Y. B. (2008). *Dimension theory in dynamical systems: Contemporary views and applications*. University of Chicago Press. <https://doi.org/10.7208/chicago/9780226662237.001.0001>. (Cit. on pp. 11, 14)
- Pfurtscheller, G., Brunner, C., Schlögl, A., & Da Silva, F. L. (2006). Mu rhythm (de) synchronization and eeg single-trial classification of different motor imagery tasks. *NeuroImage*, 31(1), 153–159. <https://doi.org/10.1016/j.neuroimage.2005.12.003> (cit. on p. 32)

- Pincus, S. M. (1991). Approximate entropy as a measure of system complexity. *Proceedings of the National Academy of Sciences*, 88(6), 2297–2301. <https://doi.org/10.1073/pnas.88.6.2297> (cit. on pp. 10, 20, 23, 24)
- Pitsik, E., Frolov, N., Hauke Kraemer, K., Grubov, V., Maksimenko, V., Kurths, J., & Hramov, A. (2020). Motor execution reduces eeg signals complexity: Recurrence quantification analysis study. *Chaos: An Interdisciplinary Journal of Nonlinear Science*, 30(2), 023111. <https://doi.org/10.1063/1.5136246> (cit. on pp. 5, 32, 33, 40, 41, 43, viii)
- Polyn, S. M., Natu, V. S., Cohen, J. D., & Norman, K. A. (2005). Category-specific cortical activity precedes retrieval during memory search. *Science*, 310, 1963–1966. https://doi.org/10.1126/SCIENCE.1117645/SUPPL_FILE/POLYN.SOM.PDF (cit. on p. 91)
- Principe, J. C. (2010). *Information theoretic learning: Renyi's entropy and kernel perspectives*. Springer Science & Business Media. <https://doi.org/10.1007/978-1-4419-1570-2>. (Cit. on p. 10)
- Prochazka, A. (1999). Quantifying proprioception. *Progress in brain research*, 123, 133–142. [https://doi.org/10.1016/s0079-6123\(08\)62850-2](https://doi.org/10.1016/s0079-6123(08)62850-2) (cit. on p. 84)
- Pyper, B. J., & Peterman, R. M. (1998). Comparison of methods to account for autocorrelation in correlation analyses of fish data. *Canadian Journal of Fisheries and Aquatic Sciences*, 55(9), 2127–2140. <https://doi.org/10.1139/f98-104> (cit. on pp. 47, 52, 58)
- Quenouille, M. H. (1947). Notes on the calculation of autocorrelations of linear autoregressive schemes. *Biometrika*, 34(3/4), 365–367. <https://doi.org/10.2307/2332450> (cit. on pp. 47, 48, 51)
- R Core Team. (2022). *R: A language and environment for statistical computing*. R Foundation for Statistical Computing. Vienna, Austria. <https://www.R-project.org/>. (Cit. on p. 49)
- Ramdani, S., Bouchara, F., Lagarde, J., & Lesne, A. (2016). Recurrence plots of discrete-time gaussian stochastic processes. *Physica D: Nonlinear Phenomena*, 330, 17–31. <https://doi.org/10.1016/j.physd.2016.04.017> (cit. on p. 93)
- Ramdani, S., Bouchara, F., & Lesne, A. (2018). Probabilistic analysis of recurrence plots generated by fractional gaussian noise. *Chaos: An Interdisciplinary Journal of Nonlinear Science*, 28(8), 085721. <https://doi.org/10.1063/1.5030522> (cit. on p. 93)
- Ramdani, S., Boyer, A., Caron, S., Bonnetblanc, F., Bouchara, F., Duffau, H., & Lesne, A. (2021). Parametric recurrence quantification analysis of autoregressive processes for pattern recognition in multichannel electroencephalographic data. *Pattern Recognition*, 109, 107572. <https://doi.org/10.1016/j.patcog.2020.107572> (cit. on p. 93)
- Rauch, H. E., Tung, F., & Striebel, C. T. (1965). Maximum likelihood estimates of linear dynamic systems. *AIAA journal*, 3(8), 1445–1450. <https://doi.org/10.2514/3.3166> (cit. on p. 73)
- Rice, S. O. (1944). Mathematical analysis of random noise. *The Bell System Technical Journal*, 23(3), 282–332. <https://doi.org/10.1002/j.1538-7305.1944.tb00874.x> (cit. on pp. 6, 48, 54, ix)
- Richman, J. S., & Moorman, J. R. (2000). Physiological time-series analysis using approximate entropy and sample entropy. *American Journal of Physiology-Heart and Circulatory Phys-*

- iology*, 278(6), H2039–H2049. <https://doi.org/10.1152/ajpheart.2000.278.6.h2039> (cit. on pp. 10, 20)
- Robinson, N., Guan, C., & Vinod, A. (2015). Adaptive estimation of hand movement trajectory in an eeg based brain–computer interface system. *Journal of neural engineering*, 12(6), 066019. <https://doi.org/10.1088/1741-2560/12/6/066019> (cit. on p. 66)
- Rosenblatt, M. (2012). *Stationary sequences and random fields*. Springer Science & Business Media. <https://doi.org/10.1007/978-1-4612-5156-9>. (Cit. on p. 48)
- Rössler, O. E. (1976). An equation for continuous chaos. *Physics Letters A*, 57(5), 397–398. [https://doi.org/10.1016/0375-9601\(76\)90101-8](https://doi.org/10.1016/0375-9601(76)90101-8) (cit. on p. 15)
- Rowe, J. B., Hughes, L. E., Barker, R. A., & Owen, A. M. (2010). Dynamic causal modelling of effective connectivity from fmri: Are results reproducible and sensitive to parkinson’s disease and its treatment? *NeuroImage*, 52, 1015–1026. <https://doi.org/10.1016/j.NEUROIMAGE.2009.12.080> (cit. on pp. 6, x)
- Satterthwaite, F. E. (1946). An approximate distribution of estimates of variance components. *Biometrics bulletin*, 2(6), 110–114. <https://doi.org/10.2307/3002019> (cit. on p. 51)
- Sauer, T., Yorke, J. A., & Casdagli, M. (1991). Embedology. *Journal of statistical Physics*, 65(3), 579–616. <https://doi.org/10.1007/bf01053745> (cit. on p. 115)
- Schalk, G., Kubanek, J., Miller, K. J., Anderson, N., Leuthardt, E. C., Ojemann, J. G., Limbrick, D., Moran, D., Gerhardt, L. A., & Wolpaw, J. R. (2007). Decoding two-dimensional movement trajectories using electrocorticographic signals in humans. *Journal of neural engineering*, 4(3), 264. <https://doi.org/10.1088/1741-2560/4/3/012> (cit. on pp. 3, vii)
- Schreiber, T., & Schmitz, A. (1996). Improved surrogate data for nonlinearity tests. *Physical review letters*, 77(4), 635. <https://doi.org/10.1103/physrevlett.77.635> (cit. on pp. 59, 89)
- Scott, D. W. (1979). On optimal and data-based histograms. *Biometrika*, 66(3), 605–610. <https://doi.org/10.1093/biomet/66.3.605> (cit. on p. 12)
- Seeber, M., Scherer, R., Wagner, J., Solis-Escalante, T., & Müller-Putz, G. R. (2014). Eeg beta suppression and low gamma modulation are different elements of human upright walking. *Frontiers in human neuroscience*, 8, 485. <https://doi.org/10.3389/fnhum.2014.00485> (cit. on p. 25)
- Seeber, M., Scherer, R., Wagner, J., Solis-Escalante, T., & Müller-Putz, G. R. (2015). High and low gamma eeg oscillations in central sensorimotor areas are conversely modulated during the human gait cycle. *Neuroimage*, 112, 318–326. <https://doi.org/10.1016/j.neuroimage.2015.03.045> (cit. on pp. 4, 25, viii)
- Sherman, M. A., Seth, A., & Delp, S. L. (2013). What is a moment arm? calculating muscle effectiveness in biomechanical models using generalized coordinates, In *International design engineering technical conferences and computers and information in engineering conference*. American Society of Mechanical Engineers. <https://doi.org/10.1115/detc2013-13633>. (Cit. on p. 76)

- Silverman, B. W. (1986). *Density estimation for statistics and data analysis* (Vol. 26). CRC press. <https://doi.org/10.1201/9781315140919>. (Cit. on pp. 2, 10–14, 97, vi)
- Sinai Ya, G. (1959). On the notion of entropy of a dynamical system, In *Doklady of russian academy of sciences*. https://doi.org/10.1007/978-0-387-87870-6_1. (Cit. on p. 20)
- Singh, A., & Priênciape, J. C. (2011). Information theoretic learning with adaptive kernels. *Signal Processing*, 91(2), 203–213. <https://doi.org/10.1016/j.sigpro.2010.06.023> (cit. on pp. 10, 11)
- Spearman, C. (1904). The proof and measurement of association between two things. *American Journal of Psychology*, 15, 72–101. <https://doi.org/10.1037/11491-005> (cit. on p. 49)
- Spiers, H. J., & Maguire, E. A. (2006). Thoughts, behaviour, and brain dynamics during navigation in the real world. *NeuroImage*, 31, 1826–1840. <https://doi.org/10.1016/J.NEUROIMAGE.2006.01.037> (cit. on p. 91)
- Spiers, H. J., & Maguire, E. A. (2007). Decoding human brain activity during real-world experiences. *Trends in Cognitive Sciences*, 11, 356–365. <https://doi.org/10.1016/J.TICS.2007.06.002> (cit. on p. 31)
- Sprott, J. C., & Rowlands, G. (2001). Improved correlation dimension calculation. *International Journal of Bifurcation and Chaos*, 11(07), 1865–1880. <https://doi.org/10.1142/s021812740100305x> (cit. on p. 17)
- Srinivasan, V., Eswaran, C., & Sriraam, N. (2007). Approximate entropy-based epileptic EEG detection using artificial neural networks. *IEEE Transactions on information Technology in Biomedicine*, 11(3), 288–295. <https://doi.org/10.1109/titb.2006.884369> (cit. on p. 22)
- Stam, C. J. (2005). Nonlinear dynamical analysis of eeg and meg: Review of an emerging field. *Clinical neurophysiology*, 116(10), 2266–2301. <https://doi.org/10.1016/j.clinph.2005.06.011> (cit. on p. 25)
- Stephan, K. E., Penny, W. D., Daunizeau, J., Moran, R. J., & Friston, K. J. (2009). Bayesian model selection for group studies. *Neuroimage*, 46(4), 1004–1017. [https://doi.org/10.1016/s1053-8119\(09\)71793-8](https://doi.org/10.1016/s1053-8119(09)71793-8) (cit. on pp. 6, x)
- Takens, F. (1981). Detecting strange attractors in turbulence. In *Dynamical systems and turbulence, warwick 1980* (pp. 366–381). Springer. <https://doi.org/10.1007/bfb0091924>. (Cit. on pp. 1, 13, 73, 89, v)
- Teka, W. W., Hamade, K. C., Barnett, W. H., Kim, T., Markin, S. N., Rybak, I. A., & Molkov, Y. I. (2017). From the motor cortex to the movement and back again. *PloS one*, 12(6), e0179288. <https://doi.org/10.1371/journal.pone.0179288> (cit. on pp. 7, 67, 84, x)
- Teukolsky, S. A., Flannery, B. P., Press, W., & Vetterling, W. (1992). Numerical recipes in c. *SMR*, 693(1), 59–70 (cit. on p. 49).
- Thiel, M., Romano, M. C., & Kurths, J. (2003). Analytical description of recurrence plots of white noise and chaotic processes. *arXiv preprint nlin/0301027*. <https://doi.org/10.1142/s0218127407019949> (cit. on p. 20)

- Thomasson, N., Hoepfner, T. J., Webber Jr, C. L., & Zbilut, J. P. (2001). Recurrence quantification in epileptic EEGs. *Physics Letters A*, 279(1-2), 94–101. [https://doi.org/10.1016/S0375-9601\(00\)00815-X](https://doi.org/10.1016/S0375-9601(00)00815-X) (cit. on p. 25)
- Úbeda, A., Azorién, J. M., Farina, D., & Sartori, M. (2018). Estimation of neuromuscular primitives from eeg slow cortical potentials in incomplete spinal cord injury individuals for a new class of brain-machine interfaces. *Frontiers in computational neuroscience*, 12, 3. <https://doi.org/10.3389/fncom.2018.00003> (cit. on p. 66)
- van Wijk, B. C., Beek, P. J., & Daffertshofer, A. (2012). Neural synchrony within the motor system: What have we learned so far? *Frontiers in human neuroscience*, 6, 252. <https://doi.org/10.3389/fnhum.2012.00252> (cit. on pp. 4, vii)
- van Wijk, B. C., Cagnan, H., Litvak, V., Kühn, A. A., & Friston, K. J. (2018). Generic dynamic causal modelling: An illustrative application to parkinson's disease. *NeuroImage*, 181, 818–830. <https://doi.org/10.1016/J.NEUROIMAGE.2018.08.039> (cit. on pp. 6, x)
- Veslin, E., Dutra, M., Bevilacqua, L., Raptopoulos, L., Andrade, W., & Soares, J. (2019). Decoding elbow movement with kalman filter using non-invasive eeg, In *2019 IEEE Colombian conference on applications in computational intelligence (colcaci)*. IEEE. <https://doi.org/10.1109/colcaci.2019.8781800>. (Cit. on p. 66)
- Virtanen, P., Gommers, R., Oliphant, T. E., Haberland, M., Reddy, T., Cournapeau, D., Burovski, E., Peterson, P., Weckesser, W., Bright, J., Et al. (2020). Scipy 1.0: Fundamental algorithms for scientific computing in python. *Nature methods*, 17(3), 261–272. <https://doi.org/10.14293/s2199-1006.1.sor-life.a7056644.v1.rysreg> (cit. on pp. 35, 49)
- Wagner, J., Solis-Escalante, T., Grieshofer, P., Neuper, C., Müller-Putz, G., & Scherer, R. (2012). Level of participation in robotic-assisted treadmill walking modulates midline sensorimotor eeg rhythms in able-bodied subjects. *Neuroimage*, 63(3), 1203–1211. <https://doi.org/10.1016/j.neuroimage.2012.08.019> (cit. on p. 25)
- Wang, W., Chan, S. S., Heldman, D. A., & Moran, D. W. (2007). Motor cortical representation of position and velocity during reaching. *Journal of neurophysiology*, 97(6), 4258–4270. <https://doi.org/10.1152/jn.01180.2006> (cit. on pp. 4, 25, viii)
- Wang, X. (2005). Volumes of generalized unit balls. *Mathematics Magazine*, 78(5), 390–395. <https://doi.org/10.2307/30044198> (cit. on p. 97)
- Webber, C., & Marwan, N. (2015). Recurrence quantification analysis. *Theory and Best Practices*. <https://doi.org/10.1007/978-3-319-07155-8> (cit. on pp. 10, 23, 25, 26, 93)
- Welch, B. L. (1947). The generalization of 'student's' problem when several different population variances are involved. *Biometrika*, 34(1-2), 28–35. <https://doi.org/10.1093/biomet/34.1-2.28> (cit. on p. 51)
- Wessberg, J., Stambaugh, C. R., Kralik, J. D., Beck, P. D., Laubach, M., Chapin, J. K., Kim, J., Biggs, S. J., Srinivasan, M. A., & Nicolelis, M. A. (2000). Real-time prediction of hand trajectory by ensembles of cortical neurons in primates. *Nature*, 408(6810), 361–365. <https://doi.org/10.1038/35042582> (cit. on pp. 3, vii)

- Worsley, K. J., & Friston, K. J. (1995). Analysis of fmri time-series revisited—again. *Neuroimage*, 2(3), 173–181. <https://doi.org/10.1006/nimg.1995.1023> (cit. on pp. 34, 48)
- Worsley, K. (1996). An unbiased estimator for the roughness of a multivariate gaussian random field. *Montreal: Department of Mathematics and Statistics, University of McGill* (cit. on pp. 48, 54, 56).
- Wu, W., & Hatsopoulos, N. (2006). Evidence against a single coordinate system representation in the motor cortex. *Experimental brain research*, 175(2), 197–210. <https://doi.org/10.1007/s00221-006-0556-x> (cit. on pp. 4, 25, viii)
- Yang, Y.-X., Gao, Z.-K., Wang, X.-M., Li, Y.-L., Han, J.-W., Marwan, N., & Kurths, J. (2018). A recurrence quantification analysis-based channel-frequency convolutional neural network for emotion recognition from eeg. *Chaos: An Interdisciplinary Journal of Nonlinear Science*, 28(8), 085724. <https://doi.org/10.1063/1.5023857> (cit. on pp. 2, 9, vi)
- Yu, D., Small, M., Harrison, R. G., & Diks, C. (2000). Efficient implementation of the Gaussian kernel algorithm in estimating invariants and noise level from noisy time series data. *Physical Review E*, 61(4), 3750. <https://doi.org/10.1103/physreve.61.3750> (cit. on p. 10)
- Zbilut, J. P., Thomasson, N., & Webber, C. L. (2002). Recurrence quantification analysis as a tool for nonlinear exploration of nonstationary cardiac signals. *Medical engineering & physics*, 24(1), 53–60. [https://doi.org/10.1016/s1350-4533\(01\)00112-6](https://doi.org/10.1016/s1350-4533(01)00112-6) (cit. on pp. 4, 25, 27, viii)
- Zbilut, J. P., & Webber Jr, C. L. (1992). Embeddings and delays as derived from quantification of recurrence plots. *Physics letters A*, 171(3-4), 199–203. [https://doi.org/10.1016/0375-9601\(92\)90426-m](https://doi.org/10.1016/0375-9601(92)90426-m) (cit. on pp. 10, 23, 24)
- Zeidman, P., Friston, K., & Parr, T. (2022). A primer on variational laplace. <https://doi.org/10.31219/osf.io/28vwh> (cit. on p. 72)
- Zhang, X., & Zhou, P. (2012). Sample entropy analysis of surface emg for improved muscle activity onset detection against spurious background spikes. *Journal of Electromyography and Kinesiology*, 22(6), 901–907. <https://doi.org/10.1016/j.jelekin.2012.06.005> (cit. on p. 41)

Présentation en français

Résumé

L'électroencéphalographie (EEG) est une méthode non-invasive largement utilisée pour observer l'activité cérébrale. La haute résolution temporelle des signaux EEG en fait une méthode pratique pour analyser l'évolution temporelle de l'activité corticale pendant une tâche donnée. Cette thèse se focalise sur la tâche de reconstruction des mouvements du membre supérieur à un rythme propre, directement à partir des signaux EEG. En effet, de nombreuses études ont rapporté une cohérence entre l'activité des motoneurones et l'activité corticale dans les zones motrices pendant les tâches motrices. L'activité des motoneurones est liée à la force musculaire et donc au couple articulaire. Par conséquent, on pourrait supposer que l'activité corticale reflète certains aspects de la cinématique de l'articulation pendant le mouvement. Néanmoins, l'EEG ne capte qu'une partie infime et filtrée de l'activité corticale. Notre objectif est alors plus modestement d'évaluer dans quelle mesure les trajectoires articulaires peuvent être reconstruites à partir des signaux EEG.

Nous cherchons à identifier les caractéristiques et les emplacements des signaux EEG qui peuvent refléter la cinématique des articulations. Tout d'abord, nous étudions les mesures permettant de représenter les signaux EEG. Comme ces derniers présentent des propriétés de systèmes dynamiques non-linéaires, nous utilisons des mesures de complexité issues de la théorie du chaos et de la physique statistique pour compléter les caractéristiques spectrales classiques dans la caractérisation des signaux EEG. La qualité des mesures de complexité considérée dans cette thèse dépend du choix judicieux d'un paramètre de résolution. Nous proposons une nouvelle approche pour déterminer ce paramètre qui permet une estimation robuste des mesures. Nous validons notre méthode sur des données EEG simulées et réelles. Ensuite, nous évaluons la corrélation des mesures de complexité EEG avec l'activité EMG et la cinématique des articulations. Nous avons enregistré l'EEG, l'électromyographie (EMG) et les trajectoires articulaires de neuf sujets effectuant des mouvements cycliques, non contraints, du coude à leur rythme. En construisant des cartes statistiques paramétriques des caractéristiques non-linéaires de l'EEG, nous identifions les emplacements et les caractéristiques les plus corrélés avec le mouvement.

La performance des modèles qui reconstruisent la trajectoire du mouvement à partir des signaux EEG est usuellement évaluée à l'aide de coefficients de corrélation. Nous montrons que la distribution du coefficient dégénère pour les séries fortement corrélées comme la trajectoire du mouvement. Dans ce cas, la distribution de test du coefficient de corrélation peut être approximée en corrigeant son nombre de degrés de liberté. Nous proposons une nouvelle approche paramétrique pour estimer le nombre de degrés de liberté, qui donne les statistiques de test appropriées. À la lumière de la distribution corrigée, nous analysons les performances d'un modèle décodant les trajectoires de mouvement à partir des signaux EEG. Enfin, nous construisons un modèle biologiquement plausible de la tâche comprenant un modèle bras dynamique, un modèle de muscle de Hill, un modèle de la moelle épinière et un modèle de masse neuronale. Nous montrons les perspectives et les limites découlant de l'utilisation d'un modèle biophysique complexe avec un schéma d'inversion Bayésien de pointe.

Remerciements

La réalisation de ce manuscrit n'aurait pas été possible sans l'immense soutien de mes directeurs de thèses, de collègues, d'amis et de ma famille. Je tiens tout d'abord à exprimer ma gratitude envers mes directeurs de thèses, Sofiane Ramdani et Abderrahmane Kheddar. Depuis le tout premier entretien pour le poste, qui s'est terminé par une passionnante séance de tableau blanc, j'ai toujours apprécié les longues discussions avec Sofiane — près de la moitié étant sur le cinéma. Sofiane a toujours écouté mes suggestions avec considération et m'a fourni des retours éclairés, et je lui dois une grande partie de mon assurance scientifique. J'ai également beaucoup aimé travailler avec Abderrahmane, qui m'a toujours encouragé à repousser mes limites. Ma méthodologie scientifique a vraiment bénéficié des questions techniques pointues d'Abderrahmane, et sa volonté de relever des défis toujours plus grands à largement contribué à trouver les questions passionnantes que nous avons essayé d'aborder dans le travail de recherche.

En outre, je remercie Philippe Faure et Julien Modolo, pour avoir relu cette thèse, ainsi que Viktor Jirsa et Annick Lesne pour l'avoir examinée. Je suis également reconnaissant à Peter Zeidman et au bureau du 4ème étage du FIL pour les discussions passionnantes qui ont grandement contribué à l'introduction et à la discussion, et plus généralement, à ma compréhension des questions de recherche en cours. Je tiens également à remercier Karl Friston, pour avoir aimablement partagé ses connaissances approfondies sur les méthodes Bayésiennes pour les systèmes dynamiques, et pour ses suggestions techniques sur l'application du filtrage variationnel aux systèmes mécaniques classiques. Je tiens à remercier Annick Lesne pour avoir aimablement partagé son expertise sur les cartes de récurrence, les systèmes dynamiques et les systèmes complexes en général. Enfin, je dois remercier Amaury Dechaux pour les discussions passionnantes sur les neurosciences, les interfaces cerveau-ordinateur, l'inférence active, l'interprétation de Copenhague, et bien d'autres sujets.

J'ai beaucoup apprécié le temps passé au LIRMM, notamment grâce à de nombreux amis de l'équipe Interactive Digital Humans. Je suis reconnaissant à Julien Roux, Célia Saghour, Antonin Dallard, Carole Fournier, Hugo Lefèvre, Camille Mutschler, Louise Scherrer, et bien d'autres, pour tous les bons moments que nous avons passés presque tous les jours à Montpellier. Je tiens également à remercier Mathis Girault, Romain Barrat, Cédric Jannot, Théo Lassaube, Arnaud Lapicorey, Lucas Gavotto, ainsi que ma famille, pour leur soutien continu depuis tant d'années. "Je suis profondément reconnaissant envers Bruno Bidaud et Jean-Cristophe Leduc pour avoir éveillé ma curiosité scientifique et m'avoir guidé dans mon parcours scientifique.

Enfin, je tiens à exprimer ma profonde gratitude à mes parents pour le soutien et les encouragements constants et dévoués qu'ils m'ont apportés tout au long de ma vie, et à mes frères, pour ces grands moments que nous partageons, pour avoir continué à suivre leurs rêves, et pour avoir ainsi généré une telle atmosphère d'émulation.

Récapitulatif

1 Préambule

L'objectif initial de cette thèse était de contribuer aux interfaces cerveau-ordinateur par EEG, en suivant l'idée que ces signaux sont générés par des systèmes dynamiques chaotiques. En général, les signaux EEG sont traités par des méthodes linéaires telles que la transformée de Fourier (Cohen, 2014). Les signaux EEG ont de larges spectres et la puissance spectrale de certaines bandes de fréquences semble modulée indépendamment des autres bandes. Ainsi, l'analyse spectrale donne indéniablement un aperçu des réponses corticales induites par un événement ou une condition particulière. Cependant, les méthodes spectrales intègrent par nature l'évolution temporelle des signaux EEG, qui est souvent apériodique et irrégulière. Par conséquent, une analyse directe de l'évolution des signaux EEG pourrait mettre en évidence des caractéristiques corticales qui ne sont pas révélées par les analyses linéaires classiques. En particulier, il est attrayant d'analyser les signaux EEG du point de vue des systèmes dynamiques non-linéaires car, comme indiqué dans (Lehnertz, 1999) : *"le chaos déterministe offre une explication patente à un comportement apparemment irrégulier, caractéristique de l'activité électrique du cerveau"*. En d'autres termes, l'évolution apparente des signaux EEG justifie de compléter les analyses fréquentielles par des méthodes issues de la théorie du chaos, sans hypothèses particulières sur la nature chaotique de l'activité cérébrale (qui a déjà été largement débattue, voir (Korn & Faure, 2003)). Ainsi, ce travail de recherche repose sur l'idée que les mesures de complexité dynamique peuvent être appropriées pour compléter l'analyse fréquentielle. Le terme mesures de complexité dynamique, désigne de manière générique des caractéristiques diverses des systèmes dynamiques chaotiques, par exemple les dimensions fractales ou les entropies métriques. Nous suivons la définition du chaos comme "dynamique bornée apériodique dans un système déterministe avec une dépendance sensible aux conditions initiales" (Kaplan & Glass, 1997, Sec. 1.7, p.p. 27-28).

2 Estimer des mesures de complexité dynamique

Sachant que nous avons besoin de calculer des mesures de complexité dynamique, la première question que nous abordons est d'ordre plutôt général : comment choisir les paramètres d'estimation des mesures de complexité dynamique ? Il y a trois paramètres qui apparaissent de manière répétée dans différentes mesures de complexité dynamique. Les deux premiers paramètres configurent la reconstruction de l'espace des phases d'une série temporelle par la méthode des délais. Cette méthode découle du théorème de plongement de Takens (Takens, 1981), qui stipule que la trajectoire d'un vecteur composé d'observations retardées d'une série temporelle générée par un système chaotique constitue un plongement de l'attracteur sur lequel évolue la trajectoire en espace de phase du système chaotique. La dimension de reconstruction définit la dimension de l'espace vectoriel de la trajectoire reconstruite, c'est-à-dire le nombre d'observations retardées dans chaque vecteur. Il existe des méthodes pour sélectionner empiriquement la dimension de reconstruction, par exemple (Cao, 1997). En général, la

sélection de la dimension de reconstruction ne pose pas de problème car les attracteurs chaotiques ont une dimension finie ; par conséquent, les mesures de complexité dynamique convergent vers une valeur finie lorsque la dimension de reconstruction devient grande. Le second paramètre est le délai, qui définit le décalage temporel entre les coordonnées consécutives. Le décalage est sélectionné à partir des points critiques de la fonction d'autocorrélation ou de l'information mutuelle, de sorte à ce que les coordonnées soient généralement deux-à-deux indépendantes (Fraser & Swinney, 1986). Le troisième paramètre à sélectionner est le rayon, également appelé seuil ou résolution, selon la littérature. Ce paramètre définit la taille d'un voisinage dans l'espace des phases et est utilisé pour construire une *somme de corrélation* qui estime le nombre moyen de voisins dans l'espace des phases. La somme de corrélation est liée à plusieurs mesures de complexité telles que la dimension de corrélation, l'entropie de Kolmogorov-Sinai, ou des mesures issues de l'analyse par quantification des récurrences. Malgré son importance dans le calcul des mesures de complexité dynamiques, il n'existe que peu de méthodes rigoureuses pour sélectionner le rayon.

Dans le chapitre 2, nous proposons une méthode pour sélectionner rigoureusement le paramètre du rayon. Nous remarquons que l'erreur relative quadratique moyenne intégrée de la somme de corrélation est en fait l'erreur quadratique moyenne intégrée d'un estimateur par noyau. En d'autres termes, nous observons que le problème de sélection du rayon est, dans une certaine mesure, identique au problème de sélection d'une largeur de fenêtre optimale pour construire un histogramme de la densité de l'espace des phases. Ce changement de perspective est important car le problème de sélection d'une largeur optimale de fenêtre a été largement étudié dans la littérature statistique. Il existe donc une grande variété de méthodes parmi lesquelles choisir. Nous utilisons une méthode proposée dans (Silverman, 1986) pour dériver une règle de référence pour le rayon. Nous obtenons une expression analytique qui adapte le rayon en fonction du nombre de points dans la série – permettant d'utiliser un rayon plus petit lorsque la série est plus longue car la densité de points est plus élevée – et avec l'"échelle" de la série – permettant d'utiliser un rayon plus grand lorsqu'un plus grand volume de l'espace des phases est occupé. Dans des configurations empiriques courantes, notre règle de référence donne des valeurs qui sont proches des valeurs obtenues avec les règles empiriques traditionnellement utilisées. Ainsi, notre approche justifie la validité des règles empiriques trouvées dans la littérature et les étend à des conditions empiriques plus générales. Nous confirmons l'adéquation de notre méthode par des expériences numériques et une application à des signaux EEG.

3 Trouver l'application appropriée

Après avoir identifié une méthode appropriée pour sélectionner les paramètres d'estimation des mesures de complexité dynamique, nous avons cherché une application adéquate pour mettre en valeur l'utilisation de ces mesures. Dans la littérature, les mesures de complexité dynamique ont été utilisées pour identifier des régimes d'activité corticale dans des conditions particulières, par exemple pour détecter des crises d'épilepsie (Ocak, 2009) ou pour reconnaître des émotions (Yang et al., 2018). Dans ces applications, les mesures de complexité dynamiques sont utilisées comme caractéristiques pour la classification. En effet, les mesures de complexité fournissent une représentation des signaux EEG dans laquelle les différentes conditions peuvent être facilement distinguées. Nous cherchons ici à utiliser les mesures de complexité dynamiques pour résoudre un problème plus difficile : régresser l'évolution temporelle de variables continues à partir de signaux EEG. La régression est un problème plus complexe que la classification. Une tâche de classification nécessite de construire une fonction d'un domaine source vers un ensemble *dénombrable* qui est généralement non ordonné (par exemple, il n'y a pas d'ordre naturel entre les deux classes "épileptique" et "sain" utilisées dans la détection de l'épilepsie). La nature dénombrable et non ordonnée du domaine cible implique que la classification revient à définir des frontières de décision dans le domaine source (Bishop & Nasrabadi, 2006). En revanche, une tâche de régression implique de construire une fonction vers un domaine cible *indénombrable* qui admet une topologie (par exemple, un angle de coude de 90° est plus grand qu'un angle de coude de 70° , et plus proche d'un

angle de 89° que d'un angle de 83°). Par conséquent, la reconstruction de variables continues à partir de signaux EEG est une question difficile car la fonction de régression doit relier la topologie du domaine source à celle du domaine cible.

Nous nous sommes intéressés à la reconstruction de mouvement de coude à partir de signaux EEG chez l'humain. Notre choix a été motivé par plusieurs raisons. Tout d'abord, les mouvements sont faciles à mesurer et il est relativement simple de restreindre ces mouvements à des articulations ou des groupes de muscles spécifiques. Ensuite, réussir à reconstruire des mouvements à partir des signaux EEG serait un premier pas vers plusieurs applications biomédicales, par exemple, le contrôle d'exosquelettes ou la restauration de mouvement pour les personnes handicapées (Chapin et al., 1999) ou le contrôle d'humanoïdes (Gergondet et al., 2011) et l'incorporation (Aymerich-Franch et al., 2016). Enfin, la reconstruction de trajectoires de mouvements à partir de signaux EEG semble réalisable d'un point de vue physiologique. En effet, l'idée de reconstruire des trajectoires de mouvement à partir de l'activité corticale n'est pas nouvelle. Des travaux avec des réseaux d'électrodes sur des primates non humains ont mis en évidence diverses propriétés du cortex moteur pendant le mouvement (Georgopoulos et al., 1986). Ces travaux ont débouché sur des applications au décodage du mouvement chez le rat (Chapin et al., 1999), le macaque rhésus (Wessberg et al., 2000) et enfin chez l'homme à partir de signaux MEG (Georgopoulos et al., 2005) et ECoG (Schalk et al., 2007). Suite aux travaux sur des signaux MEG et ECoG, les chercheurs ont essayé de reconstruire les trajectoires de mouvement à partir des signaux EEG. Depuis les premiers efforts de (Bradberry et al., 2010), plus d'une vingtaine d'articles ont abordé la reconstruction de mouvements à partir de signaux EEG, avec différents degrés de réussite. Cette collection de travaux constitue une base de connaissances précieuse à partir de laquelle nous pouvons construire des méthodes de reconstruction des trajectoires de mouvement à partir de mesures de complexité dynamiques des signaux EEG.

A notre connaissance, aucun autre travail n'a utilisé des mesures de complexité dynamique pour reconstruire des trajectoires de mouvement à partir de signaux EEG. Il est donc légitime de s'interroger sur les motivations d'une telle approche. Notre motivation provient de divers travaux scientifiques ayant décrit le comportement multi-échelle des systèmes complexes. Un travail théorique important est issu de la théorie synergétique (Haken, 1978) qui considère que les systèmes ayant un grand nombre de composants individuels peuvent présenter un comportement global assez simple. Haken s'intéresse à l'explication de la réduction apparente du nombre de degrés de liberté dans les systèmes complexes. L'approche synergétique consiste à observer que quelques variables collectives, les *paramètres d'ordre*, évoluent lentement dans le temps et gouvernent le comportement à petite échelle des composants individuels. La synergétique a été admirablement appliquée pour formuler un modèle de synchronisation de phase pendant les mouvements des doigts (Haken et al., 1985). Pour résumer, la synergétique défend l'idée que les systèmes complexes tels que le cerveau (D'Angelo & Jirsa, 2022; Haken, 2006, 2013) peuvent être décomposés en paramètres collectifs lents et en états individuels rapides. Cette idée se retrouve également dans (Lesne, 2013), où la séparation des échelles de temps est considérée comme un équivalent temporel des méthodes de champ moyen et apparaît dans les systèmes complexes multi-échelles. Dans le cas spécifique du cerveau, (Kiebel et al., 2008) soutient qu'une hiérarchie d'échelles temporelles entre différents niveaux de traitement sensoriel est nécessaire pour s'adapter à un environnement qui évolue à différentes échelles de temps.

On peut cependant se demander si ces théories s'appliquent aux signaux EEG mesurés pendant le mouvement. L'approche intuitive pour analyser une telle séparation d'échelle temporelle serait d'utiliser des représentations temps-fréquence des signaux EEG. En effet, les variations de puissance spectrale dans le temps indiquent que la composition spectrale des composantes "rapides" du signal est changeante. D'un point de vue empirique, la modulation de la composition spectrale des signaux EEG au cours du mouvement a été observée à plusieurs reprises (van Wijk et al., 2012). En particulier, une modulation de l'activité dans la bande gamma pendant le mouvement a été observée pour les signaux MEG (Cheyne et al., 2008) et EEG (Ball et al., 2008). La modulation de l'activité à haute fréquence a également été observée dans le cas de la marche sur tapis roulant, où la fréquence du pas se reflète dans

l'amplitude de l'activité de la bande gamma (Seeber et al., 2015). Ainsi, les résultats empiriques de la littérature suggèrent qu'une forme de décomposition *lent-rapide* se produit pendant le mouvement. Nous pouvons donc envisager de construire un analogue de l'analyse temps-fréquence avec des mesures de complexité dynamiques en utilisant des méthodes de fenêtrage (Zbilut et al., 2002). Dans ce cas, nous nous attendons à ce que les mesures de complexité dynamique fenêtrées reflètent des changements lents dans la dynamique des variables rapides.

En résumé, nous soutenons l'idée que le mouvement pourrait être une application appropriée pour étudier les méthodes de régression de variables à partir de signaux EEG. En partant du principe que les systèmes complexes tels que le cerveau admettent une décomposition *lent-rapide*, nous proposons de suivre les changements lents dans la dynamique rapide des signaux EEG en utilisant des mesures de complexité dynamique par fenêtre. Notre proposition est soutenue par des observations trouvées dans la littérature, qui observent indirectement une décomposition lent-rapide par le biais d'analyses temps-fréquence de signaux EEG pendant le mouvement. Nous devons à présent identifier quelle variable de mouvement reconstruire à partir des signaux EEG.

Selon la littérature des neurosciences, il existe plusieurs variables de mouvement que nous pouvons tenter de régresser à partir des signaux EEG. En particulier, nous pouvons essayer de reconstruire directement une position, une vitesse ou une accélération. Le décodage de la position et de la vitesse serait motivé par des observations sur le comportement de l'activité neuronale dans le cortex moteur primaire pendant le mouvement (Churchland et al., 2006; Kakei et al., 1999; W. Wang et al., 2007), et le décodage de l'accélération pourrait être motivé par la relation entre l'activité du cortex moteur et la force (Cheney & Fetz, 1980; Georgopoulos et al., 1992). Il est important de noter que l'on doit choisir un référentiel pour décoder la position, la vitesse ou l'accélération. Par exemple l'espace cartésien ou l'espace articulaire. Comprendre dans quel référentiel les signaux neuronaux codent les trajectoires de mouvement est loin d'être une question triviale. Généralement, on suppose que le mouvement est décomposé d'un référentiel extrinsèque de haut niveau à un référentiel intrinsèque de bas niveau (Bear et al., 2020; Kakei et al., 2001). En revanche, il n'y a aucune preuve que le mouvement soit décomposé dans un référentiel commun et il est également probable que le cerveau n'utilise aucun des référentiels qui nous sont familiers (Wu & Hatsopoulos, 2006). La cohérence entre l'activité musculaire et l'activité du cortex moteur primaire pendant le mouvement est, au contraire, bien documentée (Baker et al., 1997; Conway et al., 1995; Mima & Hallett, 1999) et ne nécessite pas de sélectionner une variable cinématique particulière ni un référentiel. Ainsi, dans un premier temps, nous nous concentrons directement sur la reconstruction de certains aspects de l'activité musculaire.

Dans le chapitre 3, nous présentons notre dispositif expérimental et notre méthode de collecte de données. Nous avons collecté les données de mouvement ainsi que les signaux EEG et EMG de 9 participants en bonne santé. Les participants devaient effectuer des mouvements non contraints de flexion/extension unilatérale du coude, continus et à un rythme non imposé, pendant des essais d'environ 23 à 24 secondes. La tâche — mouvements à un rythme propre avec de longues durées — a été choisie pour reproduire des conditions de mouvement normales. Nous avons calculé les mesures d'analyse par quantification des récurrences sur fenêtres glissantes (WRQA) des signaux EEG et EMG. Nous avons appliqué un filtre passe-haut aux signaux EEG et EMG avant de calculer les mesures afin de supprimer les interactions parasites avec les composantes basse fréquence des signaux. Nous avons ensuite effectué une analyse paramétrique pour étudier les relations entre les mesures WRQA des signaux EEG et EMG pendant le mouvement. Nos résultats indiquent qu'il y a une diminution apparente de la "complexité" des signaux EEG au début du mouvement qui est maintenue pendant le mouvement. Ce résultat avait déjà été rapporté par (Pitsik et al., 2020) et notre travail complète de manière rigoureuse ces résultats avec des cartes topographiques des corrélations entre les mesures WRQA des signaux EEG et EMG pendant le mouvement. Nous observons des corrélations négatives significatives entre les mesures des signaux EMG du bras en mouvement et les mesures des signaux EEG du côté controlatéral du cerveau.

4 Reconstruire des trajectoires de mouvement

Après avoir observé qu'il existe une corrélation significative entre les mesures de complexité dynamique des signaux EEG et EMG pendant le mouvement, nous essayons d'aborder la question de la reconstruction des trajectoires de mouvement à partir des signaux EEG. Avant de reconstruire le mouvement à partir de mesures de complexité dynamique, nous avons tenté de reproduire la littérature sur le "décodage" du mouvement à partir de signaux EEG basse fréquence tel qu'il a été décrit par certains auteurs' (Bradberry et al., 2010; Ofner & Müller-Putz, 2012). L'objectif de cette étape intermédiaire était de mieux comprendre le décodage du mouvement et de disposer d'une méthode de référence à laquelle comparer d'autres méthodes. Nous avons observé que les modèles utilisés dans la littérature avaient des performances disparates sur nos données. En particulier, la performance des modèles semble être liée négativement à la variabilité du mouvement et positivement à la vitesse du mouvement. Nos observations nous ont incité à analyser plus en profondeur la question de l'évaluation des performances des modèles de reconstruction.

Dans la littérature, le coefficient de corrélation de Pearson est la mesure généralement choisie pour évaluer la performance des modèles de reconstruction de mouvement à partir de signaux EEG. Les travaux connexes font état de coefficients de corrélation de l'ordre de 0.3, ce qui est faible par rapport aux normes de la littérature statistique. Cependant, nous pouvons nous attendre à un grand nombre de valeurs aberrantes dans une tâche de reconstruction et donc accepter qu'un faible coefficient de corrélation soit déjà un bon résultat. En d'autres termes, nous pouvons accepter qu'un bon modèle de reconstruction soit peu performant en raison du faible rapport signal/bruit des signaux EEG et de la présence d'artefacts. Nous ferons avec cette hypothèse, mais soulignons qu'utiliser un coefficient de corrélation comme mesure de performance pose un autre problème important.

Dans le chapitre 4, nous étudions le comportement des coefficient de corrélation de Pearson et de Spearman dans le cas de séries temporelles. En particulier, nous rapportons que de grands coefficients de corrélation entre deux séries aléatoires et indépendantes sont fréquemment observés lorsque les séries sont fortement autocorrélées. Par ailleurs, il est possible de corriger la distribution de test du coefficient de corrélation, qui est obtenue sous l'hypothèse que les échantillons sont non corrélés, pour prendre en compte l'autocorrélation des séries (M. Bartlett, 1935). La correction nécessite simplement de configurer la distribution de test avec un certain nombre de degrés de liberté effectifs, c'est-à-dire la taille d'un échantillon indépendant qui produirait les mêmes statistiques que la série autocorrélée (Afyouni et al., 2019). Le nombre de degrés de libertés utilisé pour configurer la distribution de test est important car il détermine l'étalement de la distribution de test et donc la probabilité qu'un coefficient de corrélation entre séries indépendantes soit observé loin de zéro.

Nous proposons une méthode paramétrique pour calculer le nombre de degrés de liberté effectifs. Notre méthode est plus simple que les méthodes trouvées dans la littérature et particulièrement adaptée à notre application. Notre approche utilise la fonction d'autocorrélation de la série en utilisant l'autocorrélation d'un processus gaussien, ce qui nous permet de dériver une expression analytique pour calculer le nombre de degrés de liberté effectifs d'une série. De plus, nous utilisons la formule de Rice (Rice, 1944), qui donne le nombre moyen de passages par zéro d'un processus stochastique (Cox & Miller, 2017). La formule de Rice nous permet d'exprimer le nombre de degrés de libertés effectifs d'un processus stochastique comme le nombre moyen de passages par zéro du processus multiplié par $\sqrt{\pi}$. Nous confirmons d'abord l'adéquation de notre méthode par des expériences numériques. Ensuite, nous reproduisons deux modèles de reconstruction de mouvement à partir de signaux EEG basse fréquence. Nous examinons de plus près la relation entre la performance des modèles et les paramètres du mouvement à la lumière de l'expression dérivée de la formule de Rice. Nous observons que les mouvements dont la période est longue ou variable sont systématiquement associés à des performances de reconstruction insignifiantes. En d'autres termes, les modèles de reconstruction ne donnent des résultats significatifs qu'avec des mouvements à oscillation rapide, c'est-à-dire avec un grand nombre de degrés de liberté effectifs et une faible variabilité du mouvement.

5 Une autre approche

Les résultats du chapitre 4 relativisent l'adéquation des modèles trouvés dans la littérature avec nos données. Une alternative serait de construire des modèles plus complexes et plus expressifs. Des modèles plus complexes pourraient théoriquement représenter des fonctions de régression plus complexes. Poussée à l'extrême, cette approche conduirait à utiliser des modèles d'apprentissage profond pour reconstruire les trajectoires de mouvement à partir des signaux EEG. Nos tentatives d'utilisation de modèles d'apprentissage profond n'ont pas donné lieu à des performances satisfaisantes. En outre, nous avons réalisé que les modèles d'apprentissage profond devaient être utilisés avec précaution sur les signaux EEG : les modèles d'apprentissage profond peuvent apprendre la tâche de reconstruction à partir d'artefacts plutôt que de signaux cérébraux. Cela est dû au faible rapport signal/bruit des signaux EEG ainsi qu'à la complexité de la tâche et à la présence répétée d'artefacts dus au mouvement. Par exemple, la contraction des muscles du cou ou les mouvements des yeux qui suivent la main pourraient être utilisés par le modèle pour reconstruire les trajectoires de mouvement, comme cela a déjà été observé dans les modèles linéaires qui, pour l'EOG, contribuent largement aux performances de reconstruction (Ofner & Müller-Putz, 2012). Par conséquent, même si un modèle d'apprentissage profond pouvait reconstruire des trajectoires de mouvement à partir des signaux EEG, il serait difficile de défendre le fait que le modèle "décode" le mouvement à partir de l'activité corticale. Nous avons donc décidé d'abandonner les modèles d'apprentissage profond en faveur d'une approche bayésienne basée sur des modèles biologiques plausibles, c'est-à-dire des modèles composés de paramètres ayant une interprétation physique et qui peuvent être estimés pour expliquer les données.

La structure et les paramètres de ces modèles sont guidés par des preuves physiques ou physiologiques (ou par l'intuition). Ces modèles sont particulièrement utiles pour découvrir les processus qui sous-tendent des situations cliniques spécifiques, par exemple dans le cas de l'épilepsie (Cooray et al., 2016; Jirsa et al., 2014; Papadopoulou et al., 2015) ou la maladie de Parkinson (Rowe et al., 2010; van Wijk et al., 2018). La distribution des paramètres du modèle peut être estimée à partir des données en utilisant des schémas d'inversion bayésiens qui permettent de pondérer les valeurs des paramètres qui expliquent correctement les données par des connaissances a priori sur leur distribution (Penny et al., 2011). La forme spécifique des modèles bayésiens permet de comparer facilement les modèles (Stephan et al., 2009) et donc de tester des hypothèses sur la structure du modèle, par exemple sur la connectivité entre différentes régions (K. J. Friston, 2011).

Nous considérons ici un modèle neuro-musculo-squelettique (NMS) intégrant des modèles de l'activité cérébrale, de l'activité musculaire et du squelette. Bien que considérer un cas général nécessiterait une modélisation complexe, nous pouvons construire un modèle simplifié mais réaliste de notre tâche de mouvement du coude. Dans le chapitre 5, nous construisons un modèle NMS de ce mouvement en assemblant des modèles du bras, des muscles triceps et biceps, et des colonnes corticales. Notre modèle squelettique est un modèle de bras simplifié en deux dimensions avec deux degrés de liberté, régi par la dynamique des corps rigides. Nous utilisons le modèle musculaire de Hill (Hill, 1938) pour le fléchisseur du coude, *biceps brachii*, et l'extenseur du coude, *triceps brachii*. Les modèles musculaires de Hill donnent une relation entre la fréquence d'activation des neurones moteurs du muscle et la force linéaire générée par les fibres musculaires. De plus, nous avons modélisé les "capteurs" du muscle, les afférents de type *Ia* et *Ib*, en utilisant une relation linéaire trouvée dans la littérature (Teka et al., 2017). Nous utilisons ensuite un modèle de la moelle épinière (Li et al., 2015), qui transforme l'activité corticale motrice en entrées musculaires. Un modèle de la moelle épinière est nécessaire pour rendre compte du phénomène d'inhibition réciproque des muscles antagonistes (Bear et al., 2020; Li et al., 2015). Enfin, nous proposons de modéliser l'activité corticale à l'aide de modèles de masse neuronale (David & Friston, 2003).

L'objectif du chapitre 5 est de mettre en évidence les perspectives d'utilisation de tels modèles mais aussi de souligner les limites actuelles des méthodes d'inversion existantes. En théorie, nous pourrions étudier des hypothèses sur l'évolution temporelle de l'activité corticale pendant le mouvement en utilisant notre modèle NMS. Cependant, il est très compliqué d'inverser un tel modèle ou de formuler

des hypothèses en raison de la nature particulière du modèle considéré ici — un modèle dynamique hiérarchique, c'est-à-dire une cascade de modèles entrée-état-sortie — et de la nature continue de notre expérience. Nous avons implémenté une des méthodes de pointe pour l'inversion de systèmes dynamiques, à savoir l'algorithme Dynamic Expectation Maximization (DEM) (K. J. Friston et al., 2008). L'algorithme DEM permet de résoudre des problèmes d'estimation triple, c'est-à-dire d'estimation conjointe de trajectoires d'états, de paramètres et des hyperparamètres du modèle (par exemple, la variance du bruit). En essayant d'inverser notre NMS avec DEM, nous avons découvert d'importants problèmes survenant lors de l'estimation d'un modèle complexe intégrant de multiples échelles temporelles au cours d'une expérience en conditions normales. Nous pensons qu'il est nécessaire de répondre à ces questions pour permettre l'exploration d'hypothèses sur les réponses du cerveau lors de telles expériences.

6 Synthèse

Dans cette thèse, nous avons voulu relever le défi d'estimer des trajectoires des mouvements du bras humain en considérant les propriétés dynamiques non-linéaires des signaux EEG. Nous avons abordé plusieurs facettes du problème. Dans le chapitre 2, nous proposons une nouvelle approche pour déterminer un paramètre important dans l'estimation des mesures de complexité non-linéaire, permettant d'obtenir des estimations robustes dans des conditions expérimentales. Dans le chapitre 3, nous étudions les relations entre les mesures de complexité dynamique des signaux EEG et EMG pendant le mouvement. Nous avons recueilli des données dans le cadre d'une expérience impliquant des mouvements libres de flexion-extension du coude. Dans le chapitre 4, nous proposons une nouvelle méthode pour estimer correctement la signification des coefficients de corrélation dans le cas de séries temporelles fortement autocorrélées. En appliquant notre méthode à des modèles classiques de reconstruction de trajectoires de mouvements à partir de signaux EEG, nous mettons en évidence les limites potentielles de l'utilisation de coefficient de corrélation comme mesure de performance. Dans le chapitre 5, nous examinons la question de l'identification d'un modèle biologiquement plausible de notre tâche de décodage du mouvement à partir des signaux EEG, et nous analysons les perspectives ainsi que les défis importants qui découlent d'une question de modélisation aussi complexe. Enfin, les leçons apprises et les extensions possibles de ce travail sont présentées dans le chapitre 6.